



TECHNISCHE  
UNIVERSITÄT  
WIEN  
Vienna | Austria

# DIPLOMA THESIS

## Bio-based Photopolymers for lithography-based 3D printing

Performed at

Institute of Applied Synthetic Chemistry

TU Wien



under the supervision of

Univ. Prof. Dipl.-Ing. Dr. techn. Robert Liska

Univ. Ass. Dipl.-Ing. Dr. techn. Stefan Baudis

by

Antonella FANTONI, BSc

01608053



---

Antonella Fantoni, BSc



Die approbierte gedruckte Originalversion dieser Diplomarbeit ist an der TU Wien Bibliothek verfügbar  
The approved original version of this thesis is available in print at TU Wien Bibliothek.



Die approbierte gedruckte Originalversion dieser Diplomarbeit ist an der TU Wien Bibliothek verfügbar  
The approved original version of this thesis is available in print at TU Wien Bibliothek.



Die approbierte gedruckte Originalversion dieser Diplomarbeit ist an der TU Wien Bibliothek verfügbar  
The approved original version of this thesis is available in print at TU Wien Bibliothek.

# Danksagung

Zunächst möchte ich mich bei **Prof. Robert Liska** bedanken. Danke, dass Du mir die Möglichkeit geboten hast, eine Diplomarbeit auf einem spannenden und nachhaltigen Themengebiet zu absolvieren. Danke, dass Du immer ein offenes Ohr für meine Probleme hattest und mir immer mit Rat zur Seite gestanden bist.

**Dr. Stefan Baudis** gilt ebenso ein besonderer Dank. Danke, dass Du als direkter Betreuer meiner Arbeit immer für Anregungen zur Seite gestanden bist und mir einen Einblick in die Welt der biobasierten Polymere gegeben hast.

Ein großes Dankeschön gebührt an dieser Stelle auch **Lisa Sinaweil**. Danke, dass Du mich als dein Küken aufgenommen hast und immer mit wertvollen Tipps zur Seite gestanden bist.

Auch bei dem Betreuer meiner Bachelorarbeit **Dr. Markus Kury** möchte ich mich bedanken. Ohne Dich wäre ich nie in der FBMC gelandet und würde diese Diplomarbeit nicht verfassen! Vielen Dank auch an **Dr. Thomas Koch** und **Stefan Zellhofer** für die Hilfe und rasche Durchführung aller mechanischen Tests.

Meinem „Spacebench-Buddy“ **Roland** möchte ich für die angenehme Arbeitsatmosphäre danken. Danke, dass Du mich so herzlich aufgenommen hast und deine Geduld für all meine Probleme.

Auch bei dir, **Florian**, möchte ich mich bedanken. Danke, dass Du als IPN Experte immer für Fragen da warst und mir von Anfang ein wichtiger Wegbegleiter warst. Danke, dass Du deine Expertise und dein Wissen mit mir geteilt hast und mir immer zur Seite gestanden bist.

Meinen Laborkollegen möchte ich für die großartige Arbeitsatmosphäre danken. Besonders **Tina, Carola, Klaus** und **Dani** möchte ich meinen Dank für eine unglaublich schöne Zeit im Labor und abseits davon aussprechen. Auch allen anderen Mitgliedern der FBMC **Ricky, Betti, Markus, Larissa, Philip, Anna, Stephan, Raffael, Pontus, Ralle, Babsi, Flocki, Michi, David, Anna Z., Jakob, Oskar** und **Sarah** möchte ich danken.

Da bekanntlich das Beste zum Schluss kommt, möchte ich mich am Ende bei meiner Familie für die nie endende Unterstützung bedanken. Danke an meine Mama **Barbara** und meinen Papa **Stefano**, ohne deren Hilfe und Vertrauen ich nie so weit gekommen wäre. Danke auch an meinen Opa **Werner** und meine Nonna **Maria**, die immer hinter mir stehen.

Zwei besonderen Menschen möchte ich diese Arbeit widmen: meiner Oma **Gerti**, die immer auf mich aufpasst und meiner Schwester **Elena**. Danke, dass Du immer für mich da bist, immer an mich glaubst und mir immer die beste Freundin sein wirst.

**DANKE!**



Die approbierte gedruckte Originalversion dieser Diplomarbeit ist an der TU Wien Bibliothek verfügbar  
The approved original version of this thesis is available in print at TU Wien Bibliothek.

## Abstract

In the last decades, the market for additive manufacturing technologies (AMTs) has grown exponentially, as they enable the fabrication of tailor-made products with complex architectures. Apart from ceramics and metals, polymers have shown great potential to be processed *via* additive manufacturing. Especially photopolymers have gained in importance and are widely used in vat photopolymerization techniques, where a liquid formulation is cured in a layer-by-layer approach upon irradiation. In general, commercially available photopolymerizable resins are based on (meth)acrylates and epoxides from fossil resources, inherently bearing a large carbon footprint. Furthermore, highly crosslinked thermosetting materials are obtained, that suffer from insufficient mechanical properties and prevent the materials to be recyclable or (bio)degradable.

Therefore, a great effort has been made to develop sustainable alternatives to accelerate the transition towards a circular economy. Popular strategies to transform biomaterials into polymerizable monomers include the epoxidation of unsaturated moieties or conversion of epoxy-, acid- or hydroxyl groups into (meth)acrylates.

Additionally, different strategies have been reported to toughen 3D printed polymers, such as addition of nanoparticles, rubber phases or chain transfer agents. Addition of photopolymerizable macromolecular compounds represents another toughening strategy, since their integration into polymer networks decreases the crosslinking density, leading to enhanced toughness.

A different approach to include toughening agents into polymer networks is the creation of interpenetrating polymer networks (IPNs). Here, at least two polymer networks are physically interlocked without being covalently bond to each other. Thereby, properties of the independent networks can be combined.

Consequently, IPNs consisting of bio-based soft and hard matrices were synthesized and investigated in this thesis. At first, both networks were optimized separately and characterized regarding their (photo)reactivity and mechanical properties. Therefore, a soft network was derived from poly(ethylene glycol), obtained *via* fermentation of sugars, which was modified with photopolymerizable methacrylate groups and providing elasticity to the IPN. To enhance the reactivity, the influence of reactive diluents was analyzed. By contrast, the hard network was composed of epoxides, that deliver hardness and rigidity. Bio-based precursors for epoxy monomers were obtained *via* dehydration of sugar or depolymerization of lignin. To overcome the inhomogeneity of photopolymerized epoxides, polyaddition agents and their applicability in AMTs was analyzed. Finally, the combination of the optimized networks gave bio-based IPNs and their (thermo)mechanical properties were determined.



Die approbierte gedruckte Originalversion dieser Diplomarbeit ist an der TU Wien Bibliothek verfügbar  
The approved original version of this thesis is available in print at TU Wien Bibliothek.



# Kurzfassung

In den letzten Jahrzehnten ist der Markt für additive Fertigungstechnologien exponentiell gewachsen, da sie die Herstellung maßgeschneiderter Produkte mit komplexen Geometrien ermöglichen. Neben Keramiken und Metallen werden Polymere immer häufiger additiv gefertigt. Insbesondere Photopolymere haben an Bedeutung gewonnen. Hier wird eine flüssige Formulierung in einem Schicht-für-Schicht-Verfahren durch Bestrahlung gehärtet. Im Allgemeinen basieren kommerziell erhältliche photopolymerisierbare Harze auf (Meth)acrylaten und Epoxiden aus fossilen Ressourcen, die von Natur aus einen großen CO<sub>2</sub>-Fußabdruck aufweisen. Darüber hinaus werden hochvernetzte Materialien erhalten, die unter unzureichenden mechanischen Eigenschaften leiden und verhindern, dass die Materialien wiederverwertbar oder (bio)abbaubar sind.

Daher wurden nachhaltige Alternativen entwickelt, um den Übergang zu einer Kreislaufwirtschaft zu beschleunigen. Beliebte Strategien zur Umwandlung von Biomaterialien in polymerisierbare Monomere umfassen die Epoxidierung ungesättigter Einheiten oder die Umwandlung von Epoxy-, Säure- oder Hydroxylgruppen in (Meth)acrylate.

Darüber hinaus wurde über verschiedene Strategien berichtet, um 3D-gedruckte Polymere zäher zu machen, wie z. B. die Zugabe von Nanopartikeln, Kautschukphasen oder Kettenübertragungsmitteln. Die Zugabe von photopolymerisierbaren makromolekularen Verbindungen stellt eine weitere Möglichkeit zur Zähigkeitsverbesserung dar, da die Vernetzungsdichte verringert wird, was zu einer erhöhten Zähigkeit führt.

Ein Weg diese hochmolekularen Komponenten in Polymere einzubauen sind interpenetrierende Polymernetzwerke (IPNs). Dabei sind mindestens zwei Polymernetzwerke physikalisch miteinander verbunden, ohne chemische Bindungen untereinander auszubilden. Somit können die Eigenschaften der unabhängigen Netzwerke miteinander kombiniert werden.

Daher wurden in dieser Arbeit IPNs bestehend aus biobasierten weichen und harten Netzwerken synthetisiert und untersucht. Zunächst wurden beide Netzwerke separat optimiert und hinsichtlich ihrer (Photo-)Reaktivität und mechanischen Eigenschaften charakterisiert.

Das weiche Netzwerk wurde von Poly(ethylenglycol) abgeleitet, erhalten durch Fermentation von Zuckern, mit photopolymerisierbaren Methacrylatgruppen modifiziert und soll dem IPN Elastizität verleihen. Zur Steigerung der Reaktivität wurde der Einfluss von Reaktivverdünnern analysiert. Im Gegensatz dazu bestand das harte Netzwerk aus Epoxiden, die für Härte und Steifigkeit sorgen. Biobasierte Vorstufen für Epoxidmonomere wurden durch Dehydratisierung von Zuckern oder Depolymerisation von Lignin gewonnen. Um die Inhomogenität von photopolymerisierten Epoxiden zu überwinden, wurden Polyadditionsmittel und ihre Anwendbarkeit in AMTs analysiert. Schließlich ergab die Kombination der optimierten Netzwerke biobasierte IPNs und ihre (thermo)mechanischen Eigenschaften wurden bestimmt.



Die approbierte gedruckte Originalversion dieser Diplomarbeit ist an der TU Wien Bibliothek verfügbar  
The approved original version of this thesis is available in print at TU Wien Bibliothek.

# Table of contents

<b>Introduction</b>	1
<b>Objective</b>	20
<b>State of the Art</b>	21
<b>General Part</b>	30
<b>Summary</b>	108
<b>Experimental Part</b>	113

	<b>Gen.Part</b>	<b>Exp.Part</b>
<b>1 Soft network from renewable resources</b>	31	113
<i>1.1 Synthesis and characterization of macromolecular component</i>	32	113
1.1.1 Synthesis of poly(ethylene glycol) dimethacrylate (PEG20kMA)	32	113
1.1.2 Hydroxyl value determination of PEG20kMA	33	114
1.1.3 Molecular weight determination <i>via</i> size exclusion chromatography	35	115
<i>1.2 Effect of PEG20kMA in photopolymerizable formulations</i>	35	116
1.2.1 Choice of a reactive diluent from renewable resources	35	116
1.2.2 Miscibility of macromolecular PEG20kMA in IBMA	36	116
1.2.3 Rheology measurements	37	116
1.2.4 Network appearance and haptic behavior of the soft network	38	117
<i>1.3 Photoreactivity of the soft matrix</i>	40	118
1.3.1 Photo-DSC analysis	40	118
1.3.2 RT-NIR-photorheology	42	119
<i>1.4 Mechanical studies of the soft matrix</i>	45	120
1.4.1 Thermomechanical properties of the soft matrix	45	120
1.4.2 Tensile tests of the soft matrix	47	120
<b>2 Hard Network from renewable resources</b>	49	122
<i>2.1 Monomers from starch and cellulose</i>	49	122
2.1.1 Overview	49	122
2.1.2 Synthesis of Epoxidized Isosorbide (ISE)	51	122

2.1.2.1 Synthesis of Diallyl Isosorbide <i>via</i> potassium tert-butoxide	-	122
2.1.2.2 Synthesis of Diallyl Isosorbide <i>via</i> phase-transfer catalyst TBAB	-	123
2.1.2.3 Synthesis of Epoxidized Isosorbide (ISE)	-	124
<i>2.2 Monomers from lignin</i>	53	126
2.2.1 Overview	53	126
2.2.2 Synthesis of Diglycidyl Ether of Vanillyl Alcohol	53	126
2.2.3 Synthesis of Triglycidyl Ether of Phloroglucinol (PHTE)	54	127
2.2.3.1. Synthesis of PHTE <i>via</i> tetraethylammonium bromide	-	127
2.2.3.2. Synthesis of PHTE <i>via</i> tetrabutylammonium chloride	-	129
<i>2.3 Photopolymerization of bio-based epoxy monomers</i>	56	130
2.3.1 Photoreactivity <i>via</i> Photo-DSC analysis	56	130
2.3.2 Epoxy group conversion <i>via</i> ATR-IR	59	130
2.3.3 Thermomechanical properties of photopolymers	60	130
2.3.4 Tensile tests of photopolymers	63	131
<i>2.4 Thermal polymerization of bio-based epoxy monomers</i>	65	132
2.4.1 Investigation of suitable co-monomers	66	132
2.4.2 Investigation of suitable catalysts	67	132
2.4.3 Proton NMR study	71	134
2.4.4 Thermal reactivity <i>via</i> differential scanning calorimetry (DSC)	77	135
2.4.5 Rheology and Storage stability	79	136
2.4.5.1 Rheology measurements	79	136
2.4.5.2 Storage stability of polyaddition formulations	80	136
2.4.6 Thermomechanical properties of polyaddition polymers	82	137
2.4.7 Tensile tests of polyaddition polymers	85	137
<b>3 Interpenetrating Polymer Networks</b>	88	138
<i>3.1 Initiation and co-reactivity study</i>	89	138
3.1.1 Proton NMR study	89	138
3.1.2 Photo-DSC study	91	138
<i>3.2 Form-stability of IPNs</i>	93	138
<i>3.3 Investigation of (thermo)mechanical properties of IPNs</i>	95	139
3.3.1 DMTA-Analysis	95	141
3.3.2 Tensile tests	101	141

<b>Abbreviations</b>	142
<b>Materials and Methods</b>	145
<b>References</b>	148
<b>Appendix</b>	157



Die approbierte gedruckte Originalversion dieser Diplomarbeit ist an der TU Wien Bibliothek verfügbar  
The approved original version of this thesis is available in print at TU Wien Bibliothek.

# Introduction

## Additive manufacturing technologies

Additive manufacturing technologies (AMTs), also known as 3D-printing, were first introduced in the late 1980s and have emerged as an important tool for the fabrication of customized parts with complex three-dimensional shapes.<sup>1</sup> AMT generate 3D objects by a controlled *layer-by-layer* addition of material. The desired product geometry is processed *via* computer-aided design (CAD) and virtually sliced to processable layers that are later fabricated in the AMT process (Figure 1). This fabrication method is in contrast to subtractive technologies, where the final object is obtained upon selective removal of a material e.g. CNC milling. The advantages of AMTs are the possibility to introduce high shape complexity, design flexibility and low material waste.<sup>2</sup>

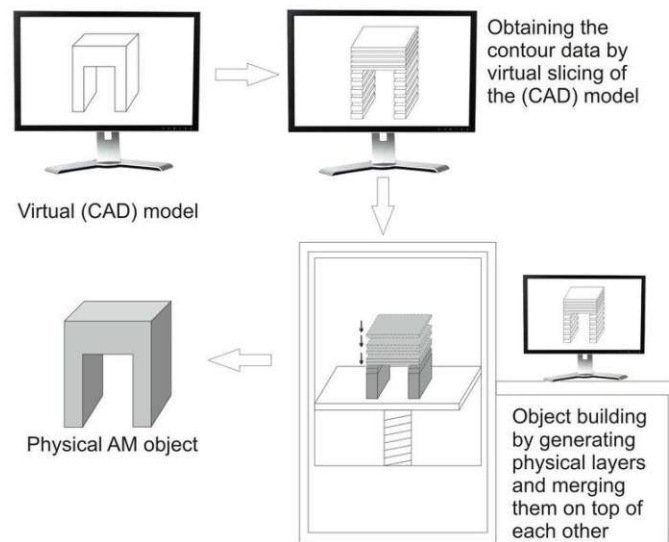


Figure 1: Principle of AMT<sup>3</sup>

Today, AMTs can be found in number of industrial sectors, such as aerospace, automotive, electronics and medical technologies.<sup>4</sup> Currently, AMT is able to produce parts from metals, ceramics and polymers, whereby polymers cover up to 50% of the AM material market.<sup>4</sup> One of the most common techniques is Fused deposition Modeling (FDM), where a thermoplastic polymer is extruded through a heated nozzle and the molten material is deposited in a layer-by-layer fashion.<sup>5</sup> Additionally, high energy of a laser beam can be used to fuse a polymer powder in Selective Laser Sintering (SLS).<sup>6</sup>

However, lithography-based AMTs (L-AMTs) focus on the curing of liquid photopolymer resins using a light source. Commonly, L-AMTs are described as vat photopolymerization, since the photoreactive formulation is placed inside a vat and the polymer is synthesized *in situ* by a

photopolymerization reaction. Depending on the light source, this process can be further divided into laser-stereolithography (L-SLA) and digital light processing-based stereolithography (DLP-SLA).<sup>1,7,8</sup>

### Laser-Stereolithography

In Laser-SLA, a laser beam is utilized to initiate the photopolymerization. As the laser beam scans the resin surface in the xy-plane, the liquid monomer formulation solidifies and one layer is formed. Depending on the arrangement of the apparatus, bottom-up or dimensional SLA (light exposure from the top to build an object in a bottom-up manner) and top-down or inverted SLA (irradiation through a transparent bottom plate) are applied (Figure 2). Following the first curing step, the building platform is moved in z-direction, immersing the solidified polymer in the liquid monomer vat and the next layer is cured. By repeating this process, the final 3D object is formed.<sup>7</sup> Hence, SLA offers the fabrication of complex structures with highest resolution provided by the accuracy of the laser and a low feature size.<sup>8</sup> Still, shrinkage during polymerization and insufficient material strength of the photopolymer may arise from this process.<sup>9</sup> Besides, SLA is constraint to low viscous and highly reactive formulations (such as epoxides and (meth)acrylates).<sup>1</sup>

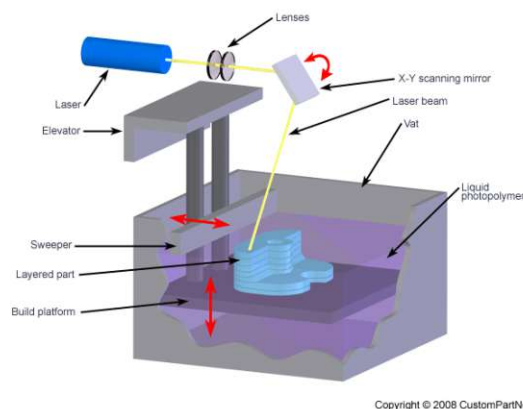


Figure 2: Schematic setup of a laser stereolithography (SLA)<sup>10</sup>

### Digital Light Processing

By contrast, DLP-SLA uses a digital mirror device, such as an LED light engine, to irradiate each layer of the photopolymer resin simultaneously. Similar to SLA, bottom-up setups are commonly in use. (Figure 3)



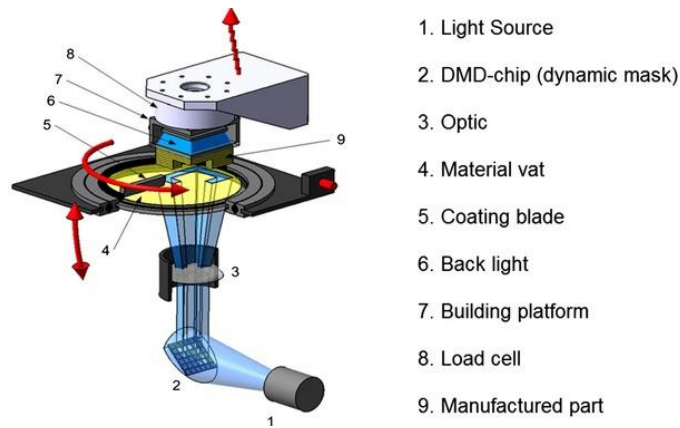


Figure 3: Schematic setup of a DLP-SLA printer<sup>11</sup>

Since photopolymerization takes place at once in each layer, the printing process is accelerated compared to L-SLA. Additionally, the light source is usually less expensive, making DLP-SLA more economical. However, poorer lateral resolution is achieved. Analogous to L-SLA, low viscous formulations comprised of (meth)acrylates and epoxides are applied.<sup>1</sup>

## Photopolymerization

The essential mechanism behind stereolithography is photopolymerization. Thereby, a liquid photoreactive formulation is irradiated by a light source (e.g. UV, visible or near IR radiation), activating the photoinitiator that induces the polymerization reaction to yield a solidified layer that is processable in L-AMTs.<sup>12</sup> Photopolymerization benefits from its rapid curing, low energy costs, solvent-free conditions and low cost of instrumentation and is commonly used for coatings, inks, dental- and biomaterials.<sup>9, 13</sup>

A typical photopolymerizable formulation is comprised of four components: photoinitiator, monomers, reactive diluents and additives.<sup>14</sup> While the main task of monomers is the network formation, their chemical nature also influences the mechanical properties of the final material.<sup>15</sup> Additionally, reactive diluents are added to decrease the viscosity of the photoresin, enhancing its processability in AMT without the use of solvents. Based on the application, additives such as antioxidants, plasticizers, fillers or pigments are added.<sup>16</sup> The crucial component to trigger photopolymerization is the photoinitiator, that enables the formation of a reactive species after the photochemical event. Depending on the generated species after photoinitiator decay, the polymerization can be divided into two subgroups: radical and ionic photopolymerization, whereby free radical and cationic photopolymerization are most common.

## Free radical photopolymerization

Radical-induced photopolymerization belongs to the class of chain-growth polymerizations and can be categorized into 4 general reaction steps: (1) initiation, (2) propagation, (3) chain transfer and (4) termination (Figure 4).<sup>13</sup>

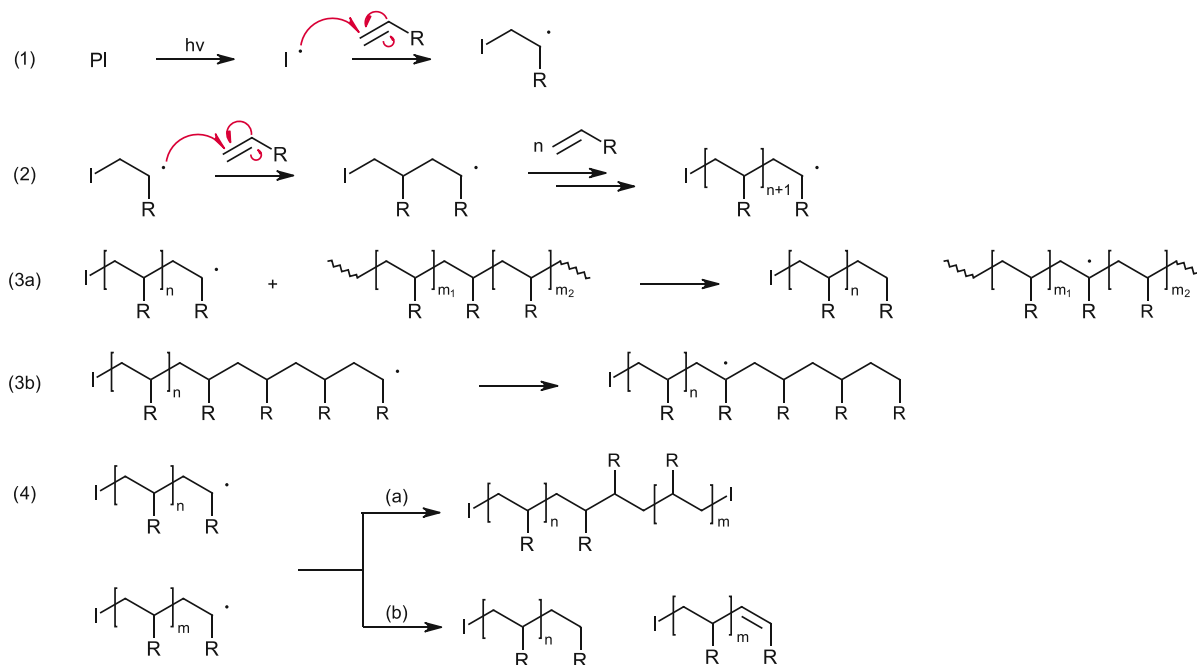


Figure 4: Steps of the radical photopolymerization: (1) initiation, (2) propagation, (3a) intermolecular chain transfer, (3b) intramolecular chain transfer and (4) termination by either combination (a) or disproportionation (b).

Upon irradiation with an appropriate wavelength, the photoinitiator (PI) undergoes homolytic dissociation to yield a radical species ( $R\cdot$ ). Thereafter, radicals add to reactive groups (unsaturated double bond) of the monomers and the propagation species is formed, that subsequently adds to consecutive monomers and polymer chain grows. The polymerization is terminated either *via* combination or disproportionation. Additionally, chain transfer can occur, transferring a radical from a growing polymer chain to another species (intermolecular) or it is stabilized intramolecularly.<sup>17</sup>

As already mentioned, photoinitiators play a key role in free radical photopolymerization, as they initiate the photopolymerization reaction. They are classified according to their dissociation mechanism into:<sup>12</sup>

- Norrish Type I
- Norrish Type II photoinitiators.

Type I photoinitiators undergo photo-fragmentation in a unimolecular reaction, whereby a homolytic  $\alpha$ -cleavage near an aromatic carbonyl groups generates radicals (Figure 6). Compounds such as hydroxyacetophenones, dialkylacetophenones, benzil ketals or benzoyl phosphine oxides follow Type I photo-fragmentation.<sup>18, 19</sup> Furthermore, acylgermanes find application as Type I PI.<sup>20</sup> Figure 5 depicts commonly used Type I PI.

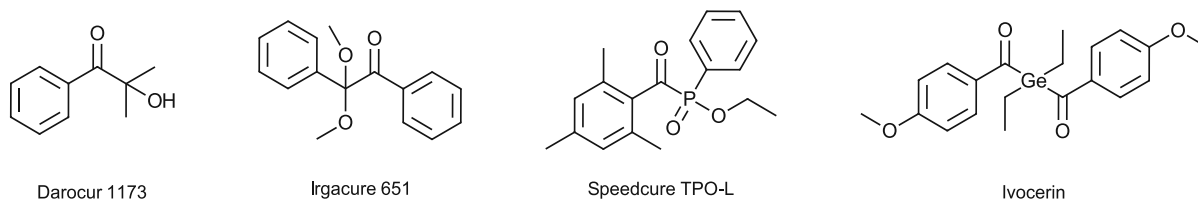


Figure 5: Commonly used Type I PI: Hydroxyacetophenone (Darocur 1173), benzil ketal (Irgacure 651), benzoyl phosphine oxide (TPO-L) and acylgermanes (Ivocerin)

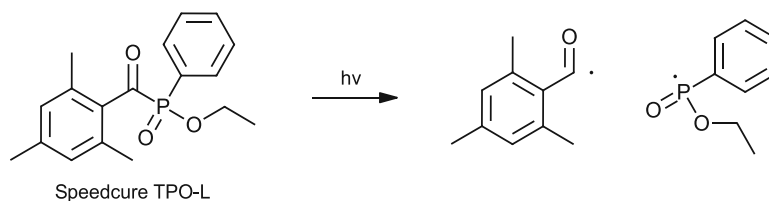


Figure 6: Photoinitiated fragmentation of TPO-L

By contrast, Type II photoinitiators follow a bimolecular initiation mechanism. Upon irradiation, radicals are formed without cleaving the initiator molecule and subsequently react with a co-initiator. *Via* proton abstraction or electron transfer, initiating radicals are formed.<sup>21</sup> Typical Type II PIs consist of campherquinone, benzophenone or thioxanthenes, while tertiary amines act as co-initiators (Figure 7).<sup>18</sup>

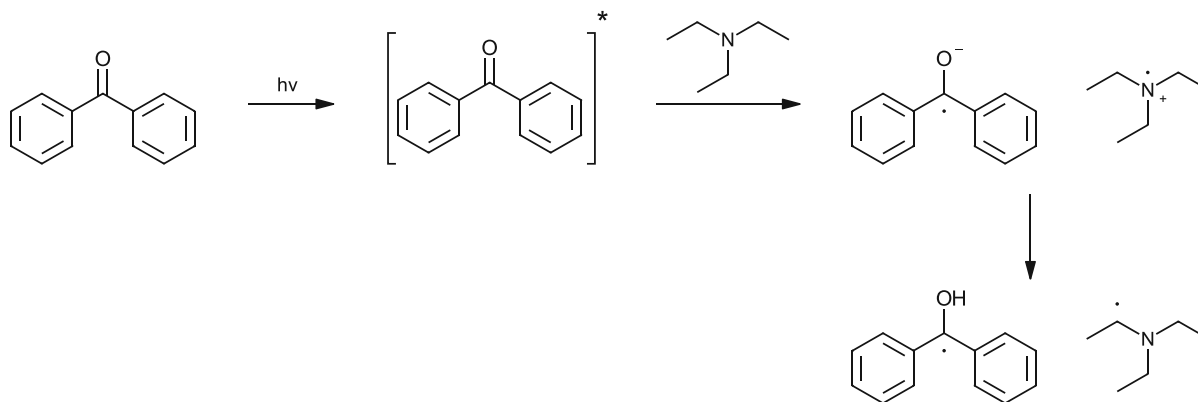


Figure 7: Generation of radicals via Type II PI: After excitation of benzophenone, the co-initiator (tertiary amine) enables the formation of initiating radicals in a bimolecular reaction.

Summarizing, type I PIs show higher reactivity since two radicals are formed during photolysis and therefore favorable for 3D printing processes.<sup>22</sup> Although type II PIs exhibit lower photoinitiation efficiency, they show higher biocompatibility and are less prone to oxygen inhibition.<sup>12</sup>

Following initiation, the generated radicals add to unsaturated double bonds of the monomers. In stereolithography, acrylates display high reactivity even at room temperature. Widely used compounds are depicted in Figure 8 and form photopolymerized networks (di- or multifunctional) or chains (monofunctional).

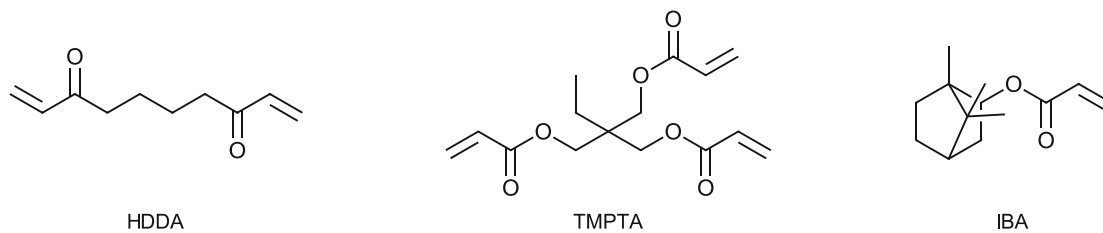


Figure 8: Frequently used acrylate monomers for coatings and stereolithography: 1,6 hexanediol diacrylate (HDDA), trimethylolpropane triacrylate (TMPTA) and isobornyl acrylate (IBA).

Methacrylates show decreased photoreactivity compared to acrylates, but exhibit lower toxicity, high heat deflection temperature and their thermal stability is enhanced.<sup>9, 23</sup> Some frequently used methacrylate monomers are depicted in Figure 9.

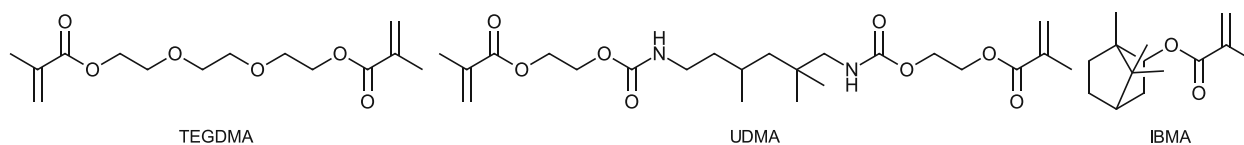


Figure 9: Methacrylate monomers triethylenglykol dimethacrylat, (TEGDMA), urethane methacrylate (UDMA) and isobornyl methacrylate (IBMA).

Apart from its high reactivity and therefore rapid curing, considerable issues arise from the radical-induced nature of the photopolymerization. Atmospheric oxygen is able to inhibit radical polymerization by the formation of low reactive peroxides, leading to incomplete polymerization on the surface.<sup>24</sup> Furthermore, termination reactions (Figure 4) lead to high molecular weight distributions in the polymer.

### Cationic photopolymerization

Another widely used light-induced polymerization is cationic photopolymerization, which represents a chain-growth polymerization *via* cationic propagating species. Similar to free radical polymerization, the reaction mixture includes a cationic photoinitiator and cationically polymerizable monomers, such as epoxides or oxetanes.<sup>25</sup>

In the case of cationic photopolymerization, strong acids are produced by photoacid generators (PAG).<sup>18</sup> Highly reactive PAG comprise diaryliodonium<sup>26</sup> and triarylsulfonium<sup>27</sup> salts (Figure 10).

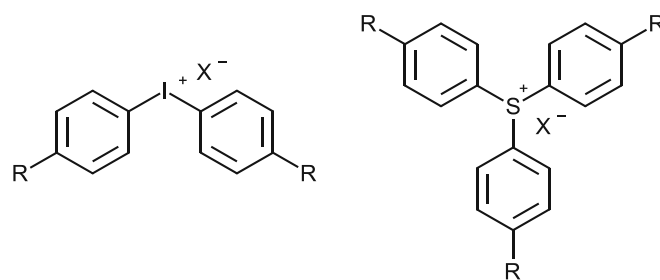


Figure 10: Diaryliodonium and triarylsulfonium salts for PAG with counterions X<sup>-</sup>.

While the cation determines the photoreactivity, bearing the chromophoric group and undergoing photo decomposition, the anion does not take part in the photochemical event. However, anions generate the photo acid and therefore influence the polymerization.<sup>28</sup>

Typically used anions are hexafluoro phosphates (PF<sub>6</sub><sup>-</sup>), hexafluoro antimonates (SbF<sub>6</sub><sup>-</sup>) and tetra(pentafluorophenyl) borates (B(C<sub>6</sub>F<sub>5</sub>)<sub>4</sub><sup>-</sup>).

Upon irradiation, the PAG is elevated into an excited singlet state. Considering the energetic instability of this state, decomposition (either homolytic or heterolytic) takes place and the formed intermediate abstracts a proton from the reaction mixture and the necessary super acid is generated.<sup>29</sup> The photolytic formation of the acid is depicted in Figure 11.

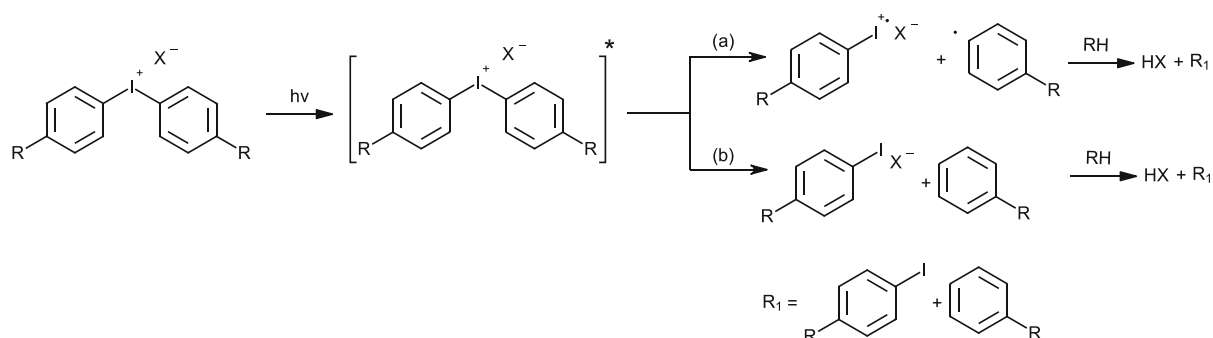


Figure 11: Decomposition of the PAG: a) via homolytic cleavage and b) via heterolytic cleavage

Cationic polymerization is initiated by strong Brønsted or Lewis acids, releasing a proton or carbocation, that adds to the monomer. In cationic photopolymerization, the super acid is produced *via* decomposition of the PAG (Figure 12, step 1). Since epoxides are the most prominent monomers for cationic photopolymerization, their polymerization mechanism is highlighted in Figure 12. After the formation of an oxonium species (Figure 12, step 2), the inherent ring strain of the oxirane ring leads to the formation of a carbocation. This highly reactive carbocation undergoes a nucleophilic attack by another monomer, giving a tertiary oxonium species and consecutive ring-opening reaction. By successive nucleophilic addition of monomers (Figure 12, step 3), the polymerization propagates to form a polymer.<sup>30</sup>

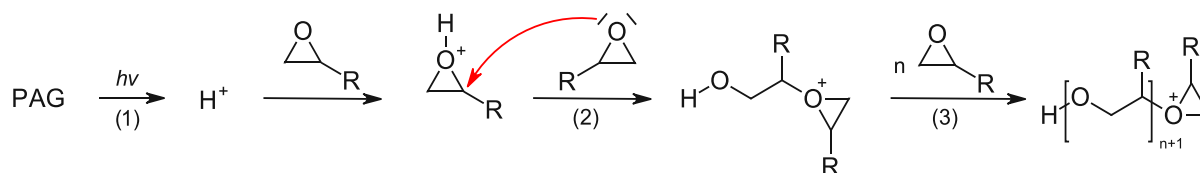


Figure 12: Scheme of cationic photopolymerization of epoxy monomers

Due to the nature of the initiating species and the polymerization mechanism, cationic photopolymerization offers beneficial curing behavior compared to radical photopolymerization. Firstly, cationic photopolymerization benefits from oxygen insensitivity. Furthermore, the polymerization can take place without light since long-lived protonic acids are generated during initiation and allow a so-called *dark-curing* reaction.<sup>31, 32</sup> Ideally, termination is solely happening *via* recombination with anions from PAGs. But alkaline species (amines, urethanes, thiols or basic fillers) are able to quench the protons and prematurely terminate the polymerization. On the other hand, small amounts of hydroxyl containing impurities such as water or alcohols act as chain transfer agents. Herein, the active center is transferred away from the growing polymer chain, promoting chain transfer events and affecting not only the speed of polymerization, but also the network structure of the polymer.<sup>33</sup> By the addition of HO-containing compounds, more flexible and more homogeneous materials may be obtained.<sup>33, 34</sup> Apart from all its advantages, cationic photopolymerization suffers from lower reactivity compared to free radical photopolymerization and only a few monomer classes meet the requirements for rapid cationic photopolymerization at moderate temperatures and ultimately their application in AMTs.<sup>35</sup>

Epoxy monomers are the most important monomer class in cationic photopolymerization, due to their exceptional mechanical properties, low shrinkage and good chemical and thermal resistance.<sup>36</sup> Figure 13 highlights the industrially most significant epoxy monomers. The aromatic bisphenol-A diglycidyl ether (BADGE) is by far the most important epoxy monomer in industry. Nevertheless, safety concerns regarding the precursors bisphenol A (potential estrogen mimic) and epichlorohydrin (oral and dermatologic toxin) address the need for safer alternatives.<sup>37, 38</sup> Cycloaliphatic epoxy monomers, as ECC, exhibit better weather resistance, lower viscosity and good electrical properties, compared to BADGE.<sup>39, 40</sup>

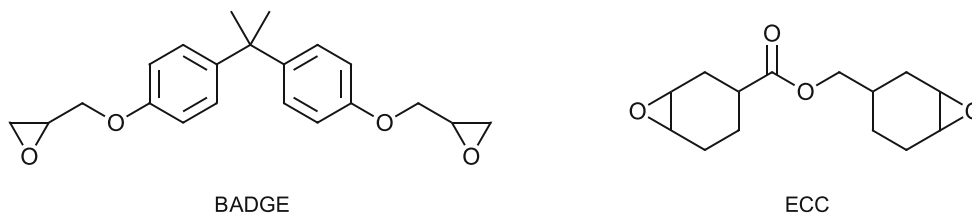


Figure 13: Examples for common used epoxy monomers bisphenol-A diglycidyl ether (BADGE) and 3,4-epoxycyclohexylmethyl-3,4-epoxycyclohexylcarboxylate (ECC).

## Thermal Epoxy Polymerization

While cationic photopolymerization enables the use of epoxy resins for L-AMTs, thermal curing of epoxy resins (for e.g. coating or structural applications) is still of higher relevance in industry. To obtain crosslinked epoxy thermosets, a variety of crosslinking agents is used, whereby (poly)amines and anhydrides represent commonly used curing agents.<sup>41,42</sup> In contrast to chain growth in radical and ionic polymerization, thermal curing of epoxy resins follows a step-growth manner (Figure 14).<sup>9</sup>

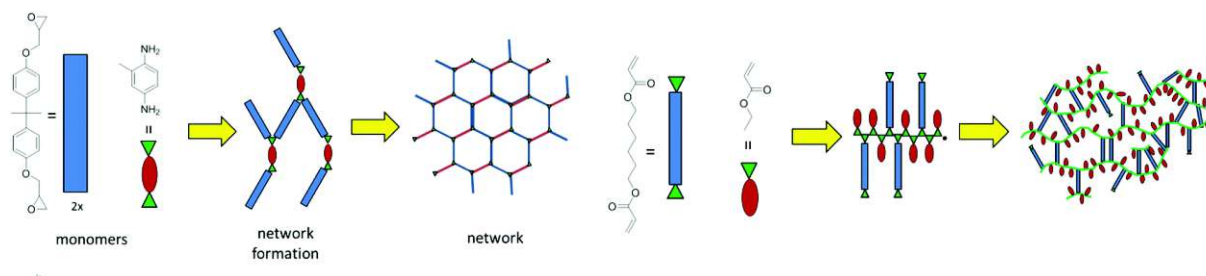


Figure 14: Network formation via step-growth is epoxy thermosets (right) and chain-growth in radical polymerization of acrylates (left), adapted from <sup>9</sup>

As discussed previously for chain growth polymerizations, only monomers react with the active site on the end of the growing polymer chain, decreasing the monomer concentration steadily with time. The kinetic chain length is rather high in the early stages of polymerization, leading to inhomogeneous network formation. This leads to high molecular weights at low conversions (see Figure 15). By contrast, step-growth polymerizations are characterized by high monomer consumption at the beginning, whereas the molecular weight increases gradually and high molecular weights are only obtained at high conversions, leading to significantly longer reaction times.<sup>43</sup>

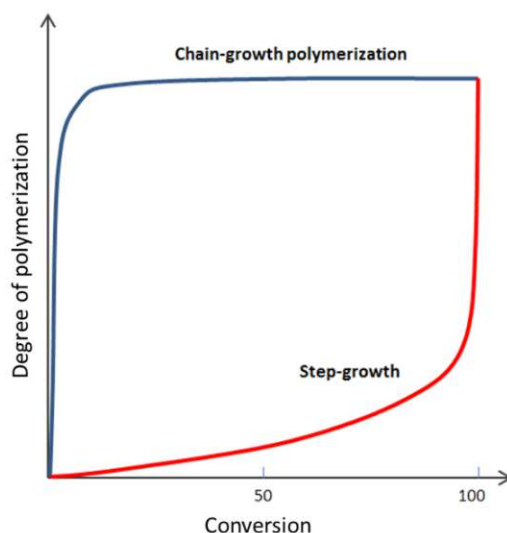


Figure 15: Schematic overview of step-growth and chain-growth polymerization, adapted from <sup>10</sup>

### (Poly)amines as curing agents

Amines are the most commonly used curing agents for epoxy resins in industry, due to their low viscosity and high reactivity.<sup>9,41</sup> Figure 16 depicts curing agents based on amine chemistry. In general, primary amines exhibit higher reactivity compared to secondary amines, leading to fast gelation but poorer storage stability. Due to the increased nucleophilicity, aliphatic amines (e.g. DETA) outperform aromatic amines (e.g. MPD), although the latter are used for their good thermal properties. Cycloaliphatic amines (e.g. PACM), although being more expensive, are exhibit low toxicity.<sup>9</sup>

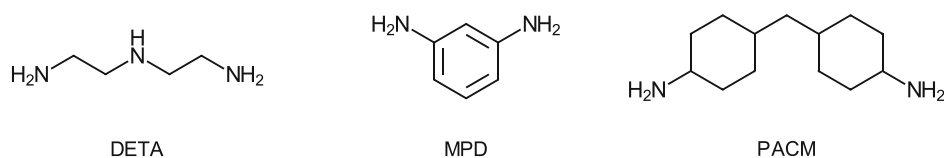


Figure 16: Commonly used amine-derived curing agents for epoxy resins. Diethylenetriamine (DETA), *m*-phenylenediamine (MPD) and 4,4-diaminodicyclohexylmethane (PACM).

The curing process of epoxy-amine systems involves a ring opening addition of the nitrogen atom to the oxirane ring. The primary amine is able to react with two epoxy moieties, whereas secondary amines add to only one epoxy ring. Therefore, primary amines exhibit higher reactivity compared to secondary amines. To obtain crosslinked networks, both epoxy and amine monomer should be at least difunctional.<sup>44</sup> Figure 17 depicts the crosslinking reaction of an epoxy monomer with primary and secondary amines.



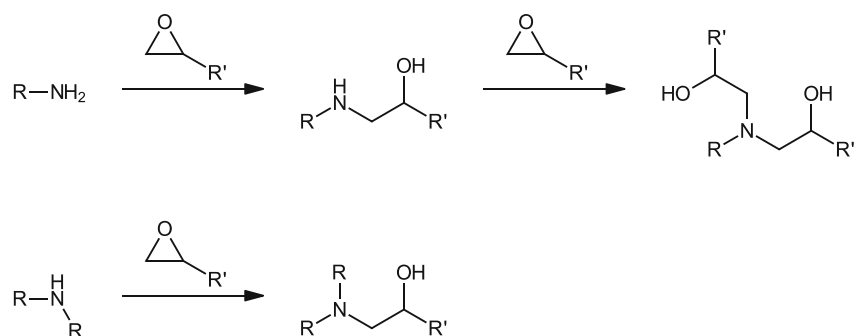


Figure 17: Mechanism of epoxy-amine curing. The primary amine (top) reacts with two epoxy moieties, while the secondary amine (bottom) only reacts with one epoxy ring

The crosslinking reaction is accompanied by the formation of hydroxy groups that catalyze the reaction. The autocatalytic behavior originates from an interaction between epoxy ring, amine and hydroxy groups, that form a trimolecular complex (Figure 18) and promote the nucleophilic attack of the amine.<sup>45</sup>

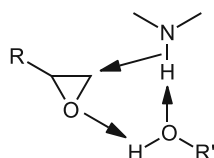


Figure 18: Catalyzed nucleophilic attack of an amino group onto an epoxy group in the presence of an alcohol.

### Acid anhydrides as curing agents

Apart from amines, acid anhydrides represent the second most used class of curing agents. Formulations of epoxy-anhydride systems benefit from better storage stability, excellent electrical properties, good chemical and physical resistance.<sup>46</sup> Widely used anhydride curing agents are phthalic anhydride (PA) and hexahydrophthalic anhydride (HHPA) (Figure 19).

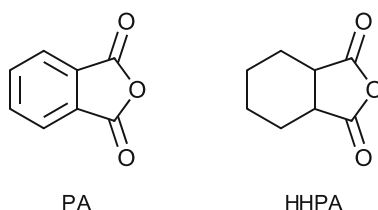


Figure 19: Acid anhydride curing agents: phthalic acid anhydride (PA) and hexahydrophthalic anhydride (HHPA).

Compared to amine curing agents, acid anhydrides require significantly higher temperatures (>200 °C) to react.<sup>47</sup> The mechanism of anhydride-epoxy crosslinking is depicted in Figure 20. Secondary alcohols, from the backbone of the epoxy resin or from a prior epoxy-amine ring-opening reaction, react with the anhydride. Therefore, catalytic amounts of tertiary amines are added to catalyze the crosslinking reaction. After the first esterification, the formed carboxylic acid may add to the oxirane ring, giving secondary hydroxy groups to propagate the reaction.<sup>48</sup>

Moreover, secondary alcohols are able to compete with the esterification by an etherification between epoxides and alcohols.

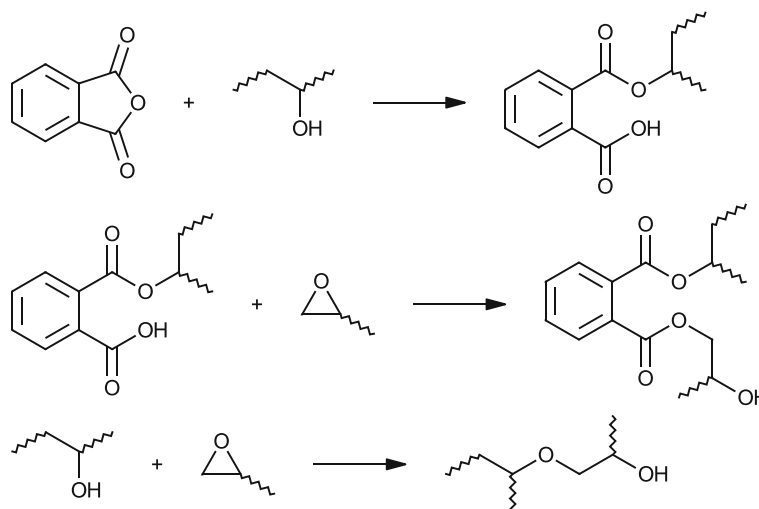


Figure 20: Mechanism of epoxy anhydride crosslinking.

### Lewis Bases as curing agents

The three membered ring structure of the epoxy ring exhibits highly polarized oxygen-carbon bonds<sup>49</sup> and therefore, also Lewis bases, such as tertiary amines or imidazoles, are commonly used to cure epoxy resins in an anionic homopolymerization. Furthermore, they can be used as co-curing agents together with amines and anhydrides. Lewis bases act as nucleophiles and attack the three-membered ring upon formation of an alkoxide (1), that can attack evermore epoxy monomers (2) and so, the polymerization propagates (3) in a chain growth reaction (Figure 21).<sup>45</sup>

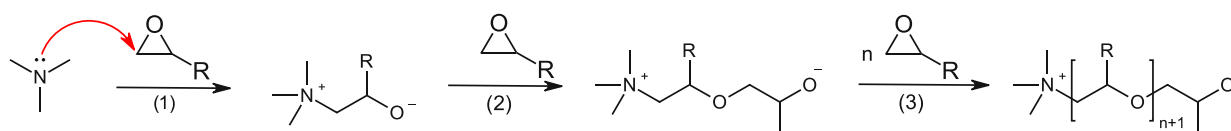


Figure 21: Mechanism of anionic ring-opening polymerization of epoxides.

Additionally, Lewis bases promote the polymerization of epoxy resins with proton donating species, such as alcohols, phenols or thiols. In the presence of weak proton donating species (alcohols), chain transfer will occur from the epoxy-amine intermediate. According to the mechanism in Figure 22, proton donors become the propagating sites. Those alkoxide ions can once again attack epoxy monomers and continue the polymerization.<sup>45</sup>

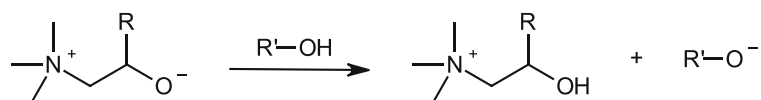


Figure 22: Chain-transfer reaction of alcohols and growing polymer chains.

In the case of stronger proton donating species (e.g. phenols, thiols), proton transfer occurs directly to the amine, generating an anion (phenyl or thiol) that acts as nucleophile and promotes the epoxy ring-opening.<sup>45</sup> Commonly used tertiary amines include DMAMP, TDMAMP and imidazoles (Figure 23).

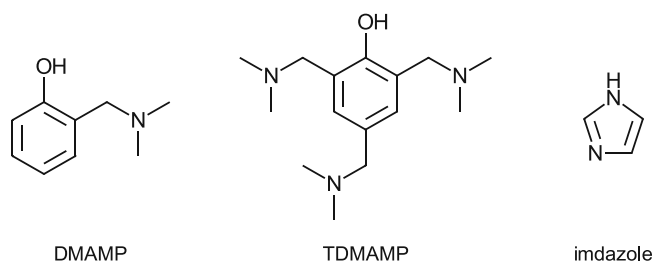


Figure 23: Commonly used tertiary amines as epoxy curing agents and curing accelerators.

## Sustainable monomers for additive manufacturing technologies

The majority of monomers for AMT, especially for L-AMT, are derived from fossil resources, inherently bearing a large carbon footprint.<sup>50, 51</sup> As previously mentioned, (meth)acrylates and epoxides from fossil resources are frequently used. In order to accelerate the transition towards a circular economy, development of bio-based, (bio)degradable and recyclable inks for L-AMT has been focused in the last decade.<sup>7</sup>

Monomers from renewable resources pave the way to substitute petroleum-based molecules with natural and abundant substances. To impart (photo)polymerizable functionalities into naturally derived precursors, different synthetic strategies are used:<sup>7</sup>

- epoxidation of unsaturated moieties using oxidation agents and
- conversion of epoxy-, acid- and hydroxyl groups into (meth)acrylates by reaction with (meth)acrylic acid or its anhydride.

Among the most commonly reported bio-based resins are modified vegetable oils. Vegetable oils such as soybean or palm oil are produced in high volumes every year, making them easily available and cheap.<sup>52</sup> A general structure of a triglyceride is depicted in Figure 24, whereby R<sub>1-3</sub> represent saturated and unsaturated C<sub>12-22</sub> chains from fatty acids that are connected via ester linkages with glycerol.

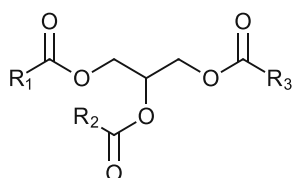


Figure 24: Scheme of a triglyceride.

The C=C double bonds of fatty acids can easily be modified to epoxy groups and thereafter used for cationic ring-opening photopolymerization.<sup>53</sup> Furthermore, epoxy moieties can be further transformed into acrylates and methacrylates, that can undergo free radical photopolymerization.<sup>54</sup> Apart from soybean, linseed<sup>55</sup>, castor<sup>56</sup> and cardanol oil<sup>57</sup> are frequently used due to their high amount of unsaturated and thus photopolymerizable moieties.

Furthermore, terpenes are widely reported and a thoroughly investigated class of bio-derived monomers for (photo)polymerization. Terpenes comprise a large number of natural compounds, that are predominantly produced in plants, such as conifers, acting as phytochemicals for their secondary metabolism.<sup>58</sup> Limonene and pinene (Figure 25) exhibit not only C=C bonds, that can undergo radical and ionic (photo)polymerization<sup>59</sup>, but also provide the possibility for further modification towards the epoxidized species, that have been successfully photopolymerized via cationic photopolymerization.<sup>60</sup>

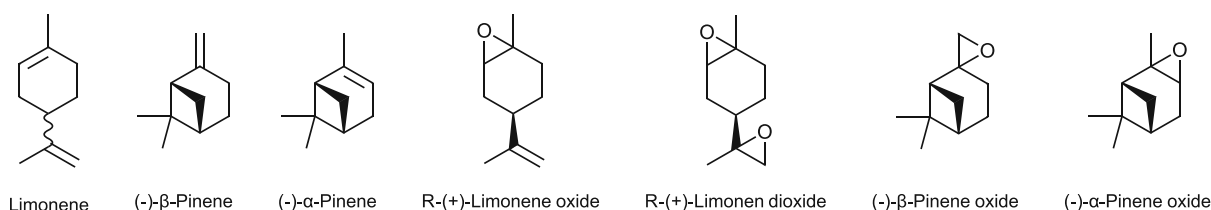
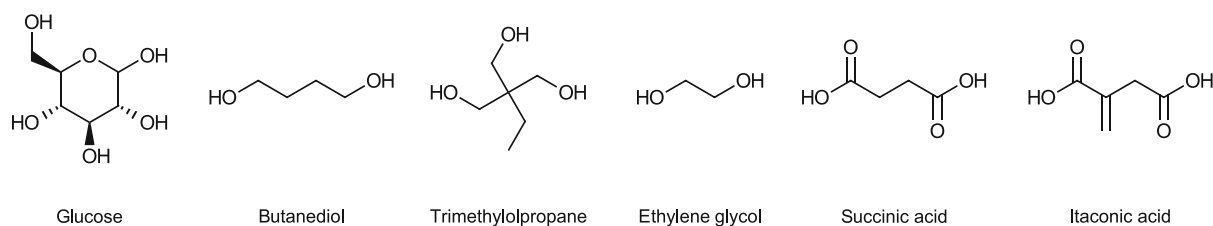


Figure 25: Limonene, terpene and their oxidized modifications

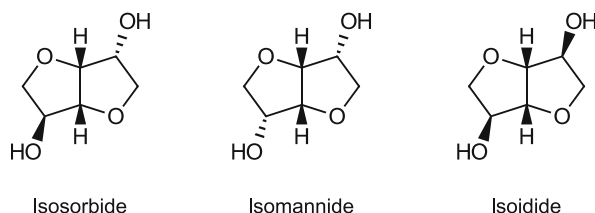
Moreover, starch and cellulose represent readily accessible plant-based starting materials. Via acrylation of the hydroxyl groups on the polymeric backbone, starch was successfully cured using radical photopolymerization.<sup>61</sup> Furthermore, using enzymatic degradation, hydrolysis or fermentation, polysaccharides are degraded into oligo- and monosaccharides, with glucose being the most prominent representative. Additionally, hydroxyl-containing compounds such as 1,4-butanediol, trimethylolpropane, ethylene glycol, succinic acid or itaconic acid can be obtained from polysaccharides (Figure).<sup>62-64</sup>



*Figure 26: Hydroxyl- and acidic compounds from aliphatic biomass*

Their hydroxyl and acid groups possess the ability for modification with (meth)acrylic acid and subsequent use in photopolymerization or polycondensation to obtain high molecular weight compounds (e.g. polyesters, polyurethanes).<sup>63, 65</sup>

Of special interest is the synthon isosorbide and its stereoisomers isomannide and isoidide, (Figure 27), that are obtained *via* double dehydration of glucose and commonly used for the replacement of bisphenol-A, due to the rigid bicyclic backbone. Modified isosorbide has been efficiently used in radical and cationic photopolymerization.<sup>66, 67</sup>



*Figure 27: Structures of 1,4-3,6-dianhydrohexitols isosorbide, isomannide and isoidide*

Another widely used source is lignin, being the most abundant biomass on earth together with cellulose. Furthermore, it represents an inexpensive side-product in the paper and pulp industry.<sup>68, 69</sup> Its highly conjugated, poly-phenolic backbone offers a large number of aliphatic and phenolic -OH groups as well as carboxylic acids, that are easily modified (as explained for sugar-derived molecules) and used for stereolithography purposes.<sup>70</sup> However, the complex chemical nature and variability, depending on the extraction method, prevent the large-scale application of lignin as a material in L-AMT.<sup>71</sup> Of higher interest are low molecular weight compounds, derived *via* depolymerization and degradation of lignin, such as vanillin, eugenol, guaiacol or phloroglucinol.<sup>53, 71, 72</sup> Figure 28 depicts the structure of lignin-derived components.

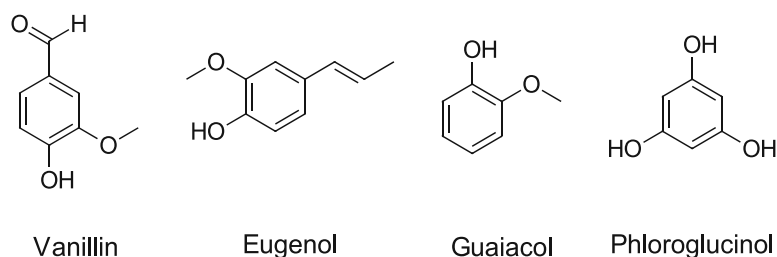


Figure 28: Aromatic precursors derived from lignin.

The phenolic low-molecular weight compounds from Figure 28 were all successfully applied in L-AMT, as their phenyl groups can easily be modified into (meth)acrylates as well as epoxides and used in UV curing applications.<sup>72</sup>

However, using bio-derived monomers and precursors does not make polymers inherently recyclable or (bio)degradable and thus sustainable. Additionally, parameters such as energy consumption over the life cycle of the polymers and economic competitiveness with conventional petroleum-based polymers have to be considered.<sup>73</sup> In the end, the task to replace petroleum-based monomers with bio-based compounds gets even more complex, considering the above-mentioned difficulties and is therefore a highly important and intensively investigated nowadays.



therefore enhance the toughness of a material and additionally lead to lower shrinkage stress and are less prone to oxygen inhibition.<sup>78</sup>

Additionally, network homogeneity can be increased *via* addition fragmentation chain transfer (AFCT). Just like thiols, more homogeneous and tougher networks are obtained by shorter kinetic chain lengths. Beneficial compared to thiols is their better storage stability and lower odor, since thiol-ene formulations tend to gel prematurely and exhibit unpleasant scents.<sup>23, 78, 79</sup> Both CTA strategies have been successfully applied in 3D printing of photopolymer networks.<sup>23, 80</sup>

Considering cationic photopolymerization, alcohols and residual humidity can act as chain transfer agents. Without the presence of those CTAs, cationic photopolymerization follows an activated chain end mechanism (AC) that was highlighted in Figure 12. Upon the addition of evermore monomers to the end of a polymer chain, chain growth is happening. In contrast, in the activated monomer mechanism (AM) the active center is transferred away from the growing polymer chain by mildly nucleophilic compounds such as alcohols, promoting chain transfer events and once again decreasing the kinetic chain length (Figure 30). Besides, the AM mechanism is affecting not only the polymerization speed, but also the network structure of the polymer.<sup>33</sup>

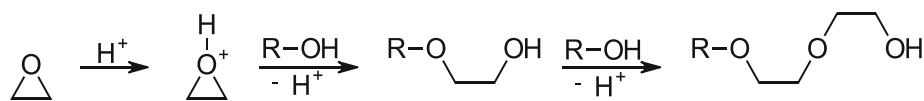


Figure 30: AM mechanism: chain transfer promoted by alcohols R-OH.

### Photopolymer toughening *via* high molecular weight components

Lowering the high crosslinking density of multifunctional (meth)acrylate polymers can furthermore contribute to enhanced toughness, since brittleness of the polymers is decreased. So, polyesters, polyether or polyurethanes with photopolymerizable endgroups can be incorporated into photo-resins, giving thermoplastic-like materials after UV curing. Improved toughness is achieved due to an internal strengthening mechanism, whereby the long polymer chains entangle and adjust into the direction of stretching.<sup>81</sup> Disadvantageous is the high viscosity of such resins, making them unsuitable for conventional vat photopolymerization.

### Photopolymer toughening *via* Interpenetrating Polymer Networks

While the aforementioned strategies focus on co-polymerizing toughening or chain-transfer agents, a different approach is used for interpenetrating polymer networks (IPNs). IPNs comprise two or more independent polymer networks, that show only physical but no chemical interaction with each other. Since there are no covalent bonds between the networks,



separation of an IPN is only possible by disrupting the chemical crosslinks in each network.<sup>82, 83</sup>

L.H. Sperling investigated IPNs from the 1970s on and divided them, according to their polymerization mode and network structure:<sup>82</sup>

- semi-IPN: a linear or branched polymer present together with a crosslinked polymer network
- simultaneous IPN: the monomers of all polymer network are cured simultaneously, forming independent networks and not interfering with each other's polymerization
- sequential IPN: only after the first polymer network is established, the components of the second network are swollen into the existing one and subsequently cured.

Although initially used in damping materials, IPNs find widespread application in impact resistance materials, coatings and biomedical purposes.<sup>84</sup> Emerging from the 1960s on, IPNs were used to toughen polymer materials, although initial research focused more on polystyrene and butadiene IPNs.<sup>82</sup> Photopolymer research started to experiment with IPNs in the early 2000s, combining UV curing of epoxy/(meth)acrylate<sup>85, 86</sup> or vinyl ether/acrylate<sup>87</sup> systems. Here, the orthogonal polymerization modes of free radical and cationic photopolymerization were combined, overcoming common drawbacks of the single polymerization mode, such as oxygen sensitivity<sup>24</sup> and shrinkage stress<sup>88</sup> for free radical photopolymerization or low epoxy conversion and sensitivity towards humidity for cationic photopolymerization.<sup>36</sup> Next to morphological investigations, the focus lies in improving the final material properties (e.g. toughening).<sup>85</sup>

Apart from combining multiple UV-cured networks, photopolymers were furthermore toughened in a dual-cure mode, combining free radical photopolymerization of (meth)acrylates and thermal curing of epoxy resins in sequential IPNs.<sup>89-91</sup>

## Objective

Lithography-based additive manufacturing technologies (L-AMTs) have gained in importance in industry in the last decade. In vat photopolymerization, liquid resins solidify upon irradiation, allowing the creation of complex 3D objects in a layer-by-layer approach. Photopolymerization is the underlying process of L-AMTs and offers a broad spectrum of advantages such as energy efficiency, cost- and time- effectiveness. Nevertheless, this polymerization method suffers from several disadvantages such as the creation of highly crosslinked materials and the lack of environmentally-friendly monomers. Consequently, photopolymers bear a large carbon footprint and are not recyclable due to their crosslinked macromolecular network.

In order to reduce the environmental impact of L-AMT resins, research has focused on providing “green” alternatives for today’s petroleum-based resources. Additionally, brittleness of the materials has to be addressed, making photopolymer toughening another big research field.

The aim of this thesis is to overcome the aforementioned difficulties by the creation of bio-based and toughened photopolymers *via* interpenetrating polymer networks (IPNs).

In order to obtain toughened materials, two independent networks following orthogonal polymerization modes have to be developed. In this work, free radical photopolymerization of macromolecular components is chosen to enhance to elasticity of the final polymer, whereas thermal polymerization of the hard network will contribute to the strength of the materials.

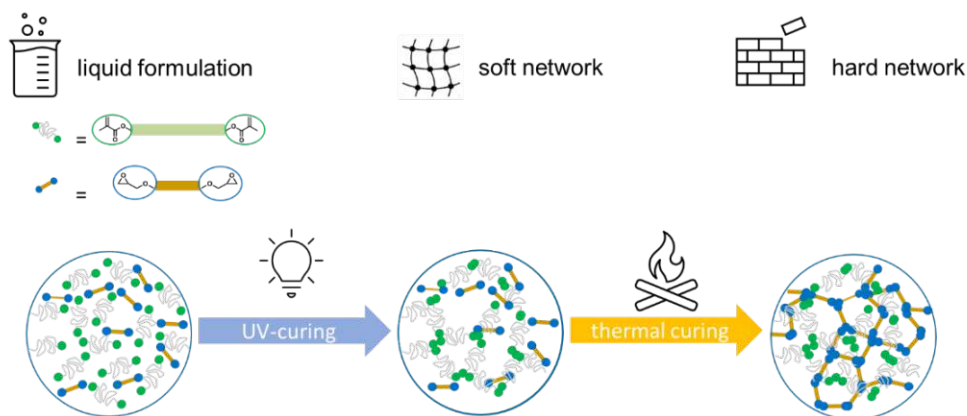


Figure 31: Schematic overview over the IPN formation

Several bio-based polymerizable monomers should be examined regarding their photo- and thermal reactivity *via* (photo)-DSC, RT-NIR photorheology and proton NMR spectroscopy. Furthermore, thermomechanical properties of the individual networks should be characterized using DMTA and tensile test as well as the final IPNs.

## State of the Art

### Sustainable monomers for additive manufacturing technologies

Sustainability, recycling and waste-management has become one of the most investigated fields in polymer chemistry. Therefore, it is not surprising, that evermore resins for additive manufacturing technologies (AMTs) are derived from natural and renewable resources. Especially in vat photopolymerization, bio-based and possible (bio)degradable inks have become a highly investigated research topic. Although the biggest challenge lies in replacing well-established petrochemicals, it is nevertheless important to explore the possibilities and limitations of monomers from renewable resources. Hence, a lot of attention was paid to the development of bio-based monomers for photopolymerization and subsequently their application in 3D printing applications and a lot of literature was published in the last decade.

Modified vegetable oils represent a class of high-potential bio-based photopolymers. The double bonds in the fatty acids are prone to chemical modification, usually *via* epoxidation or further derivatization with acrylates and methacrylates. Figure 32 depicts an overview of unsaturated fatty acids and their chemical modifications.

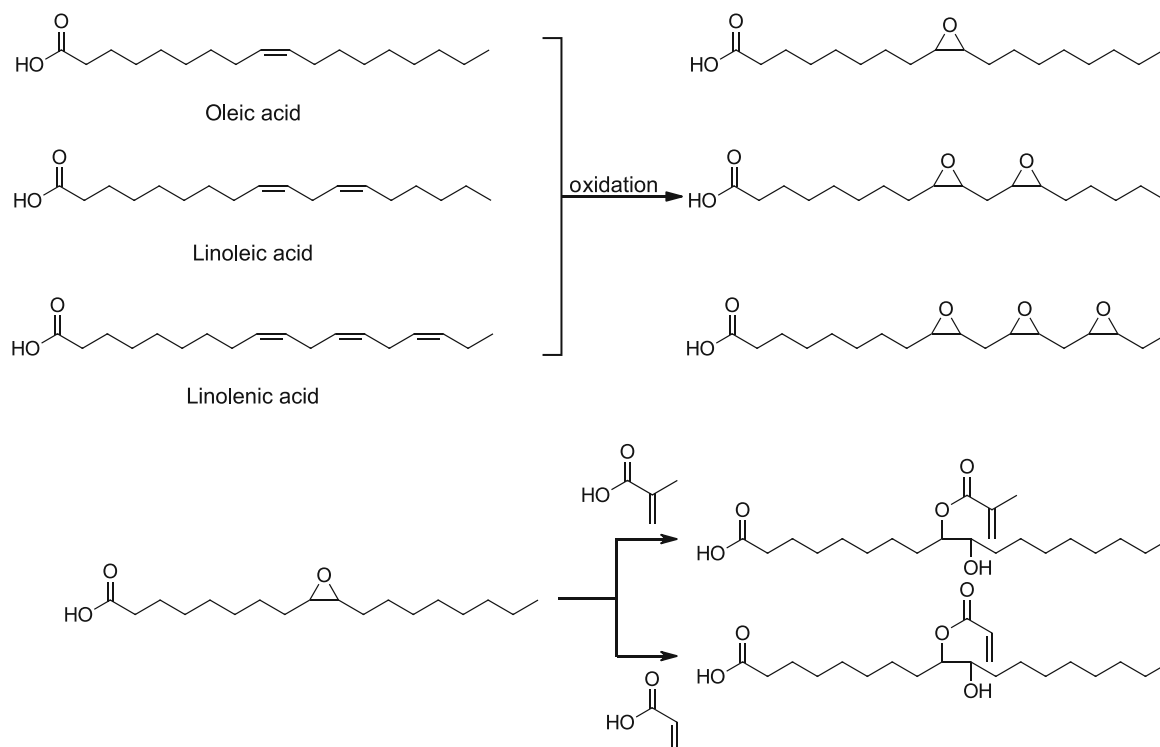


Figure 32: Modification of fatty acids of vegetable oils. Epoxidation of the unsaturated bonds with oxidizing agents (top) and (meth)acrylation (bottom).

Modified soybean oil was one of the first natural materials for 3D printing. In 2016, Miao and coworkers used epoxidized soybean acrylate (ESOA) to prepare shape memory bioscaffolds for tissue engineering.<sup>92</sup> Lebedevaite *et al.* cured ESOA with vanillin dimethacrylate and vanillin diacrylate (Figure 37). The resins were laser polymerized using ultrashort pulses by multiphoton absorption and avalanche induced cross-linking without a photoinitiator, promoting additive manufacturing of pure renewable resources.<sup>93</sup> The group of Guit successfully 3D printed ESOA as well as epoxidized soybean methacrylate (ESOMA) *via* direct laser writing (DLP) using tetrahydrofurfuryl (THFMA) and isobornyl methacrylate (IBMA) as reactive diluents (Figure 33). The 3D-printed materials exhibited  $T_G$  of  $\sim 80$  °C and tensile strength of up to 44 MPa.<sup>54</sup>



Figure 33: Reactive diluents for vat photopolymerization of vegetable oils. Tetrahydrofurfuryl methacrylate (THFMA), isobornyl methacrylate (IBMA), isobornyl acrylate (IBA) and poly(ethylene glycol) diacrylate (PEGDA).

Hybrid free radical and cationic photopolymerization of epoxidized soybean urethane and isobornyl acrylate (IBA) and poly(ethylene glycol) diacrylate (PEGDA,  $M_w = 600$  g/mol) led to the formation of a 3D printable interpenetrating polymer networks (IPNs) using a radical and cationic photoinitiator. The resulting polymers exhibited tensile strength of up to 40 MPa and elongations at break of  $\sim 25\%$  when up to 30 wt% of the epoxy monomer were added to the pristine acrylate formulation.<sup>94</sup> Additionally, Branciforti *et al.* demonstrated, that epoxidized linseed, sunflower, corn and tung oil can be processed and polymerized with diaryliodonium salts using a digital light projector (DLP).<sup>55</sup> While the above-mentioned oils have to compete with human consumption, efforts have been made by Simpson and coworkers to use acrylated waste cooking oil from McDonald's restaurants. 3D printed materials demonstrated a low  $T_G$  of around  $-10$  °C, but excellent biodegradability in soil burial tests.<sup>95</sup>

Starch and cellulose are amongst the most abundantly available polysaccharides. Moreover, starch was successfully applied in photopolymerization and 3D printing. In 2007, Li and coworkers produced starch hydrogels *via* photopolymerization with an acetophenone photoinitiator<sup>61</sup>, while the group of Sangermano successfully applied methacrylated starch and acrylated  $\gamma$ -cyclodextrines, a torus-shaped starch-derivate, in DLP, producing hydrogels for efficient waste-water treatment.<sup>96</sup> The same group furthermore printed formulations containing acrylated  $\gamma$ -cyclodextrines and methacrylated poly(ethylene glycol) with high resolutions.<sup>97</sup>

*Via* hydrolysis or fermentation, starch can be decomposed into low molecular (cyclo)aliphatic polyols and acids. Miao *et al.* prepared photopolymers from aliphatic biomass with outstanding

mechanical properties containing modified itaconic (BHMP2) and succinic acid (BHMP3). Figure 34 depicts modified succinic and itaconic acid that were used for this study.

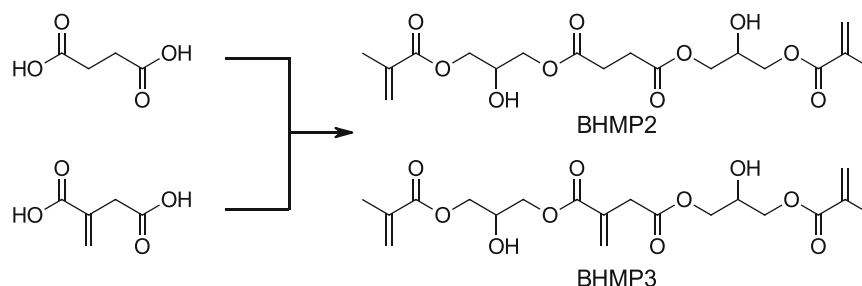


Figure 34: Modification of succinic acid (top) and itaconic acid with glycidyl methacrylate to obtain BHMP2 and BHMP3

The difunctional acids were reacted with glycidyl methacrylate and cured *via* DLP. Cured specimens exhibited high glass transition temperatures (147 °C for BHMP2 and 183 °C for BHMP3) and high tensile moduli (1563 MPa for BHMP2 and 4480 MPa for BHMP3).<sup>63</sup>

Another widely investigated bio-based monomer is isosorbide. Isosorbide is prepared *via* a double-dehydration from D-sorbitol. It is noteworthy to mention, that D-sorbitol can be obtained by hydrogenation of glucose. Glucose, on the other hand, is obtained by hydrolysis of starch or cellulose. Therefore, isosorbide represents a fully biobased, green and environmentally friendly monomer.<sup>98</sup> Figure 35 depicts the structure of isosorbide and its UV-curable monomer modifications.

It was extensively used as a rigid diol in polyesters<sup>99</sup> or polyurethanes<sup>100</sup>, but the diol can also be modified in order to promote photopolymerization. Although research focused on its applicability as Bisphenol-A diglycidyl ether (BADGE) replacement in thermally cured epoxy thermosets<sup>101</sup>, recent studies reported several methods to cure modified isosorbide with UV irradiation. In 2015, Fertier *et al.* reported both acrylated (ISDA) and methacrylated (ISDMA) isosorbide modifications as suitable monomers for UV-cured coatings<sup>67</sup>, while Herrera-Gonzàles *et al.* used the ISDMA as for dental applications due to its low cytotoxicity.<sup>102</sup> Moreover, Owji and coworkers prepared carbamate derivatives of bis(2-hydroxyethyl) isosorbide (CSMA), cured the monomers with a camphorquinone photoinitiator *via* DLP and successfully obtained 3D printed isosorbide-derived photopolymers.<sup>103</sup>

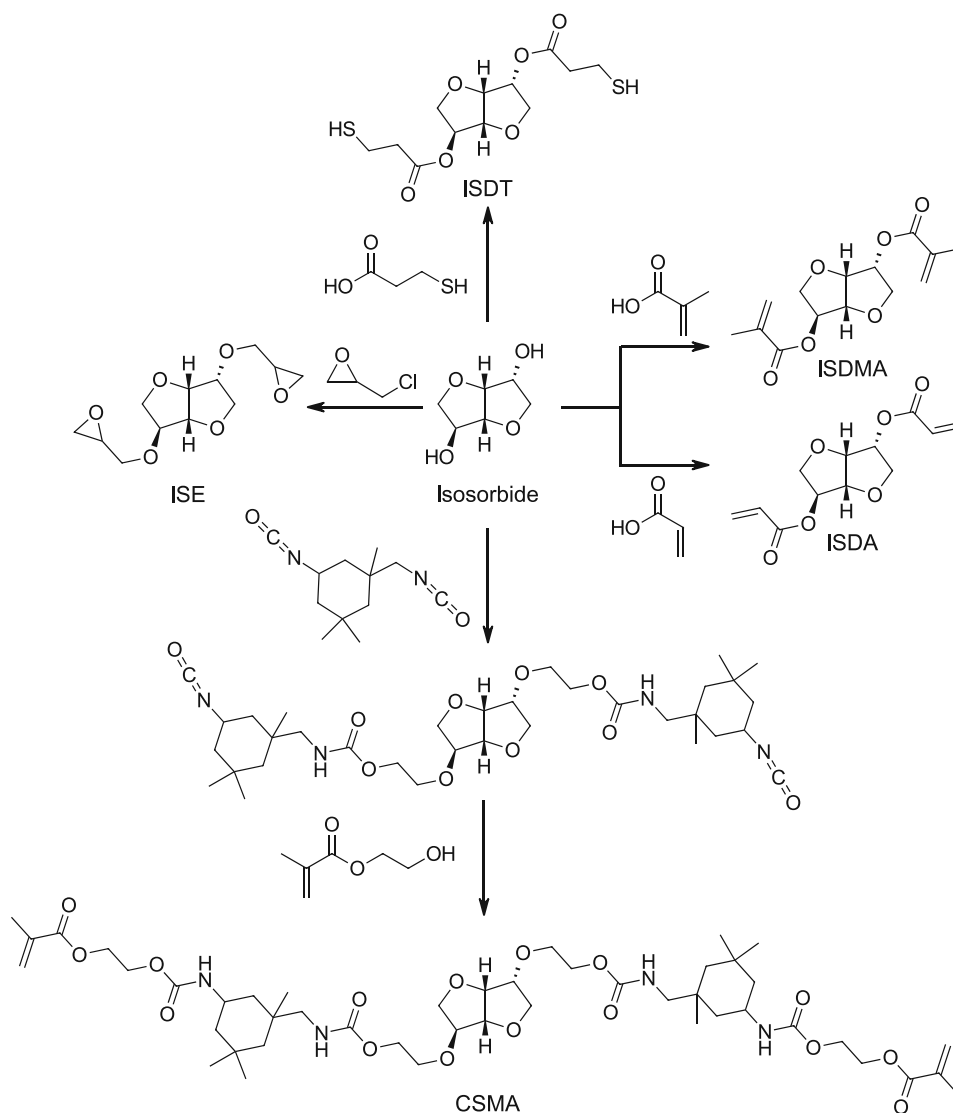


Figure 35: Isosorbide and its UV-curable modifications: isosorbide dimethacrylate (ISDMA), isosorbide diacrylate (ISDA), isosorbide dithiol (ISDT), isosorbide epoxide (ISE) and urethane-containing isosorbide methacrylate (CSMA).

Lignocellulose is the second most abundant renewable biomass, next to cellulose and is an inexpensive side-product in the pulp and paper industry.<sup>69</sup> While lignin has been used as an elastic macro-polyol in polyesters<sup>104</sup>, polyurethanes<sup>105</sup> and epoxide resins<sup>106</sup>, Sutton produced a photoactive methacrylated lignin. After mixing with commercially available acrylates and further application in stereolithography, lignin turned out to function as a plasticizer.<sup>70</sup> Furthermore, dealkaline lignin was used as a photoinitiator, due to the production of free radicals under light-exposure. In this recent study, dealkaline lignin was alkylated and polymerized with 1,6-hexanediol acrylate. Since the alkylated species contained polymerizable groups, the PI was partially incorporated in the network.<sup>107</sup>

Furthermore, phenolic compounds, that are obtained *via* depolymerization of lignin, such as vanillin<sup>108</sup>, eugenol and guaiacol have been successfully applied in 3D printing applications.<sup>109</sup>

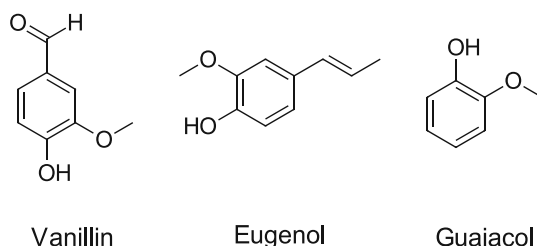


Figure 36: Chemical structure of vanillin, eugenol and guaiacol.

In 2018, Navaruckiene and coworkers experimented with thiol-ene photopolymerization of vanillin diacrylate (VA) and vanillin dimethacrylate (VMA) (Figure 37) and demonstrated, that formulations containing modified vanillin monomers and a dithiol were possible candidates for 3D printing applications due to the quick formation of crosslinked networks and good mechanical properties.<sup>110</sup>

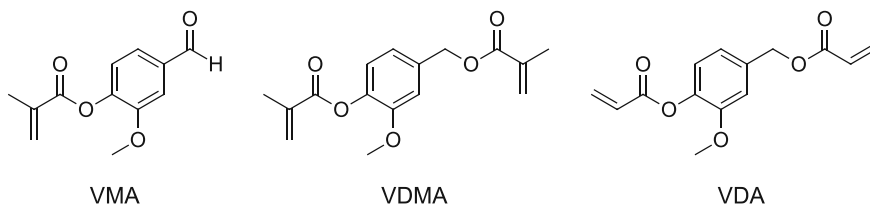


Figure 37: Vanillin modifications vanillin methacrylate (VMA), dimethacrylate (VDMA) and diacrylate (VDA).

Basset and coworkers prepared vanillin methacrylate (VMA), combined it with glycerol dimethacrylate and obtained a high strength material (tensile strength 4900 MPa,  $T_g$  153 °C) after SLA and post-processing steps.<sup>108</sup> Ding *et al.* thoroughly investigated phenolic lignin derivatives for SLA. Formulations containing VDA, methacrylated guaiacol (GMA) and an acrylated eugenol-thiol derivative (ATE) were processed *via* SLA, obtaining materials with high thermal and mechanical properties, that could compete with common photocurable resins on the market.<sup>109</sup>

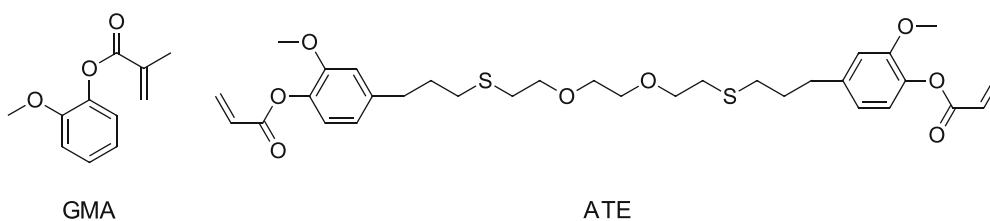


Figure 38: Guaiacol methacrylate (GMA) and acrylated eugenol-thiol derivative (ATE).

## Interpenetrating Polymer Networks

Interpenetrating polymer networks (IPNs) were discovered by Aylsworth in 1914, when a patent was filed for a phenol-formaldehyde resin that was cured together with rubber and sulfur, creating a material that showed higher toughness and elongation than conventional phenol-formaldehyde resins.<sup>111</sup> However, the concept of IPNs was not understood until 1960 when Millar established the term interpenetrating polymer network.<sup>112</sup> He prepared ion-exchange materials and soaked cross-linked copolymers of divinylbenzene and polystyrene in a mixture of styrene and divinylbenzene. Thermal curing led to formation of a second network, that was only partially linked to the existing first one.<sup>112</sup>

Early research was furthermore done by Sperling, Frisch, Klempner and Shibayama as they explored different aspects of IPNs such as phase-separation thermodynamics and the resulting mechanical behavior of IPN materials.<sup>83, 113, 114</sup>

In recent years, different kinds of IPNs have been investigated, dividing IPNs into different categories: porous IPNs, Latex IPNs, hydrogel-IPNs and photopolymerized IPNs.<sup>115</sup>

Porous polymers can be produced *via* curing IPNs and thereafter selectively extracting/dissolving one network. Widmaier and Sperling synthesized a sequential IPN, where the first network consisted of n-butyl acrylate that was crosslinked with divinyl benzene or acrylic anhydride using a photoinitiator (benzoin). Afterwards, the polymer was swollen with a mixture of styrene, crosslinkers and benzoin as PI, obtaining the second phase of the IPN after photopolymerization. By selectively removing the acrylic anhydride crosslinks with ammonium hydroxide solution, a porous IPN was obtained.<sup>116, 117</sup> Recently, porous materials were created by means of ring-opening polymerization of  $\epsilon$ -caprolactone and radical polymerization of divinyl benzene. Hydrolysis of the linear polyester resulted in a porous network.<sup>118</sup>

By contrast, Latex IPNs are produced *via* sequential emulsion polymerization and were first studied by Sperling.<sup>119</sup> As they are usually produced in oil-water emulsions, the presence of an external aqueous phase can affect the polymer topology, resulting in a variety of multiphase structures such as core-shell or nanoparticles.<sup>119, 120</sup>

Hydrogels represent another important field for IPN synthesis. In 1991 Illmain *et al.* published a hydrogel IPN consisting of poly(acryl amide) and poly(acrylic acid), which exhibited large volume transitions by hydrogen bonding between the networks.<sup>121</sup> In the following years, extensive research focused on the preparation of robust hydrogels. As an example, Gudeman and Peppas prepared hydrogels with different cross-linking ratio by the combination of poly(vinyl alcohol) and poly(acrylic acid) and the swelling behavior in different pH buffered media was investigated.<sup>122</sup> In 2013, Schoener and coworkers presented novel hydrogel IPNs consisting of hydrophilic poly(methacrylic-grafted-ethylene glycol) and hydrophobic poly(n-butyl acrylate) for oral delivery of chemotherapeutics.<sup>123</sup>



While the aforementioned IPNs mainly focused on thermal polymerization modes, photopolymerization has also been proposed to produce IPNs in an environmentally friendly approach, since polymerization can take place at room temperature, thus saving (thermal) energy. Commonly, cationic and free radical photopolymerization of (meth)acrylate/epoxy, (meth)acrylate/oxetane and (meth)acrylate/vinyl ether monomers is used to generate IPNs.<sup>84</sup> The chemical structures of the IPN monomers are depicted in Figure 39.

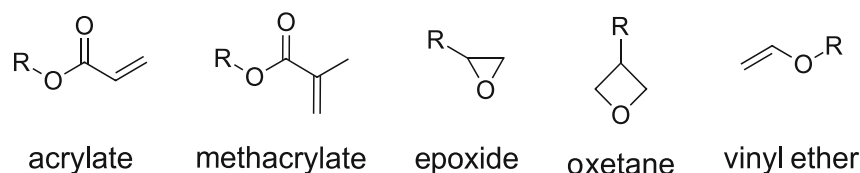


Figure 39: Monomers for photopolymerized IPNs

One of the earliest publications concerning hybrid radical and cationic photopolymerization was released in 1997 by Decker and Decker.<sup>87</sup> Simultaneous photopolymerization of vinyl ether and acrylate monomers with radical and cationic photoinitiators was studied. Since vinyl ether monomers tend to polymerize both radically and cationically, some degree of copolymerization was observed.<sup>87</sup>

In 2001 Decker *et al.* prepared IPNs *via* photopolymerization of epoxy and acrylate monomers. They reported that the acrylate system showed less oxygen inhibition due to a solvent effect, while the epoxy monomers profited from air humidity, resulting in an accelerated cationic polymerization. Besides, a thermal post-curing step increased to final epoxy conversion due to the living character of cationic photopolymerization.<sup>86</sup>

Furthermore, the group of Sangermano contributed to photopolymerized IPNs: they showed that the addition of epoxy monomers increased the rate of cationic photopolymerization of oxetanes. Additionally, they claimed that cationic photoinitiators may generate radicals upon photolytic decay, which initiated radical polymerization of acrylate monomers.<sup>124</sup> Moreover, thermomechanical properties of UV-cured acrylate and epoxy monomers were studied by the same group.<sup>125</sup> Broad  $\tan\delta$  peaks were observed, resulting from complex co-continuous phases in the polymer networks. In the same work, a reduction in shrinkage and an increase in adhesion properties was observed with increasing epoxy content.<sup>125</sup>

Photopolymerization kinetics of diepoxy and dimethacrylate monomers were studied by Bunel and coworkers.<sup>126</sup> They demonstrated that methacrylates react faster at 30 °C during IPN formation, but by increasing the temperature to 90°C, the rate of epoxy photopolymerization accelerates. While the double bond conversion was nearly 90% in the first case, it decreased to roughly 50% at higher temperatures, indicating that high epoxy conversion has a negative effect on the methacrylate network development.<sup>126</sup>

Formation and phase separation of IPNs was intensively studied by Rocco *et al.*<sup>85</sup> By variation of the epoxy and methacrylate ratio, miscible and highly interpenetrated networks as well as

immiscible and thus phase-separated polymers were obtained. Miscible IPNs exhibited one narrow  $\tan\delta$  maximum, whereas phase-separated IPNs showed two distinct  $\tan\delta$  peaks, corresponding to the two independent networks, that were also visible using atomic force microscopy.<sup>85</sup>

Finally, IPNs have successfully been applied in 3D printing applications. Salmoria and coworkers evaluated post-curing conditions of an epoxy/acrylate stereolithography ink.<sup>127</sup> After 3D printing, the objects were exposed to thermal treatment that led to more uniform and isotropic materials, since unreacted epoxy groups post-cured in a dark reaction.<sup>127</sup> Additionally, Huang *et al.* showed, that hybrid radical-cationic 3D printed materials exhibited reduced curing shrinkage.<sup>128</sup> Recently, Zhao *et al.* incorporated silicon-based epoxy monomers into multi-functional acrylate systems. Secondary electron microscopy (SEM) indicated no macro phase separation of the 3D UV cured parts, resulting in homogeneous 3D printed materials that exhibited only one  $\tan\delta$  peak.<sup>129</sup> In another work, the same group produced hybrid epoxy/acrylate shape-memory polymers.<sup>130</sup>

Bio-based inks were also used to 3D print IPNs. Cui *et al.* used vegetable oils for 3D printing by implying a dual-curing resin consisting of bio-derived acrylates and epoxidized vegetable oils. Hybrid free radical and cationic photopolymerization led to the formation of environmentally friendly 3D printed objects.<sup>94</sup> Additionally, Tataru and coworkers were able to 3D print a hybrid cationic and radical photopolymer consisting of epoxidized linseed oil and acrylated soybean oil. Their study revealed, that polymerization rates were strongly affected by the cationic and radical photoinitiator system.<sup>131</sup>

Sequentially dual-curing systems differ from the above-mentioned 3D printing methods. Here, only one polymerization reaction is triggered by UV light in the 3D printing process, while the second polymer is activated by temperature or catalysts, if needed (Figure 40).

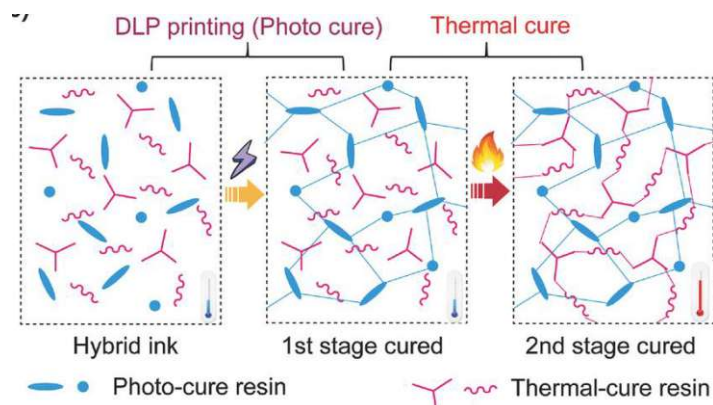


Figure 40: Overview over dual-cure systems. In a first step, the hybrid ink is exposed to UV light, leading to the formation of one network (photo-cure resin), while the second network is obtained in a second thermal curing step (thermal-cure resin).<sup>131</sup>

Reaction kinetics, morphology and (thermo)mechanical properties of UV-cured (meth)acrylates and thermally cured epoxy systems have been thoroughly investigated<sup>89, 132, 133</sup>, although only recently a publication of the Stanzione group demonstrated the applicability in stereolithography (SLA) processes.<sup>90</sup> SLA was used to photopolymerize a dimethacrylate resin, whereas the epoxy-amine curing took place after the 3D printing process at elevated temperatures. Obtained materials showed high glass transition temperature of ~120 °C.<sup>90</sup> By contrast, Kuang *et al.* used anhydride chemistry to cure epoxy monomers in the second step.<sup>134</sup>

Concluding, IPNs have found wide-spread application in polymer chemistry, by the combination of two polymer networks with different properties and/or polymerization kinetics to yield new materials, that benefit from the properties of the homopolymers. Although their use is popular for coatings or damping materials, photopolymerized IPNs especially for AMTs have become of interest only in the last decade. Nevertheless, there is still an immense potential in developing 3D structured IPN photopolymers.

## General Part

The creation of interpenetrating polymer networks (IPNs) requires two independent polymer networks, that do not interfere with each other's polymerization modes, thus polymerize orthogonally. The first step towards IPNs is therefore the evaluation of both networks and their polymerization modes. Since the goal is to find resins that are applicable in 3D printing technologies, the first network should be cured *via* photopolymerization. Meanwhile the components of the second network remain unreacted in the polymerized matrix and should react in a second, thermal curing step. The idea of sequential-IPN creation is depicted in Figure 41. In the end, two separated networks are formed. While the soft, flexible network provides elasticity, the hard network contributes strength and stiffness to the final polymer.

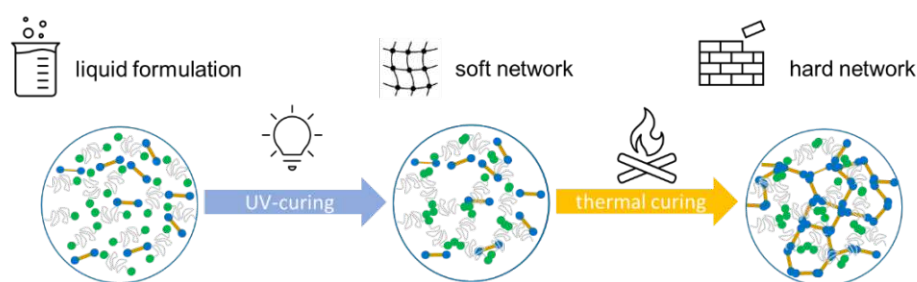


Figure 41: Model for IPN curing. The first step is initiated by UV light (photopolymerization) while the second network is cured thermally

Before the creation of the final IPN-material, a detailed study of each network will be conducted. The first part is dedicated to the synthesis and characterization of the soft network, as well as its thermomechanical behavior and photoreactivity.

Afterwards, the focus is shifted towards the development of the hard matrix, which was the major part of this thesis. This includes the synthesis of aliphatic, cycloaliphatic and aromatic epoxy monomers, as well as their purification. Furthermore, different polymerization routes of epoxy monomers will be highlighted and analyzed regarding their reactivity. In the end, thermomechanical tests will provide information on the applicability of the monomers for IPNs. Finally, the best performing monomer-combinations from both the soft and hard matrix will be combined to form interpenetrating polymer networks, that will be analyzed regarding their (photo)reactivity and (thermo)mechanical properties.

In each part, special focus will be dedicated to the bio-derived nature of each monomer that will be used throughout this thesis, since the ultimate goal was to synthesize sustainable photopolymers that might find application in lithography-based 3D printing technologies.

## 1 Soft network from renewable resources

The evaluation of the soft network will be the starting point of this thesis. Since the primary aim of this network will be to contribute elasticity and flexibility to the final material, macromolecular compounds should be used. On a molecular level, the long chains of the soft network detangle under mechanical stress, thus leading to enhanced elongation of the material. Therefore, the macromolecular nature reduces the brittleness and stiffness of a material.

Furthermore, it has to be considered that a formulation of such components contains only few reactive and photopolymerizable end groups. To enhance the photoreactivity, reactive diluents will be added. Moreover, they decrease the viscosity of the formulations and improve form stability of the polymer.

In order to obtain photopolymerizable materials, reactive end groups have to be added to high-molecular weight precursors, e.g. polyethers. Although petroleum-based compounds dominate the market, various polyethers can be derived from renewable resources. Poly(ethylene glycol), for example, is produced by polymerization of ethylene oxide, which can be obtained from renewable biomass as depicted in Figure 42. Hereby, ethanol is produced by fermentation of sugars, thereafter dehydrated to yield ethylene which is finally oxidized to ethylene oxide.<sup>135</sup>

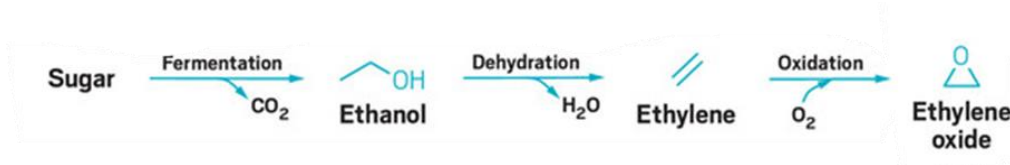


Figure 42: Production of ethylene oxide from biomass<sup>135</sup>

Apart from polyethers, polyesters are frequently used as macromolecular precursors for high molecular weight photoresins. *Via* anionic ring-opening polymerization of  $\epsilon$ -caprolactone, poly(caprolactone) (PCL) bearing hydroxyl end-groups is obtained. Although its synthesis is in general carried out using petrochemically derived monomers, efforts have been made to derive  $\epsilon$ -caprolactone from renewable biomass (Figure 43). Hydroxymethylfurfural (HMF), which is obtained *via* depolymerization of lignocellulosic biomass, can be converted into  $\epsilon$ -caprolactone *via* multiple hydrogenation steps.<sup>136</sup>

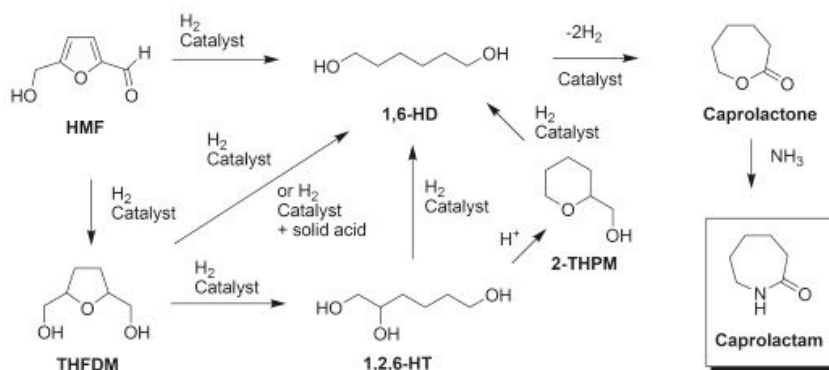


Figure 43: Conversion of hydroxymethylfurfural (HMF) into  $\epsilon$ -caprolactone. <sup>136</sup>

In contrast to polyethers, polyesters tend to degrade under alkaline and acidic conditions. It is well known in literature that (photo)acids are capable of degrading linear polyesters (such as PCL).<sup>137</sup>

A preliminary study on the base-catalyzed degradation of PCL can be found in the Appendix. As a consequence of significant depolymerization of the PCL backbone, polyethers were finally selected and investigated in this thesis.

## 1.1 Synthesis and characterization of macromolecular component

### 1.1.1. Synthesis of poly(ethylene glycol) dimethacrylate (PEG20kMA)

Poly(ethylene glycol) (PEG) was chosen to serve as macromolecular backbone for the soft network. Bearing terminal hydroxyl groups, end-group modification was achieved *via* base-catalyzed one-step esterification with methacrylic anhydride in a procedure similar to Fiore *et al.*<sup>138</sup>

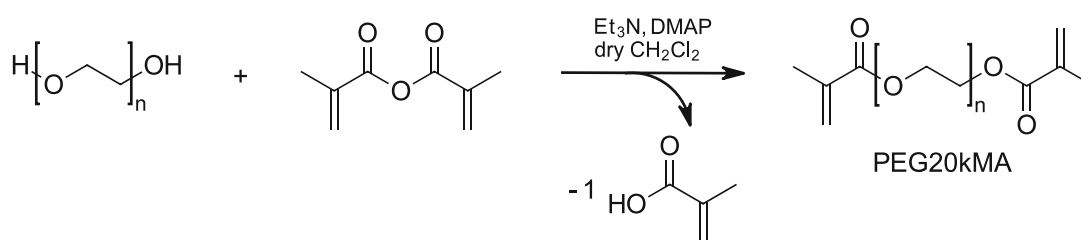


Figure 44: Schematic representation of the synthesis of PEG20kMA <sup>138</sup>

For the synthesis of **PEG20kMA**, 1 equivalent (eq) of PEG (with a molecular weight of 20 kDa), 8 eq of triethylamine ( $\text{Et}_3\text{N}$ ) and 0.3 eq of 4-dimethylaminopyridine (DMAP) were reacted with 8 eq of methacrylic anhydride in a base-catalyzed esterification reaction. The reaction mixture was precipitated into cold diethyl ether, where the product precipitated as a white powder with a yield of 98%.

### 1.1.2. Hydroxyl value determination of PEG20kMA

Hydroxyl value (OH-value) titration was used to monitor both the progress of the PEG to **PEG20kMA** conversion as well as the molecular weight of the unmodified PEG diol. OH-value titration relies on the principle of end group modification.

Here, quantitative  $^{31}\text{P}$ -NMR-spectroscopy was applied. This procedure was reported by Pu *et al.* and is depicted in Figure 45.<sup>139</sup> In this approach, hydroxyl end groups of a macrodiol react with the phosphorylation agent 2-chloro-4,4,5,5-tetramethyl-1,3,2-dioxaphospholane (TMDP) and can be quantified *via* an internal standard in a  $^{31}\text{P}$ -NMR experiment.



Figure 45: Schematic representation of phosphorylation of hydroxyl groups<sup>139</sup>

Due to the high reactivity of TMDP, hydroxyl endgroups of the sample react immediately with the phosphorylation agent and no further reaction step is necessary. Consequently, the sample has to be anhydrous, since hydrolysis of TMDP can happen, leading to an increased formation of HCl gas upon mixing, additionally to the gas that is formed as by-product of the phosphorylation reaction. (Figure 46).

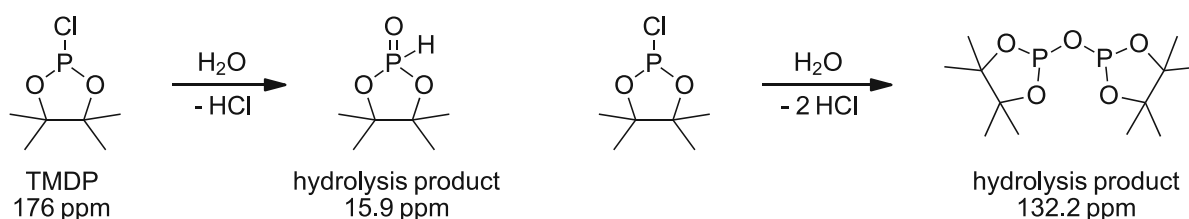


Figure 46: Possible hydrolysis reactions with TDMP. The signals in the  $^{31}\text{P}$ -NMR are depicted.

To buffer the formed HCl coming from the phosphorylation agent and hydrolysis reactions, pyridine is added. Cyclohexanol acts as internal standard, as it reacts with TMDP, allowing a quantification of the NMR signals. The cyclohexanol standard is prepared with a known concentration (~40 mg/mL in pyridine) and to that is added the relaxation agent chromium(III)acetylacetonate ( $\text{Cr}(\text{acac})_3$ ) with a concentration of ~5 mg/mL.

#### Sample preparation

An exact amount of both unmodified PEG and modified PEG20kMA was mixed with an internal standard (~40 mg/mL cyclohexanol and ~5 mg/mL  $\text{Cr}(\text{acac})_3$  in pyridine). Afterwards, the solution was mixed with a solution of TMDP in dry  $\text{CDCl}_3$  and a  $^{31}\text{P}$ -NMR was measured immediately afterwards.



## NMR evaluation

<sup>31</sup>P-NMR spectra were recorded with a 600 MHz NMR spectrometer and analyzed using *MestreNova*. After an automated phase correction and manual baseline correction (polynomial fit), the spectrum was referenced to the signal of the hydrolysis product (Figure 46) at 132.2 ppm (CDCl<sub>3</sub>). Then, the NMR peaks were integrated, setting the integral of the internal standard (145 ppm) to 10.

The OH-value can be calculated *via* the equation ( 1 ) using the integrals from the <sup>31</sup>P-NMR spectra:

$$OH - value = \frac{c_{Standard} \cdot V_{standard} \cdot I_{sample}}{M_{standard} \cdot I_{standard} \cdot m_{sample}} \quad (1)$$

*OH - value*... mmol OH groups per g sample [mmol/g]

*c<sub>standard</sub>*... concentration of cyclohexanol standard: 40 mg/mL

*V<sub>standard</sub>*... volume of cyclohexanol standard: 100 μL

*I<sub>sample</sub>*... integral of the functional group

*M<sub>standard</sub>*... molecular mass of cyclohexanol standard: 100.158 g/mol

*I<sub>standard</sub>*... integral of cyclohexanol standard at 145 ppm = 10

*m<sub>sample</sub>*... mass of the sample [mg]

Furthermore, as a result from equation ( 1 ), OH-value is obtained in mmol/g of polymer, that can be converted into the molecular weight by using equation ( 2 ).

$$M_n = \frac{z \cdot f}{OH - value} \quad (2)$$

*M<sub>n</sub>*... number average molecular mass [g/mol]

*z*... number of OH-groups per macrodiol (= 2)

*f*... factor to convert mol to mmol (= 1000)

*OH - value*... mmol OH groups per g sample [mmol/g]

Following these steps, the results of the analysis are displayed in Table 1.

Table 1: Results of the <sup>31</sup>P-NMR spectroscopy

	<i>I<sub>sample</sub></i>	<i>m<sub>sample</sub></i> [mg]	OH-value [mmol/g]	<i>M<sub>n</sub></i> [g/mol]
<b>PEG20k</b>	0.69	29	0.095	21 000
<b>PEG20kMA</b>	0.010	31	~0	-

Finally, the conversion can be calculated using equation ( 3 ):

$$Conversion (\%) = \left( 1 - \frac{OH_{PEG20kMA}}{OH_{PEG20k}} \right) \cdot 100 \quad (3)$$

*OH<sub>PEG20kMA</sub>*... OH-value of modified PEG20kMA

*OH<sub>PEG20k</sub>*... OH-value of the unmodified PEG20k

The conversion was calculated as 99%, indicating that nearly all terminal OH groups of the



macrodiol backbone have been successfully modified. Concerning the molecular weight of the unmodified PEG, the calculated value is in correspondence with the molecular weight provided by the supplier Sigma-Aldrich (20 kDa).

### 1.1.3. Molecular weight determination *via* size exclusion chromatography

Besides the calculation of the molecular weight ( $M_n$ ) from OH-value titrations, it can be determined using size exclusion chromatography (SEC), also known as gel permeation chromatography (GPC). In general, polymer samples are diluted in tetrahydrofuran (THF, spiked with butylhydroxytoluol BHT as a flowrate marker) as eluent for conventional calibration with a concentration of ~2-4 mg/mL. However, **PEG20k** and **PEG20kMA** could not be dissolved in THF even at elevated temperatures (90 °C). Hence, 1,1,1,3,3,3-hexafluoroisopropanol (HFIP) was used. The polymer samples were dissolved in HFIP and diluted with THF in a ratio of 10/90% v/v. Before the measurement, sample solutions were syringe-filtered to prevent insoluble components from entering into the column.

The results of the GPC analysis are displayed in Table 2.

Table 2: GPC results with conventional calibration against polystyrene standards.

	$M_n$ [g/mol]	$M_w$ [g/mol]	PDI
<b>PEG20k</b>	23600	24800	1.05
<b>PEG20kMA</b>	23900	24200	1.02

The results from Table 2 are slightly higher than the molecular weight provided by the supplier (~20 kDa). As the calibration was performed using polystyrene standards, the deviations are expected. Moreover,  $M_n$  from OH-value titrations from 1.1.2 correspond well with  $M_n$  from GPC analysis.

## 1.2. Effect of PEG20kMA in photopolymerizable formulations

### 1.2.1. Choice of a reactive diluent from renewable resources

Due to the long polyether chains and thus high molecular weight of PEG20kMA, full conversion of the double bonds is difficult to reach in the short UV curing period, as the number of photo-reactive units is rather low. Furthermore, the macromolecular backbone leads to highly viscous resins. Hence, low molecular methacrylates have to be added in order to overcome the above-mentioned difficulties. Reactive diluents do not only decrease the viscosity of a resin, but by increasing the number of reactive groups per formulation, photo-reactivity is enhanced.

Isobornyl methacrylate (**IBMA**) is a commonly used reactive diluent, derived from pine resin and produced *via* derivatization of camphene or isoborneol with methacrylic acid. Homopolymers of IBMA exhibit a glass transition temperature ( $T_g$ ) of 125 °C<sup>140</sup>, additionally

increasing the form-stability of the cured polymer specimens, which is of great importance for sequential IPNs.

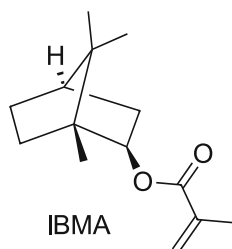


Figure 47: Chemical structure of isobornyl methacrylate (IBMA).

At first, the purity of a commercially available **IBMA** resin was checked using proton NMR spectroscopy. The spectrum is depicted in Figure 48 and the peaks match with those reported in literature.<sup>140</sup> As only expected signals could be detected, the amount of impurities should be negligible and the substance was used without further purification.

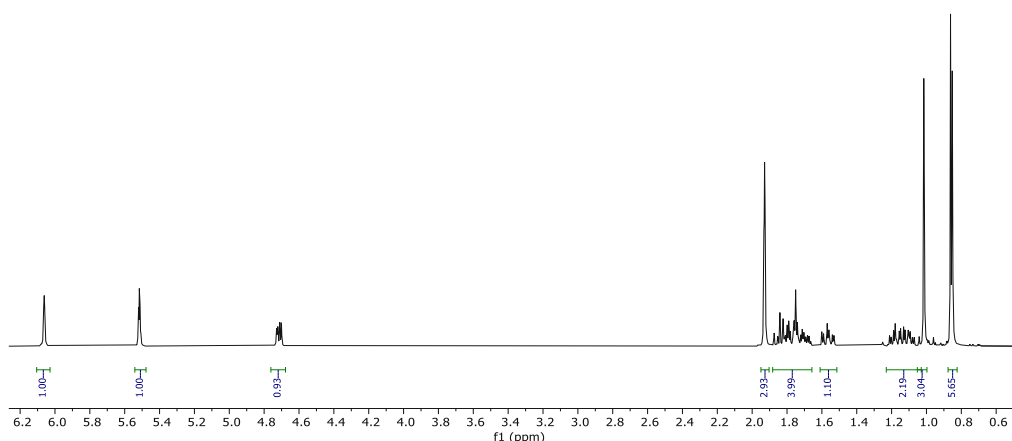


Figure 48: Proton NMR of IBMA. Measured peaks were integrated.

### 1.2.2. Miscibility of macromolecular PEG20kMA in IBMA

Miscibility of components in a photopolymerizable formulation is important, not only to obtain homogeneous formulations, but also to ensure good diffusion of all components. Otherwise, inhomogeneous polymers might be obtained after UV-curing.

So, miscibility of **PEG20kMA** in **IBMA** was studied. Therefore, 10-90 wt% of **IBMA** were added to **PEG20kMA**. Since **PEG20kMA** is a solid with a melting point around 58 °C, formulations with high content of the macromolecular compound (up to 50 wt%) had to be carefully heated to 60 °C in an ultrasonic bath to melt the solid component and homogenize the formulations. With higher reactive diluent content (60-90 wt%), formulations were miscible at room temperature, giving colorless solutions.

### 1.2.3. Rheology measurements

Rheology measurements were performed to investigate the influence of the reactive diluent **IBMA** on the viscosity of **PEG20kMA**. As already presented in 1.1.1, the high molecular weight component **PEG20kMA** is a white solid with a melting point of  $\sim 58$  °C. Hence, viscosity of **PEG20kMA** was measured from 60-100 °C with a shear rate of  $100 \text{ s}^{-1}$ . Furthermore, the reactive diluent **IBMA** was added in 10-90 wt% to the neat resin.

The viscosity of the formulations over as a function of temperature is displayed in Figure 49. Additionally, viscosity at 60 °C ( $\eta_{60^\circ\text{C}}$ ) and 90 °C ( $\eta_{90^\circ\text{C}}$ ) are depicted in Figure 50. As expected, the formulation **100PEG**, containing no reactive diluent, exhibited the by far the highest viscosity ( $\sim 50 \text{ Pa}\cdot\text{s}$  at 60 °C) as a consequence of the high molecular weight and long aliphatic chains of the polyether backbone. By increasing the amount of **IBMA**, viscosity of the formulations decreased. Interestingly, there is a significant drop in viscosity from 10 wt% ( $\sim 32 \text{ Pa}\cdot\text{s}$  at 60 °C) to 20 wt% ( $\sim 11 \text{ Pa}\cdot\text{s}$  at 60 °C) **IBMA** in **PEG20kMA**. Formulations containing 30-50 wt% **IBMA** exhibited similar viscosities of  $\sim 8 \text{ Pa}\cdot\text{s}$  at 60 °C, whereby  $\eta_{60^\circ\text{C}}$  of **60IBMA40PEG** was  $4.6 \text{ Pa}\cdot\text{s}$ . Formulations with even higher reactive diluent content ( $\geq 80$  wt%) exhibited  $\eta_{60^\circ\text{C}}$  of  $\sim 4 \text{ mPa}\cdot\text{s}$ .

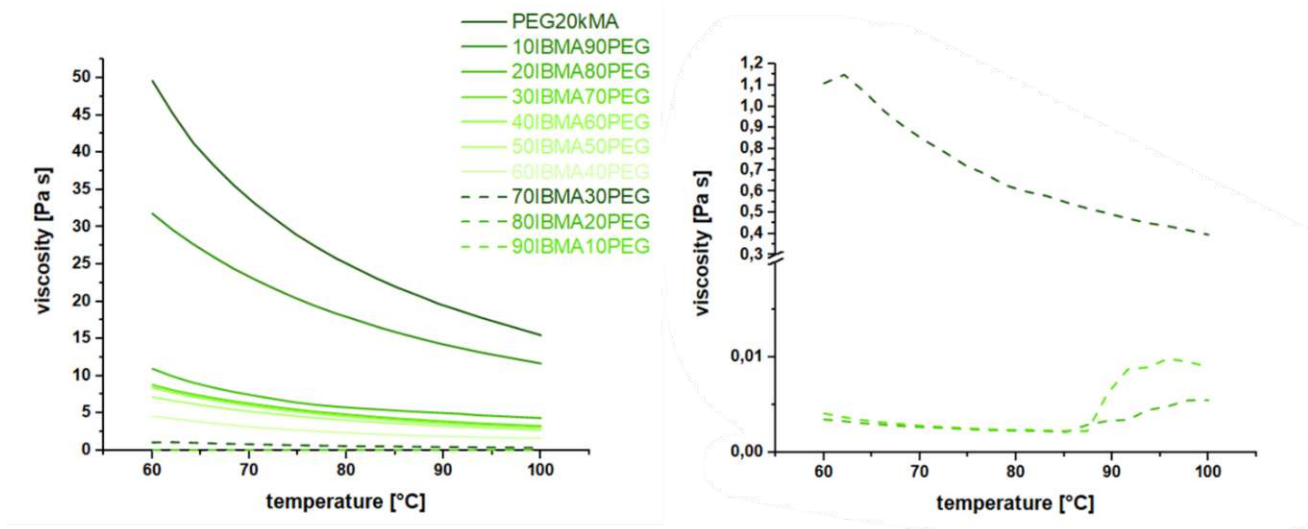


Figure 49: Viscosity of 100PEG (-), 10IBMA90PEG (-), 20IBMA80PEG (-), 30IBMA70PEG (-), 40IBMA60PEG (-), 50IBMA50PEG (-), 60IBMA40PEG (-), 70IBMA30PEG (-), 80IBMA20PEG (-) and 90IBMA10PEG (-).

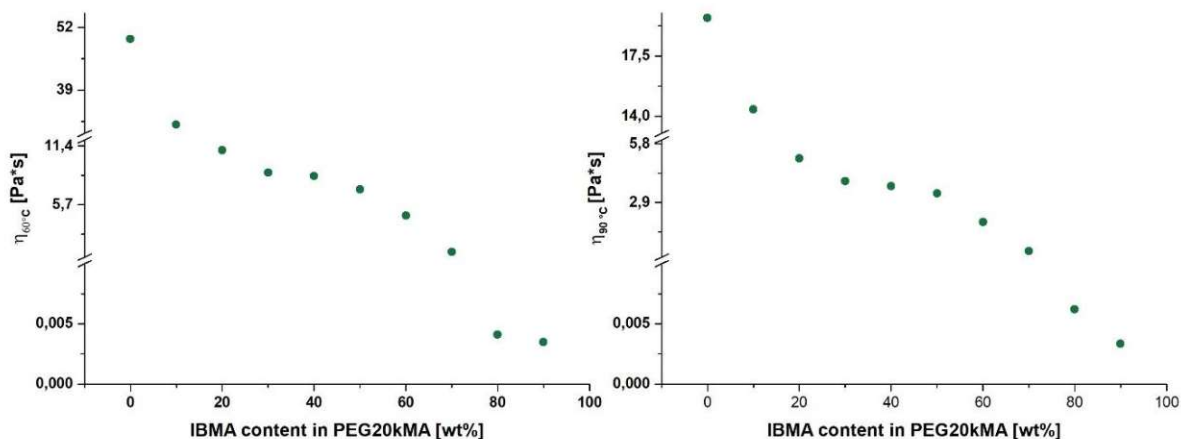
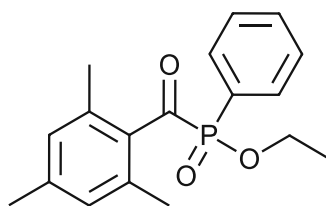


Figure 50: Viscosities at 60 °C (left) and 90 °C (right) of formulations containing 0-90 wt% IBMA in PEG20kMA.

#### 1.2.4. Network appearance and haptic behavior of the soft network

The function of the soft network was already highlighted in the beginning of this chapter. Long, macromolecular chains of the crosslinked polymer should provide elasticity and flexibility to the final IPN, ideally functioning as a toughening agent. While pure poly(ethylene glycol) exhibits  $T_G$  of  $-55\text{ °C}$ <sup>141</sup>, the chosen reactive diluent has a  $T_G$  of  $125\text{ °C}$ <sup>140</sup>, so with increased IBMA content, the soft matrix will become stiffer and brittle, which would contradict the function of the soft matrix. Hence, a maximum IBMA concentration in respect to the mechanical properties is expected.

Although mixtures from 10-90 wt% **PEG20kMA** in **IBMA** were tested regarding their rheological behavior, only formulations with a lower content of the reactive diluent were prepared, since an **IBMA** content above 50 wt% was expected to give too brittle polymers (see Table 3). Additionally, 1 wt% of the photoinitiator TPO-L (Figure 51) was added and the mixtures were homogenized at 60 °C with an ultrasonic bath.



Speedcure TPO-L

Figure 51: Chemical structure of the photoinitiator TPO-L

One polymer specimen ( $5 \times 2 \times 40\text{ mm}^3$ ) per formulation was casted in a silicon mold and irradiated for 10 min on each side in a UV-chamber.

Table 3: Variation of IBOMA content in UV crosslinked specimens

	IBMA [wt%]	PEG20kMA [wt%]	network appearance
poly(10IBMA90PEG)	10	90	white, soft polymer easily demolished by hand
poly(20IBMA80PEG)	20	80	opaque, flexible polymer stable upon compression
poly(30IBMA70PEG)	30	70	opaque, less flexible stable upon compression
poly(40IBMA60PEG)	40	60	opaque, slightly flexible stiffer than previous polymers
poly(50IBMA50PEG)	50	50	white, stiff polymer

For first examinations, the cured polymers were simply tested manually to get an impression about their network appearance. By bending the test specimens, the haptic behavior was evaluated to see which composition would be suitable in IPNs. As depicted in Table 3, the polymers remain flexible upon the addition of up to 30 wt%, whereas 40 and 50 wt% of the reactive diluent already led to a significant increase in the stiffness of the specimens. Furthermore, adding only 10 wt% of **IBMA** led to a very soft and squishy polymer, that ruptured when it was bent by hand.

From those test specimens it was decided to work with the formulation containing 20 wt% **IBMA** and 80 wt% **PEG20kMA**, since it met the requirements for the soft matrix better than all other compositions. This formulation was thereafter used to conduct further reactivity and (thermo)mechanical tests to fully characterize the soft matrix.

### 1.3. Photoreactivity of the soft matrix

#### 1.3.1. Photo-DSC analysis

After evaluation of the right ratio between reactive diluent and **PEG20kMA**, photoreactivity of the formulation was at first determined using photo differential scanning calorimetry (photo-DSC). As a reference, the monofunctional reactive diluent **IBMA** was tested.

All measurements were performed with 1 wt% of the photoinitiator (PI) TPO-L. A broadband UV/VIS lightsource (320-500 nm) with an intensity of 64 mW/cm<sup>2</sup> at the sample surface was used to trigger photopolymerization and the released heat of polymerization was recorded. The reactive diluent was measured at 25 and 60 °C, whereas the formulation of the soft matrix (20IBMA80PEG) was tested at 60 °C, to ensure that all monomers remain liquid before irradiation. From each formulation, triplicates were measured.

For characterization of the photoreactivity, different key figures were determined: the area below the curve ( $\Delta H_p$ ) can be used to calculate the double bond conversion (DBC). Furthermore, the time until reaching the peak maximum of the polymerization ( $t_{max}$ ) and the time until 95% of the heat of polymerization ( $t_{95}$ ) are valuable parameters to study photopolymerization kinetics.

After the measurement, the samples containing only **poly(IBMA)** were dissolved in THF to determine the molecular weight by GPC and CDCl<sub>3</sub> to calculate the double bond conversion *via* proton NMR. This procedure could not be used for **poly(20IBMA80PEG)** due to the crosslinked nature of the sample. Figure 52 represents one exemplary photo-DSC plot per tested formulation and Table 4 summarizes the results of the photo-DSC analysis.

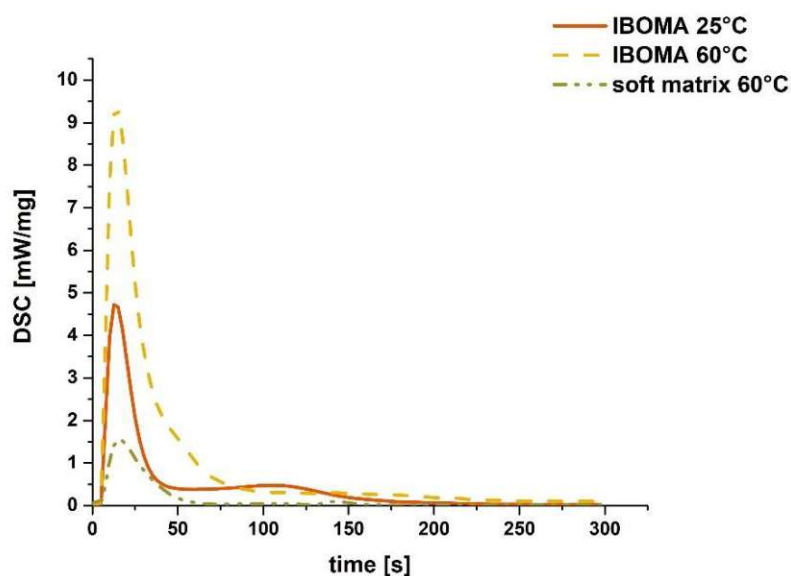


Figure 52: Exemplary photo-DSC plots for IBMA at 25 °C (-) and 60 °C (--) and 20IBMA80PEG (---) at 60 °C

Table 4: Results of the photo-DSC and GPC measurements. \* $DBC_{theo}$  was determined by comparing the measured heat of polymerization with the theoretical heat of polymerization of methacrylates ( $\sim 56$  kJ/mol).<sup>142</sup>

	$t_{max}$ [s]	$t_{95}$ [s]	$\Delta H_p$ [J/g]	$DBC_{theo}^*$ [%]	$DBC_{NMR}$ [%]	$M_n$ [kDa]	$M_w$ [kDa]	PDI [-]
<b>IBMA_25 °C</b>	13.4 ± 0.6	150 ± 5	109 ± 1.6	43.4 ± 2.6	52.4 ± 2.2	55.3	117	2.10
<b>IBMA_60 °C</b>	13.1 ± 0.9	117 ± 2	248 ± 2	98.4 ± 0.6	97.3 ± 0.8	13.5	69.1	5.12
<b>20IBMA80PEG</b>	15.3 ± 2.5	137 ± 3	42.3 ± 1.9	77.1 ± 3.5	-	-	-	-

As can be seen in Figure 52 and Table 4, the reactive diluent **IBMA** shows similar fast  $t_{max}$  at 25 °C (13.4 s) and 60 °C (13.1 s), whereby  $t_{95}$  is drastically reduced at higher temperatures (150 s at 25 °C and 117 s at 60 °C). This was expected since higher temperatures increases to mobility of macro-radicals and thus increase the photoreactivity. Looking at the photo-DSC plot of monomer IBMA at 25 °C, a second peak maximum at around 100-125 s is observed. Since monofunctional monomers results in linear polymers, an increase in viscosity during polymerization hinders propagation of radicals, resulting in a decelerated polymerization over time that leads to a broadening or even to the formation of a second exothermic peak in the photo-DSC measurement. Enhanced photoreactivity at elevated temperatures can be seen when comparing the DBC: increasing the temperature from 25 °C to 60 °C leads to an enhanced  $DBC_{theo}$  (43% and 98%), that is calculated from the theoretical heat of polymerization ( $\Delta H_{p,0}$ ) from a methacrylate ( $\sim 56$  kJ/mol).<sup>142</sup> The double bond conversion ( $DBC_{NMR}$ ) via proton NMR is in good accordance with  $DBC_{theo}$ . Furthermore, the molecular weight is higher at 25 °C ( $M_n \sim 55$  kDa and  $M_w \sim 116$  kDa) than at 60 °C ( $M_n \sim 14$  kDa and  $M_w \sim 69$  kDa), leading to a PDI of 2.1 (IBMA\_25°C) and 5.1 (IBMA\_60°C). Higher temperatures in radical polymerization lead to an increase of side reactions, such as backbiting or H-abstraction reactions. Grady *et al.* showed, that thereby the reactivity of the functionalized polymer is affected, leading to polymers with decreased molecular weight.<sup>143</sup>

In comparison, the soft matrix formulation **20IBMA80PEG** exhibits higher  $t_{max}$  (15.3 s) and  $t_{95}$  (137.2 s) than **IBMA** at 60 °C. Furthermore,  $DBC_{theo}$  is significantly reduced to 77%. This behavior was expected, since the high molecular weight of PEG20kMA hinders mobility of generated radicals, leading to decelerated polymerization speed and lower conversion.

Nevertheless, the synthesized **PEG20kMA** in combination with 20 wt% **IBMA** exhibits good photoreactivity at 60 °C, keeping in mind that the long polyether chains hinder mobility of radicals and thus, a conversion of  $\sim 77\%$  is satisfactory.



### 1.3.2. RT-NIR-photorheology

Real-time (RT) NIR-photorheology measurements were conducted to obtain information about the kinetic and rheological behavior of the soft matrix (**20IBMA80PEG**) simultaneously.

Thus, a rheometer is combined with an UV or LED irradiation unit and a RT-NIR spectrometer to gain both chemical and rheological information in one single measurement. A schematic overview of the setup is presented in Figure 53 and was previously described in detail in literature.<sup>144</sup>

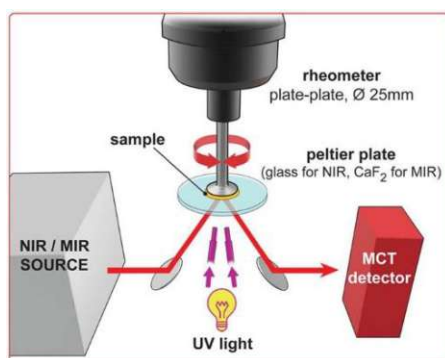


Figure 53: RT-FTIR-Photorheology setup with an illustration of the IR beam and irradiation via UV light.<sup>144</sup>

During RT-NIR-photorheology, the measuring system oscillates with a predetermined frequency and data of the shear storage- and shear loss modulus is provided by the rheometer during the curing process. Of special interest for photopolymerization is the so-called gel point ( $t_g$ ), where the curves of both shear moduli intersect. Furthermore, double bond conversion (DBC) is obtained *via* NIR analysis. By reduction of the peak area of the methacrylate double bonds, DBC can be calculated in real time. Over the measuring period, the IR signal at  $\sim 6140$   $\text{cm}^{-1}$  is recorded and integrated and thereafter related to the integral at the start of the measurement ( $t_0$ ). Hence, DBC and the gel point ( $\text{DBC}_g$ ) and the final double bond conversion ( $\text{DBC}_{\text{final}}$ ) are obtained.

The measurements were performed in triplicates, using 1 wt% of TPO-L as a photoinitiator at 60 °C. A broadband UV lightsource (320-500 nm) was used to irradiate the samples with an intensity of 64  $\text{mW}/\text{cm}^2$  at the sample surface, similar to the photo-DSC analysis. For each measurement,  $\sim 150$   $\mu\text{L}$  of the sample were transferred on the glass disk of the rheometer, which was previously protected with polyethylene (PE) tape. The gap between the glass disk and the measuring system (PP25) was kept constantly at 200  $\mu\text{m}$ .

In order to receive rheological and kinetic data of the soft matrix formulation, photorheology measurements were conducted. In addition to the soft matrix formulation **20IBMA80PEG**, a commercially available polyethylene glycol dimethacrylate (**PEGDMA**) with a molecular weight of 750 g/mol was used as reference. Due to the shorter chain length between the methacrylate end-groups and thus higher concentration of functional groups, enhanced photo-reactivity is



expected from **PEGDMA**. Table 5 summarizes the results of the RT-NIR-photorheology analysis.

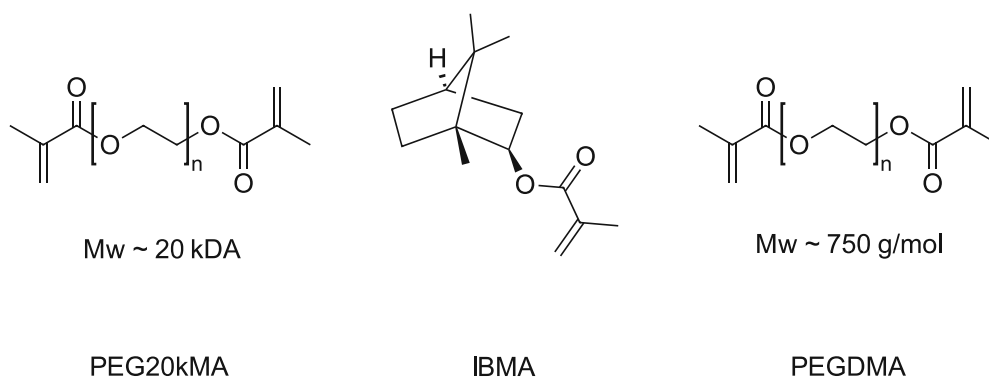


Figure 54: Chemical structures of PEG20kMA, IBMA and the reference PEGDMA.

Table 5: Results of the RT-NIR-photorheology study of 20IBMA80PEG and PEGDMA. Presented are time to gelation ( $t_g$ ), double bond conversion at  $t_g$  ( $DBC_g$ ), time to reach 95% conversion ( $t_{95}$ ) and final double bond conversion ( $DBC_{final}$ ).

	$t_g$ [s]	$DBC_g$ [%]	$t_{95}$ [s]	$DBC_{final}$ [%]
<b>20IBMA80PEG</b>	$11.3 \pm 1.7$	$23.1 \pm 1.9$	$75.5 \pm 3.1$	$91.8 \pm 0.6$
<b>PEGDMA</b>	$5.1 \pm 0.4$	$45.8 \pm 4.6$	$19.8 \pm 0.6$	$95.6 \pm 0.5$

Considering the process of photopolymerization, the gel point is the first characteristic point, at which storage and loss modulus intersect. Furthermore, NIR spectroscopy provides information about the DBC at the gel point. As can be seen in Table 5, **PEGDMA** reaches  $t_g$  after 5.1 s much faster than **20IBMA80PEG** with 11.3 s. It can also be seen, that the DBC at this point is nearly twice as high for **PEGDMA** (46%) compared to **20IBMA80PEG** (23%). This behavior can be explained by consideration of the chain length between the double bonds in the **PEGDMA** formulation: the shorter chain length between the photoreactive bonds and the lower molecular weight of the aforementioned monomer allow enhanced mobility of propagating radicals, leading to a high DBC in short time. Furthermore, **20IBMA80PEG** gives a more flexible network upon gelation, leading to higher  $t_g$ .

Following gelation, crosslinked networks are formed during further polymerization reactions. The time until reaching 95% conversion ( $t_{95}$ ) and the final DBC ( $DBC_{final}$ ) provide further information about the efficiency of the photopolymerization. **PEGDMA** reaches  $t_{95}$  nearly 4-times faster (19.8 s) than **20IBMA80PEG** (75.5 s). Considering  $DBC_{final}$ , high DBC of over 90% is reached for both monomer formulations. Since the measurements were performed at elevated temperatures (60 °C), diffusion of propagating radicals is increased, allowing high overall DBCs. In the case of **20IBMA80PEG**, the reactive diluent **IBMA** decreases the viscosity of the formulation, which can additionally promote the mobility of radicals and monomers, leading to higher DBCs.

While the DBC is calculated from the decrease of the IR signal over the course of the measurement, the conversion was obtained from the theoretical heat of polymerization via photo-DSC analysis in chapter 1.3.1. A comparison of both values is given in Table 6, showing that via RT-NIR-photoreology higher final DBC were obtained (92%) compared to the values received via photo-DSC analysis (77%). An explanation for the deviation of both values can be given, considering that for the calculation of  $DBC_{DSC}$  the theoretical heat of polymerization of the methacrylate bond was used. Furthermore, although photo-DSC and photo-rheology measurements were performed with the same light intensity, the light exposure of the sample is different in both experiments, explaining the different final double bond conversions.

Table 6: Comparison of DBC obtained via RT-NIR-photoreology ( $DBC_{final}$ ) and photo-DSC ( $DBC_{DSC}$ ).

	$DBC_{final}$ [%]	$DBC_{DSC}$ [%]
<b>20IBMA80PEG</b>	$91.8 \pm 0.6$	$77.1 \pm 3.5$

Concluding, the commercially available **PEGDMA** reached  $t_g$  faster and with a higher DBC than **20IBMA80PEG**. However, both monomer formulations reached high final DBC (> 90%) as the measurements were performed at 60 °C. Finally, gathered data indicates that the synthesized **PEG20kMA** in combination with the reactive diluent **IBMA** exhibits good photoreactivity and allows fast formation of a crosslinked soft network for the desired application in IPNs.

## 1.4. Mechanical studies of the soft matrix

### 1.4.1. Thermomechanical properties of the soft matrix

In order to evaluate the time-resolved strain-rate dependent viscoelastic properties of a material, dynamic mechanical thermoanalysis (DMTA) was performed. Hereby, the material experiences a sinus-shaped force, which causes a measurable deformation as a function of time and temperature. The method is used to determine the glass transition temperature ( $T_G$ ), as well as the dynamic storage modulus ( $G'$ ), loss modulus ( $G''$ ) and loss factor  $\tan\delta$ , which is defined as  $\tan\delta=G''/G'$ . Glass transition describes a reversible transition from a hard and brittle (so called “glassy”) state to a viscous/rubbery state. It can be determined by observation of the maximum of  $G''$  and *via* the maximum of  $\tan\delta$ . For applications, the storage modulus at room temperature ( $G'_{25}$ ) and at the rubber plateau ( $G'_r$ ) are of interest.  $G'_r$  is characteristic for the degree of crosslinking as it indicates the minimum of  $G'$ . A typical DMTA plot is depicted in Figure 55.

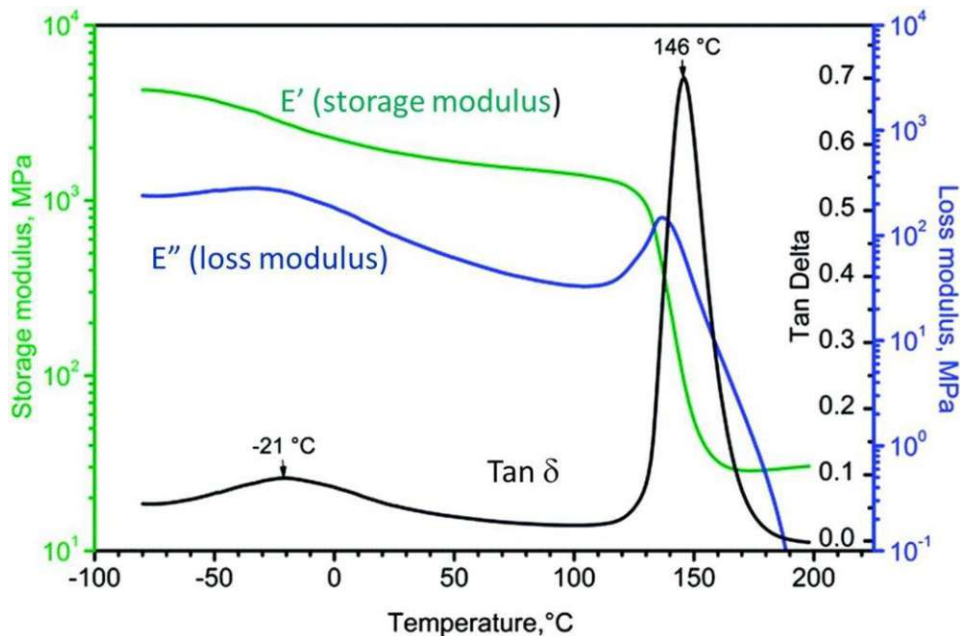


Figure 55: Schematic representation of a DMTA-plot ( $G'$ ,  $G''$ ,  $\tan\delta$ ).<sup>145</sup>

The measurements of the soft matrix were performed in torsion mode from -100 °C to 200 °C with a heating rate of 2 K/min, a torsion strain of 0.1 % and a frequency of 1 Hz. The reference poly(PEGDMA) was measured in 3-point bending mode from -100 to 200 °C with a heating rate of 3K/min and a frequency of 1 Hz. Formulations from chapter 1.2.4 were polymerized using a silicon mold (sticks of 5 x 2 x 40 mm<sup>3</sup>) with broadband UV-light source (400-500 nm) for 10 min on both sides. Due to the high reproducibility of the method, cured specimens were tested once per formulation. Figure 56 represents the storage modulus ( $G'$ ) and loss modulus ( $\tan\delta$ ) of **poly(20IBMA80PEG)** and **poly(PEGDMA)** is depicted as reference. The exact values are presented in Table 7. Since the specimens were analyzed using to different methods (torsion and 3-point bending mode) the values of the storage moduli may deviate and are not

perfectly comparable with one another. Nevertheless, an evaluation of the thermomechanical properties and the glass transition temperatures of the specimens are still possible. The exact values are presented in Table 7.

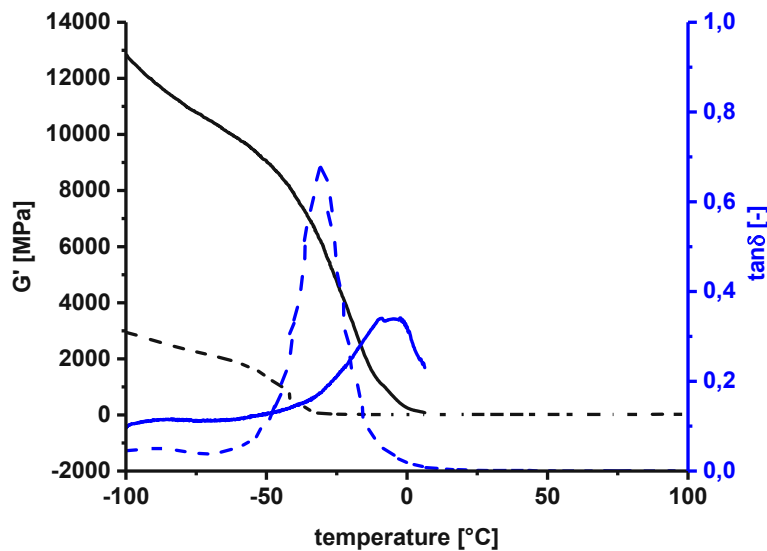


Figure 56: Storage modulus ( $G'$ ) and loss factor ( $\tan\delta$ ) over temperature for poly(20IBMA80PEG) (--) and the reference poly(PEGDMA) (-).

The maximum of the loss factor correlates with the glass transition temperature of a cured polymer specimen. From Figure 56 it can be seen, that a maximum of the  $\tan\delta$  plot of **poly(20IBMA80PEG)** is reached at  $-35\text{ }^{\circ}\text{C}$ , whereby the loss factor peak starts to rise at around  $-50\text{ }^{\circ}\text{C}$  and reaches its baseline at around  $0\text{ }^{\circ}\text{C}$ . This broadening of the  $\tan\delta$  peak maximum is characteristic for chain growth polymerizations, due to its unregulated nature and the formation of highly crosslinked polymers. As the glass transition temperature is reached below room temperature, both  $G'_{25}$  (15.8 MPa) and  $G'_r$  (16.3 MPa) have similar values, as the rubbery plateau is formed at around  $0\text{ }^{\circ}\text{C}$ . By contrast, the reference **poly(PEGDMA)** exhibits a glass transition temperature of  $-10\text{ }^{\circ}\text{C}$  and before reaching the  $T_G$ , the storage modulus is significantly higher. As a result of the shorter poly(ethylene glycol) backbone between the methacrylate linkers, **poly(PEGDMA)** exhibits a higher crosslinking density that leads to the formation of a less flexible photopolymer. Consequently, higher storage moduli and  $T_G$  values are expected.

Table 7:  $G'_{25}$ ,  $T_G$  and  $G'_r$  of poly(20IBMA80PEG) and the reference poly(PEGDMA).

	$G'_{25}$ [MPa]	$T_G$ [ $^{\circ}\text{C}$ ]	$G'_r$ [MPa]
<b>poly(20IBMA80PEG)</b>	15.8	-35	16.3
<b>poly(PEGDMA)</b>	17.3	-10	17.1

In conclusion, **poly(20IBMA80PEG)** exhibits a glass transition temperature well below room temperature (-35 °C). At room temperature, the polymer is in its viscous and rubbery state, making it a suitable soft matrix for future IPNs.

#### 1.4.2. Tensile tests of the soft matrix

Apart from the glass transition temperature, toughness and deformation behavior are the most characteristic mechanical properties of a material. In a tensile test, material specimens are exposed to a uniaxial deformation until material failure. While highly crosslinked polymers (also called thermosets) exhibit brittle fracture behavior (high modulus and low elongation at break), elastomers are characterized by high elongations at break and low modulus. It has to be mentioned, that tensile tests are strongly dependent on the temperature. So, high  $T_G$  will lead to brittle fracture behavior, whereas polymers exhibiting  $T_G$  below the measuring temperature will act as elastomers.

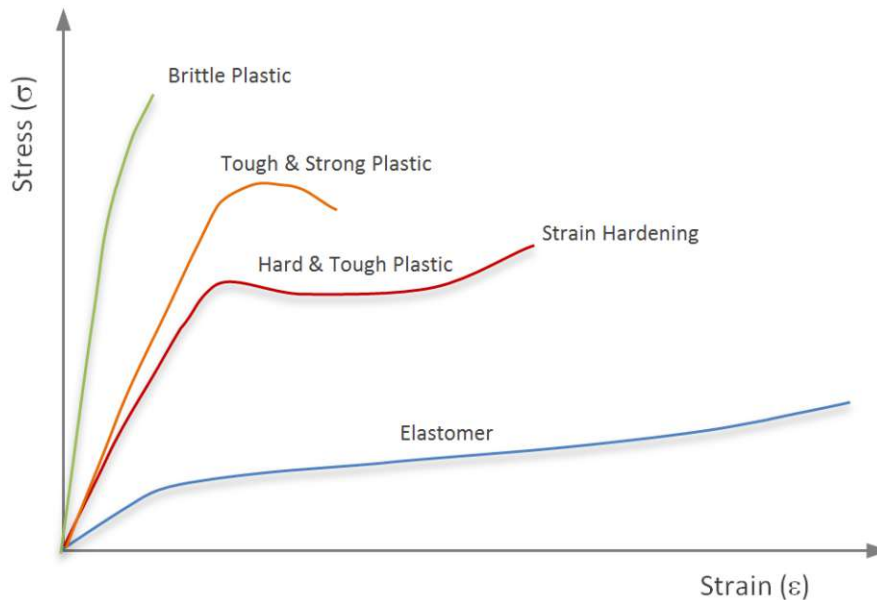


Figure 57: Schematic representation of stress-strain behavior of polymers.<sup>146</sup>

In order to obtain material-specific characteristics such as maximum stress ( $\sigma_M$ ) and elongation at break ( $\epsilon_B$ ), tensile tests of **poly(20IBMA80PEG)** and **poly(PEGDMA)** as reference were performed. Therefore, the polymer specimens were cured in a 5B-shaped silicon mold and made out of the same formulation that was used for DMTA specimens (see 1.4.1). Measurements were performed in accordance with ISO 527 with a traverse speed of 5 mm/min. Figure 58 depicts one representative stress-strain curve of **poly(20IBMA80PEG)** and **poly(PEGDMA)**, whereas Table 8 summarizes the results of all measured specimens ( $n=5$ ). As can be seen in Figure 58, the tensile tests of **poly(20IBMA80PEG)** revealed, that the soft matrix shows expected elastomeric behavior, with a maximum tensile strength ( $\sigma_M$ ) of 0.8 MPa and high elongation at break of roughly 55%. By contrast, **poly(PEGDMA)** displayed higher

maximum tensile strength (2.8 MPa) and lower elongation at break (13%). The poly(ethylene glycol) backbone of **PEGDMA** is significantly shorter (~750 g/mol) compared to **PEG20kMA** (~20 000 g/mol), thus resulting in higher crosslinking density and lower elongation at break of the polymer.

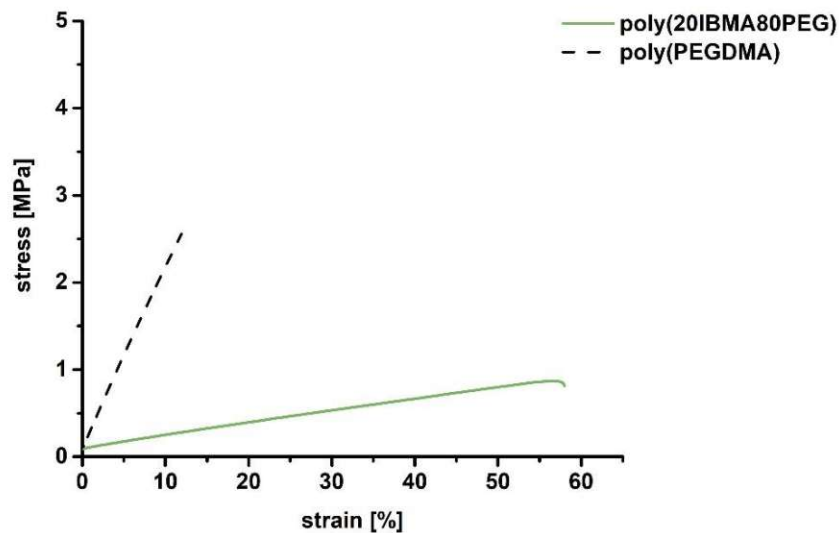


Figure 58: Stress-strain plot of poly(20IBMA80PEG)

Table 8: Maximum tensile strength ( $\sigma_M$ ) and elongation at break ( $\epsilon_B$ ) of the soft matrix

	$\sigma_M$ [MPa]	$\epsilon_B$ [%]
<b>poly(20IBMA80PEG)</b>	$0.77 \pm 0.19$	$54 \pm 12$
<b>poly(PEGDMA)</b>	$2.8 \pm 0.9$	$13 \pm 5$

Although, the tensile tests confirmed the previous findings *via* haptic examination and DMTA measurements of the soft matrix, it has to be mentioned, that due to the high viscosity of the resin (11 Pa·s at 60 °C), processability of the formulation was challenging. Even after ultrasonic treatment, bubble formation could not be avoided while preparing the test specimens, that could explain the rather high deviation of both  $\sigma_M$  and  $\epsilon_B$ .

## 2 Hard Network from renewable resources

After the evaluation of both photo-reactivity and (thermo)mechanical properties the elastic soft matrix, the examination of the hard matrix will be the next part of this thesis. As the term “hard matrix” suggests, the second network should provide the final material with strength and stiffness. Therefore, epoxides were chosen, as this class of monomers is known for its high crosslinking-density and high glass transition temperature ( $T_G$ ), resulting in stiff and rigid polymers. In analogy to the soft matrix, the hard matrix was tested separately, regarding (photo)reactivity and (thermo)mechanical properties.

Epoxy resins can be cured in a plethora of ways, whereby thermal polyaddition with so-called curing agents (amines, anhydrides, thiols, etc.) is frequently used in industry. Due to the high reactivity and low thermal stability of those resins, their use in additive manufacturing technologies (AMTs) is limited. By contrast, cationic photopolymerization allows the use of epoxy resins in 3D printing technologies. Furthermore, epoxides do not co-polymerize with methacrylates and therefore represent ideal monomers for the second network of the final IPNs.<sup>147</sup>

As a starting point of this chapter, different bio-derived epoxy monomers were synthesized and their potential use in cationic photopolymerization was evaluated. Additionally, different network-regulation strategies were evaluated, with special focus on thermal polyaddition of epoxy and hydroxyl components. In the end, the most promising polymers were tested regarding their (photo)reactivity and (thermo)mechanical properties.

### 2.1. Monomers from starch and cellulose

#### 2.1.1. Overview

A wide range of polyols can be obtained from renewable resources and can act as bio-based precursors for epoxy resins. Prominent starting materials are starch, cellulose or glycerol. Starch and cellulose are enzymatically degraded into mono- and oligosaccharides, such as D-glucose or D-mannose. Hydrogenation of those sugars leads to the formation of a variety of aliphatic and alicyclic polyols, such as trimethylolpropane or sorbitol. Further dehydration of sorbitol leads to a ring-closing reaction, yielding isosorbide.<sup>148</sup>





### 2.1.2. Synthesis of Epoxidized Isosorbide (ISE)

Chrysanthos *et al.* described the conversion from isosorbide into its epoxidized modification in 2011 via two different strategies.<sup>101</sup> The most straightforward method to obtain epoxidized isosorbide is its reaction with epichlorohydrin (Figure 61), similar to the production of epoxy resins in industry. Unfortunately, this synthetic route leads to the formation of oligomers, instead of the desired monomer **ISE**.

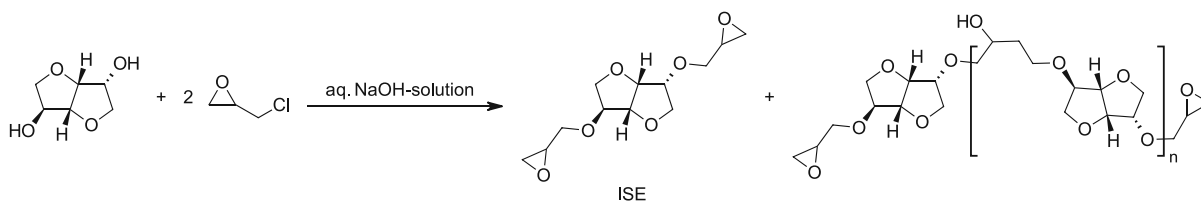


Figure 61: Synthetic route to ISE via epichlorohydrin

Therefore, a two-step procedure, that was proposed by Feng and coworkers, was used to synthesize **ISE**.<sup>149</sup>

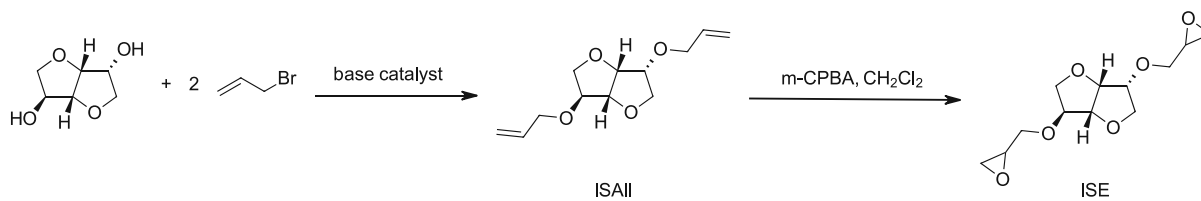


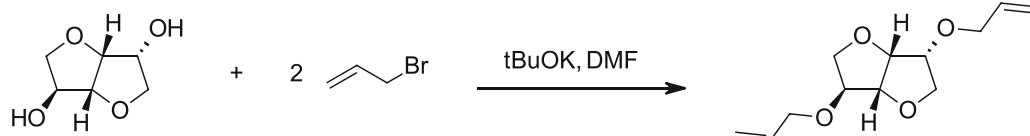
Figure 62: Two-step procedure towards ISE.<sup>149</sup>

In a first step, isosorbide can be reacted with allyl bromide in a base-catalyzed Williamson etherification (Figure 62). Subsequently, allyl moieties of the intermediate isosorbide diallyl ether (**ISAll**) can be oxidized using m-CPBA (m-chloroperbenzoic acid) in a Prilezhaev reaction.

#### Synthesis of Diallyl Isosorbide (ISAll)

For the synthesis of **ISAll**, two different procedures were attempted according to Stensrud<sup>150</sup> and Feng<sup>149</sup> as depicted in Figure 63.

Attempt A:



Attempt B:

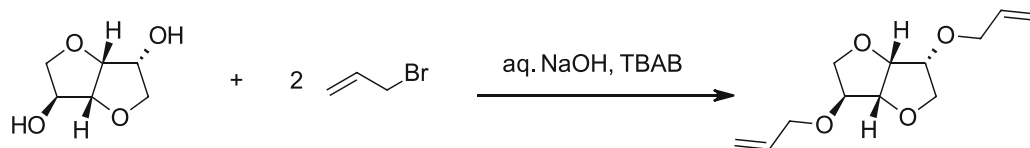


Figure 63: Attempts towards the synthesis of ISAll.<sup>149, 150</sup>

Approach A was carried out according to Stensrud.<sup>150</sup> For the synthesis, 1 eq. of Isosorbide were activated by 2.3 eq. of Potassium tert-butoxide in dry DMF. Under cooling, 2.2 eq. of Allyl bromide were added as allylation reagent. The product was purified by extraction.  $^1\text{H-NMR}$  showed that a highly pure orange oil was obtained in 90% yield.

Unfortunately, potassium tert-butoxide was not available for further upscaling of the reaction. So, Approach B was carried out according to Feng *et al.*<sup>149</sup> Here, 1 eq. of Isosorbide, 2.2 eq. of  $\text{NaOH}$  and the phase transfer catalyst Tetrabutylammonium bromide were dissolved in  $\text{H}_2\text{O}$ , before 2.2 eq. of Allyl bromide were added. After one day, extraction was performed to give a yellow crude oil in 75% yield.

### Synthesis of Epoxidized Isosorbide (ISE)

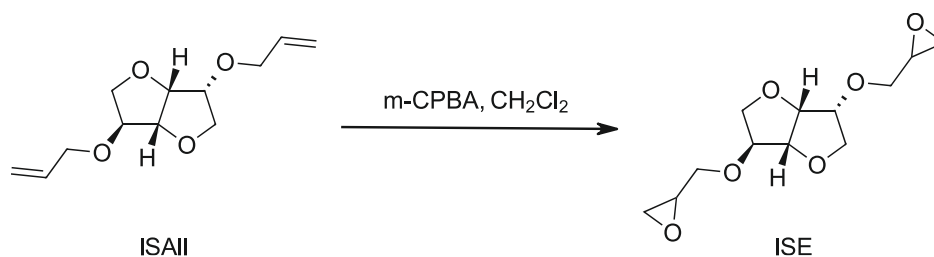


Figure 64: Schematic overview over the synthetic procedure towards ISE.

According to Feng<sup>149</sup>, for the synthesis of ISE 2.2 eq. of the oxidizing agent  $m\text{-CPBA}$  in dry  $\text{CH}_2\text{Cl}_2$  were used to oxidize the double bonds of the precursor ISAll. After 1 day,  $^1\text{H-NMR}$  confirmed full conversion of starting material and the product was purified by extraction and column chromatography, to give the desired compound as a colorless oil in 65% yield.

## 2.2. Monomers from lignin

### 2.2.1. Overview

Apart from cellulose and starch, lignin represents an abundant renewable biomass. Via depolymerization and degradation of the complex polyphenolic backbone, low molecular weight lignin-derivatives can be obtained (see Figure 65).<sup>151</sup>

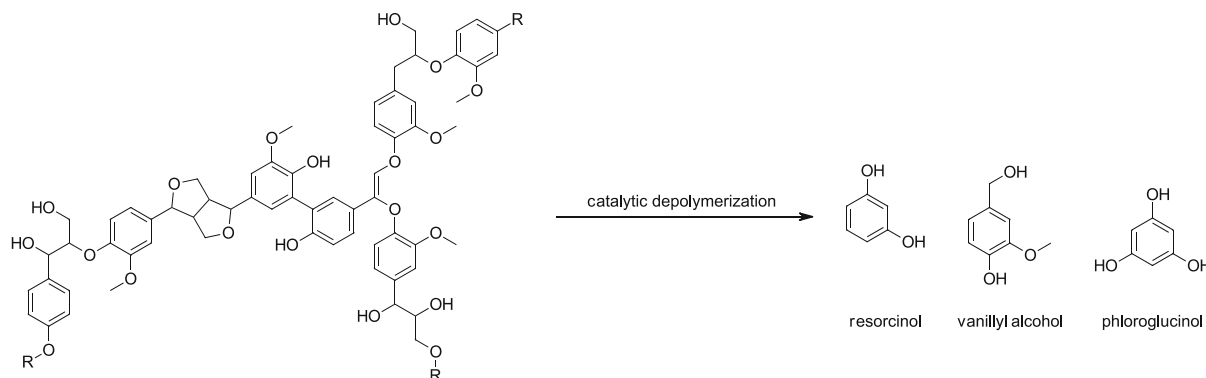


Figure 65: Schematic representation of lignin depolymerization and possible products.<sup>72, 151, 152</sup>

Their rigid phenolic backbone is known to enhance the (thermo)mechanical properties of crosslinked epoxy resins, resulting in high  $T_G$  and stiff materials. In this work, diglycidyl ether of resorcinol (**RDGE**), diglycidyl ether of vanillyl alcohol (**DGEVA**) and triglycidyl ether of phloroglucinol (**PHTE**) were investigated. While the monomer **RDGE** was commercially available, **DGEVA** and **PHTE** were synthesized according to literature.<sup>53, 153</sup>

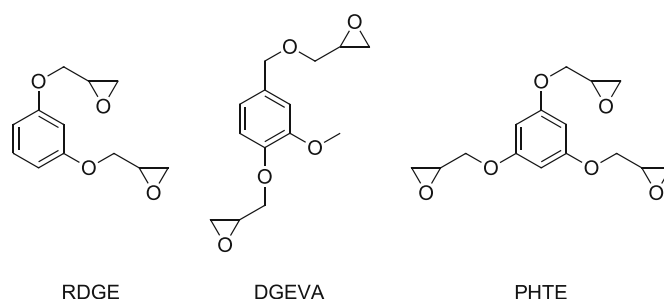


Figure 66: Schematic representation of aromatic epoxy monomers: resorcinol diglycidyl ether (RDGE), diglycidyl ether of vanillyl alcohol (DGEVA) and triglycidyl ether of phloroglucinol (PHTE).

### 2.2.2. Synthesis of Diglycidyl Ether of Vanillyl Alcohol

**DGEVA** was synthesized in a two-step one-pot process as previously reported by Noè *et al.*<sup>53</sup> This synthetic route is similar to the one used in industry to produce epoxy resins, as the diol vanillyl alcohol is treated with an excess of epichlorohydrin and sodium hydroxide solution. This way, the formation of oligomeric products is prohibited, giving preferably the monomer **DGEVA**.

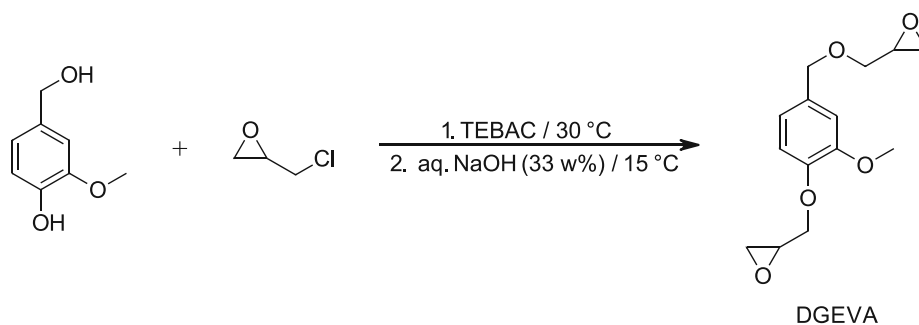


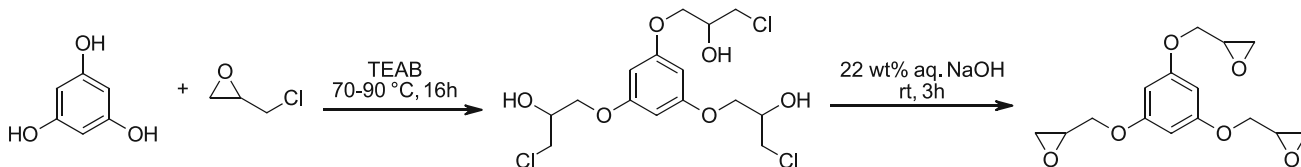
Figure 67: Scheme of the synthesis towards DGEVA. <sup>53</sup>

For the synthesis of DGEVA, Vanillyl alcohol (1 eq) was stirred with an excess of Epichlorohydrin (10 eq) and Benzyl triethylammonium chloride (TEBAC, 0.1 eq) was used as a phase transfer catalyst. After the addition of an aqueous NaOH solution (15 eq) the reaction was stirred overnight. After work-up *via* extraction, a solid crude product was purified *via* column chromatography, giving the desired compound in a yield of 82 % as a white solid with a melting point of 52.7-53.1 °C.

### 2.2.3. Synthesis of Triglycyl Ether of Phloroglucinol (PHTE)

For the synthesis of **PHTE**, two synthetic procedures were attempted according to Noè *et al.*<sup>53</sup> and Guzman<sup>153</sup>, as depicted in Figure 68.

Approach A:



Approach B:

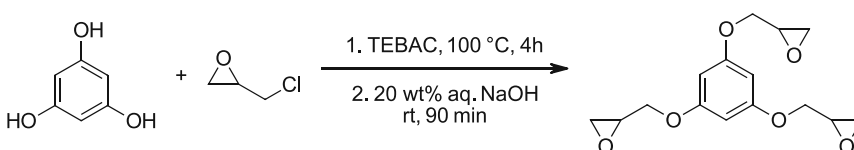


Figure 68: Scheme of the synthesis attempts towards PHTE

In a first approach, **PHTE** was synthesized as reported by Noè *et al.*<sup>53</sup> This synthetic route consisted of a 2-step procedure towards the desired compound starting from phloroglucinol.

As a first step, Phloroglucinol (1 eq) was stirred with 15 eq of Epichlorohydrin and 0.75 eq of Tetraethylammonium bromide (TEAB) for 16h at elevated temperatures. The crude product was poured into  $\text{CH}_2\text{Cl}_2$  and after extraction, the solvent and excess of Epichlorohydrin were recovered. The red liquid was used for the second step without further purification.

The intermediate from step 1 (1 eq) was dissolved in  $\text{CH}_2\text{Cl}_2$  and after adding Tetrabutylammonium bromide (TBAB, 0.07 eq) and reacted with an excess (1.4 eq) of an

aqueous NaOH solution. The yellow crude oil was purified *via* column chromatography, to give a white solid in 36% yield with a melting point of 52.8 – 54.0 °C.

Due to the low yield of the first synthetic route, another procedure (Approach B in Figure 68) was attempted, as reported by Guzman *et al.*<sup>153</sup> Following the synthetic procedure, phloroglucinol (1 eq) was reacted with an excess of epichlorohydrin (19 eq) at 100 °C and benzyltriethylammonium chloride (TEBAC, 0.14 eq) was added as a phase transfer catalyst. Upon addition of an aqueous solution of NaOH, a suspension was stirred at room temperature. After extraction the crude oil was purified using column chromatography, to give a white solid in 62% yield with a melting point of 53.1-53.8 °C.

Concluding, the synthetic procedure was optimized using Approach B, giving a yield of 62% instead of 36 %. In literature<sup>153</sup>, the yield after purification was around 55%. According to Nouailhas and co-workers, one by-product corresponds to the condensation of the resin (PHTE with  $n > 0$ ).<sup>154</sup>

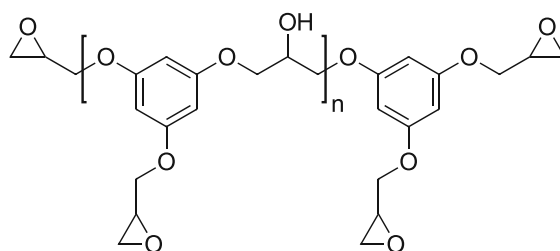


Figure 69: Oligomerization of PHTE as reported by Noè *et al.*<sup>53</sup>

Indeed, oligomerization of di-epoxy phenolic monomers is a common phenomenon observed in industrial epoxy resins and conduct to the repetition of the monomer unit ( $n$ ). Moreover, some other by-products may result from polyaddition of epichlorohydrin, formation of  $\beta$ -chlorohydrin, or  $\alpha$ -glycol, explaining the comparably low yield of such synthetic procedures. As a matter of fact, all of these by-products have also been observed in the case of Bisphenol A glycidylation.<sup>155</sup>

## 2.3. Photopolymerization of bio-based epoxy monomers

Next, the aromatic epoxy-monomers **RDGE**, **DGEVA** and **PHTE** as well as the (cyclo-)aliphatic monomers **ISE** and **TMPTG** were analyzed regarding their reactivity *via* photo-DSC. Furthermore, ATR-IR was used to evaluate the epoxy group conversion of cured polymer specimens. Finally, thermomechanical properties of all monomers were evaluated using both DMTA and tensile tests.

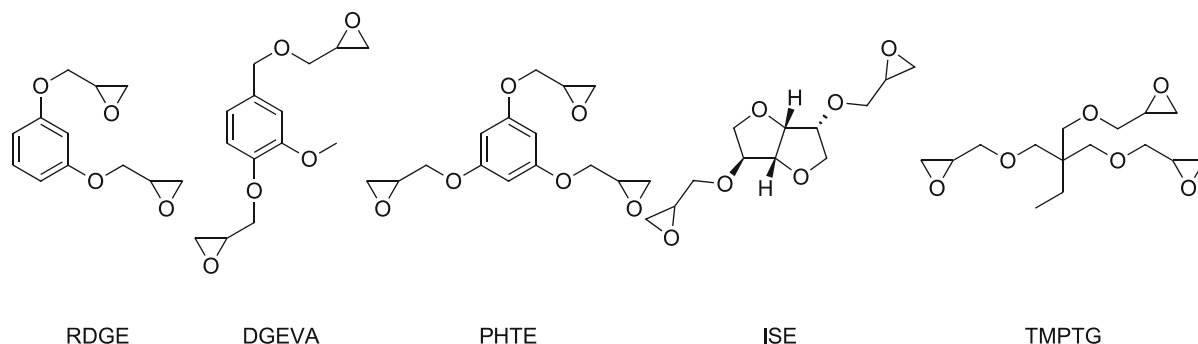


Figure 70: Schematic overview over bio-based epoxy monomers RDGE; DGEVA, PHTE, ISE and TMPTG.

### 2.3.1. Photoreactivity *via* Photo-DSC analysis

Photo-DSC analysis was performed similar to chapter 1.3, with the exception that this time the cationic photoinitiator UVI 6976 (Figure 71) was used, which is composed of a mixture of triarylsulfonium hexafluoroantimonate salts in propylene carbonate.

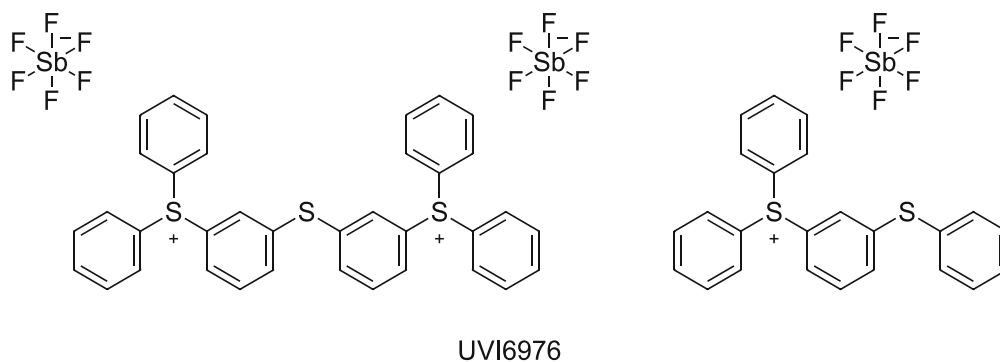


Figure 71: Chemical structure of the cationic photoinitiator UVI6976.

All measurements were performed with 1 wt% of the cationic photoinitiator UVI 6976. A broadband UV/VIS lightsource (320-500 nm) with an intensity of 64 mW/cm<sup>2</sup> at the sample surface was used to trigger photopolymerization and the released heat of polymerization was recorded. Measurements of the liquid monomers **TMPTG**, **ISE** and **RDGE** were performed at 25 °C and 60 °C, whereas the solid monomers **DGEVA** and **PHTE** were only analyzed at 60 °C, to ensure both components were liquid before photopolymerization, as they had a melting point of 52-54 °C.

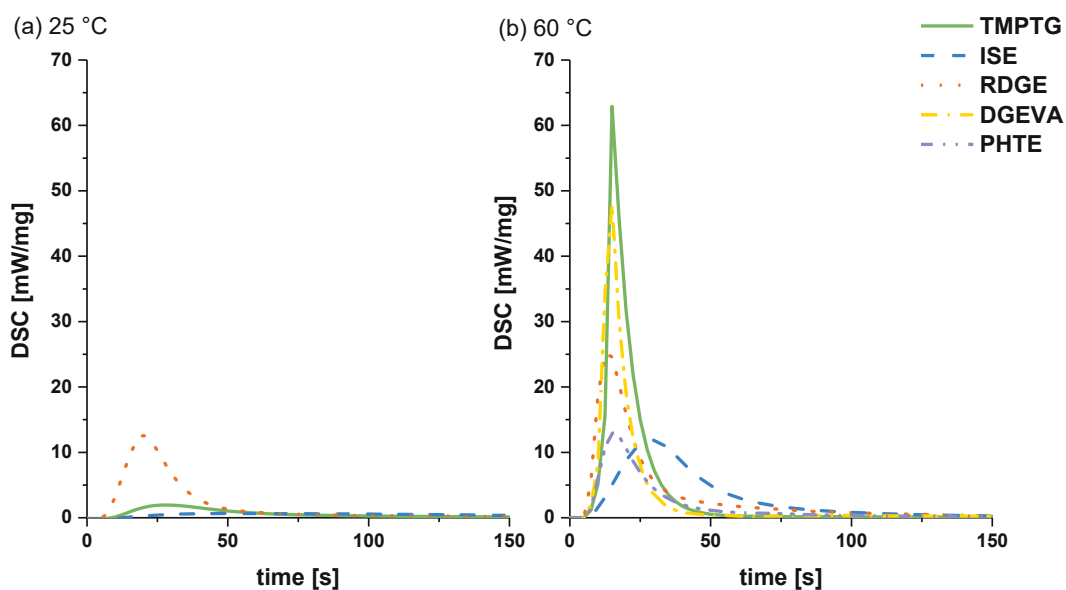


Figure 72: Exemplary photo-DSC plots of TMPTG (-), ISE (--), RDGE (···), DGEVA (-·-·) and PHTE (-·-·-) at 25 °C (a) and 60 °C (b).

As can be seen in Figure 72 (a) and Table 9, all monomers show rather low reactivity towards photopolymerization at ambient temperatures, whereby **RDGE** shows the lowest  $t_{\max}$  (19.7 s) and  $t_{95}$  (100.1 s) of all tested monomers. **TMPTG**, on the other hand shows slightly higher  $t_{\max}$  and  $t_{95}$  values (25.6 s and 157.6 s). Concerning **ISE**, highest  $t_{\max}$  (57.2 s) and  $t_{95}$  (213.7 s) values of all tested monomers are obtained. In fact, it seems that ISE exhibits no tendency towards photopolymerization at 25 °C, when comparing its rather flat curve to **RDGE** and **TMPTG**. Furthermore, conversion of the monomers was calculated by comparing measured  $\Delta H_p$  values to the theoretical heat of polymerization of epoxy groups (~100 kJ/mol).<sup>156</sup> Once again, **RDGE** shows highest conversion (33%), followed by very low conversions of 14 % for **TMPTG** and 8 % for **ISE**.

Crivello *et al.*, intensively discussed the reactivity of glycidyl ethers towards cationic photopolymerization.<sup>157</sup> Glycidyl ethers are prone to hydrogen-bonding during initiation since the neighboring ether-oxygen exhibits similar proton affinity as the oxirane ring oxygen. So, a pseudo five-membered transition state is formed, stabilizing the secondary oxonium ion and leading to significant induction periods at room temperature (Figure 73).



Figure 73: Coordination of protons in glycidyl ether monomers.

The metastable state is less pronounced for aromatic glycidyl ethers, as the basicity of the ether oxygen is reduced, leading to a destabilization of the cyclic intermediate. With that, the

different photo-reactivity of aromatic **RDGE** and aliphatic **TMPTG** and cycloaliphatic **ISE** can be explained.

Concerning **ISE**, an even better proton stabilization might be induced by the ring-oxygens of the isosorbide core (Figure 74). *Via* rotation of the epoxy moieties, an even stronger proton clamp might be formed, that could lead to even stronger retardation of the initiation.<sup>158</sup>

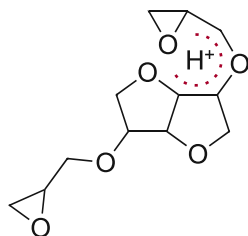


Figure 74: Proton clamp formation in the ISE monomer.

Table 9: Summarized results of photo-DSC analysis of the monomers **TMPTG**, **ISE** and **RDGE** at 25 °C.

	$t_{\max}$ [s]	$t_{95}$ [s]	$\Delta H_p$ [J/g]	conversion [%]
<b>TMPTG</b>	$25.6 \pm 2.1$	$158 \pm 11$	$94.4 \pm 5.8$	$14.3 \pm 0.8$
<b>ISE</b>	$57.2 \pm 5.0$	$214 \pm 9$	$65.1 \pm 3.2$	$8.41 \pm 0.43$
<b>RDGE</b>	$19.7 \pm 1.2$	$100 \pm 23$	$298 \pm 17$	$33.1 \pm 1.8$

Nevertheless, increasing the temperature to 60 °C, leads to higher reactivity towards photopolymerization, as can be seen in Figure 72 (b) and Table 10. All tested monomers exhibit  $t_{\max}$  at around 14 s, with the exception of **ISE** ( $t_{\max} = 30.4$  s). Regarding  $t_{95}$ , **TMPTG** shows a low value of 49.3 s, whereas  $t_{95}$  of aromatic **DGEVA** was 67.9 s and all other monomers exhibit  $t_{95}$  of around 120 s. However, both  $t_{\max}$  and  $t_{95}$  decrease significantly for **TMPTG**, **ISE** and **RDGE** at elevated temperatures. Same trend is observed when looking at the calculated conversion: aliphatic **TMPTG** reaches nearly full conversion (94%), whereas cycloaliphatic **ISE** and aromatic **RDGE** and **DGEVA** polymerize with a moderate conversion of around 60%. Rather low conversion is observed for the trifunctional epoxy monomer **PHTE** (29%).

Table 10: Summarized results of photo-DSC analysis of the monomers **TMPTG**, **ISE**, **RDGE**, **DGEVA** and **PHTE** at 60 °C.

	$t_{\max}$ [s]	$t_{95}$ [s]	$\Delta H_p$ [J/g]	conversion [%]
<b>TMPTG</b>	$14.3 \pm 0.7$	$49.3 \pm 8.3$	$622 \pm 24$	$94.1 \pm 3.7$
<b>ISE</b>	$30.4 \pm 2.1$	$118 \pm 4$	$455 \pm 8$	$58.8 \pm 1.1$
<b>RDGE</b>	$13.9 \pm 2.5$	$112 \pm 10$	$618 \pm 15$	$68.7 \pm 1.7$
<b>DGEVA</b>	$13.6 \pm 0.1$	$67.9 \pm 16.7$	$476 \pm 15$	$63.4 \pm 1.9$
<b>PHTE</b>	$15.9 \pm 0.1$	$123 \pm 4$	$290 \pm 7$	$28.5 \pm 0.7$

However, it is important to keep in mind, that epoxy group conversion values were calculated using theoretical heat of polymerization. Therefore, ATR-IR was used to further investigate the conversion of epoxy groups in more detail.



### 2.3.2. Epoxy group conversion *via* ATR-IR

In order to obtain a more detailed information about the conversion of the epoxy monomers, ATR-IR measurements were performed. FT-IR spectra were recorded from each formulation of 2.3.1 before and after the photo-DSC measurement in a wavenumber range from 4000 to 500 cm<sup>-1</sup>. Furthermore, one photo-DSC crucible per monomer was thermally treated (90 °C) after the photo-DSC analysis for 18h and analyzed using ATR-IR as well.

In the spectra, the signal at 915 cm<sup>-1</sup> was assigned to the epoxy group. Additionally, aromatic ring and phenyl ether signals were observed at around 750 cm<sup>-1</sup> and 1180 cm<sup>-1</sup> and used as references.<sup>159</sup> For the cycloaliphatic monomer **ISE**, the -C-H signal at 1460 cm<sup>-1</sup> was used as reference IR signal<sup>101</sup>, whereby for **TMPTG** the reference IR-band was the -C-H signal at 2900 cm<sup>-1</sup>.<sup>160</sup>

The epoxy group conversion was calculated by reducing the area of the signal at 915 cm<sup>-1</sup> compared to the reference signal according to equation ( 4).

$$\text{Epoxy group conversion (\%)} = \left( 1 - \frac{\frac{A_{\text{Epoxy,Polymer}}}{A_{\text{Ref,Polymer}}}}{\frac{A_{\text{Epoxy,Monomer}}}{A_{\text{Ref,Monomer}}}} \right) \cdot 100\% \quad (4)$$

$A_{\text{Epoxy,Polymer/Monomer}}$ ... area of epoxy signal at 915 cm<sup>-1</sup> in the polymer/monomer

$A_{\text{Ref,Polymer/Monomer}}$ ... area of the reference band in the polymer/monomer

Table 11: Comparison of epoxy group conversion of the photo-DSC analysis calculated via DSC and ATR-IR.

	conversion DSC [%]	conversion IR [%]	conversion DSC [%]	conversion IR [%]
	photo-DSC at 25 °C		photo-DSC at 60 °C	
<b>TMPTG</b>	14.3	17.0	94.1	97.9
<b>ISE</b>	8.41	8.47	58.8	65.1
<b>RDGE</b>	33.1	26.2	68.7	77.2
<b>DGEVA</b>	-	-	63.4	75.3
<b>PHTE</b>	-	-	28.5	32.9

As can be seen in Table 11, calculated conversion values from photo-DSC analysis correspond well with those obtained *via* ATR-IR. Furthermore, Figure 75 depicts the calculated epoxy group conversion (measured *via* ATR-IR) after photo-DSC analysis and after thermal post-curing. As expected, thermal treatment at 90 °C after photopolymerization led to a significant increase in epoxy group conversion for all monomers.

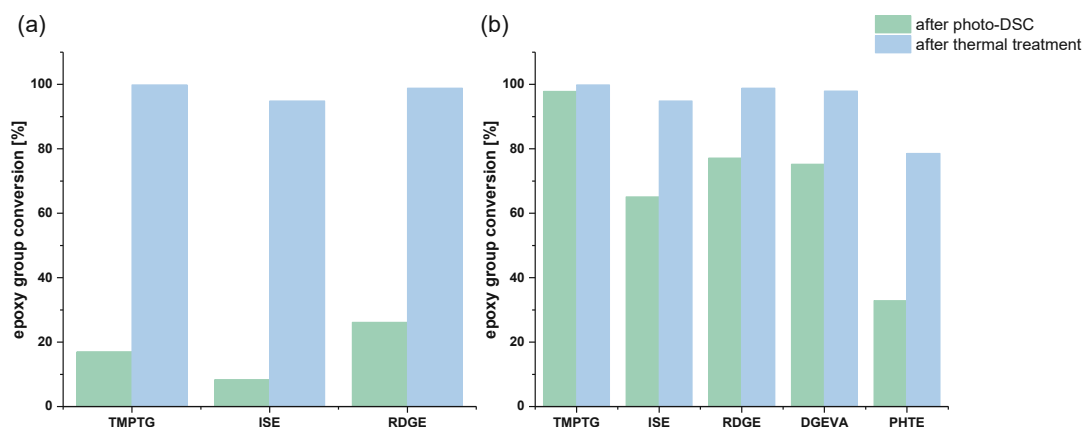


Figure 75: Epoxy group conversion of photo-DSC specimens via ATR-IR. (a) photo-DSC measurements at 25 °C, (b) photo-DSC measurements at 60 °C. Green columns: epoxy group conversion via ATR-IR directly after photo-DSC, blue column: epoxy group conversion via ATR-IR after thermal post-curing at 90 °C.

Figure 75 (a) depicts the epoxy group conversion of photo-DSC crucibles, that were measured at 25 °C and were post-cured for 18h at 90 °C. As already discussed in the previous chapter, the conversion of all monomers is low (**TMPTG**: 17%, **ISE**: 8%, **RDGE**: 26%) after photopolymerization. Additional thermal treatment leads to nearly full conversion (> 97%) of all polymers. The same trend is observed for those polymers, that were cured at 60 °C in the photo-DSC device. While **TMPTG** exhibits nearly full conversion (97%) after irradiation with UV light, **ISE** (65%), **RDGE** (77%), **DGEVA** (75%) and **PHTE** (33%) suffer from lower epoxy group conversion after photopolymerization. Nevertheless, thermal post-curing leads to a significant decrease in epoxy signals in the ATR-IR, resulting high epoxy group conversions. This can be attributed to a so-called dark-curing reaction. During initiation, long-lived cations are generated, that can continue cationic polymerization even after the irradiation period.<sup>31</sup>

### 2.3.3. Thermomechanical properties of photopolymers

Determination of the viscoelastic properties of photopolymerized epoxy monomers was done by DMTA measurements as stated in 1.4.1. Therefore, monomer formulations containing 1 wt% of the cationic photoinitiator UVI 6976 were prepared. For curing, an Intelli-Ray 600 broadband UV oven (320-580 nm) was used. Specimens were irradiated for 300s on both sides. It has to be mentioned, that liquid monomers **TMPTG**, **ISE** and **RDGE** were photopolymerized at ambient temperatures, whereas the solid monomers **DGEVA** and **PHTE** were cured in its molten state at 60 °C. After the irradiation period, polymerized specimens were thermally post-cured at 90 °C for 16-18h, to increase the total epoxy conversion. Epoxy group conversion of cured polymer specimens was determined as stated in 2.3.2 and is depicted in Table 12.

Table 12: Epoxy groups conversion determined via ATR-IR of photopolymers after photopolymerization and post-curing at 90 °C.

	epoxy group conversion [%]
poly(TMPTG)	> 99
poly(ISE)	98
poly(RDGE)	98
poly(DGEVA)	87
poly(PHTE)	97

Storage modulus ( $G'$ ) and loss factor ( $\tan\delta$ ) are depicted in Figure 76 (a) and (b), the exact values are summarized in

Table 13.

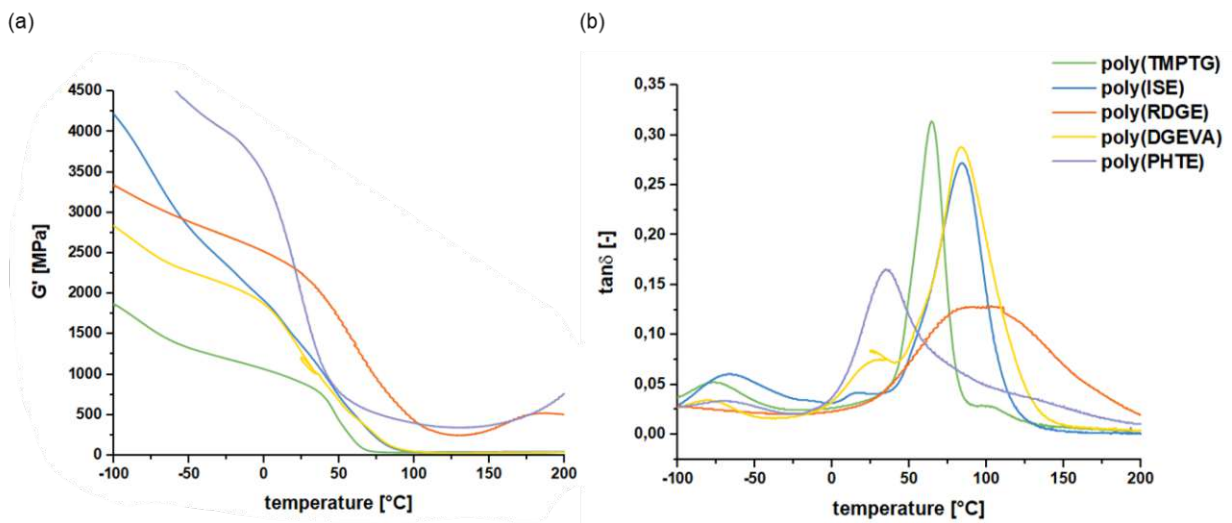


Figure 76: a) Storage modulus ( $G'$ ) over temperature and (b) loss factor over temperature of poly(TMPTG) (-), poly(ISE) (-), poly(RDGE) (-), poly(DGEVA) (-) and poly(PHTE) (-).

In order to obtain the glass transition temperature of every polymer, the maximum loss factor was observed. Overall, all tested photopolymers exhibit  $T_g$  well above room temperature. Aromatic **poly(RDGE)** exhibits highest  $T_g$  (91 °C), although having a very broad  $\tan\delta$  maximum (-25 °C to 200 °C). Cycloaliphatic **poly(ISE)** and aromatic **poly(DGEVA)** exhibit  $T_g$  around 20 °C lower (73 °C and 76 °C). **Poly(TMPTG)** (62 °C) and **poly(PHTE)** (35 °C) show even lower glass transition temperatures.

Overall, it has to be mentioned that higher conversion can lead to a broadening of the loss factor curve. When comparing the epoxy groups conversion *via* photo-DSC from chapter 2.3.1, the monomer **RDGE** polymerized at higher conversions than **DGEVA** and **ISE** and therefore the peak broadening of **poly(RDGE)** might be explained by this phenomenon. More generally, photopolymerization leads to the formation of highly crosslinked and inhomogeneous polymer networks. This network formation additionally contributes to broad glass transition temperature ranges.

Moreover, when looking at Table 13, high  $G'_{25}$  values for **poly(RDGE)** (2251 MPa) and **poly(PHTE)** (1982 MPa) can be observed. Additionally, both polymers exhibit highest  $G'_r$  values (252 MPa for **poly(RDGE)** and 346 MPa **poly(PHTE)**), indicating high crosslinking density of the polymers. Interestingly, both polymers did not show a real rubbery plateau, but rather a minimum in the storage modulus at around 125 °C, followed by a slight increase. Additionally,  $G'_{25}$  (897 MPa) **poly(TMPTG)** is the lowest measured value, originating from the more flexible aliphatic chains of the polymer.

Table 13:  $G'_{25^\circ\text{C}}$ ,  $G'_R$  and  $T_G$  of photopolymerized epoxy monomers.

	$G'_{25}$ [MPa]	$T_G$ [°C]	$G'_r$ [MPa]
<b>poly(TMPTG)</b>	897.1	62	35.21
<b>poly(ISE)</b>	1361	73	40.72
<b>poly(RDGE)</b>	2251	91	251.7
<b>poly(DGEVA)</b>	1268	76	34.17
<b>poly(PHTE)</b>	1983	35	346.1

Concluding, DMTA measurements show, that cationic photopolymerization of epoxy monomers leads to rather inhomogeneous polymer networks, that can clearly be seen by the broad maxima in the loss factor curves, caused by the high reactivity and high crosslinking density of the photopolymers. Broadening of the loss factor curve is a common phenomenon in chain-growth polymerizations, since high rates of polymerization lead to early vitrification and thus irregular kinetic chain lengths.<sup>9</sup>

### 2.3.4. Tensile tests of photopolymers

To complete the study on the thermomechanical properties of cationically photopolymerized monomers, tensile tests were conducted. Tensile tests specimens of shape 5B were prepared as stated in 2.3.3 and the measurements were conducted as previously described in 1.4.2. One exemplary stress-strain curve of each polymer is depicted in Figure 77, while Table 14 summarizes the exact values of the tensile test measurements.

Table 14: Maximum tensile strength  $\sigma_M$  and elongation at break  $\epsilon_B$  of analyzed polymers.

	$\sigma_M$ [MPa]	$\epsilon_B$ [%]
<b>poly(TMPTG)</b>	$35.6 \pm 4.5$	$4.44 \pm 1.16$
<b>poly(ISE)</b>	$71.7 \pm 1.9$	$9.31 \pm 2.87$
<b>poly(RDGE)</b>	$82.5 \pm 1.6$	$5.14 \pm 0.93$
<b>poly(DGEVA)</b>	$67.1 \pm 5.8$	$5.19 \pm 0.90$
<b>poly(PHTE)</b>	$65.8 \pm 4.1$	$8.07 \pm 1.20$

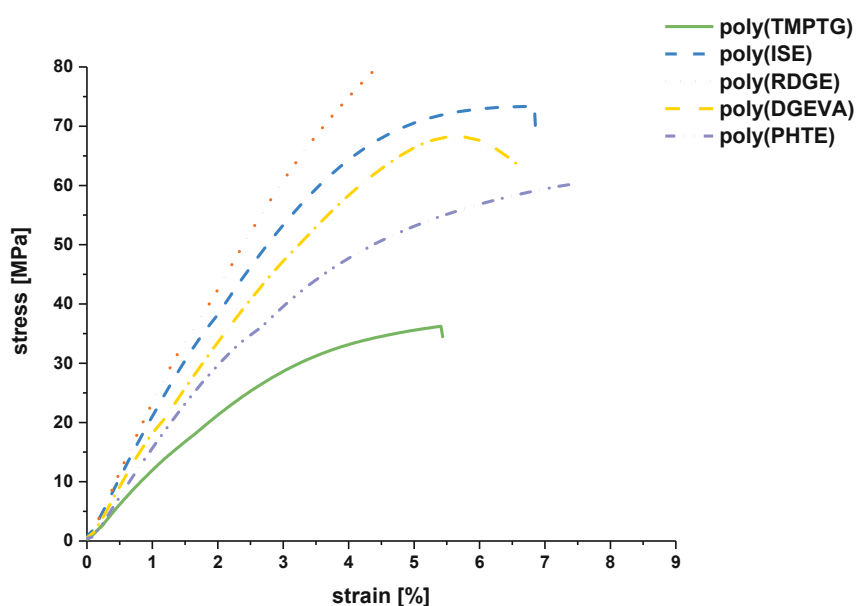


Figure 77: Exemplary stress-strain plot of poly(TMPTG) (—), poly(ISE) (---), poly(RDGE) (···), poly(DGEVA) (-·-·) and poly(PHTE) (-·-·-)

As can be seen in Figure 77, most polymers exhibit rather brittle fracture behavior, characterized by low elongation at break ( $\epsilon_B$ ) and high maximum tensile strength ( $\sigma_M$ ), typical for chain-growth photopolymers. The aliphatic **poly(TMPTG)** shows lowest maximum tensile strength ( $\sigma_M$  of 35 MPa) of all tested specimens, whereas **poly(ISE)**, **poly(DGEVA)** and **poly(PHTE)** show similar  $\sigma_M$  of around 65-70 MPa. Highest  $\sigma_M$  is achieved by the aromatic **poly(RDGE)** (82 MPa). Due to stiff aromatic and cycloaliphatic backbone of those polymers, higher mechanical stress can be withstood before the material ruptures.

Concerning strain at break, **poly(TMPTG)**, **poly(DGEVA)** and **poly(RDGE)** exhibit similar elongation of ~5%, whereas  $\epsilon_B$  is increased for **poly(ISE)** (9%) and **poly(PHTE)** (8%).

Summarizing, cationic photopolymerization leads to the formation of rather brittle materials. Due to the highly crosslinked and unregulated nature of this polymerization mode, this behavior is expected. Finally, when comparing DMTA and tensile tests, the highest  $T_G$  polymer **poly(RDGE)** also shows highest tensile strength. The stiff aromatic backbone of **poly(PHTE)** contributes to comparably high tensile strength, even though having a  $T_G$  of 35 °C. Since tensile tests were conducted at room temperature and therefore in the glass transition state of **poly(PHTE)**, polymer chains start to transition into the viscous state, explaining the higher elongation at break. Both **poly(DGEVA)** and **poly(ISE)** show a  $T_G$  of ~75 °C and similar tensile strength as well as elongation at break. Lowest tensile strength and elongation at break is observed by **poly(TMPTG)**, since the more flexible aliphatic chains do not contribute to high mechanical strength.

## 2.4. Thermal polymerization of bio-based epoxy monomers

Cationic photopolymerization of bio-derived epoxy resins was thoroughly studied in the last chapters. Advantageous for AMTs are next to its fast curing, the creation of high  $T_G$  materials with good mechanical properties (stiff and strong materials). Unfortunately, cationic photopolymerization of multifunctional monomers suffers from the creation highly crosslinked and inhomogeneous polymer networks, due to its unregulated chain growth mechanism. To overcome the inhomogeneity of the networks, the focus will be shifted towards more a regulated polymerization mechanism. Thermal polyaddition of epoxy monomers with curing agents, such as (poly)amines, anhydrides or thiols, is known to proceed as a step-growth polymerization.<sup>9</sup> Figure 78 depicts a schematic pathway of a step-growth polymerization.<sup>43</sup> Herein, two monomers (represented as black and white dots) react *via* a polyaddition reaction, forming low-molecular-weight oligomers in the beginning. Although monomer consumption is high at the beginning, high molecular weight polymers are obtained after long reaction times.

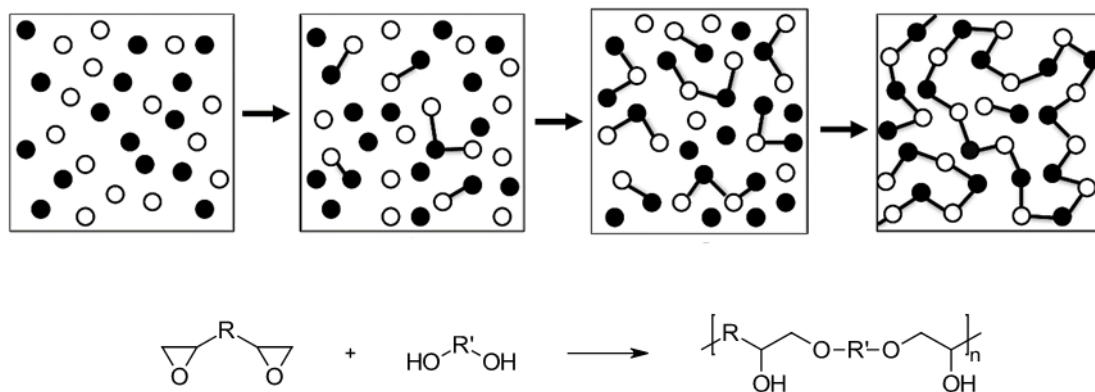


Figure 78: Top: Scheme of a step-growth polymerization of two co-monomers. At first, low molecular weight oligomers are formed and only after long reaction times, high molecular weight polymers are obtained. Bottom: Scheme of an epoxy-alcohol polyaddition.

In the following chapters, polyaddition of epoxy monomers **TMPTG**, **ISE**, **DGEVA**, **RDGE** and **PHTE** with alcohols *via* thermal polymerization will be studied.

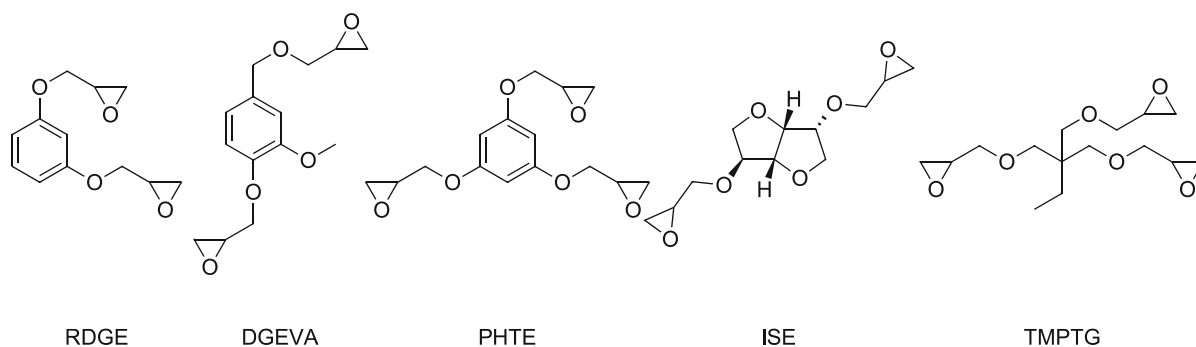


Figure 79: Chemical structure of the analyzed epoxy monomers.

At first, a suitable catalyst will be investigated and afterwards the system should be tested regarding its reactivity and polymerization mode. Finally, (thermo)mechanical properties of the networks will be evaluated using DMTA and tensile tests and compared to those networks, that were obtained using light-induced cationic polymerization.

### 2.4.1. Investigation of suitable co-monomers

Polymerization of epoxy monomers with proton donating species, such as alcohols, require not only suitable catalysts, but also compatible co-monomers. In this work, alcohols were chosen as a second type of monomers besides epoxides. Since all of the previously used epoxy monomers are derived from alcohols, first miscibility experiments were conducted using trimethylolpropane, isosorbide, resorcinol, vanillyl alcohol and phloroglucinol.

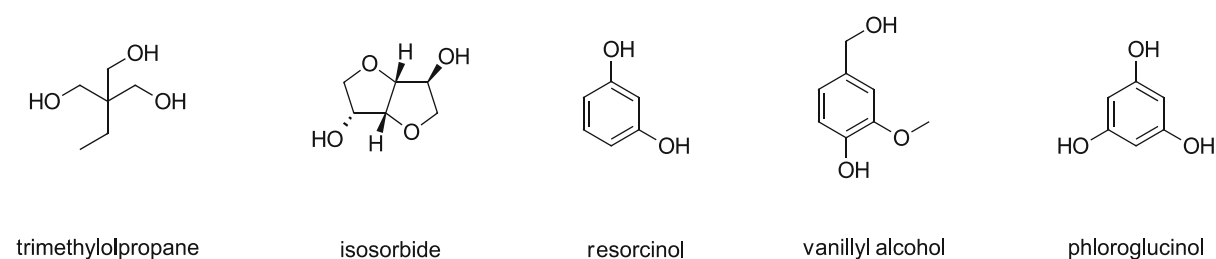


Figure 80: Chemical structure of used alcohols as co-monomers for epoxy-alcohol polyaddition.

All of the alcohols from Figure 80 are white solids with melting points of 58 °C (trimethylolpropane), 60 °C (isosorbide) or even higher for vanillyl alcohol (114-115 °C), resorcinol (110 °C) and phloroglucinol (218-222 °C).

At first, epoxy monomers (Figure 79) were mixed in an equimolar ratio of epoxy to alcohol moieties with all alcohols at elevated temperatures (60 °C and 100 °C) since insufficient solubility was observed at room temperature. While trimethylolpropane and isosorbide showed good miscibility with all epoxides at 60 °C, the more rigid phenolic polyols could only be dissolved at temperatures above 110 °C, since the solid components had to melt before giving clear, colorless solutions. Upon cooling ( $T < 100$  °C), the solid components rapidly recrystallized from the melt and are therefore not further investigated.

Thus, trimethylolpropane (**TMP**) and isosorbide (**IS**) were preliminary chosen due to their good miscibility with the epoxy monomers. Although the rigid cycloaliphatic core of **IS** would be beneficial in order to obtain a hard matrix with high strength, its difunctional nature is disadvantageous for crosslinked step-growth polymers. Since epoxy monomers **ISE**, **DEGVA** and **RDGE** are difunctional, the alcoholic co-monomer has to be at least trifunctional to ensure the formation of crosslinked networks. In the end, trimethylolpropane remains the only suitable co-monomer.



## 2.4.2. Investigation of suitable catalysts

After the investigation of a suitable alcohol as co-monomer for the polyaddition, an efficient thermal polymerization catalyst had to be found. Lewis bases are commonly used in literature to catalyze the step-growth polymerization of epoxides and conventional curing agents, such as amines or anhydrides.<sup>44</sup>

Additionally, tertiary amines are used as initiators for the anionic polymerization of epoxy resins (Figure 81, path A) or act as catalysts for the reaction of epoxy resins with hydroxyl containing reagents, such as alcohols, phenols or thiols (path B). In the presence of weak proton donating species (e.g. alcohols), chain transfer will occur from the epoxy-amine intermediate. According to the mechanism in Figure 81 proton donors become the propagating sites. Those alkoxide ions can once again attack epoxy monomers and continue the polymerization.<sup>45</sup>

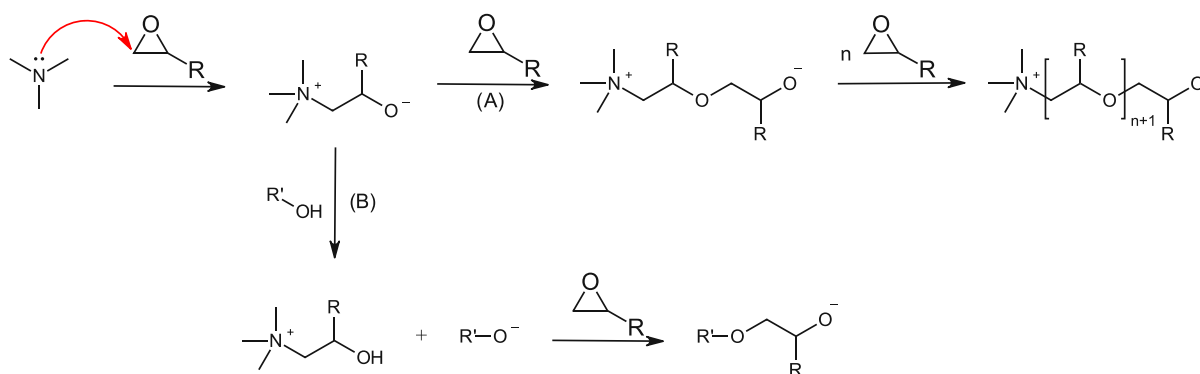


Figure 81: Mechanism of epoxy polymerization using tertiary amines as catalysts. (A): Anionic homopolymerization of epoxy monomers. (B): Chain transfer using proton donating species.

Hence, a variety of commercially available Lewis-base catalysts (see Figure 82) was screened as they are used in literature for the curing of epoxy resins.

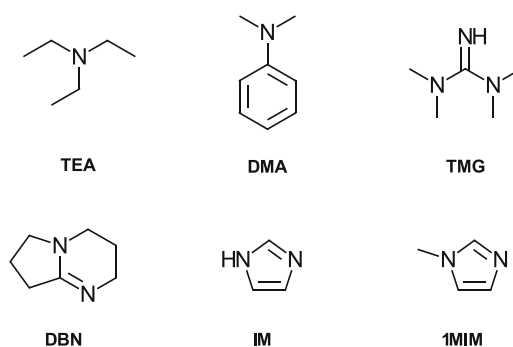


Figure 82: Screened catalysts: triethylamine (TEA), dimethylaniline (DMA), 1,1,3,3-tetramethylguanidine (TMG), 1,5-diazabicyclo[4.3.0]non-5-en (DBN), imidazole (IM) and 1-methylimidazole (1MIM)

Apart from triethylamine (TEA), dimethylaniline (DMA) is used as accelerator for epoxy-anhydride reactions.<sup>161, 162</sup> Modified 1,1,3,3-tetramethylguanidine (TMG) and 1,5-diazabicyclo[4.3.0]non-5-ene (DBN) are used as photo-latent bases for the epoxy-thiol step-growth

polymerization.<sup>163</sup> Herein, the tertiary amine is released upon irradiation and photolytic decay of the photobase generator. In a proposed mechanism, the strong base generates a thiolate anion followed by protonation of the alcoholate anion *via* the quaternary ammonium that was formed in the reaction of the base catalyst and thiol to generate the initiating thiolate, as depicted in Figure 83.<sup>164</sup>

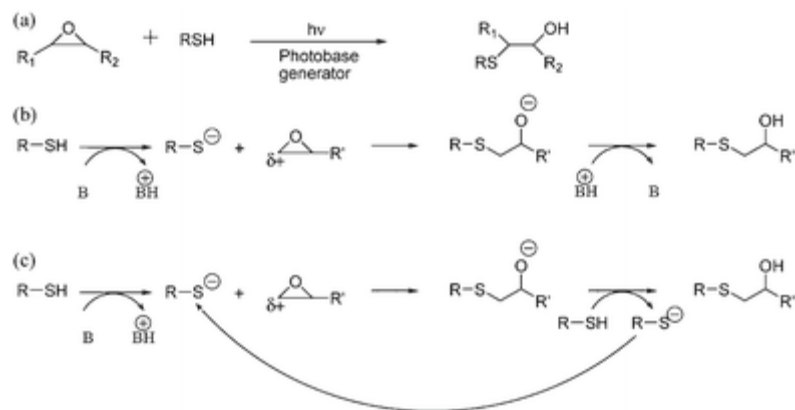


Figure 83: Proposed mechanism of the epoxy-thiol reaction.<sup>164</sup>

Furthermore, imidazoles are reported in literature as (co)-curing agents for epoxy resins. Figure 84 depicts two possible reactions of epoxy groups with 1-methylimidazole (**1MIM**). The strong basicity of the imidazole enables the anionic polymerization of epoxy resins (top), while the presence of hydroxyl containing species leads to chain-transfer. *Via* deprotonation of OH-components, alcoholate anions are produced that facilitate yet another ring-opening reaction of the epoxy monomers in a step-growth manner.<sup>165</sup>

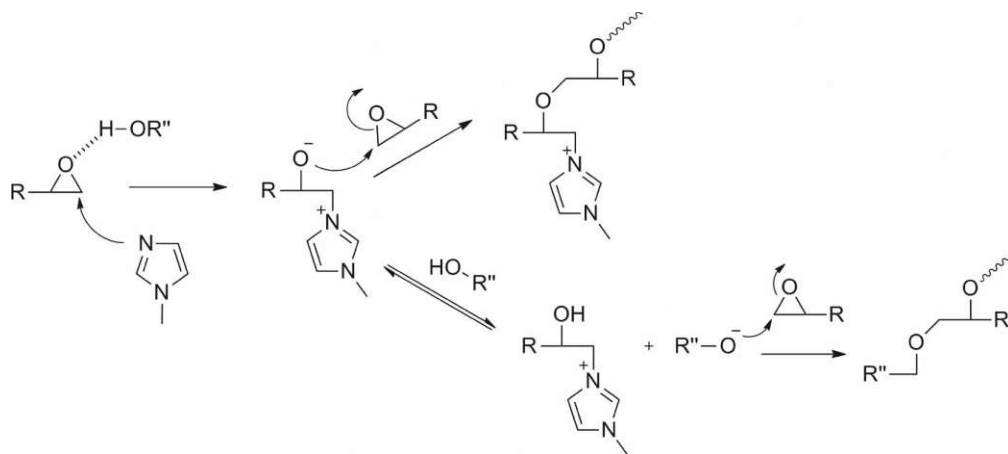


Figure 84: Proposed mechanism for the reaction of epoxy monomers with 1-methylimidazole. Top: Anionic homopolymerization, bottom: step-wise polyaddition of epoxy and hydroxyl containing monomers.<sup>165</sup>

After the selection of possible catalysts (Figure 82), the screening was conducted using **TMPTG** as epoxy monomer and **TMP** as alcohol component, since both chemicals are commercially available and their trifunctional nature should ensure the formation of crosslinked polymers.

The monomers were mixed in an equimolar ratio of epoxy to alcohol moieties at 60 °C and 5 wt% or 10 wt% of the catalyst were added for first screening trials. One polymer specimen (5 x 2 x 40 mm<sup>3</sup>) per formulation was casted in a silicon mold and thermally treated as depicted in Table 15 and Table 16. Furthermore, epoxy group conversion was obtained using ATR-IR (as described in 2.3.2) to gain information about the efficiency of the curing procedure.

Table 15: Summary of the screening conditions and results of the catalyst screening using TMPTG and TMP as monomers and 5 wt% of a catalyst. The polymerization was conducted at various temperatures (90-120 °C) for 18-48 h.

catalyst	conditions	epoxy group conversion [%]
TEA	120 °C, 20 h	12
DMA	120 °C, 48 h	<1
TMG	120 °C, 24 h	23
DBN	120 °C, 24 h	26
IM	90 °C, 18 h	>99
1MIM	90 °C, 18 h	>99

As Table 15 depicts, most of the used catalysts (in a concentration of 5 wt%) do not show sufficient catalytic efficiency for the attempted epoxy-alcohol polymerization. In general, aromatic amines (such as **DMA**) are less reactive than aliphatic amines (e.g. **TEA**), due to their weaker nucleophilicity.<sup>44</sup> Therefore, **TEA** acts as a better catalyst than **DMA**. **TMG** and **DBN** represent a class of non-nucleophilic bases with a pK<sub>a</sub> ~14. Due to their strong base character, epoxy group conversion is enhanced compared to **TEA** and **DMA**. Among the screened tertiary amines, imidazoles **IM** and **1MIM** perform best, as full epoxy group conversion was achieved within 18 h.

In a parallel experiment, 10 wt% of each catalyst were added to the monomer formulations to determine if a higher concentration of the catalyst would enhance the reactivity of the polymerization. It should be noted that the screening conditions were not changed to ensure reproducibility of the experiments.

Table 16: Summary of the screening conditions and results of the catalyst screening using TMPTG and TMP as monomers and 10 wt% of a catalyst. The polymerization was conducted at various temperatures (90-120 °C) for 1-48 h.

catalyst	conditions	epoxy group conversion [%]
TEA	120 °C, 20 h	23
DMA	120 °C, 48 h	<1
TMG	120 °C, 24 h	45
DBN	120 °C, 24 h	39
IM	90 °C, 1 h	>99
1MIM	90 °C, 1 h	>99

Similar to the previous findings, 10 wt% of the catalyst does not lead to full conversion of the epoxy moieties for the catalysts **TEA**, **DMA**, **TMG** and **DBN**, even though a slight improvement of the epoxy group conversion is observed in all cases. On the other hand, the imidazole-based catalysts **IM** and **1MIM** outperform all other systems, reaching full epoxy group conversion in one hour.

Therefore, it was decided to further investigate imidazoles as potential catalysts for the epoxy-alcohol polyaddition. Nevertheless, 10 wt% of catalyst catalyze the reaction way too fast, and so, curing experiments with a decreased amount of the catalyst **IM** were conducted. By that, the stability of the formulations should be enhanced to prevent premature polymerization. Once again, **TMPTG** and **TMP** were used as monomers, maintaining an equimolar ratio of epoxy and alcohol moieties. The formulations were cured at 90 °C overnight and ATR-IR spectra were recorded to calculate the epoxy group conversion.

Table 17: Calculated epoxy group conversion of formulations containing TMPTG and TMP as monomers and 0.1-10 wt% of the catalyst imidazole. Experiments were conducted at 90 °C overnight (16-18 h).

amount of catalyst [wt%]	epoxy group conversion [%]
10	>99
5	>99
1	98
0.1	<1

As can be seen in Table 17, 1 wt% of imidazole seems to be enough to enable a polyaddition reaction of epoxy and alcohol moieties, whereas decreasing the catalyst amount to 0.1 wt% leads to no conversion of epoxy moieties.

Concluding, optimization of the catalyst concentration showed, that 1 wt% of imidazole enables the polyaddition of epoxy and alcohol moieties in a reasonable amount of time. Therefore, it

will be used as catalyst for further characterization of the reactivity and thermomechanical properties of thermally cured epoxy polymers.

### 2.4.3. Proton NMR study

Step-growth polymerizations are characterized by the stepwise reaction of bi- or multifunctional monomers to form high-molecular-weight polymers after a large number of steps. In strong contrast to chain growth polymerizations, all monomers are reactive and consequently a high number of monomers is consumed in the early stages of the reaction.

To prove whether epoxides and alcohols proceed in a stepwise polyaddition reaction, a proton NMR model study was conducted. Ideally, *via* the reaction of diepoxy and diol monomers, linear polymers, that are soluble in NMR solvents should be obtained. So, difunctional epoxy monomers **ISE**, **DGEVA** and **RDGE** were mixed with **hexanediol** in an equimolar ratio of reactive groups. Furthermore, 1 wt% of the catalyst imidazole was added. The formulations were heated to 60 °C, stirred and samples were drawn every 15 min and diluted in  $d_6$ -DMSO.

At first, the reaction between **ISE** and **hexanediol** is studied. Figure 85 shows the chemical structure of both molecules. Additionally, the relevant molecular fragments for the proton NMR analysis are marked and will also be used for the interpretation of the proton NMR spectra. Glycidyl ether peaks  $-CH_2-CH-$  (2.84-2.62 ppm) are labelled green and the hydroxyl groups  $-OH$  (4.31 ppm) of hexanediol are highlighted in blue. For **ISE**, the exocyclic protons are used as reference (4.40-4.61 ppm, red) and for **hexanediol**, the  $-CH_2-$  signal at 1.26 ppm (black) is chosen as reference. Figure 86 depicts the measured proton NMR spectra after 0h, 1h, 2h and 4h of reaction.

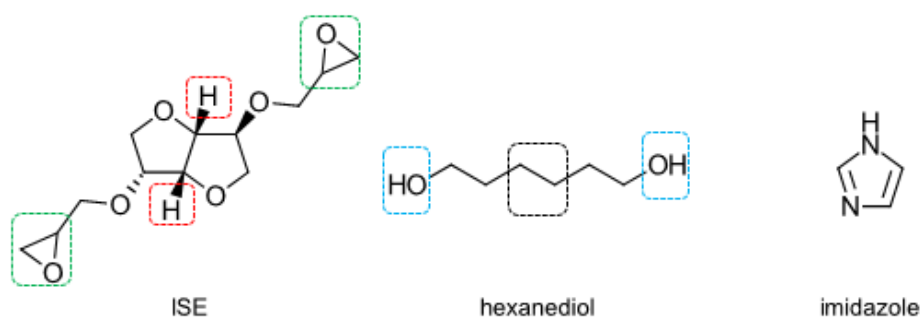


Figure 85: Chemical structure of the monomers used for the  $^1H$ -NMR model study: isosorbide diglycidyl ether (ISE), hexanediol and imidazole. Molecular fragments for the analysis are labelled.

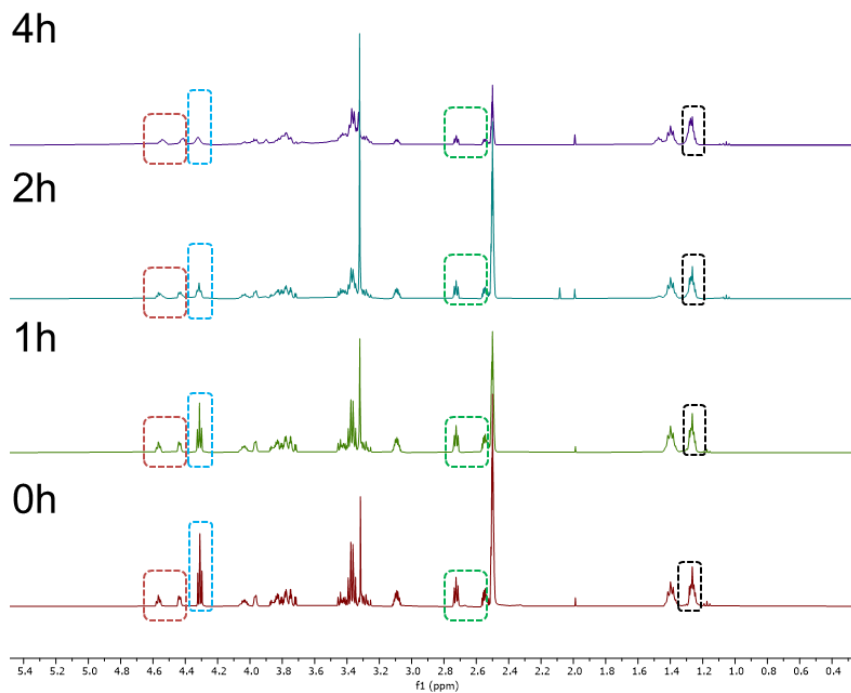


Figure 86: NMR study of ISE and hexanediol, the corresponding peaks are allocated.

Via integration of the OH peaks of hexanediol and the glycidyl ether peaks in respect to the -CH<sub>2</sub>- of hexanediol and the exocyclic -H of isosorbide, conversion of the reactive moieties is calculated using equation ( 5 ) and is displayed in Figure 87.

$$\text{Conversion (\%)} = \left( 1 - \frac{\text{integral}(t_x)}{\text{integral}(t_0)} \right) \cdot 100\% \quad (5)$$

*integral t<sub>x</sub>*... integral of the corresponding peak at t=t<sub>x</sub>

*integral t<sub>0</sub>*... integral of the corresponding peak at the beginning (t=t<sub>0</sub>)

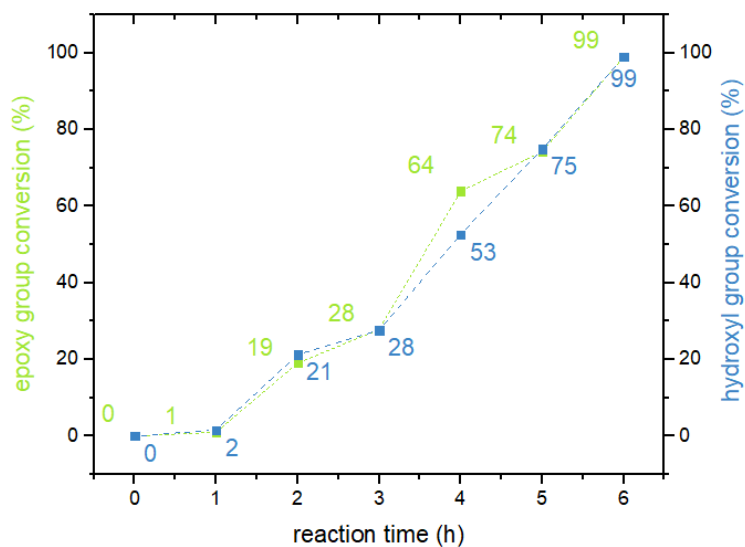


Figure 87: Epoxy group conversion (green) and hydroxyl group conversion (blue) of the reaction between ISE and hexanediol.

As can be seen in Figure 87, epoxy group conversion (in green) as well as the -OH group conversion (in blue) proceed in a comparable way. In the early stages of the polymerization (up to 1h), low conversions of both monomers are observed, before the reaction starts at around 2h, when both monomers show a conversion of about 20%. After 4h, nearly half of the reactive groups in hexanediol have reacted with approximately 60% of the epoxy groups in ISE, while after 6h full conversion of both monomers is reached. Hence, gathered data shows that both monomers react similarly with each other. Therefore, epoxy groups and hydroxyl groups react homogeneously to give regulated polyaddition polymers.

Next, the model study was conducted for the aromatic diglycidyl ethers **DGEVA** and **RDGE**. Similar to ISE, the aromatic monomers were reacted with **hexanediol** as well as 1 wt% of imidazole as catalyst. Figure 88 depicts the used molecular fragments for the proton NMR analysis. Glycidyl ether peaks of both **RDGE** and **DGEVA** can be found at 2.85-2.55 ppm. To standardize those signals, the peaks for the phenyl backbone (6.58 ppm) were used in the case of **RDGE**. For **DGEVA**, the methyl ether -O-CH<sub>3</sub> peaks (3.82 ppm) served as reference. Figure 89 depicts the measured proton NMR spectra after 0h, 1h, 2h and 3h of reaction for **RDGE** and Figure 91 depicts the measured proton NMR spectra for **DGEVA** over the course of the reaction.

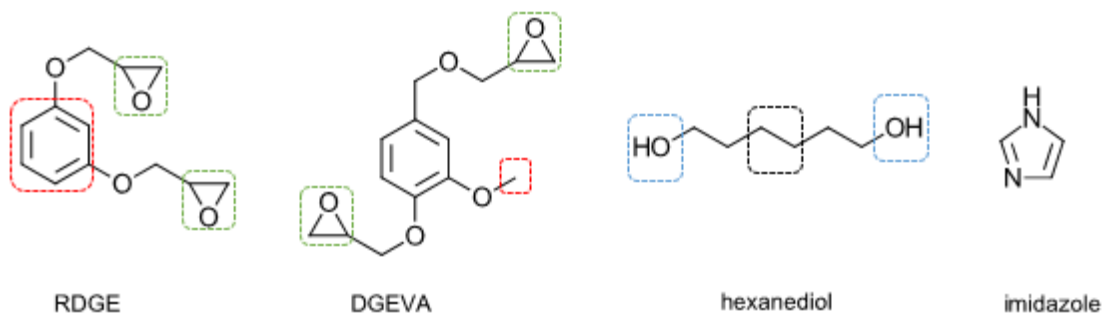


Figure 88: Chemical structure of the monomers used for the <sup>1</sup>H-NMR model study: resorcinol diglycidyl ether (RDGE), diglycidyl ether of vanillyl alcohol (DGEVA), hexanediol and imidazole. Molecular fragments for the analysis are labelled.

Conversion of the epoxy groups and hydroxyl groups was calculated according to equation (5) and is presented in Figure 90. Similar to **ISE**, the reaction between **RDGE** and **hexanediol** proceeds with low conversion of both monomers (<10%) at the beginning. Thereafter, the reaction continues with similar epoxy and alcohol conversions, leading to 50% hydroxyl- and 66% epoxy group conversion after 2h. Finally, after 3h of reaction time full conversion of both monomers is observed. Due to the similar conversion of **RDGE** and **hexanediol**, it can be assumed that the monomers polymerize in a stepwise polyaddition.

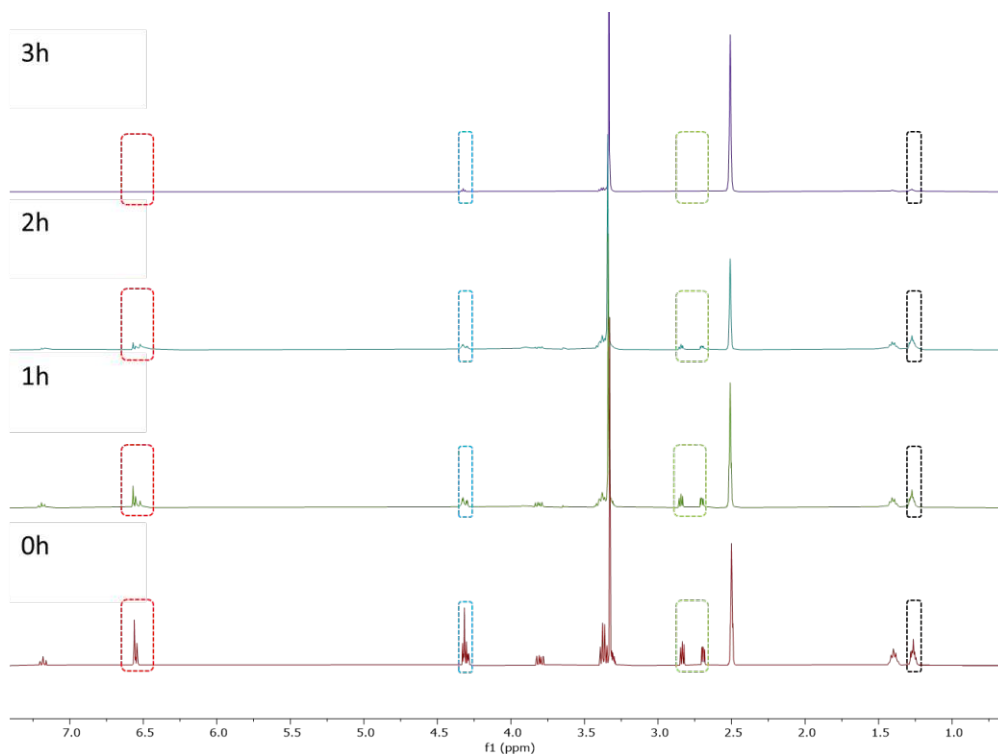


Figure 89: NMR study of RDGE and hexanediol, the corresponding peaks are allocated.



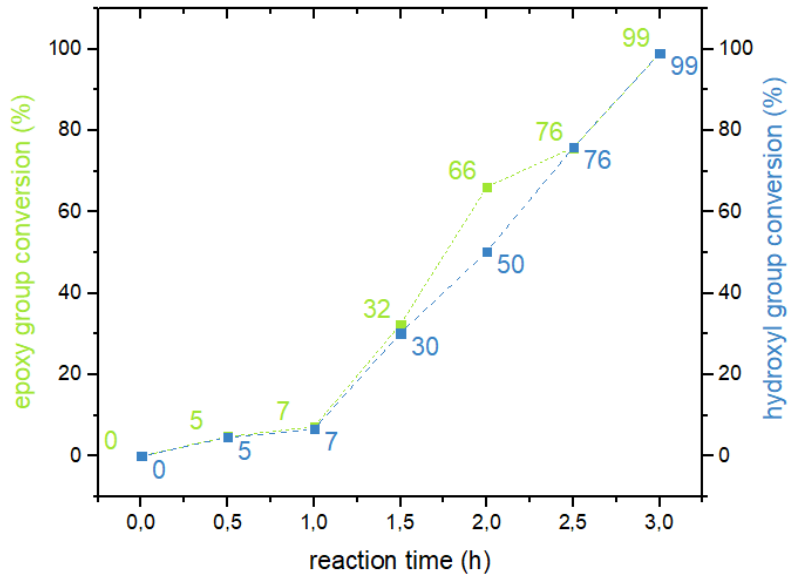


Figure 90: Epoxy group conversion (green) and hydroxyl group conversion (blue) of the reaction between RDGE and hexanediol.

Finally, the same analysis will be made for DGEVA and hexanediol. Conversion of epoxy and alcohol moieties was once again accomplished using equation ( 5 ) and is depicted in Figure 92.

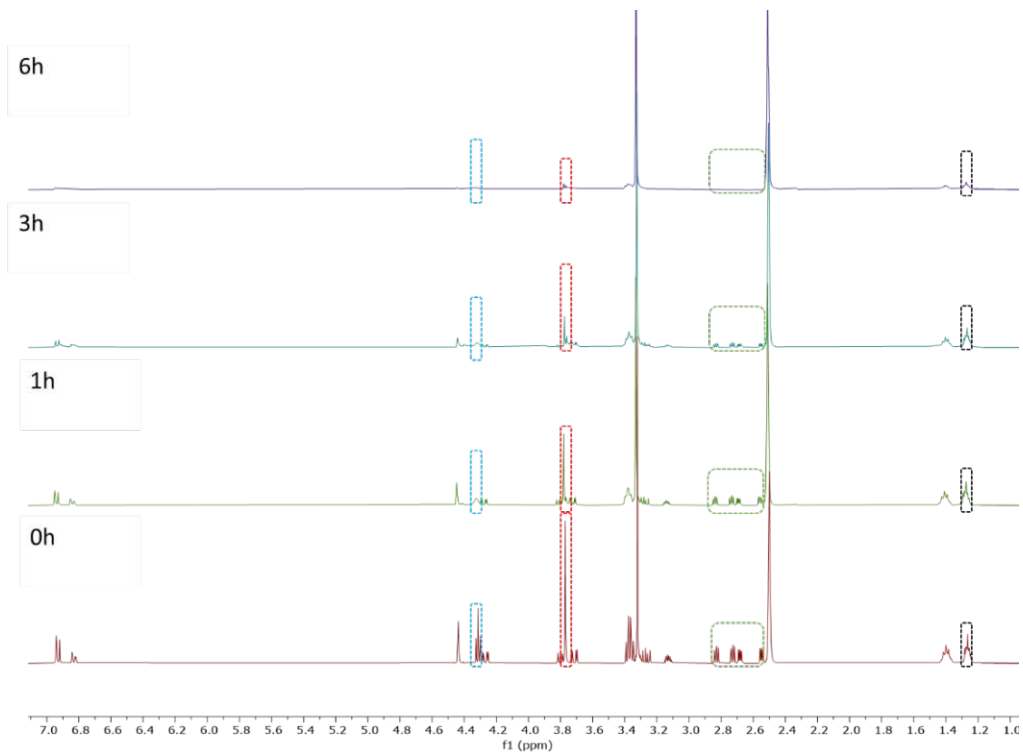


Figure 91: NMR study of DGEVA and hexanediol, the corresponding peaks are allocated.

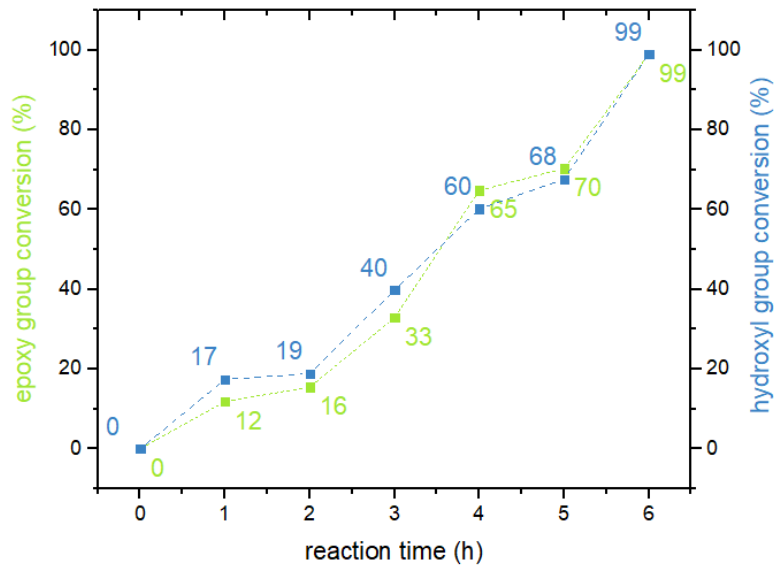


Figure 92: Epoxy group conversion (green) and hydroxyl group conversion (blue) of the reaction between DGEVA and hexanediol.

Similar to the analysis of **ISE** and **RDGE**, **DGEVA** and **hexanediol** react in a homogeneous and similar way with one another. In contrast to the monomers before, higher conversion (up to 19%) of both monomers is achieved in the early stages of the polymerization. In the further process, **DGEVA** and **hexanediol** react in a comparable way, leading to roughly 60-65% conversion after 4h and full conversion of both monomers after 6h.

Finally, rate of polymerization ( $R_p$ ) was determined from the data obtained *via* the proton NMR study and is defined as concentration of the monomers [mol/L] per time [1/s]. From the slope of the conversion per time diagrams (Figure 87, Figure 90 and Figure 92) and the density of the monomers at 60 °C,  $R_p$  was calculated and is depicted in Table 17. All formulations showed an induction period of 1h, after which the monomers started to react with each other. Consequently, the rate of polymerization was determined at  $t=1h$  until full consumption of monomers. As displayed below, it can be seen that the epoxy monomers **ISE** and **DGEVA** show similar rate of polymerization of 24 mmol/L\*s, whereas  $R_p$  of **RDGE** is nearly 2.5-times higher (74 mmol/L\*s). This trend is in correspondence with the data presented previously, as the sample containing **RDGE** showed full conversion after 3h and those containing **ISE** and **DGEVA** exhibited full monomer conversion after 6h. Therefore, it can be concluded that **RDGE** reacts faster in a thermal polyaddition with the diol hexanediol compared to **ISE** and **DGEVA**, even epoxy groups and hydroxyl groups of all monomers are consumed evenly, suggesting a regulated polyaddition between epoxy and alcohol monomers.

Table 18: Calculated rate of polymerization ( $R_p$ ) of the thermal polymerization of difunctional epoxy monomers ISE, RDGE and DGEVA and the difunctional alcohol hexanediol.

epoxy monomer	$R_p$ [mmol/L*s]
ISE	24.0
RDGE	74.0
DGEVA	24.1

#### 2.4.4. Thermal reactivity via differential scanning calorimetry (DSC)

After the evaluation of the polymerization mechanism via proton NMR, the reactivity of all monomers towards thermal polyaddition was studied via differential scanning calorimetry (DSC). Hereby, thermally reactive formulations are heated with a gradient 5 K/min from 25 °C to 200 °C and the released heat of polymerization is recorded over the temperature range. Similar to chapter 2.3.1, the heat of polymerization can be used to calculate the final conversion of the polymerization. Furthermore, by determination of the onset temperature, information about the thermal stability each formulation is gained. A low onset temperature may indicate poor storage stability, as the polymerization may be initiated at lower temperatures.

Consequently, the epoxy monomers **TMPTG**, **ISE**, **DGEVA**, **RDGE** and **PHTE** were mixed in a molar ratio of 1:1 in respect to reactive groups with the trifunctional alcohol **TMP** and additionally 1 wt% of the catalyst imidazole was added. As an explanation, the formulation **TMPTG:TMP** contains an equimolar amount of the epoxy monomer **TMPTG** and the alcohol **TMP**. The results of the DSC analysis are depicted in Table 19.

Table 19: Onset temperature, peak temperature and heat of polymerization of formulations containing epoxy monomers **TMPTG**, **ISE**, **RDGE**, **DGEVA** and **PHTE** and **TMP** as alcohol component and 1 wt% imidazole.

	Onset temperature [°C]	peak temperature [°C]	Heat of polymerization [J/g]
<b>TMPTG:TMP</b>	118 ± 4	129 ± 2	470 ± 1
<b>ISE:TMP</b>	115 ± 2	127 ± 2	543 ± 6
<b>DGEVA:TMP</b>	94.3 ± 0.6	111 ± 1	558 ± 2
<b>RDGE:TMP</b>	86.6 ± 1.8	104 ± 1	585 ± 7
<b>PHTE:TMP</b>	91.1 ± 0.4	111 ± 1	659 ± 5

The following parameters were used to determine the reactivity of the monomers: first, the onset temperature gives information about the stability of the formulations. High onset temperatures lead to thermally more stable formulations and are therefore desirable. All formulations containing aromatic monomers **DGEVA**, **RDGE** and **PHTE** start to polymerize around 90 °C and exhibit a peak maximum at around 110 °C. By contrast, the onset temperature of the formulations **TMPTG:TMP** and **ISE:TMP** with the cycloaliphatic epoxy

monomer is significantly higher with 118 °C and 114 °C, respectively. Additionally, the peak temperature of the aliphatic and cycloaliphatic monomers is around 20 °C higher (129 °C for **TMPTG:TMP** and 127 °C for **ISE:TMP**) compared to the phenol-derived epoxy monomer formulations. This behavior might be explained by the different chemical environment of the glycidyl ethers since the phenolic ring in proximity to the epoxy moiety has a higher electronic density than the aliphatic heterocycle of the ISE monomer or the aliphatic chain of TMPTG and could increase the reactivity of phenolic resins.

On the other hand, the exothermic peak of the polymerization can be used to determine the epoxy conversion. By integration of the peak, the heat of polymerization is obtained and by comparison with the theoretical heat of polymerization (~100 kJ/mol).<sup>156</sup> For comparison, the epoxy group conversion was determined of the polymerized specimens after the DSC analysis using FT-IR spectroscopy, similar to 2.3.2. A summary of the calculated conversions is depicted in Table 20.

Table 20: Comparison of epoxy group conversion of the DSC analysis calculated via heat of polymerization (DSC) and ATR-IR.

	Conversion via DSC [%]	conversion via IR [°C]
<b>TMPTG:TMP</b>	95	>99
<b>ISE:TMP</b>	95	>99
<b>DGEVA:TMP</b>	94	>99
<b>RDGE:TMP</b>	92	98
<b>PHTE:TMP</b>	98	98

As depicted in Table 20, high conversions of over 90% are observed for all polymers, regardless of their structure. In general, the formulation containing the trifunctional monomer **PHTE** leads to the highest conversion (98%) according to DSC, whereas formulations with **TMPTG**, **ISE**, **DGEVA** and **RDGE** still reached high conversions of 95%, 94% and 92%, respectively.

By contrast, using FT-IR leads to slightly higher calculated conversions for all polymers (≥98%). This can be attributed to the fact, that for the DSC analysis, only the heat of polymerization was used for the calculation of the conversion, even though DSC was operating at even higher temperatures, that could lead to a thermal post-curing effect, increasing the epoxy group conversion. Furthermore, the conversion was calculated using the literature-known value of 100 kJ/mol for the heat of polymerization for one epoxy group. Nevertheless, the chemical environment of every molecule may lead to an increase or decrease of said value, explaining the deviation of the conversion that was calculated *via* DSC and ATR-IR.

To conclude, all tested monomers show high reactivity towards base-catalyzed thermal polyaddition, reaching high epoxy group conversions of >90%. Regarding thermal stability, formulations containing phenol-based monomers **RDGE**, **DGEVA** and **PHTE** exhibit an onset temperature around 90 °C, whereby (cycloaliphatic) **ISE** and **TMPTG** show higher onset temperatures of over 110 °C, suggesting higher thermal stability of those formulations.

## 2.4.5. Rheology and Storage stability

### 2.4.5.1. Rheology measurements

In order to determine the processability of the formulations for polyaddition, rheology measurements were conducted. Therefore, formulations from 2.4.3 were measured with a shear rate of 100 s<sup>-1</sup> from 60-100 °C and the viscosity of each formulation is depicted in Figure 93. Exact viscosities at 60 °C and 90 °C are depicted in Table 21.

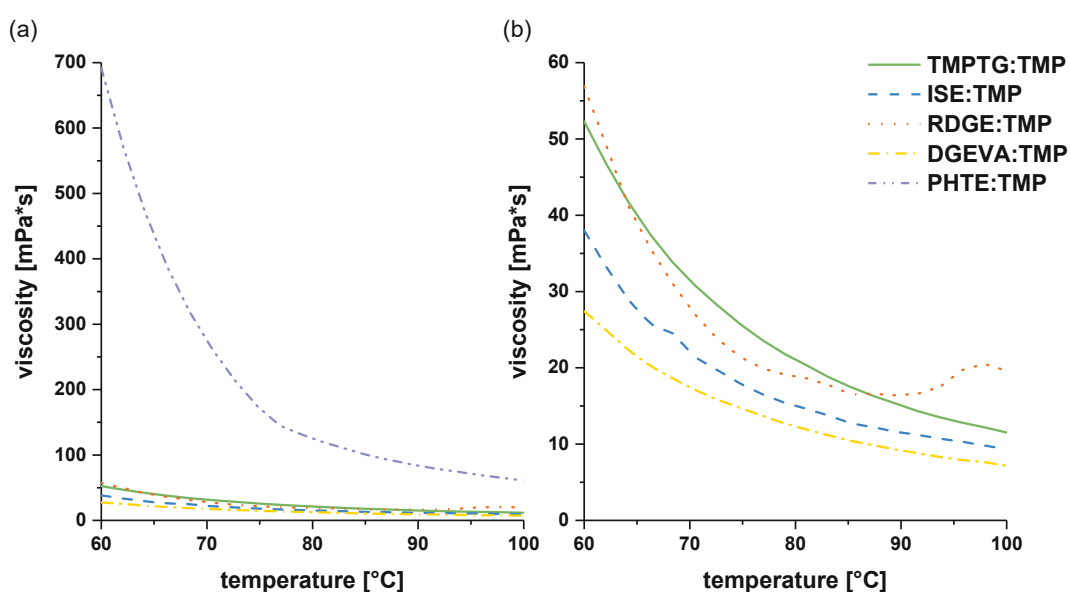


Figure 93: Viscosity plots of polyaddition formulations from 60-100 °C.

(a) All formulations and (b) without PHTE:TMP.

Table 21: Formulations and viscosities of polyaddition formulations at 60 °C and 90 °C.

	$\eta_{60^{\circ}\text{C}}$ [mPa·s]	$\eta_{90^{\circ}\text{C}}$ [mPa·s]
<b>TMPTG:TMP</b>	52.3	15.3
<b>ISE:TMP</b>	38.0	11.6
<b>RDGE:TMP</b>	56.9	16.4
<b>DGEVA:TMP</b>	27.4	9.29
<b>PHTE:TMP</b>	692	85.1

From Figure 93 (a) it can be seen that the formulation containing the trifunctional monomer PHTE (**PHTE:TMP**) exhibits the highest viscosity ( $\eta_{60^{\circ}\text{C}} = 692$  mPa·s) of all formulations, due

to its rigid tri-phenolic backbone. Formulations containing the aromatic diglycidyl ether RDGE (**RGDE:TMP**,  $\eta_{60^\circ\text{C}} = 56.9 \text{ mPa}\cdot\text{s}$ ) and the aliphatic triglycidyl ether TMPTG (**TMPTG:TMP**,  $\eta_{60^\circ\text{C}} = 52.3 \text{ mPa}\cdot\text{s}$ ) exhibit viscosities of around  $50 \text{ mPa}\cdot\text{s}$ . Lower viscosities are determined for **ISE:TMP** ( $38.0 \text{ mPa}\cdot\text{s}$ ) and lowest viscosity is measured for **DGEVA:TMP** ( $27.4 \text{ mPa}\cdot\text{s}$ ). At  $90^\circ\text{C}$ , **PHTE:TMP** exhibits a viscosity of  $\sim 85 \text{ mPa}\cdot\text{s}$ , while all other formulations show low viscosity values of  $\sim 10\text{-}15 \text{ mPa}\cdot\text{s}$ . Regarding **RDGE:TMP**, unwanted thermal polymerization at around  $95^\circ\text{C}$  is observed, leading to an increase in viscosity to  $22 \text{ mPa}\cdot\text{s}$ . Finally, it is demonstrated, that all formulations exhibit viscosities of below  $1 \text{ Pa}\cdot\text{s}$  at  $60^\circ\text{C}$ , making them applicable for 3D printing.

#### 2.4.5.2. Storage stability of polyaddition formulations

To manufacture 3D printed parts, pot-life or storage stability of the formulation is crucial. By that, storage conditions can be evaluated and how long the formulations can be stored after being prepared. Since polyaddition of epoxy and alcohol monomers is initiated thermally, a storage stability study was conducted to investigate thermal stability of the formulations. In this study, 1 wt% of the initiator imidazole were added to the formulations containing an equimolar ratio of epoxy and alcohol monomers, in respect to reactive groups. Formulations were stored at room temperature ( $25^\circ\text{C}$ ) for one month. Following a predetermined time schedule, small amounts of the formulations were taken out of the vials and the viscosity at  $60^\circ\text{C}$  was determined with a shear rate of  $100 \text{ s}^{-1}$ . The measurements were conducted at elevated temperatures, to ensure good miscibility of all components.

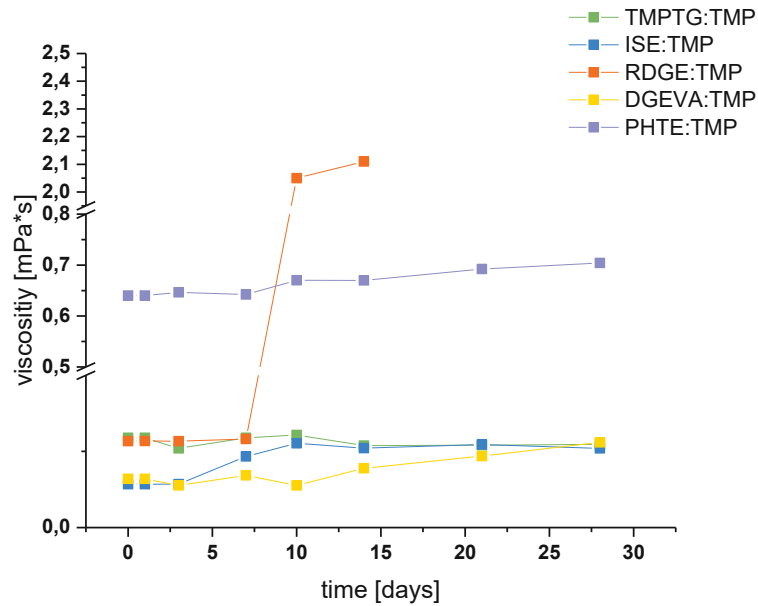


Figure 94: Storage stability study at room temperature for polyaddition formulations. TMPTG:TMP (●), ISE:TMP (●), RDGE:TMP (●), DGEVA:TMP (●) and PHTE:TMP (●)

From Figure 94 it can be seen, that up to 7 days, all formulations are stable at room temperature, as the viscosity of the formulations does not increase significantly. A slight increase in viscosity for **ISE:TMP** is observed after approximately 10 days (46.6 mPa·s to 52.2 mPa·s), whereby the viscosity does not increase significantly at longer times, reaching a viscosity of 51.9 mPa·s after 28 days. An increase of viscosity is very pronounced for **RDGE:TMP** after 10 days (58.1 mPa·s to 2.05 Pa·s), indicating poorest storage stability of all formulations. For **DGEVA:TMP** a marginal increase in viscosity is exhibited after 14 days, whereby **TMPTG:TMP** and **PHTE:TMP** show no increase in viscosity over 28 days.

## 2.4.6. Thermomechanical properties of polyaddition polymers

To complete the studies on the polyaddition of epoxy and alcohol monomers via polyaddition, thermally initiated bulk polymerization and thermomechanical properties of the resulting poly(ether)s were investigated in more detail. As a start, dynamic mechanical analysis (DMTA) of the polymers was measured. Therefore, formulations containing an equimolar amount of epoxy and alcohol monomers, in respect to reactive groups, were prepared from the monomers depicted in

Figure 95. Thereafter, one DMTA specimen of each formulation was casted for 16-18h at 90 °C in a silicon mold, to obtain specimens of 2x5x40 mm<sup>3</sup>. Epoxy group conversion of cured polymer specimens was determined as stated in 2.3.2 and is depicted in Table 22.

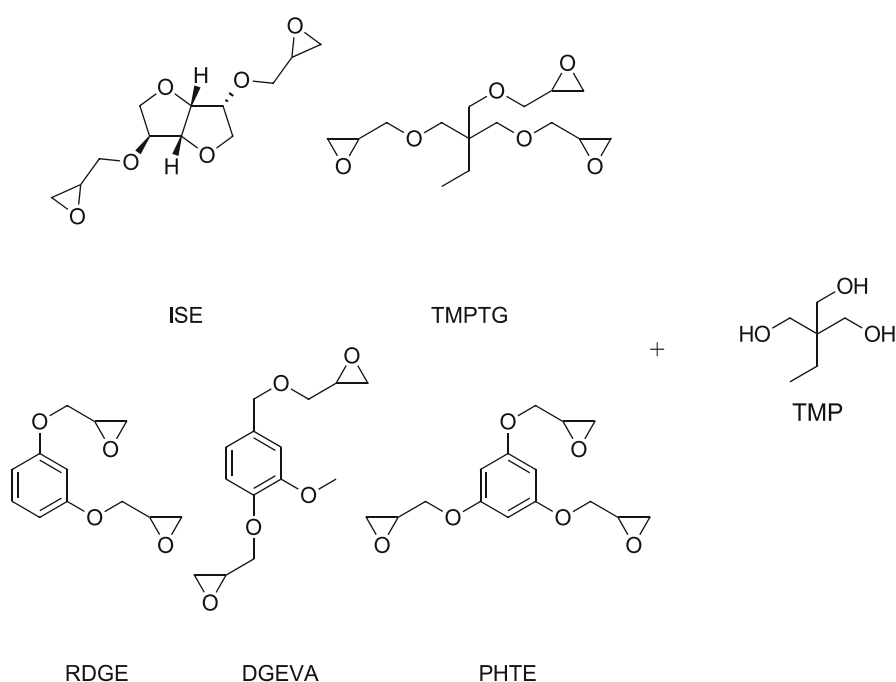


Figure 95: Monomers used for the determination of thermomechanical properties of poly(ethers) that were cured via thermally initiated polyaddition.

Table 22: Epoxy group conversion of polyaddition polymers determined via ATR-IR. Polymerization was conducted at 90 °C for 18h.

	epoxy group conversion [%]
poly(TMPTG:TMP)	98
poly(ISE:TMP)	>99
poly(RDGE:TMP)	98
poly(DGEVA:TMP)	>99
poly(PHTE:TMP)	>99



As can be seen in Table 22, thermal polymerization leads to high epoxy group conversion for all polymers. After determination of the epoxy group conversion, specimens were prepared for DMTA analysis and the viscoelastic properties of the polymers were analyzed as stated in 2.3.3.

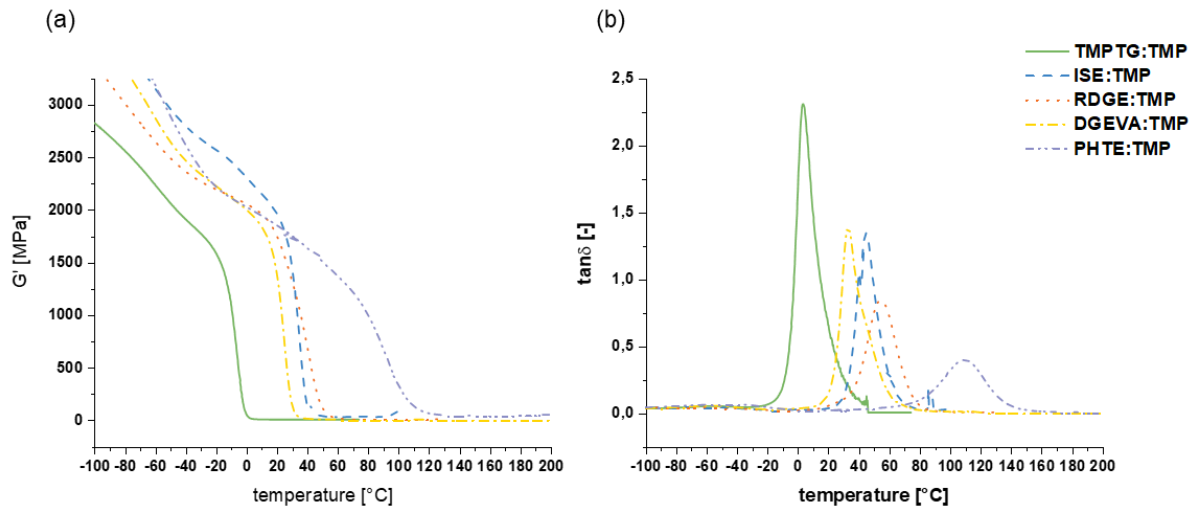


Figure 96: (a) Storage modulus ( $G'$ ) and (b) loss factor ( $\tan\delta$ ) of TMPTG:TMP (-), ISE:TMP (- -), RDGE:TMP (· ·), DGEVA:TMP (- · -) and PHTE:TMP (- · · -)

Figure 96 (a) depicts the storage modulus  $G'$  and Figure 96 (b) depicts the loss factor  $\tan\delta$  of **poly(TMPTG:TMP)**, **poly(ISE:TMP)**, **poly(RDGE:TMP)**, **poly(DGEVA:TMP)** and **poly(PHTE:TMP)**. Furthermore, Table 23 summarizes the exact values of the analysis. In order to obtain the glass transition temperature of every polymer, the maximum loss factor was observed. **Poly(TMPTG:TMP)** exhibits a sharp maximum in the loss factor at 2°C, which is well below room temperature. This can be attributed to the high flexibility of the aliphatic chains in the polymers. By contrast, the more rigid cycloaliphatic core of ISE leads to a higher glass transition temperature for **poly(ISE:TMP)** (48 °C). The aromatic backbone of RDGE and DGEVA additionally increases the rigidity of the polymers, leading to higher  $T_G$  for **poly(DGEVA:TMP)** (35 °C) and **poly(RDGE:TMP)** (52 °C). Due to the trifunctional nature of both PHTE and TMP, highly crosslinked **poly(PHTE:TMP)** shows the highest glass transition temperature (104 °C) of all specimens. Overall, sharp glass transitions are observed for all polymers, indicating homogeneous and more regulated polymers *via* step-growth polyaddition.

Table 23:  $G'_{25^\circ\text{C}}$ ,  $G'_R$  and  $T_G$  of thermally cured epoxy:alcohol polymers.

	$G'_{25}$ [MPa]	$T_G$ [°C]	$G'_r$ [MPa]
<b>poly(TMPTG:TMP)</b>	0.591	2	0.513
<b>poly(ISE:TMP)</b>	1800	48	23.4
<b>poly(RDGE:TMP)</b>	1560	52	4.58
<b>poly(DGEVA:TMP)</b>	755	35	1.85
<b>poly(PHTE:TMP)</b>	1810	104	39.9

Summarizing, due to the thermal step-growth polyaddition sharp glass transitions were determined for all tested specimens, indicating the formation of regulated polymer networks. Furthermore, polymers based on **ISE:TMP**, **DGEVA:TMP**, **RDGE:TMP** and **PHTE:TMP** exhibit  $T_G$  well above 30 °C, making them suitable for the hard matrix of IPNs. **Poly(TMPTG:TMP)** with its low  $T_G$  of 2 °C contradicts the desired properties of a hard matrix. Therefore, it was decided not to conduct further tensile testing or incorporate **TMPTG:TMP** into the future IPNs.

### 2.4.7. Tensile tests of polyaddition polymers

To complete the study on the thermomechanical properties of thermally polymerized monomers, tensile tests were conducted. DMTA analysis indicated the formation of regulated and homogeneous polymer networks that can be seen by sharp glass transitions. Therefore, tensile tests were measured to determine the influence of more homogeneous polymer networks on their mechanical properties.

Tensile tests specimens of shape 5B were prepared from the DMTA-formulations in 2.4.6 and the measurements were conducted as previously described in 1.4.2. One exemplary stress-strain curve of each polymer is depicted in Figure 97, while Table 14 summarizes the exact values of the tensile test measurements.

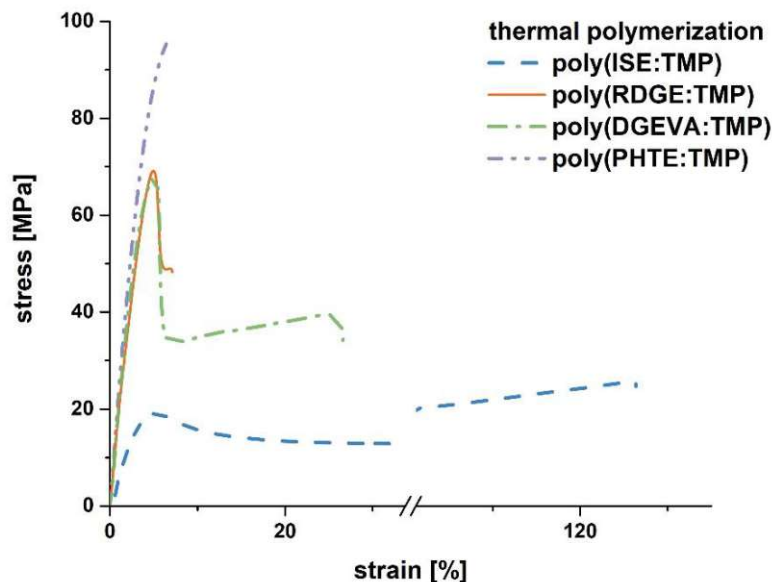


Figure 97: Exemplary stress-strain plots of thermally cured poly(ISE:TMP) (---), poly(RDGE:TMP) (-), poly(DGEVA:TMP) (-.-) and poly(PHTE:TMP) (-.-.-).

As can be seen in Figure 98, **poly(PHTE:TMP)** exhibits highest maximum tensile strength with 90 MPa, while **poly(DGEVA:TMP)** and **poly(RDGE:TMP)** reach similar values of around 65 MPa. Interestingly, the polymers which are produced from diglycidyl ether monomers both display a distinct yield point after reaching  $\sigma_m$ , that could indicate more regulated and toughened polymers. This behavior is particularly pronounced for **poly(DGEVA:TMP)**: after reaching its yield point, the specimens show the ability for plastic deformation and consequently highest elongation at break (27%) is observed. Considering **poly(RDGE:TMP)** and **poly(PHTE:TMP)**, similar  $\epsilon_B$  of around 7% is observed. Compared to the aromatic polymers, **poly(ISE:TMP)** displays rather elastomeric behavior with a low maximum tensile stress of 21 MPa and high elongation at break of 125%. By that, it was shown that the aromatic backbone of **poly(RDGE:TMP)**, **poly(DGEVA:TMP)** and **poly(PHTE:TMP)** contributes to the

mechanical properties of the materials. Strong and tough polymers were obtained compared to the elastic ISE-derived **poly(ISE:TMP)**. Tensile tests show, that the cycloaliphatic core of the ISE monomer does not deliver as much strength to the polymers as an aromatic backbone.

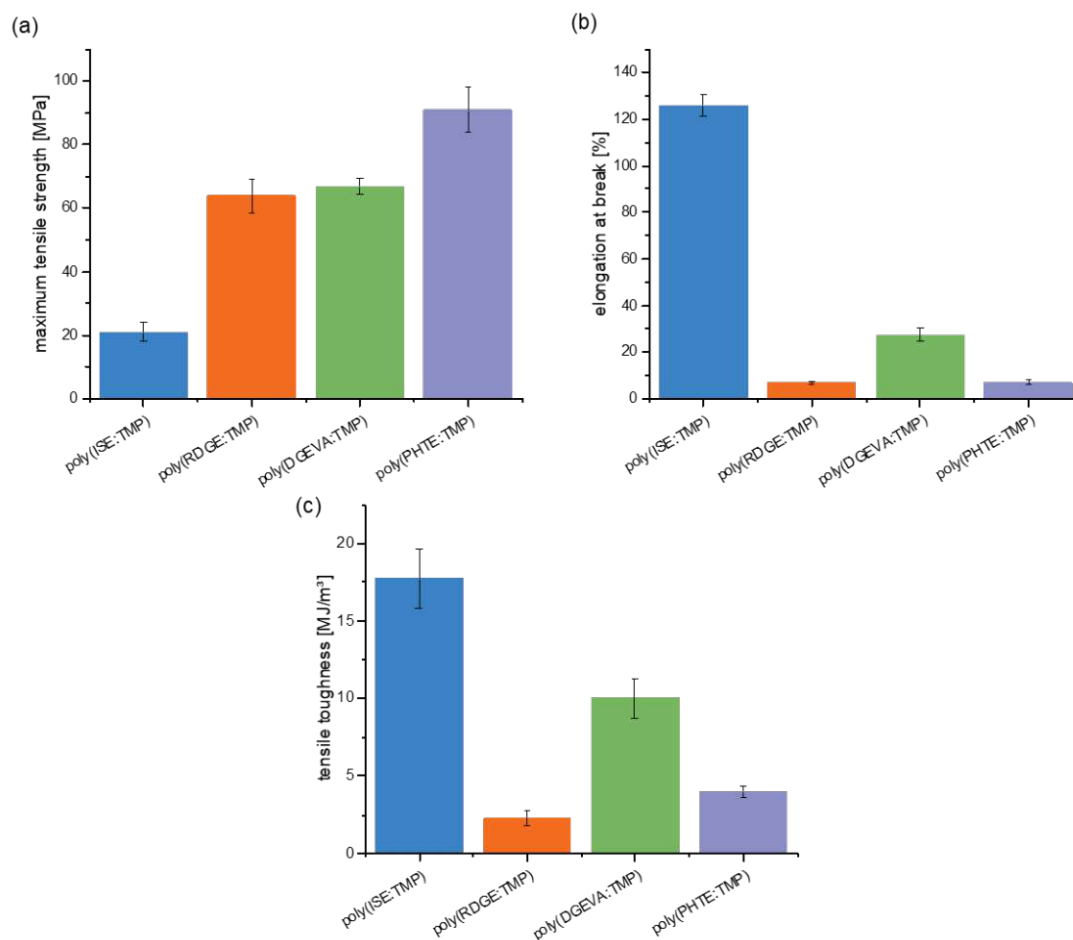


Figure 98: Comparison of  $\sigma_M$  [MPa] and  $\epsilon_B$  [%] and  $U_T$  [MJ/m<sup>3</sup>] for polyaddition polymers

Table 24: Average  $\sigma_M$  [MPa],  $\epsilon_B$  [%] and  $U_T$  [MJ/m<sup>3</sup>] values for polyaddition polymers.

	$\sigma_M$ [MPa]	$\epsilon_B$ [%]	$U_T$ [MJ/m <sup>3</sup> ]
<b>poly(ISE:TMP)</b>	21.0 ± 3.0	126 ± 5	17.7 ± 1.9
<b>poly(RDGE:TMP)</b>	63.7 ± 5.2	6.82 ± 0.61	2.30 ± 0.47
<b>poly(DGEVA:TMP)</b>	66.9 ± 2.7	27.3 ± 2.8	10.0 ± 1.27
<b>poly(PHTE:TMP)</b>	91.0 ± 7.2	7.20 ± 0.71	3.96 ± 0.41

Moreover, by integration of the tensile stress-strain plots, tensile toughness can be calculated and is depicted in Figure 98. Thermal polyaddition of **ISE:TMP** results in polymers with the highest tensile toughness (17.7 MJ/m<sup>3</sup>) as a result of the high elongation at break of these specimens. Polymers derived from **DGEVA:TMP** exhibit a tensile toughness of 10 MJ/m<sup>3</sup> and

followed by specimens containing **PHTE:TMP** ( $U_T \sim 4 \text{ MJ/m}^3$ ). Finally, **poly(RDGE:TMP)** shows the lowest tensile toughness ( $2.3 \text{ MJ/m}^3$ ) of all polymers.

Concluding, thermal polyaddition of ISE, DGEVA, RDGE and PHTE with TMP leads to homogeneous polymer networks. Increased network regulation can not only be observed in sharp glass transitions, but also in enhanced mechanical properties. While **poly(PHTE:TMP)** exhibited high  $T_G$  and high tensile strength due to its high crosslinking density, **poly(RDGE:TMP)** and **poly(DGEVA:TMP)** show strong and tough behavior. Although **poly(ISE:TMP)** displayed elastomeric behavior, it exhibited highest tensile toughness of all polymers.

### 3 Interpenetrating Polymer Networks

As already mentioned in the beginning, the aim of this thesis is to create interpenetrating polymer networks (IPNs) from bio-based resources. In the previous chapters, the soft and hard network were analyzed and optimized separately and now, both networks will be combined to yield IPNs. The strategy in this thesis combines a photo-curable soft network with a thermally polymerizable hard network (Figure 99).

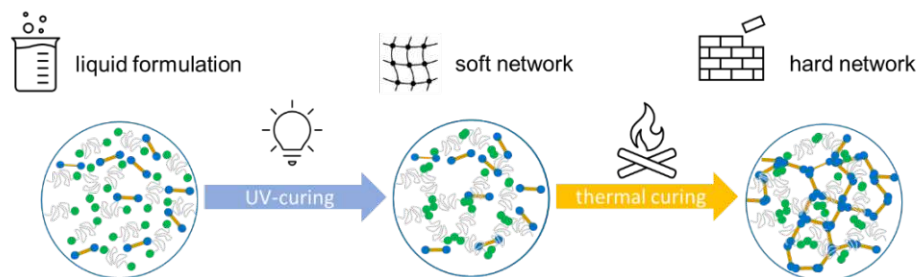


Figure 99: Scheme of IPN synthesis.

Ideally, the soft network represents the “3D-printable” network and was therefore designed to show high photoreactivity. Both photo-DSC and photo-rheology proved, that a high molecular weight methacrylate (**PEG20kMA**) in combination with low molecular weight reactive diluents (**IBMA**) show high reactivity towards photopolymerization.

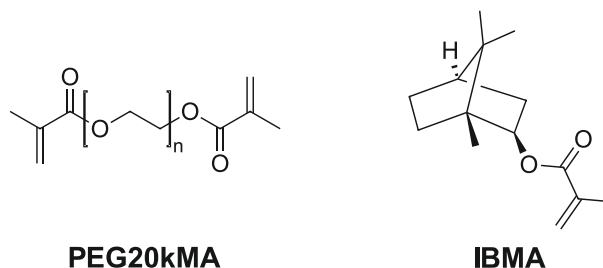


Figure 100: Chemical structure of soft matrix monomers PEG20kMA and IBMA.

Furthermore, epoxides were tested as possible hard matrix monomers, as previous works in this group suggested no co-polymerization between methacrylates and epoxides.<sup>147</sup> At first, cationic photopolymerization of epoxy monomers was analyzed. To further improve the (thermal) reactivity and mechanical properties, polyaddition between epoxy monomers and alcohols was investigated, showing that polyaddition polymers show enhanced reactivity and (thermo)mechanical properties. Therefore, the matrix will be comprised of various bio-derived epoxy monomers (**TMPTG**, **ISE**, **DGEVA**, **RDGE** and **PHTE**) and a trifunctional alcohol, that are cured thermally using imidazole as polyaddition catalyst.

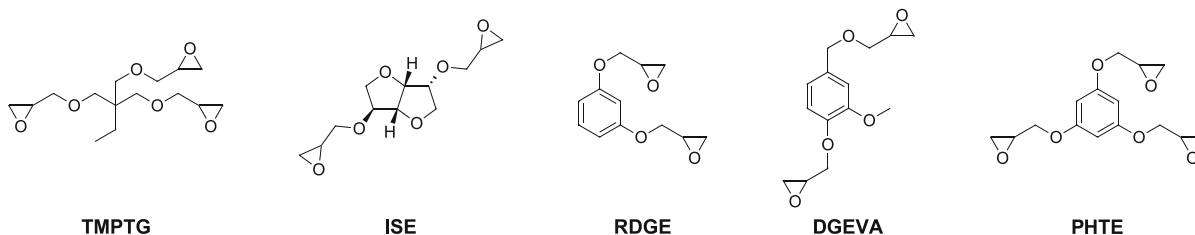


Figure 101: Chemical structures of epoxy monomers TMPTG, ISE, RDGE, DGEVA and PHTE.

Finally, by the combination of both networks, IPNs will be created. Ideally, by combination of the stiff hard-matrix and ductile soft-matrix, thermoplastic-like materials will be obtained. Thus, in this last part, an ideal ratio of soft to hard network will be evaluated and (thermo)mechanical tests of the final IPNs will be presented.

### 3.1. Initiation and co-reactivity study

Previous work in this group showed, that co-polymerization between methacrylates and epoxy monomers with radical and cationic initiators can be excluded.<sup>147</sup> Nevertheless, in this thesis epoxy monomers were cured in a thermal manner, using an imidazole as catalyst, and co-reactivity will be evaluated once again. Thus, two strategies were applied to test possible co-polymerization of the networks. At first, a model methacrylate monomer (benzyl methacrylate, **BMA**) was reacted with the polyaddition catalyst imidazole and its reaction monitored *via* proton NMR. Thereafter, a photo-DSC study was conducted to exclude radical initiated reaction between hard matrix monomers (**RDGE:TMP**). RDGE was chosen as model epoxy monomers due to its commercial availability, since all other epoxy monomers had to be synthesized.

#### 3.1.1. Proton NMR study

In order to exclude initiation of the UV-curable methacrylates by the thermal initiator imidazole, a model substance (benzyl methacrylate, **BMA**) was reacted with 1 wt% of imidazole. Figure 102 depicts the monomer BMA and the catalyst imidazole.

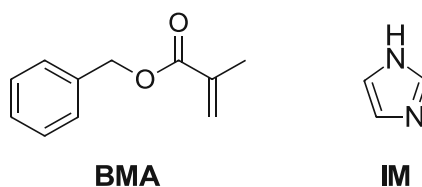


Figure 102: Monomer benzyl methacrylate (BMA) and the catalyst imidazole (IM).

In chapter 1.4, the photopolymerization procedure was described in detail: due to the high viscosity of the soft matrix formulation (80 wt% **PEG20kMA** and 20 wt% **IBMA**), UV curing was conducted at 60 °C. Therefore, the model substance **BMA** was stirred with the thermal catalyst

at 60 °C, to imitate the UV curing process. After predetermined time points, a sample was prepared for proton NMR analysis and the decay of the double bond was analyzed.

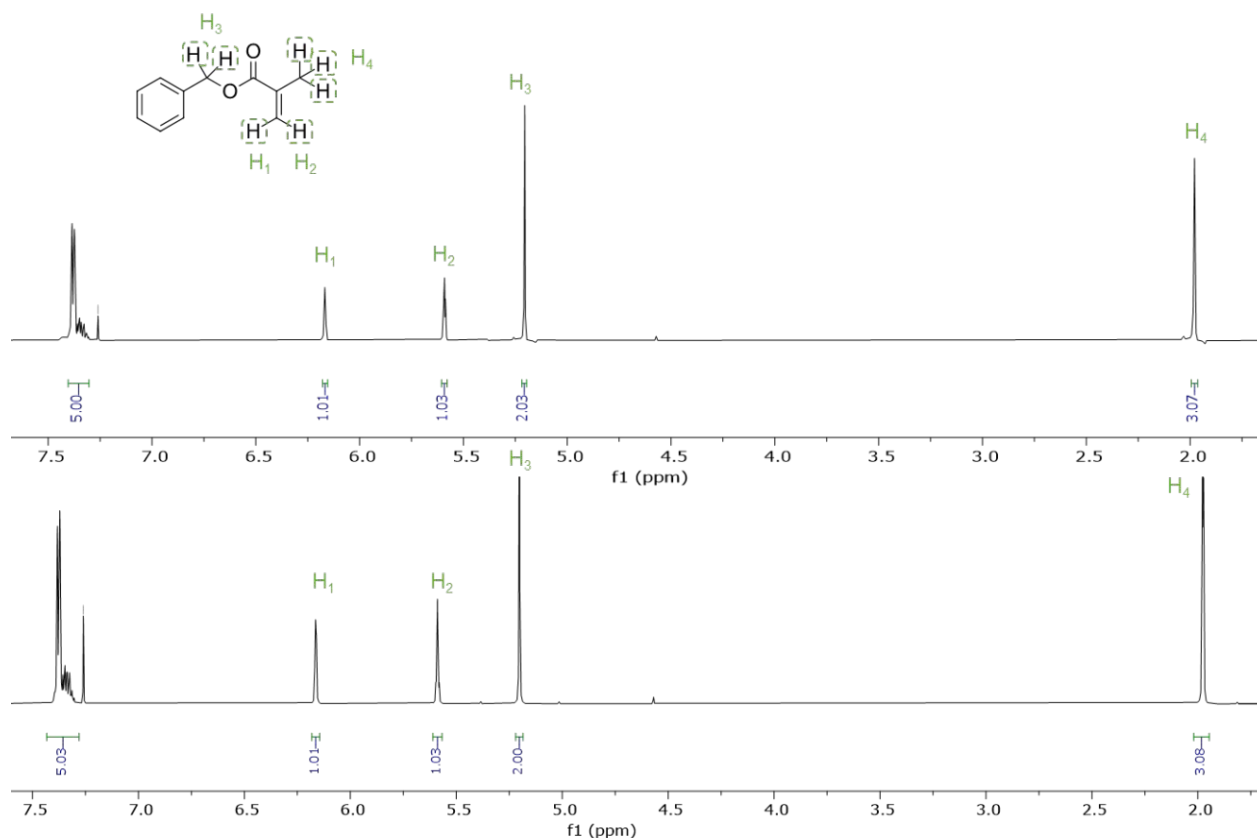


Figure 103: Proton NMR of the resin at the beginning of the experiment (top) and after 20 min (bottom).

In Figure 103, the proton NMR of the neat resin is depicted at the top and the resin after 20 min of stirring is depicted at the bottom, with the protons of the monomer allocated. As expected, the peaks of the methacrylate double bond at 6.2 ppm and 5.6 ppm remain unchanged. Since the resin does not show any tendency towards polymerization during the first 20 min, another proton NMR sample was drawn after 2 hours and is depicted in Figure 104.



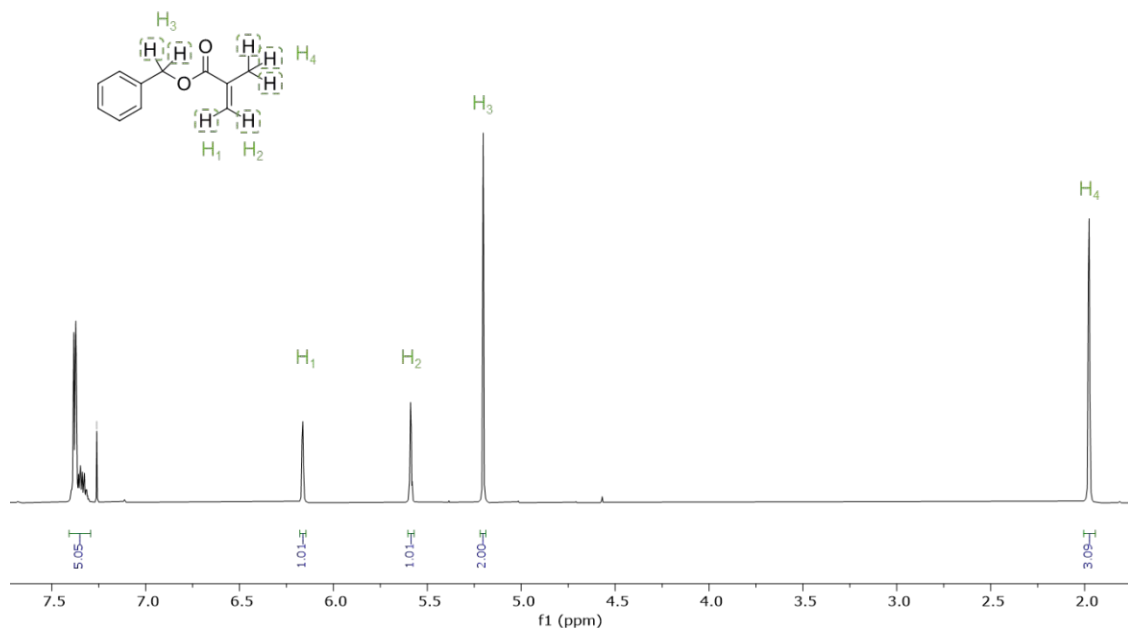


Figure 104: Proton NMR of the resin after 120 min.

Again, the signals for the methacrylate double bond show no shifting or decrease. Therefore, the polyaddition catalyst imidazole does not react with the methacrylate bonds of the model monomer **BMA** and thus, polymerization initiated by imidazoles can be excluded and imidazoles can be used as thermal catalysts for the polymerization of the second network, as they do not interfere with the radical polymerization of the soft network.

### 3.1.2. Photo-DSC study

After determination of the reactivity of methacrylate bonds with an imidazole catalyst, monomers from the hard matrix were analyzed regarding their photopolymerization tendency using the radical PI TPO-L. In chapter 1.3.1, photoreactivity of the reactive diluent IBMA with the photoinitiator TPO-L was tested. Additionally, a formulation of IBMA and 1 wt% of imidazole will be tested in the photo-DSC, to exclude any photochemical events between the substances.

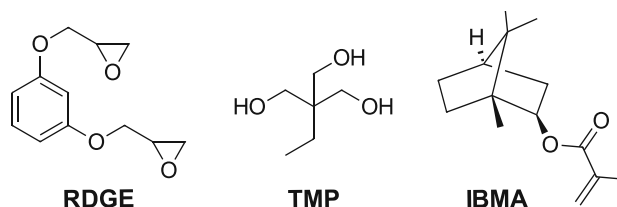


Figure 105: Monomers used for the photo-DSC study. Resorcinol diglycidyl ether (RDGE), trimethylolpropane (TMP) and isobornyl methacrylate (IBMA)

Therefore, two formulations were prepared: the first formulation (**RDGE:TMP\_TPO-L**) contains an equimolar ratio of the hard matrix monomers **RDGE** and **TMP** as well as the radical PI TPO-L. Furthermore, **IBMA** was mixed with 1 wt% of imidazole (**IBMA\_IM**) and analyzed as well. The measurements were performed under the same conditions as in chapter 1.3.1 with

a broadband UV-lamp (320-500 nm) at 60 °C. Per formulation, triplicates were measured and one exemplary photo-DSC plot is depicted in Figure 106. After the measurement, the samples were dissolved in THF to determine the molecular weight *via* GPC and CDCl<sub>3</sub> to calculate the double bond conversion *via* proton NMR. Table 25 summarizes the results of the analysis.

Table 25: Results of the photo-DSC experiment with IBMA and RDGE:TMP.

	t <sub>max</sub> [s]	t <sub>95</sub> [s]	ΔH <sub>p</sub> [J/g]	DBC/ EGC [%]	DBC/EGC NMR [%]	M <sub>n</sub> [kDa]	M <sub>w</sub> [kDa]	PDI [-]
<b>IBMA_IM</b>	-	-	<1	<1	<1	-	-	-
<b>RDGE:TMP_ TPO-L</b>	17.4 ± 0.9	164 ± 124	10.6 ± 8.7	<1	<1	-	-	-

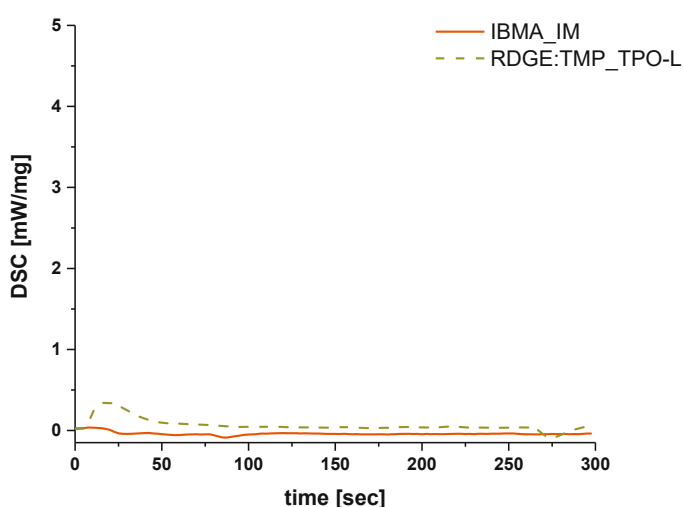


Figure 106: Exemplary photo-DSC plot of IBMA\_IM (—) and RDGE:TMP\_TPO-L (---)

As can be seen in Figure 106, **IBMA\_IM** shows no significant photoreactivity, represented by a flat curve in the photo-DSC plot. Furthermore, characteristic values such as t<sub>max</sub> and t<sub>95</sub> are not obtained since no heat of polymerization is detectable. After the measurement, proton NMR analysis of the irradiated sample shows no decrease in the methacrylate bond signal, proving the previous assumption of no photoreactivity. Additionally, GPC analysis supports these findings, as no peaks besides the flow marker BHT are detected.

Similar results are obtained for **RDGE:TMP\_TPO-L** since the photo-DSC curve is comparably flat (t<sub>max</sub> of ~17 s and t<sub>95</sub> of ~164 s) and no significant heat of polymerization is measurable (~11 J/g). Furthermore, epoxy group conversion from both photo-DSC data (<1%) and proton NMR analysis (<1%) shows, that monomers from the hard matrix do not interact with the radical PI TPO-L. Again, GPC analysis supports previous conclusions, as no peaks besides the flow marker BHT are detected.

Concluding, the photo-DSC study proves, that neither the soft matrix nor hard matrix react with the initiating/catalytic system of the opposite system. Therefore, IPNs can be formed from the

combination of radically initiated photopolymerization of methacrylate monomers and thermally polymerized epoxy-alcohol systems.

### 3.2. Form-stability of IPNs

Interpenetrating polymer networks can be cured in a variety of ways and for this thesis a sequential curing procedure is investigated, yielding sequential IPNs. As already mentioned, the first step comprises the photopolymerization of the soft network. For additive manufacturing technologies (AMTs), such as 3D printing, it is necessary to obtain form stable specimens before subjecting the 3D printed objects to post-curing procedures. Hence, form stability of photopolymerized specimens after the UV curing process were investigated, to gather information about the influence of soft matrix as well as different amounts of the reactive diluent **IBMA** in the IPN formulations.

Thus, form-stability experiments were conducted using the commercially available **RDGE** as epoxy component, **TMP** as polyaddition alcohol component and **PEG20kMA** and **IBMA** as soft matrix monomers. Additionally, imidazole was used as polyaddition catalyst and TPO-L as photoinitiator. The monomers are depicted in Figure 107.

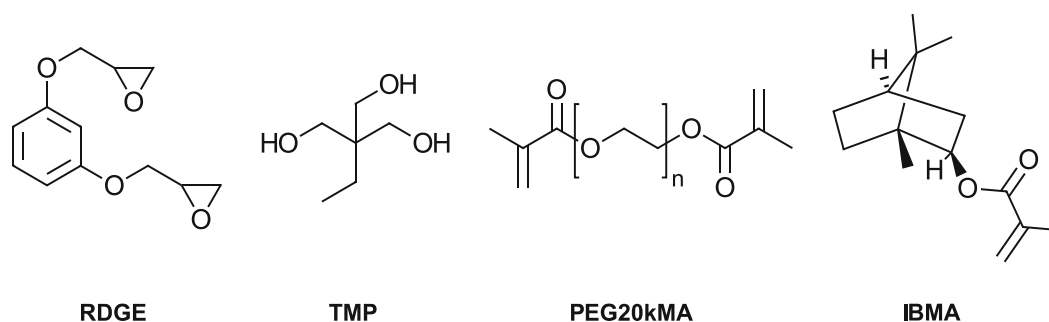

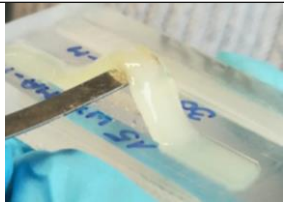






Figure 107: Monomers for the form-stability study.

To investigate a broad range of soft to hard matrix concentration, 15, 30 and 45 wt% of the soft matrix formulation were added to the hard matrix formulation. Furthermore, the reactive diluent IBMA was added in 0, 20 and 50 wt% to PEG20kMA and to analyze its influence on the form-stability of the photopolymerized specimens, as it increases both reactivity and stiffness of the soft matrix (see chapter 1.2).

Therefore, to a 1:1 mixture (in respect to reactive groups) of **RDGE:TMP** were added 15-45 wt% of the soft matrix and 1 wt% of the thermal catalyst imidazole (in respect to the epoxy matrix) as well as 1 wt% TPO-L (in respect to the soft matrix). The soft matrix consisted furthermore of 0, 20 and 50 wt% of **IBMA** in the pristine **PEG20kMA**. After heating the formulation to 60 °C, the components were homogenized and poured in a silicon mold. Then, the soft matrix was cured as described in chapter 1.4, taken out of the silicon mold and its properties inspected. Table 26 summarizes the results of the form-stability study.

Table 26: Investigation of the impact of IBMA as reactive diluent and of uncured hard matrix monomers on the form-stability of photopolymerized parts.

	0 wt% IBMA	20 wt% IBMA	50 wt% IBMA
15 wt% soft matrix	x		
30 wt% soft matrix	x		
45 wt% soft matrix	soft gel		

As can be seen in Table 26, the use of the reactive diluent is necessary, since no form-stable green bodies were obtained after UV curing of the neat **PEG20kMA**. Photopolymerization results in highly viscous gels, that cannot be taken out of the mold. It seems, that the neat **poly(PEG20kMA)** network exhibits too low crosslinking density to form stable IPN green bodies, which contain the uncured hard matrix monomers.

On the contrary, by using the reactive diluent **IBMA**, the soft matrix becomes more form stable and can be taken out of the silicon mold without rupturing. However, specimens with 15 wt% of the soft matrix (regardless of the reactive diluent content) still appear very soft and not form-stable enough for future AMT applications. Increasing the soft matrix content to 30 wt%, form-stability after photopolymerization is significantly improved. Same accounts for specimens containing 45 wt% of the soft matrix. Hence, a minimum soft network content of 30 wt% seems necessary to give form-stable specimens.

Having in mind that increased content of **IBMA** leads to stiffer polymer networks, it was decided to investigate IPNs that contain 20 wt% **IBMA** and 80 wt% **PEG20kMA** as a soft matrix. Although giving poorly form-stable polymers, IPNs with 15 wt% of soft network will be investigated in addition to the previously mentioned IPNs with 30 and 45 wt% of soft network to investigate the (thermo)mechanical properties of the IPNs in more detail.

### 3.3. Investigation of (thermo)mechanical properties of IPNs

After the evaluation of reactivity and form-stability of the networks, the final (thermo)mechanical properties of IPNs were investigated. First, DMTA measurements will provide information about the thermomechanical properties of IPNs. Moreover, tensile tests were performed to analyze the mechanical properties of the material.

#### 3.3.1. DMTA-Analysis

Dynamic mechanical thermoanalysis (DMTA) was performed to gain information about the thermomechanical properties of cured IPNs. The specimens contained different concentrations of soft and hard network, whereby each network was polymerized using 1 wt% of the respective initiator. For the soft network, 1 wt% of the radical PI TPO-L was used and polyaddition of the hard network was initiated by 1 wt% of imidazole. In order to investigate the influence on different soft network concentrations in the IPNs, 15, 30 and 45 wt% of **20IBMA80PEG** were added to **ISE:TMP**, **RDGE:TMP**, **DGEVA:TMP** and **PHTE:TMP**. Since **poly(TMPTG:TMP)** exhibited  $T_G$  of  $<10$  °C, it contradicted the properties of a hard matrix and was not further investigated. In addition to the formulations that were tested regarding their form-stability, one last IPN formulation was prepared and consisted of 10 wt% soft and 90 wt% hard matrix.

IPNs were prepared similar to 1.2.4, adding the thermal curing step at 90 °C for 16-18h. Thereafter, DMTA measurements were performed according to chapter 1.4.1. and will be presented for each hard matrix monomer combination consecutively. To facilitate the nomenclature of IPNs, an example is given: when RDGE:TMP is used as hard matrix and 15 wt% of soft network are added, the IPN will be called poly(IPN15RDGE).

At first, IPNs containing ISE:TMP were tested and the results are depicted in Figure 108 and Table 27.

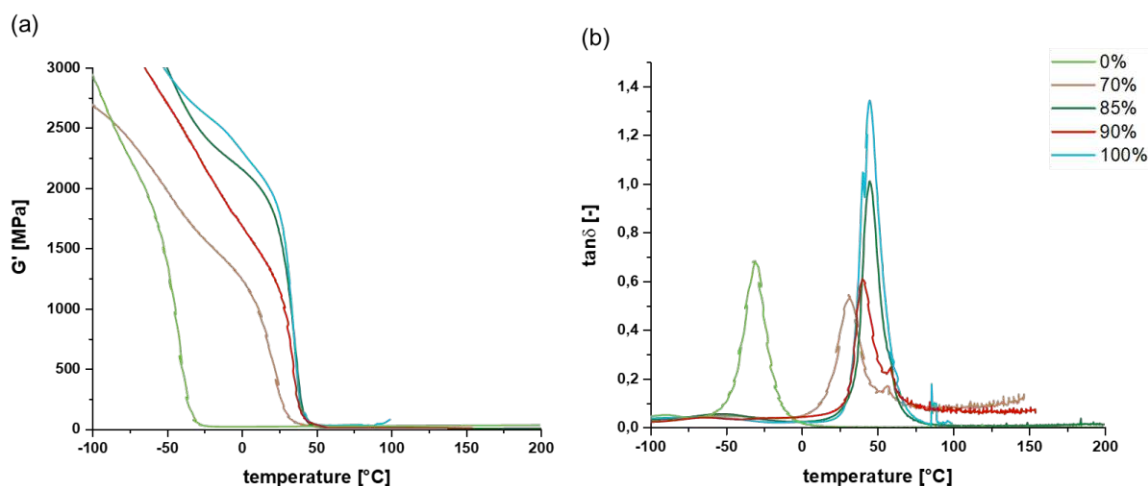


Figure 108: (a) Storage modulus  $G'$  and loss modulus ( $\tan\delta$ ) over temperature for IPNs containing ISE:TMP as hard network and 20IBMA80PEG as soft network. The content of the hard network was varied from 0-100%.

Table 27:  $G'_{25^\circ\text{C}}$ ,  $G'_R$  and  $T_G$  of IPNs containing ISE:TMP and 20IBMA80PEG in various compositions.

\*poly(IPN45ISE) could not be analyzed as it ruptured several times during analysis.

	hard network [%]	$T_G$ [°C]	$G'_{25}$ [MPa]	$G'_R$ [MPa]
<b>poly(20IBMA80PEG)</b>	0	-35	15.8	16.3
<b>poly(IPN45ISE)</b>	55	-*	-*	-*
<b>poly(IPN30ISE)</b>	70	35	368	1.87
<b>poly(IPN15ISE)</b>	85	42	1160	5.55
<b>poly(IPN10ISE)</b>	90	46	1660	1.22
<b>poly(ISE:TMP)</b>	100	48	1800	23.4

As expected, the glass transition temperatures of the IPNs are situated in between the  $T_G$  of hard ( $T_G$  of **poly(ISE:TMP)** is 48 °C) and soft network ( $T_G$  of **poly(20IBMA80PEG)** is -35 °C). When adding 10 wt% of the soft matrix to neat hard matrix (**poly(IPN10ISE)**), the glass transition temperature is slightly decreased to 46 °C. Unsurprisingly, with higher soft network content, the  $T_G$  is further decreased to 42 °C (**poly(IPN15ISE)**) and 35 °C (**poly(IPN30ISE)**). Regarding **poly(IPN45ISE)**, no DMTA analysis could be performed since the specimen was very brittle and ruptured several times during the measurement. When comparing the storage modulus at 25 °C ( $G'_{25}$ ), the same trend is observed: highly crosslinked **poly(ISE:TMP)** has the highest  $G'_{25}$  value (1803 MPa), while an increase in soft matrix also leads to a decrease in crosslinking density. This phenomenon is observable as  $G'_{25}$  of **poly(IPN10ISE)** (1658 MPa) is higher than  $G'_{25}$  of **poly(IPN15ISE)** (1157 MPa). Additionally, at 25 °C the specimen **poly(IPN30ISE)** is already in its glass transition state, further decreasing  $G'_{25}$  to 368 MPa.

Furthermore, by looking at the  $\tan\delta$  maximum, sharp loss factor maxima are exhibited by all IPNs, indicating network regulation and homogenization *via* IPNs.

Next, focus will be shifted towards IPNs derived from the epoxy monomer RDGE. Obtained data from DMTA analysis is depicted in Table 28 and Figure 109.

Table 28:  $G'_{25^\circ\text{C}}$ ,  $G'_R$  and  $T_G$  of IPNs containing RDGE:TMP and 20IBMA80PEG in various compositions.

	hard network [%]	$T_G$ [°C]	$G'_{25}$ [MPa]	$G'_R$ [MPa]
poly(20IBMA80PEG)	0	-35	15.8	16.3
poly(IPN45RDGE)	55	47	940	1.87
poly(IPN30RDGE)	70	51	1040	2.27
poly(IPN15RDGE)	85	49	997	6.08
poly(IPN10RDGE)	90	50	925	7.22
poly(RDGE:TMP)	100	52	1560	4.58

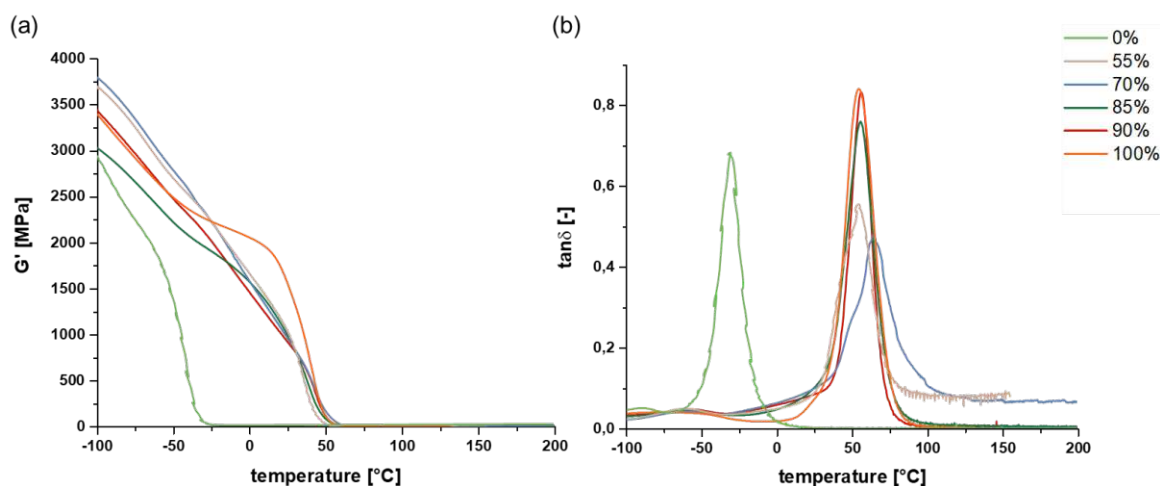


Figure 109: (a) Storage modulus  $G'$  and loss modulus ( $\tan\delta$ ) over temperature for IPNs containing RDGE:TMP as hard network and 20IBMA80PEG as soft network. The content of the hard network was varied from 0-100%.

According to the results, the hard matrix **poly(RDGE:TMP)** exhibits the highest glass transition temperature (52 °C) and storage modulus at 25 °C ( $G'_{25}$  is 1560 MPa), as a result of the highest crosslinking density of all specimens. With increasing amount of soft matrix, IPNs show decreasing  $T_G$ s: **poly(IPN10RDGE)** and **poly(IPN15RDGE)** show  $T_G$ s at 50 °C and 49 °C, respectively. Unexpectedly, **poly(IPN30RDGE)** shows a slightly higher glass transition temperature (51 °C) and higher  $G'_{25}$  (1041 MPa), even though containing significantly higher amount of the soft network. On the other hand, **poly(IPN45RDGE)** presents a lowered  $T_G$  of 47 °C and  $G'_{25}$  (940 MPa) as a consequence of the higher amount of macromolecular components.



When comparing the maximum of the loss factor  $\tan\delta$ , a difference between IPNs containing 10 or 15 wt% and 30 or 45 wt% of the soft network can be distinguished. IPNs with lower amount of the soft matrix exhibit narrowed maxima, whereas the specimens with higher soft network content show broadening of the  $\tan\delta$  maximum. Concluding, IPNs with lowered amount of the hard network seem to form less regulated and homogeneous polymer networks compared to the neat **poly(RDGE:TMP)**. An explanation for this phenomenon can be found when looking at the evolution of morphology during IPN synthesis. In the first stages of polymerization, two independent networks are formed, leading to phase-separation. Depending on the size of the generated domains, different properties of the final IPN are obtained. While large domains lead to the formation of broadened or multiple  $T_G$ s, smaller domains show inward shifted  $T_G$ s as a results of homogeneously blended networks at the molecular scale.<sup>166</sup> Thus, it can be assumed that lower amounts of the soft network lead to the formation of more homogeneous IPNs.

Following, IPNs containing DGEVA:TMP as hard matrix and 20IBMA80PEG as soft matrix will be evaluated. Therefore, Figure 110 presents storage modulus and loss factor over time of those polymers, whereas Table 29 summarizes the results of the analysis.

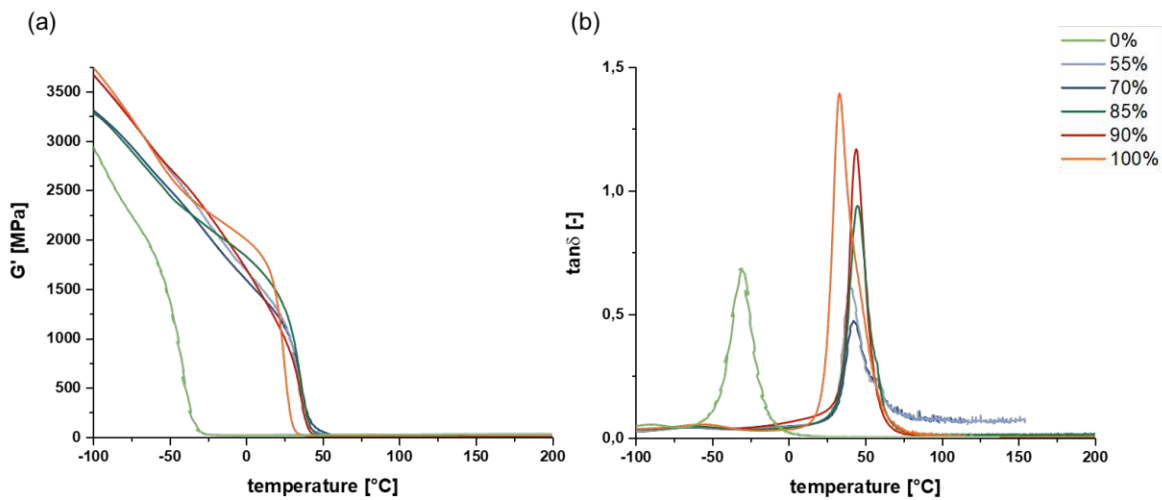


Figure 110: (a) Storage modulus  $G'$  and loss modulus ( $\tan\delta$ ) over temperature for IPNs containing DGEVA:TMP as hard network and 20IBMA80PEG as soft network. The content of the hard network was varied from 0-100%.



Table 29:  $G'_{25^{\circ}\text{C}}$ ,  $G'_R$  and  $T_G$  of IPNs containing DGEVA:TMP and 20IBMA80PEG in various compositions.

	hard network [%]	$T_G$ [°C]	$G'_{25}$ [MPa]	$G'_R$ [MPa]
poly(20IBMA80PEG)	0	-35	15.8	16.3
poly(IPN45DGEVA)	55	36	1120	1.22
poly(IPN30DGEVA)	70	39	1160	2.09
poly(IPN15DGEVA)	85	40	1310	5.07
poly(IPN10DGEVA)	90	41	1010	6.33
poly(DGEVA:TMP)	100	35	755	1.85

For IPNs containing DGEVA:TMP as hard matrix, unexpected thermomechanical properties are obtained. While **poly(DGEVA:TMP)** exhibits glass transition temperature of 35 °C and  $G'_{25}$  of 756 MPa, all IPNs show unexpectedly higher  $T_G$  and  $G'_{25}$ . Nevertheless, a trend is observed among the IPNs: highest  $T_G$  is exhibited by **poly(IPN10DGEVA)** (41 °C), followed by **poly(IPN15DGEVA)** (40 °C), **poly(IPN30DGEVA)** (39 °C) and **poly(IPN45DGEVA)** (37 °C) and all IPNs show  $G'_{25}$  above 1000 MPa. As previously mentioned,  $T_G$  of homogeneously blended IPNs should be in between  $T_G$ s of each network. Hence, it can be assumed that the combination of DGEVA:TMP and 20IBMA80PEG leads to the formation of phase separated and discontinuous IPNs. Additionally, hydrogen bonds between the poly(ethylene glycol) backbone and the polyethers formed from DGEVA and TMP could contribute to enhanced thermomechanical properties.

Finally, IPNs derived from the trifunctional PHTE are analyzed. Therefore, storage modulus  $G'$  and loss factor  $\tan\delta$  over temperature are depicted in Figure 111 and the results of the analysis are depicted in Table 30.

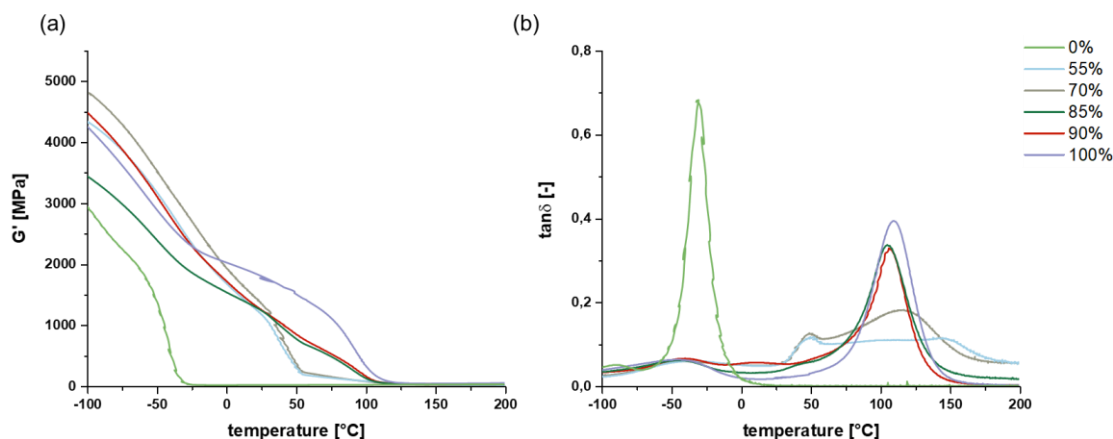


Figure 111: (a) Storage modulus  $G'$  and loss modulus ( $\tan\delta$ ) over temperature for IPNs containing PHTE:TMP as hard network and 20IBMA80PEG as soft network. The content of the hard network was varied from 0-100%.

Table 30:  $G'_{25^\circ\text{C}}$ ,  $G'_R$  and  $T_G$  of IPNs containing PHTE:TMP and 20IBMA80PEG in various compositions.

	hard network [%]	$T_G$ [°C]	$G'_{25}$ [MPa]	$G'_R$ [MPa]
<b>poly(20IBMA80PEG)</b>	0	-35	15.8	16.3
<b>poly(IPN45PHTE)</b>	55	52 & 105	1180	14.2
<b>poly(IPN30PHTE)</b>	70	52 & 105	1360	15.1
<b>poly(IPN15PHTE)</b>	85	102	1240	2.57
<b>poly(IPN10PHTE)</b>	90	103	1250	3.48
<b>poly(PHTE:TMP)</b>	100	104	1810	39.9

According to the results, IPNs derived from PHTE:TMP can be divided into two groups. At first, IPNs containing 10 wt% (**poly(IPN10PHTE)**) and 15 wt% (**poly(IPN10PHTE)**) of the soft network show one distinct loss factor maximum in Figure 111 at around 102-103 °C and  $G'_{25}$  of ~1240 MPa, while  $T_G$  of pure **poly(PHTE:TMP)** is slightly higher with 104 °C ( $G'_{25}$ : 1805 MPa). By contrast, increasing the amount of soft matrix in the IPNs, leads to different thermomechanical behavior. Both **poly(IPN30PHTE)** and **poly(IPN45PHTE)** show one maximum in the loss factor curve at ~50 °C and a second maximum is present at ~100-110 °C for **poly(IPN30PHTE)**. The specimen containing 45 wt% of the soft network exhibits one broad  $\tan\delta$  peak, extending from ~75-120 °C. Furthermore, both IPNs show a weak  $\tan\delta$  maximum at -35 °C, which corresponds with the maximum of  $\tan\delta$  of the soft matrix. According to Rocco *et al.*, this behavior can be explained through the morphology of IPNs: when miscible monomers lead to the formation homogeneous polymers, one distinct loss factor maximum is observed. Two or more  $\tan\delta$  peaks indicate poor or absent miscibility and compatibility of the networks, presented by heterogeneous materials.<sup>85</sup> Hence, IPNs with 30 wt% and 45 wt% of soft matrix show poor compatibility in the polymeric state, even though the monomers are

miscible. Thereby, strong phase separation might prevent the IPNs from forming highly interpenetrated networks, explaining the poor thermomechanical properties. Another indicator for a strong phase separation between the polymer networks is the opacity of the polymer specimens. Figure 112 displays a DMTA specimen of **poly(IPN30PHTE)** and the polymer presents itself as with turbid-opaque appearance.



Figure 112: DMTA specimen of poly(IPN30PHTE).

By contrast, **poly(IPN10PHTE)** shows one sharp  $\tan\delta$  maximum, resulting from more homogeneous polymer networks. Here, the polymer specimen was colorless and showed no opacity.

### 3.3.2. Tensile tests

After determination of the thermomechanical properties of IPNs containing **ISE:TMP**, **RDGE:TMP**, **DGEVA:TMP** and **PHTE:TMP** as hard matrix and **20IBMA80PEG** as soft matrix, tensile tests were performed to investigate the influence of hard : soft matrix ratio on the mechanical properties, such as tensile toughness. To ensure reproducibility, tensile test specimens were fabricated from the same formulations as DMTA specimens and tensile tests were performed according to ISO 527 as stated in 1.4.2.

Similar to DMTA analysis, IPNs containing **ISE:TMP** will be discussed first and one representative stress-strain plot is depicted in Figure 113, while Table 31 summarizes the results (maximum tensile strength  $\sigma_M$ , elongation at break  $\epsilon_B$  and tensile toughness  $U_T$ ) of the analysis.

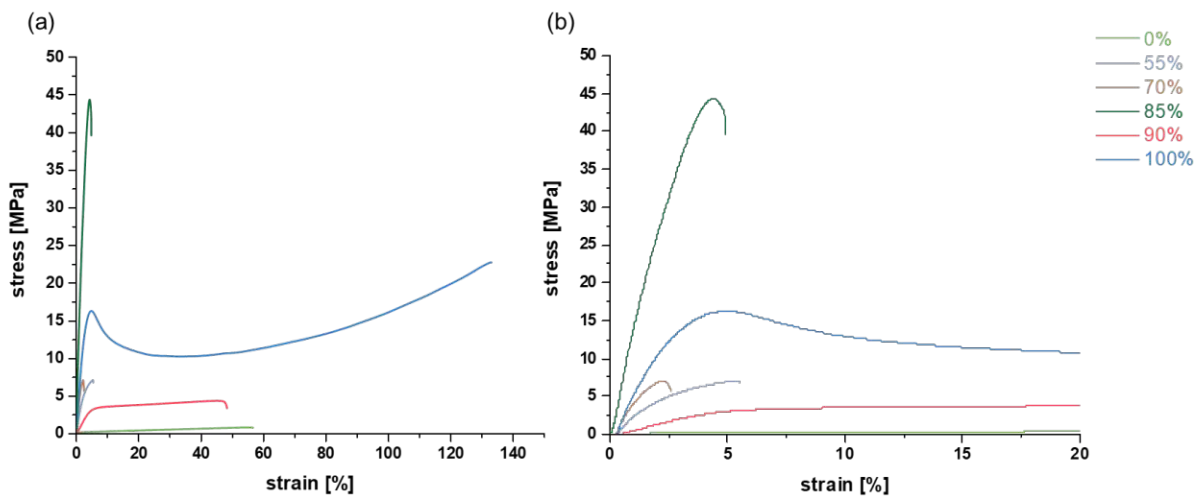


Figure 113: (a) Representative stress-strain curves of IPNs containing ISE:TMP as hard matrix and 20IBMA80PEG as soft matrix in various compositions (0-100% hard network). As reference, the hard matrix poly(ISE:TMP) and the soft matrix poly(20IBMA80PEG) are depicted. (b) Magnification with special emphasis on IPNs containing 55 and 70 wt% of the hard matrix.

Table 31: Maximum tensile strength  $\sigma_M$ , strain at break  $\epsilon_B$  and tensile toughness  $U_T$  of IPNs containing ISE:TMP and 20IBMA80PEG

	hard network [%]	$\sigma_M$ [MPa]	$\epsilon_B$ [%]	$U_T$ [MJ/m <sup>3</sup> ]
poly(20IBMA80PEG)	0	0.77 ± 0.18	54.2 ± 2.6	0.29 ± 0.13
poly(IPN45ISE)	55	5.69 ± 0.97	4.83 ± 0.61	0.18 ± 0.06
poly(IPN30ISE)	70	7.44 ± 1.52	2.83 ± 0.81	0.15 ± 0.05
poly(IPN15ISE)	85	43.2 ± 2.3	4.6 ± 0.6	1.27 ± 0.26
poly(IPN10ISE)	90	5.11 ± 0.54	41.8 ± 2.5	1.63 ± 0.37
poly(ISE:TMP)	100	21.0 ± 3.0	126 ± 5	17.7 ± 1.8

According to the results, IPNs derived from ISE:TMP show dissimilar mechanical behavior. While **poly(IPN10ISE)** exhibits elastomeric behavior ( $\sigma_M$  of 5 MPa,  $\epsilon_B$  of 42%), **poly(IPN15ISE)** shows entirely inverse behavior with high maximum tensile strength of 43 MPa and low elongation at break of 5%. However, both polymers exhibit a similar tensile toughness of 1.3-1.6 MJ/m<sup>3</sup>, indicating that high  $\epsilon_B$  of the specimens containing 10 wt% soft network and high  $\sigma_M$  of the specimens containing 15 wt% soft network counterbalance each other. By contrast, specimens containing even higher amounts of **poly(20IBMA80PEG)**, show unfavorable mechanical properties, displayed by high brittleness ( $\sigma_M < 8$  MPa and  $\epsilon_B < 5\%$ ). This behavior can be explained by strong phase-separation resulting in heterogeneous polymer specimens. As a result, mechanical deformation cannot be dissipated between the macromolecular domains, leading to premature failure of the material.

Unexpectedly, best mechanical performance is observed by the pure hard matrix **poly(ISE:TMP)** with intermediate  $\sigma_M$  (21 MPa) and highest  $\epsilon_B$  (126%), which is even higher than the pure soft matrix ( $\epsilon_B$  is 54%). Thereby, the hard matrix exhibits the highest tensile toughness and the concept of material toughening *via* IPNs cannot be achieved using this particular polymer combination.

Thereafter, IPNs containing the phenol-based difunctional epoxy monomer **RDGE** are analyzed. Once again, one representative stress-strain plot is depicted in Figure 114 and the results of the analysis are depicted in Table 32.

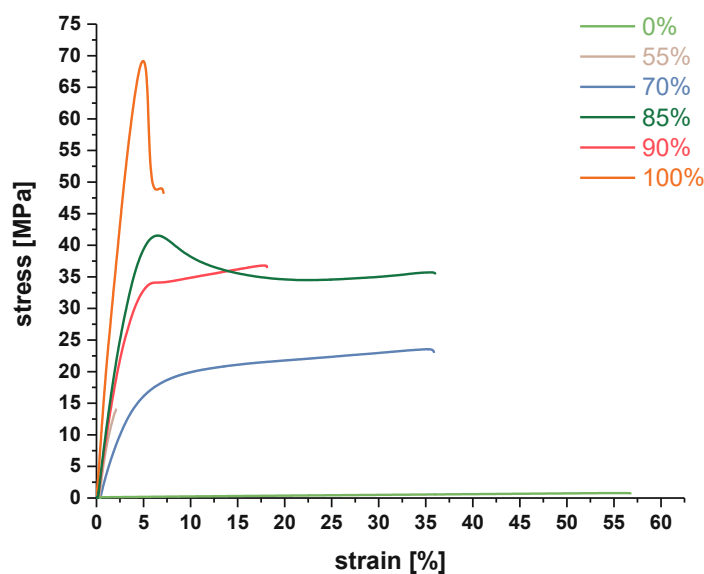


Figure 114: Representative stress-strain curves of IPNs containing RDGE:TMP as hard matrix and 20IBMA80PEG as soft matrix in various compositions (0-100 wt% hard matrix content). As reference, the hard matrix poly(RDGE:TMP) and the soft matrix poly(20IBMA80PEG) are depicted.

Table 32: Maximum tensile strength  $\sigma_M$ , strain at break  $\epsilon_B$  and tensile toughness  $U_T$  of IPNs containing RDGE:TMP and 20IBMA80PEG.

	hard network [%]	$\sigma_M$ [MPa]	$\epsilon_B$ [%]	$U_T$ [MJ/m <sup>3</sup> ]
poly(20IBMA80PEG)	0	0.77 ± 0.18	54.2 ± 2.6	0.29 ± 0.13
poly(IPN45RDGE)	55	11.3 ± 1.8	4.31 ± 1.30	0.17 ± 0.03
poly(IPN30RDGE)	70	23.0 ± 2.6	41.7 ± 4.2	8.12 ± 0.94
poly(IPN15RDGE)	85	43.7 ± 2.1	37.4 ± 5.3	12.6 ± 2.5
poly(IPN10RDGE)	90	37.4 ± 1.8	18.1 ± 3.7	5.44 ± 1.4
poly(RDGE:TMP)	100	63.7 ± 5.2	6.28 ± 0.57	1.32 ± 0.81

Looking at the results, IPNs containing **RDGE:TMP** perform better compared to those containing **ISE:TMP**. While the hard matrix **poly(RDGE:TMP)** exhibits highest  $\sigma_M$  (64 MPa) and low  $\epsilon_B$  (~6%), resulting in a comparably low tensile toughness of 1.3 MJ/m<sup>3</sup>. Adding 10 wt% of the soft matrix to RDGE:TMP (**poly(IPN10RDGE)**) leads to an increased tensile toughness (5.4 MJ/m<sup>3</sup>) as a result of increased elongation at break (18%). Even higher tensile toughness is achieved by **poly(IPN15RDGE)** (13 MJ/m<sup>3</sup>), resulting from high  $\sigma_M$  (44 MPa) and  $\epsilon_B$  (37%). Similar results are displayed by **poly(IPN30RDGE)** with  $\sigma_M$  of 23 MPa and enhanced  $\epsilon_B$  of 42%. Thereby, tensile toughness is modestly decreased to 8 MJ/m<sup>3</sup> and it seems, that maximum tensile toughness is reached somewhere in between 10 and 30 wt% soft network content. Unpredictably, higher soft network content leads to poorer mechanical properties, since low  $\sigma_M$  of 11 MPa and  $\epsilon_B$  of 4% expose brittle fracture behavior. As aforementioned for ISE:TMP and highlighted in the DMTA analysis, strong phase separation and formation of discontinuous polymer networks manifest in poor mechanical properties. However, an increase in tensile toughness is presented by IPNs containing up to 30 wt% of the soft matrix and therefore, material toughening is achieved.

When the sterically more hindered epoxy monomer DGEVA is used in the hard matrix, modified mechanical properties are expected. Thus, tensile test results are depicted in Figure 115 and Table 33.

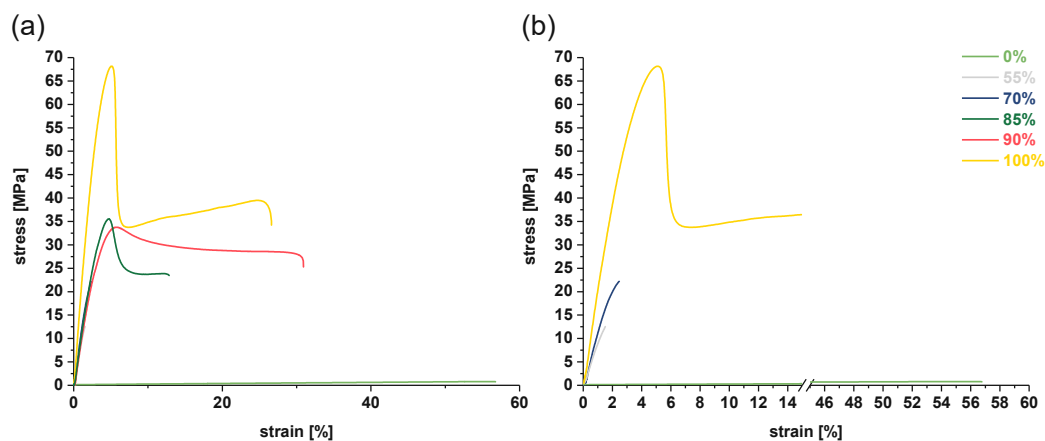


Figure 115: Left: Representative stress-strain curves of IPNs containing DGEVA:TMP as hard matrix and 20IBMA80PEG as soft matrix in various compositions (0-100 wt% hard matrix). As reference, the hard matrix poly(RDGE:TMP) and the soft matrix poly(20IBMA80PEG) are depicted. Right: Magnification with special emphasis on IPNs containing 55 and 70 wt% of the hard matrix.

Table 33: Maximum tensile strength  $\sigma_M$ , strain at break  $\epsilon_B$  and tensile toughness  $U_T$  of IPNs containing DGEVA:TMP and 20IBMA80PEG.

	hard network [%]	$\sigma_M$ [MPa]	$\epsilon_B$ [%]	$U_T$ [MJ/m <sup>3</sup> ]
poly(20IBMA80PEG)	0	0.77 ± 0.18	54.2 ± 2.6	0.29 ± 0.13
poly(IPN45DGEVA)	55	12.6 ± 4.0	1.50 ± 0.44	0.10 ± 0.06
poly(IPN30DGEVA)	70	18.4 ± 2.7	1.94 ± 0.40	0.21 ± 0.07
poly(IPN15DGEVA)	85	40.2 ± 1.4	8.86 ± 2.2	3.05 ± 0.71
poly(IPN10DGEVA)	90	33.9 ± 1.8	25.8 ± 4.6	10.4 ± 2.5
poly(DGEVA:TMP)	100	66.9 ± 2.7	27.3 ± 2.8	10.0 ± 1.2

As depicted in Figure 115, the hard matrix **poly(DGEVA:TMP)** displays tough and strong behavior, without the addition of any macromolecular toughening agents, as a result of the regulated polyaddition polymerization. Hence, highest maximum tensile strength (67 MPa) and high strain at break (27%) result in considerable tensile toughness of 10 MJ/m<sup>3</sup>. Similar results are presented by the **poly(IPN10DGEVA)**, that contains only 10 wt% of **poly(20IBMA80PEG)**.  $\sigma_M$  of 34 MPa and  $\epsilon_B$  of 26% result in the highest achieved tensile toughness (10.4 MJ/m<sup>3</sup>). By increasing the amount of soft network to 15 wt%,  $\sigma_M$  is enhanced (40 MPa), while concurrently  $\epsilon_B$  is reduced (9%), additionally leading to a decrease in toughness of roughly 60% (3 MJ/m<sup>3</sup>). Moreover, an inversion on the mechanical properties is observed for **poly(IPN30DGEVA)** and **poly(IPN45DGEVA)** since both materials show brittle characteristics ( $\sigma_M < 19$  MPa and  $\epsilon_B < 2\%$ ). Once again, the sudden change in properties is assumed to arise from heterogeneous, strongly phase-separated polymers.

Ultimately, IPNs comprising the epoxy monomer PHTE are characterized. It was shown in chapter 2.4.7 that the trifunctional nature of the monomer leads to highly crosslinked and stiff polymers. Therefore, Figure 116 and Table 34 present the influence of adding a soft network to **poly(PHTE:TMP)**.

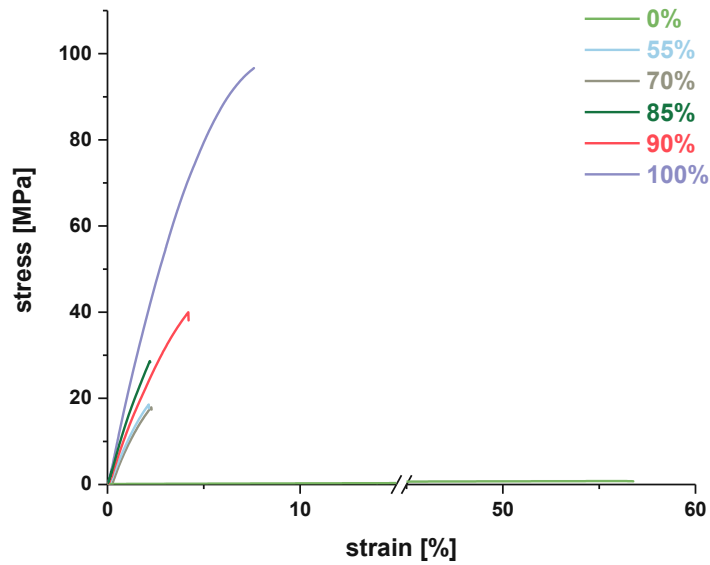


Figure 116: Representative stress-strain curves of IPNs containing PHTE:TMP as hard matrix and 20IBMA80PEG as soft network in various compositions (0-100 wt% hard matrix). As reference, the hard matrix poly(PHTE:TMP) and the soft matrix poly(20IBMA80PEG) are depicted

Table 34: Maximum tensile strength  $\sigma_M$ , strain at break  $\epsilon_B$  and tensile toughness  $U_T$  of IPNs containing PHTE:TMP and 20IBMA80PEG.

	hard network [%]	$\sigma_M$ [MPa]	$\epsilon_B$ [%]	$U_T$ [MJ/m <sup>3</sup> ]
poly(20IBMA80PEG)	0	0.81 ± 0.20	54.2 ± 2.6	0.29 ± 0.13
poly(IPN45PHTE)	55	16.5 ± 5.4	1.98 ± 0.66	0.22 ± 0.10
poly(IPN30PHTE)	70	15.8 ± 3.3	1.69 ± 0.52	0.16 ± 0.04
poly(IPN15PHTE)	85	26.9 ± 5.5	2.01 ± 0.40	0.29 ± 0.04
poly(IPN10PHTE)	90	38.7 ± 6.0	4.27 ± 1.05	0.90 ± 0.18
poly(PHTE:TMP)	100	91.0 ± 7.2	7.17 ± 0.74	3.96 ± 0.40

High crosslinking density of **poly(PHTE:TMP)** results in brittle, but strong behavior with highest maximum tensile strength (91 MPa), whereby elongation at break (~7%) is comparably high for thermosetting materials. Consequently, tensile toughness of 4 MJ/m<sup>3</sup> is calculated. Regarding IPNs from PHTE:TMP, lower tensile strength and unexpectedly lower elongation at break is observed for all specimens, regardless of the soft network content.

**Poly(IPN10PHTE)** and **poly(IPN15PHTE)** still show high  $\sigma_M$  of 39 MPa and 27 MPa, respectively. Unfortunately, addition of the soft network does not increase elongation at break (<5%), resulting in tensile toughness of <1 MJ/m<sup>3</sup>. Considering that both polymers show  $T_G$  of ~103 °C, this behavior is expected.



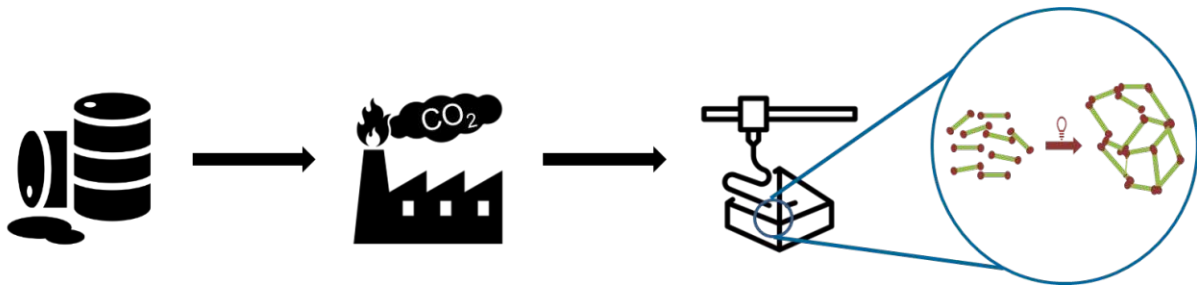
**Poly(IPN30PHTE)** and **poly(IPN45PHTE)** should, at least in theory, profit from the higher soft network content and display increased elongation at break. By contrast,  $\epsilon_B$  is furthermore reduced to <2% and low  $\sigma_M$  (~16 MPa) is determined. Including the data from DMTA analysis (3.3.1), three distinct  $\tan\delta$  maxima were determined, indicating the formation of large macroscopic domains (soft network, “IPN” and hard network). Consequently, mechanical force cannot dissipate between the phases, resulting once more in decreased toughening ability for IPNs with high soft matrix content.

Concluding, IPNs containing the hard matrices **poly(ISE:TMP)** and **poly(PHTE:TMP)** show no increase in tensile toughness regardless of the soft matrix content. However, for IPNs with up to 15 wt% soft network content, DMTA indicated the formation of more homogeneous and regulated polymer networks.

By contrast, when difunctional phenolic epoxy monomers **RDGE** and **DGEVA** are used in the hard matrix, enhanced mechanical properties are observed, displayed by an increase in toughness by the addition of up to 15 wt% **poly(20IBMA80PEG)**. These findings are supported by sharpened  $\tan\delta$  maxima *via* DMTA analysis and thus, network homogenization and regulation were achieved for the difunctional monomers. In the end, IPNs could be derived from bio-based building blocks and, at least for selected compositions, polymer toughening was achieved.

## Summary

Nowadays, photopolymerization finds wide-spread use in a variety of industrial sectors, such as additive manufacturing, coatings, dental or medical applications, as it enables fast, energy- and cost-efficient processes as well as solvent-free usage. Besides all of its advantages, photopolymerization suffers from several problems that still limit its application. Firstly, high crosslinking density and unregulated chain-growth polymerization lead to the formation of brittle thermosets, making photopolymers unsuitable for high-performance applications. Furthermore, the majority of today's photopolymer resins are still derived from fossil resources, preventing a transition towards a circular economy.



*Figure 117: Major problems of photopolymers: production from fossil resources and insufficient mechanical properties.*

Therefore, multiple strategies have been investigated to overcome the abovementioned difficulties. On the one hand, optimization of mechanical properties is achieved by various photopolymer toughening methods (e.g. adding rubber particles, macromolecular components or chain-transfer agents). Herein, interpenetrating polymer networks (IPNs) proved to be an auspicious alternative, combining soft and hard networks to tune the final properties of a material.

On the other hand, the scientific community has made an enormous effort to impart photopolymerizable resins from renewable or bio(degradable) resources. Thereby, the environmental impact of 3D printed scaffolds can be optimized, ideally pathing the way for a circular economy.

Consequently, the scope of this thesis was to combine IPNs as a strategy for photopolymer toughening with bio-based monomers, by the creation of a composite material comprised of a soft network, imparting ductility, and a hard network, providing stiffness and strength.

For this reason, both networks were tested separately by using (photo)-DSC and RT-NIR photorheology to analyze their reactivity before their thermomechanical behavior was investigated by DMTA and tensile tests.

The first step of IPN synthesis comprised the photopolymerization of a soft network, delivering both elasticity and ductility to the material, while the second network (“hard network”) remained unreacted in the photopolymerized scaffold. As a starting point, a photopolymerizable macromolecular compound, derived from poly(ethylene glycol) was synthesized (**PEG20kMA**). Thereafter, the influence of the reactive diluent isobornyl methacrylate (**IBMA**) on the viscosity and mechanical properties was investigated and revealed, that the addition of 20 wt% of the reactive diluent was suitable for the soft network (**20IBMA80PEG**).

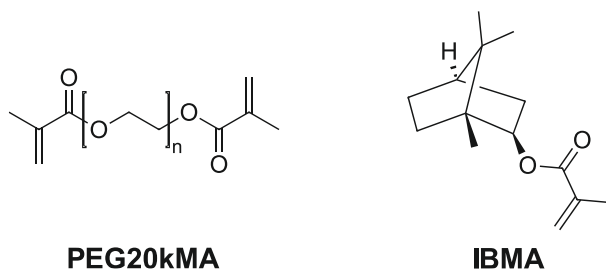


Figure 118: Schematic representation of PEG20kMA and IBMA.

After the determination of the reactive diluent content, reactivity of the photo-resin was investigated by means of photo-DSC and RT-NIR photorheology. Photo-DSC analysis revealed, that **20IBMA80PEG** polymerized at moderate conversion of 77% at 60 °C whereby RT-NIR photorheology indicated even higher double bond conversions (> 90%) and fast gelation ( $t_g$  of 11 s), making the resin applicable for 3D printing. Moreover, DMTA measurements provided a  $T_G$  of -35 °C and tensile tests showed that an elastomeric material was produced.

Thereafter, the main focus of this thesis was shifted towards the optimization of the hard matrix. In literature, epoxides are known for their high  $T_G$  and hardness, making them ideal hard matrix monomers. For IPNs, orthogonal polymerization modes have to be employed in order to exclude co-polymerization of the networks. Thus, cationic photopolymerization and thermal polyaddition of epoxy monomers were studied.

As a starting point for this second chapter, epoxy monomers were synthesized (**ISE**, **DGEVA** and **PHTE**) or purchased (**TMPTG**, **RDGE**), to investigate the influence of the chemical structure on thermomechanical properties.

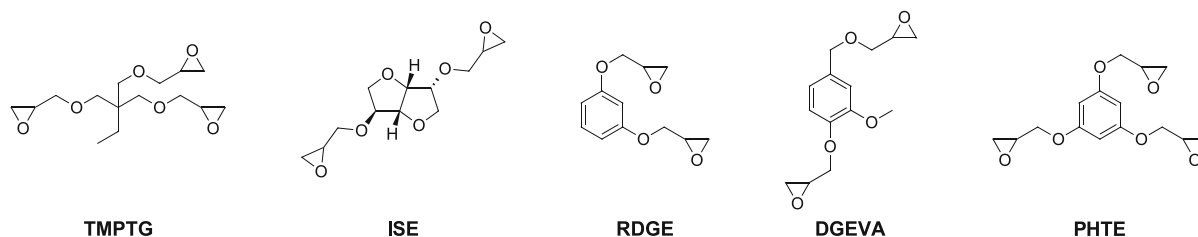


Figure 119: Schematic representation of epoxy monomers.

At first, photoreactivity of the monomers was tested *via* photo-DSC, revealing that cationic photopolymerization at ambient temperatures led to low conversions (< 30%). Therefore, photo-DSC measurements were conducted at elevated temperature (60 °C), which led to a significant increase in epoxy group conversion. Since cationic photopolymerization has a living character, conversion could be furthermore enhanced by adding a thermal post-polymerization treatment.

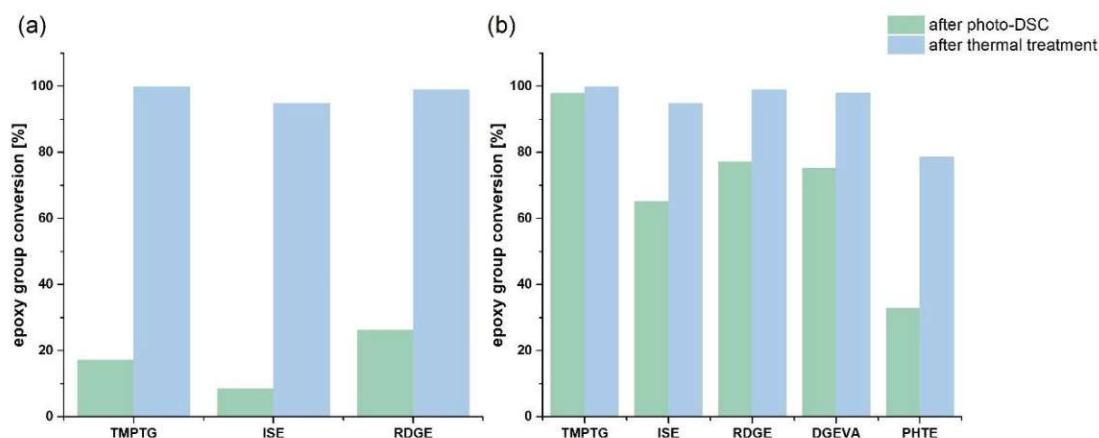


Figure 120: Epoxy group conversions for photo-DSC measurements (green) at (a) 25°C and (b) 60 °C as well as for thermally treated polymers (blue).

Furthermore, DMTA measurements and tensile tests were conducted: aliphatic **TMPTG** ( $T_G$  of 62 °C) showed less stiffness than **ISE** ( $T_G$  of 73 °C), since the cycloaliphatic core provides strength to the material. Difunctional aromatic epoxides **RDGE** ( $T_G$  of 91 °C) and **DGEVA** ( $T_G$  of 76 °C) showed high tensile strength, imparted by the rigid aromatic backbone. Unexpectedly, the trifunctional **PHTE** exhibited lowest  $T_G$  of 35 °C, as a result of lower epoxy group conversion and early vitrification.

By contrast, the second strategy for epoxy curing was a thermally induced polyaddition between epoxy monomers and polyols. Polyaddition reactions proceed *via* regulated step-growth polymerizations.

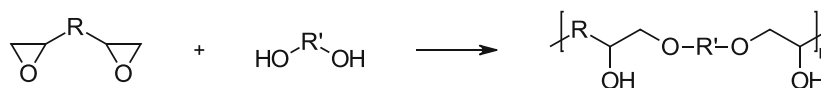


Figure 121: Scheme of the epoxy alcohol polyaddition.

The triol trimethylolpropane was chosen as co monomer since the trifunctional nature leads to crosslinked step-growth polymers. At first, a broad catalyst search revealed, that imidazoles are potent catalysts for the polyaddition reaction. Additionally, a proton NMR study was conducted to gain information on the polymerization mechanism. Indeed, epoxy and alcohol monomers reacted in a comparable manner to yield step-growth polymers. Reactivity of the thermally induced polymerization was investigated using differential scanning calorimetry (DSC), showing that all monomers (**TMPTG:TMP**, **ISE:TMP**, **RDGE:TMP**, **DGEVA:TMP** and **PHTE:TMP**) exhibited excellent reactivity, reaching conversions of >90%.

Additionally, DMTA analysis and tensile tests were performed to investigate the influence of step-growth polymerization and compared to cationically photopolymerized (chain-growth polymerization) specimens. Linear aliphatic chains of **poly(TMPTG:TMP)** led to the formation of a soft and elastic materials, with a  $T_G$  of 2 °C. A decrease in  $T_G$  was also observed for **poly(ISE:TMP)** (48 °C), **poly(RDGE:TMP)** (52 °C) and **poly(DGEVA:TMP)** (35 °C). As a result of the more homogeneous polymer networks, identified by sharpened glass transitions, tough and strong polymers were obtained. While early vitrification led to low conversion for photopolymerized **poly(PHTE)**, high conversion and crosslinking density of **poly(PHTE:TMP)** resulted in higher  $T_G$  (105 °C) and highest tensile strength of all materials (~100 MPa). Results of the thermomechanical analysis proved, that thermal induced polyaddition led to the formation of more regulated polymers with enhanced materials properties.

Finally, by combination of a photopolymerized soft network and thermally polymerized hard network, sequential IPNs were fabricated and their potential application for 3D printing accessed.

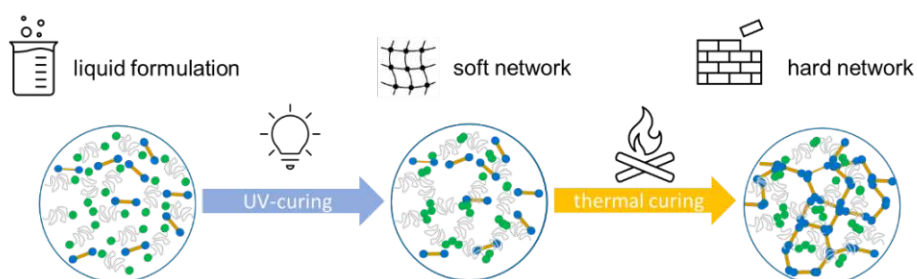


Figure 122: Scheme of sequential-IPN fabrication.

It was shown, that at least 30 wt% the soft network (**20IBMA80PEG**) were necessary to obtain form-stable specimens after photopolymerization. Nevertheless, 10-45 wt% of soft matrix were added to **ISE:TMP**, **RDGE:TMP**, **DGEVA:TMP** and **PHTE:TMP**. DMTA analysis proved, that by the addition of up to 15 wt% soft network sharper glass transitions were obtained. When performing tensile tests, increased toughness was yielded for IPNs with low (<30 wt%) amounts of soft network. Contradictory results were obtained for IPNs containing 30-45 wt% of **poly(20IBMA80PEG)**: DMTA analysis indicated formation of heterogeneous and phase separated IPNs as a result of poor miscibility of the networks. Consequently, brittle materials were obtained and therefore, toughening was not achieved.

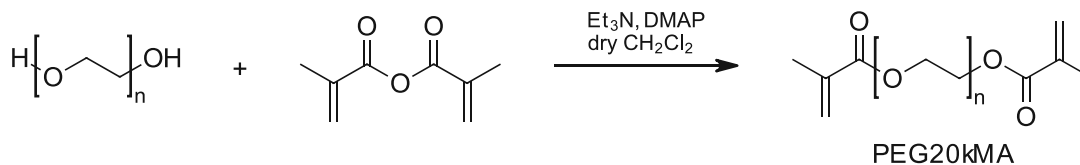
Overall, IPNs with high amount of **poly(20IBMA80PEG)** showed no indications of material toughening, as a result of poor miscibility of soft and hard network. On the contrary, when the soft network content was below 30 wt%, an increase in tensile toughness was observed and glass transition was furthermore sharpened. In the end, IPNs could be derived from bio-based building blocks and, at least for selected compositions, polymer toughening was achieved.

# Experimental Part

## 1 Soft network from renewable resources

### 1.1 Synthesis and characterization of macromolecular component

#### 1.1.1. Synthesis of poly(ethylene glycol) dimethacrylate (PEG20kMA)



	M [g/mol]	Eq.	n [mmol]	m [g]	V [mL]
Poly(ethylene glycol)	~20 000	1.00	1.00	20.0	-
Methacrylic anhydride	154.2	8.00	8.00	-	1.20
Triethylamine	101.2	8.00	8.00	-	1.10
4-(Dimethylamino)pyridin (DMAP)	122.2	0.300	0.300	0.0380	-
dry DCM	-	-	-	-	100

The synthesis was conducted according to Fiore *et al.*<sup>138</sup> Poly(ethylene glycol) (19.98 g, 1 mmol, 1 eq) was dissolved in 100 mL of dry DCM and the flask purged with argon. Triethylamine (1.10 mL, 8 mmol, 8 eq) and DMAP (0.038 g, 0.3 mmol, 0.3 eq) were added to the stirred solution. The flask was cooled to 0 °C with an NaCl/ice bath and Methacrylic anhydride (1.2 mL, 8 mmol, 8 eq) was added dropwise. The flask was allowed to warm up to room temperature and the colorless solution was stirred for 4 days. Thereafter, the solution was precipitated two times into 3L of cold diethyl ether, giving a white solid that was dried in a vacuum oven for 16 h. 19.96 g of a white solid were obtained and it was stored under inert atmosphere in a desiccator.

**Yield:** 19.96 g (98% of theory), white solid

**Melting point:** 57.8 - 58.3 °C (lit.: 57.5 °C<sup>167</sup>)

**<sup>1</sup>H NMR** (400 MHz, CDCl<sub>3</sub>) δ 6.13 (s, 2H), 5.58 (d, J = 1.63 Hz, 2H), 3.64 (s, 2463H), 1.95 (dd, J = 1.56, 1.03 Hz, 6H).

Proton NMR is in accordance with literature and confirms the introduction of methacrylate endgroups.<sup>168</sup>

### 1.1.2. Hydroxyl value determination of PEG20kMA

For the determination of end group modification of PEG20k to PEG20kMA,  $^{31}\text{P}$ -NMR was used. All used chemicals were dried over molecular sieve and their water content analyzed using a Karl-Fischer titration device. Water content of all chemicals was well below 50 ppm.

~30 mg of both modified and unmodified PEG were dissolved in 100  $\mu\text{L}$  dry  $\text{CDCl}_3$  and 100  $\mu\text{L}$  dry pyridine were added. Then, 100  $\mu\text{L}$  of a prepared cyclohexanol/ $\text{Cr}(\text{acac})_3$  solution (40 mg/mL cyclohexanol and 5 mg/mL  $\text{Cr}(\text{acac})_3$ ) was added and vortexed until complete homogenization of all components. Separately, to 400  $\mu\text{L}$  dry  $\text{CDCl}_3$  were added 50  $\mu\text{L}$  of 2-chloro-4,4,5,5-tetramethyl-1,3,2-dioxaphospholane (TMDP). This solution was pipetted into the PEG containing vial and mixed again. The red solution was transferred into an NMR tube under inert atmosphere and the  $^{31}\text{P}$ -NMR spectrum measured immediately afterwards. The spectra were recorded on a Bruker Avance 600 NMR spectrometer with an igated mode (128 scans, 25s relaxation time, duration 50 min).

The typical integration areas for  $^{31}\text{P}$ -NMR spectra are listed in Table 35.

Table 35: Peak areas for  $^{31}\text{P}$  NMR spectroscopy

functional group assignment	integration area $\delta$ [ppm]
TMDP	176.0
aliphatic OH	145.2-150.0
cyclohexanol (internal standard)	144.7-145.2
phenolic OH	136.5-144.5
carboxylic OH	133.5-136.5
hydrolysis product of TMDP	132.1 & 15.9

The spectra were analyzed with the program *Mestrenova*. Firstly, a manual phase and baseline correction was performed. Afterwards, the signals were referenced to the signal at 132.2 ppm and then the other signals were integrated as usual. The signal of the internal standard (145 ppm) was set to 10.



### 1.1.3. Molecular weight determination *via* size exclusion chromatography

Gel permeation chromatography (GPC) was used to obtain the molecular weight of the modified and unmodified polyethylene glycol. ~3-6 mg of sample were dissolved in 200  $\mu$ L hexafluoro isopropanol and afterwards diluted with THF (spiked with 0.5 mg/mL BHT as a flow marker). The solutions were syringe filtrated and transferred into GPC glass vials. Table 36 displays the concentrations of the GPC samples.

Table 36: Sample concentrations for GPC measurements

	concentration [mg sample /mL THF]
PEG20k	3.17
PEG20kMA	2.48

GPC measurements were performed on a Malvern VISCOTEK TDA system equipped with a VISCOTEK SEC MALS 9 light scattering detector, a Viscotek TDA 305-021 RI+Visc detector, and a UV Detector Module 2550 for TDA 305. Separation was conducted through three consecutive PSS SDC columns (100 Å, 1000 Å, and 100000 Å) using THF as solvent at a flow rate of 0.8 ml/min.

Conventional calibration was performed with polystyrene standards (PSS) between 375 and 177 000 Da. In order to evaluate the GPC data, OmniSEC v05.12.461 from Malvern was used.

## 1.2. Effect of PEG20kMA in photopolymerizable formulations

### 1.2.1. Choice of a reactive diluent from renewable resources

For the determination of the purity of a commercially available IBMA resin (see Figure 47), proton NMR analysis was conducted. Obtained  $^1\text{H-NMR}$  codes are depicted below.

$^1\text{H NMR}$  (400 MHz,  $\text{CDCl}_3$ )  $\delta$  6.06 (dt,  $J = 2.0, 1.0$  Hz, 1H), 5.52 (p,  $J = 1.6$  Hz, 1H), 4.72 (dd,  $J = 7.7, 3.3$  Hz, 1H), 1.93 (dd,  $J = 1.6, 1.0$  Hz, 3H), 1.88 – 1.65 (m, 4H), 1.62 – 1.51 (m, 1H), 1.22 – 1.06 (m, 2H), 1.02 (s, 3H), 0.86 (d,  $J = 4.1$  Hz, 6H).

### 1.2.2. Miscibility of macromolecular PEG20kMA in IBMA

To study the miscibility of PEG20kMA in IBMA, 10-90 wt% of IBMA were added to PEG20kMA. Formulations with high content of PEG20kMA (up to 50 wt%) were heated to 60 °C in an ultrasonic bath to homogenize the formulations. With higher IBMA content (60-90 wt%), formulations were miscible at room temperature and homogenized with a vortex. Table 37 depicts the exact amount of used chemicals.

Table 37: Miscibility experiments for PEG20kMA and IBMA

	$m_{\text{IBMA}}$ [mg]	$m_{\text{PEG20kMA}}$ [mg]
<b>10IBOMA90PEG</b>	50.71	449.2
<b>20IBOMA80PEG</b>	102.4	398.9
<b>30IBOMA70PEG</b>	148.2	352.7
<b>40IBOMA60PEG</b>	202.2	299.7
<b>50IBOMA50PEG</b>	247.2	248.2
<b>60IBOMA40PEG</b>	298.7	199.9
<b>70IBOMA30PEG</b>	350.3	152.6
<b>80IBOMA20PEG</b>	400.0	102.5
<b>90IBOMA10PEG</b>	452.0	49.01

### 1.2.3. Rheology measurements

To gain information about the temperature-dependent viscosity ( $\eta$ ), rheology measurements were performed. The measurements were performed on an Anton Paar MCR 300 apparatus and a CP-25-1 measuring system, using a gap distance between stamp (cone) and bottom plate of 48  $\mu\text{m}$  and a constant shear rate of 100  $\text{s}^{-1}$ . A temperature range of 60-100 °C was used. Roughly 80  $\mu\text{L}$  per formulation were used for each measurement. Table 38 depicts the exact compositions of the formulations.

Table 38: Formulations containing different ratios of PEG20kMA and IBMA and measured viscosities at 60 °C and 90 °C.

	$m_{\text{IBMA}}$ [mg]	$m_{\text{PEG20kMA}}$ [mg]	$\eta_{60^\circ\text{C}}$ [Pa·s]	$\eta_{90^\circ\text{C}}$ [Pa·s]
<b>100PEG</b>	-	100.1	49.6	19.7
<b>10IBMA90PEG</b>	57.42	453.2	31.8	14.4
<b>20IBMA80PEG</b>	99.11	405.9	11.0	5.08
<b>30IBMA70PEG</b>	150.4	349.1	8.82	3.97
<b>40IBMA60PEG</b>	202.1	302.1	8.47	3.72
<b>50IBMA50PEG</b>	258.3	249.7	7.19	3.35
<b>60IBMA40PEG</b>	300.2	199.2	4.61	1.93
<b>70IBMA30PEG</b>	349.9	151.0	1.11	0.50
<b>80IBMA20PEG</b>	400.0	102.1	$4.10 \cdot 10^{-3}$	$6.19 \cdot 10^{-3}$
<b>90IBMA10PEG</b>	447.9	51.23	$3.48 \cdot 10^{-3}$	$3.32 \cdot 10^{-3}$

#### 1.2.4. Network appearance and haptic behavior of the soft network

For the determination of the IBMA content in the soft matrix, formulations were mixed. Formulations containing 10-50 wt% IBOMA and 90-50 wt% PEG20kMA were prepared as follows: the monomers were weighed into amber glass vials and gently heated to 60 °C. Thereafter, 1 wt% of the radical photoinitiator TPO-L (Figure 51) was added and the mixtures homogenized using an ultrasonic bath.

The exact compositions of the formulations are depicted in Table 39.

Table 39: Composition of formulations containing IBOMA and PEG20kMA in different w% ratios

	$m_{\text{IBMA}}$ [mg]	$m_{\text{PEG20kMA}}$ [mg]	$m_{\text{TPO-L}}$ [mg]
<b>10IBMA90PEG</b>	50.71	449.2	6.12
<b>20IBMA80PEG</b>	102.4	399.0	5.23
<b>30IBMA70PEG</b>	149.2	349.0	4.89
<b>40IBMA60PEG</b>	202.2	299.7	5.67
<b>50IBMA50PEG</b>	247.2	248.2	5.17

The resins were poured into silicon molds for DMTA specimens ( $2 \times 5 \times 40 \text{ mm}^3$ ) and irradiated in a Lumamat 100 light oven, provided by Ivoclar Vivadent AG, with 6 Osram Dulux L Blue 18 W lamps. The emitted wavelength spectrum of this oven ranges from 400-580 nm at a measured total intensity of  $\sim 20 \text{ mW/cm}^2$ . Samples were cured on both sides in a transparent silicon mold for 10 min. After irradiation, the specimens were taken out of the mold and their haptic behavior analyzed by bending them by hand.

### 1.3. Photoreactivity of the soft matrix

#### 1.3.1. Photo-DSC analysis

The Photo-DSC (Differential Scanning Calorimetry) measurements were performed in triplicates on a Netzsch DSC 204 F1 with autosampler at 25 °C or 60 °C under N<sub>2</sub> atmosphere. For each measurement, 10 ± 2 mg of the respective formulation were irradiated twice with a filtered UV-light (320-500 nm) with an Exfo OmniCure™ series 2000 broadband Hg-lamp at 25 °C or 60 °C under constant N<sub>2</sub> flow rate (20 mL/min). The light intensity was set to 64 mW/cm<sup>2</sup> at the sample surface, which corresponds to 1 W/cm<sup>2</sup> at the tip of the light guide. Before irradiation, every sample was conditioned for four minutes (isothermal phase) at the measurement temperature.

During the measurement, the heat flow of the polymerization reaction was recorded as a function of time. By integration of the peak area, the polymerization enthalpy ΔH<sub>p</sub> [J/g] is obtained. The released heat during photopolymerization can be used to calculate the double bond conversion, following equation ( 6 ). Theoretical heat of polymerization (ΔH<sub>p,0</sub>) for methacrylates was ~56 kJ/mol.<sup>142, 156</sup>

$$Conversion (\%) = \left( \frac{H_p}{\sum \frac{H_{0,p}^i}{M_i} \cdot x_i} \right) \cdot 100\% \quad (6)$$

*H<sub>p</sub>*... recorded heat of polymerization [J/g]

*H<sub>0,p</sub><sup>i</sup>*... theoretical heat of polymerization [J/mol]

*M<sub>i</sub>*... molecular weight [g/mol]

*x<sub>i</sub>*...molar proportion of component i [-]

Furthermore, two characteristic time points can be determined: *t*<sub>max</sub> (time point when the maximum heat evolution is reached) and *t*<sub>95</sub> (time point when 95% of the overall heat has evolved). The evaluation of the measurements was conducted with Proteus-Thermal Analysis (version 5.2.1) from Netzsch.

After the photo-DSC analysis, formulations containing monofunctional IBMA were dissolved in CDCl<sub>3</sub> and proton NMR spectra were measured. Monomer conversion was calculated by the intensity decrease of the respective monomer peaks in the spectra. NMR spectra were evaluated with the software MestreNova 12.0.4 by Mestrelab research.

Furthermore, GPC analysis was performed as described in 1.1.3.

### 1.3.2. RT-NIR-photorheology

Real-time (RT) NIR-photorheology measurements were conducted on a RT-NIR photorheometer device. Therefore, an Anton Paar MCR 302 WESP rheometer, equipped with a P-PTD 200/GL Peltier glass plate and a PP25 measuring system is coupled with a Bruker Vertex 80 Fourier-Transform Infrared (FTIR) spectrometer, that measures the conversion of the monomers over time. In the IR spectrometer, the IR-light is led from the NIR-spectrometer *via* external mirrors through an optical window and the sample onto the bottom of the rheology plate (see Figure 123). Thereby, the IR-beam interacts with the sample and is reflected to an external mercury cadmium telluride (MCT) detector.

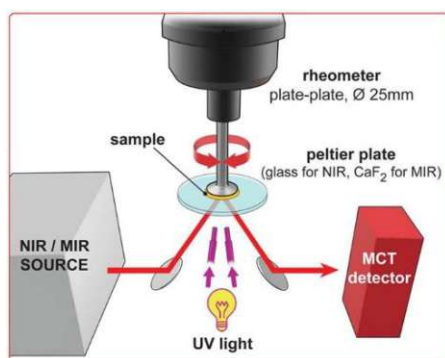


Figure 123: RT-FTIR-Photorheology setup with an illustration of the IR beam and irradiation via UV light. <sup>144</sup>

The measurements were performed in triplicates, using 1 wt% of TPO-L as a photoinitiator at 60 °C. A broadband UV lightsource (320-500 nm) was used to irradiate the samples with an intensity of 64 mW/cm<sup>2</sup> at the sample surface, similar to the photo-DSC analysis. For each measurement, ~150  $\mu$ L of the sample were transferred on the glass disk of the rheometer, which was previously protected with polyethylene (PE) tape. The gap between the glass disk and the measuring system (PP25) was kept constant at 200  $\mu$ m. Temperature was controlled by using an Anton Paar H-PTD 200 heating hood. Formulations were sheared with a strain of 1 % and a frequency of 1 Hz. An Exfo OmniCure<sup>TM</sup> 2000 device with a broadband Hg-lamp (300s, 320-500 nm) was used to irradiate the samples. Calibration of the light source was done using an Ocean Optics USB 2000+ spectrometer.

During RT-NIR-photorheology, the measuring system oscillates with a frequency of 1 Hz and data of the shear storage ( $G'$ )- and shear loss modulus ( $G''$ ) is provided by the rheometer according to the following time interval: one measurement point per s before initiation, one measurement point per 0.2 s during the first 60 s, one measurement point per s till irradiation period ends (4 min). Of special interest for photopolymerization is the so-called gel point ( $t_g$ ), where the curves of both shear moduli intersect.

Furthermore, double bond conversion (DBC) is obtained *via* NIR analysis. By the decrease of the peak area of the methacrylate double bonds, DBC can be calculated in real time. Over the

measuring period, the IR signal at  $\sim 6140 \text{ cm}^{-1}$  is recorded and integrated and thereafter related to the integral at the start of the measurement ( $t_0$ ). Hence, DBC and the gel point ( $\text{DBC}_g$ ) and the final double bond conversion ( $\text{DBC}_{\text{final}}$ ) are obtained.

The double bond conversion (DBC) of the methacrylic double bond was obtained by recording a set of single spectra (time interval  $\sim 0.26 \text{ s}$ ) with an OPUS 7.0 software and integrating the double bond signals at a wavelength of  $\sim 6140 \text{ cm}^{-1}$ .

## 1.4. Mechanical studies of the soft matrix

### 1.4.1. Thermomechanical properties of the soft matrix

Formulations (see Table 40) containing 1 wt% of the radical photoinitiator TPO-L and PEG20kMA (80 wt%) and IBMA (20 wt%) were homogenized using a vortex mixer and an ultrasonic bath at  $60 \text{ }^\circ\text{C}$ . Thereafter, formulations were polymerized in silicon molds (sticks,  $5 \times 2 \times 40 \text{ mm}^3$ ) using a Lumamat 100 light oven (provided by Ivoclar Vivadent AG) with 6 Osram Dulux L Blue 18 W lamps for 10 min on each side of the sample. The light source (400-500 nm) emitted UV light with an intensity of  $\sim 20 \text{ mW/cm}^2$  as determined with an Ocean Optics USB 2000+ spectrometer. The cured polymer specimens were sanded to obtain a uniform dimension ( $< \pm 0.1 \text{ mm}$ ).

Table 40: Composition of the formulation for the soft matrix for mechanical tests.

	$m_{\text{IBMA}}$ [mg]	$m_{\text{PEG20kMA}}$ [mg]	$m_{\text{TPO-L}}$ [mg]
<b>20IBMA80PEG</b>	1002	4000	50.12
<b>PEGDMA</b>	-	5001	49.89

The DMTA (dynamic mechanic thermal analysis) measurements of the soft matrix were performed with an Anton Paar MCR 301 with a CTD 450 oven and an SRF 12 measuring system. The polymer specimens were tested in torsion mode with a frequency of 1 Hz and a strain of 0.1%. The temperature was increased from  $-100 \text{ }^\circ\text{C}$  to  $200 \text{ }^\circ\text{C}$  with a heating rate of  $2 \text{ }^\circ\text{C/min}$ . The storage modulus and the loss factor of the polymer samples were recorded with the software Rheoplus/32 V3.40 from Anton Paar. The reference poly(PEGDMA) was measured on a TA instrument 2980 instrument in 3-point bending mode set to an amplitude of  $10 \text{ }\mu\text{m}$  and a auto-tension of 0.05 N. The oscillation was set to 1 Hz and the measurement was conducted from  $-100$  to  $200 \text{ }^\circ\text{C}$  with a heating rate of  $3 \text{ K/min}$ .

### 1.4.2. Tensile tests of the soft matrix

Photopolymerization of tensile test specimens was performed in accordance to the procedure for DMTA specimens in 1.4.1. Dimension of the dog-chew-bone-shaped samples was in accordance to ISO 527 test specimen 5B (total length of 35 mm and a parallel region dimension of  $2 \times 2 \times 12 \text{ mm}^3$ ). Six specimens were tested for each formulation and tensile tests were

performed on a Zwick Roell Z050 with a maximum test force of 50 kN. The samples were fixed between two clamps and strained with a traverse speed of 5 mm/min. During the measurement, a stress-strain plot was recorded for analysis.

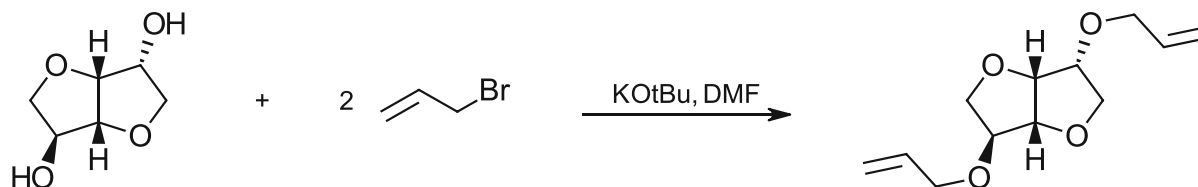
## 2 Hard Network from renewable resources

### 2.1. Monomers from starch and cellulose

#### 2.1.1. Overview

#### 2.1.2. Synthesis of Epoxidized Isosorbide (ISE)

##### 2.1.2.1. Synthesis of Diallyl Isosorbide *via* potassium tert-butoxide



	M [g/mol]	Eq.	n [mmol]	m [g]	V [mL]
Isosorbide	146.1	1.00	48.0	6.99	-
Allyl Bromide	120.9	2.20	105	-	9.10
Potassium tert-Butoxide (KOtBu)	112.2	2.30	110	12.4	-

The synthesis was carried out according to *Stensrud*.<sup>150</sup> Isosorbide (6.99 g, 48 mmol, 1 eq) and Potassium tert-butoxide (12.4 g, 110 mmol, 2.3 eq) were dissolved in 115 mL of anhydr. DMF under inert conditions. After stirring for 60 min at room temperature, the orange solution was cooled to 0 °C and Allyl bromide (9.1 mL, 105 mmol, 2.2 eq) was added dropwise over the course of 40 min. The heterogeneous mixture was warmed up to room temperature and stirred for 15 h. TLC (PE:EE = 5:1) indicated full conversion of starting material. The suspension was filtrated and the filtrate was concentrated *in vacuo*. The obtained oil was diluted with 100 mL CH<sub>2</sub>Cl<sub>2</sub> and washed with 75 mL H<sub>2</sub>O. The aqueous layer was extracted with 2 x 100 mL CH<sub>2</sub>Cl<sub>2</sub>. Combined organic layers were washed with 50 mL brine, dried over Na<sub>2</sub>SO<sub>4</sub> and concentrated *in vacuo* to yield 9.86 g (91 %) of a light orange oil.

**Yield:** 9.86 g (91% of theory), orange oil

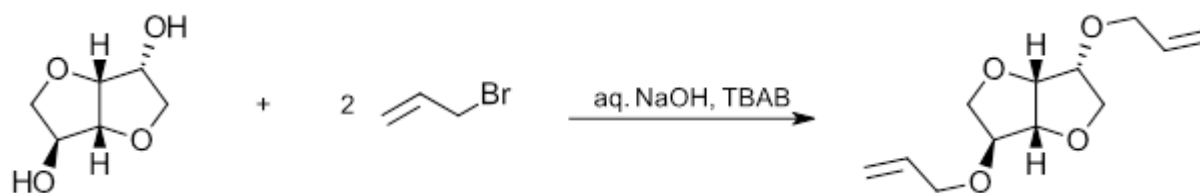
**R<sub>f</sub>:** 0.32 (PE:EE = 3:1)

**<sup>1</sup>H NMR** (400 MHz, CDCl<sub>3</sub>) δ 6.00 – 5.83 (m, 2H), 5.29 (ddq, J = 17.2, 7.1, 1.6 Hz, 2H), 5.20 (ddq, J = 10.4, 5.4, 1.3 Hz, 2H), 4.63 (t, J = 4.4 Hz, 1H), 4.51 (dd, J = 4.3, 1.1 Hz, 1H), 4.20 (ddt, J = 12.6, 5.6, 1.4 Hz, 1H), 4.04 (dddd, J = 12.3, 6.8, 6.1, 2.1 Hz, 5H), 3.99 – 3.90 (m, 3H), 3.63 – 3.57 (m, 1H).

<sup>1</sup>H NMR spectrum is in accordance with literature.<sup>66</sup>



### 2.1.2.2. Synthesis of Diallyl Isosorbide *via* phase-transfer catalyst TBAB



	M [g/mol]	Eq.	n [mmol]	m [g]	V [mL]
Isosorbide	146.1	1.0	205.0	30.01	-
Allyl Bromide	120.9	2.2	452.1	-	40.00
NaOH	40.00	2.2	452.2	18.07	-
Tetrabutylammonium bromide (TBAB)	322.4	0.05	9.020	2.980	-

The synthesis was conducted according to Çakmakci and coworkers.<sup>169</sup> Isosorbide (30.01 g, 205 mmol, 1 eq) was mixed with NaOH (18.70 g, 452 mmol, 2.2 eq) and 50 mL water. After 10 minutes, TBAB (2.98 g, 9 mmol, 0.05 eq) was added as a phase catalyst and the mixture was stirred for 5 minutes. Allyl bromide (40 mL, 452 mmol, 2.2 eq) was added dropwise and the mixture was thereafter heated to 65-70 °C for 7 h, followed by stirring at room temperature for 16 h. After TLC (PE:EE = 5:1) indicated full consumption of starting material, the biphasic solution was extracted with 3x80 mL DCM. Combined organic layers were washed with 200 mL 1N aq. HCl, 3x80 mL H<sub>2</sub>O and dried over Na<sub>2</sub>SO<sub>4</sub>. The solvent was stripped on the rotary evaporator, yielding 34.72 g of the desired product. The product was not further purified for the synthesis of ISE.

**Yield:** 34.72 g (75 % of theory), yellow oil

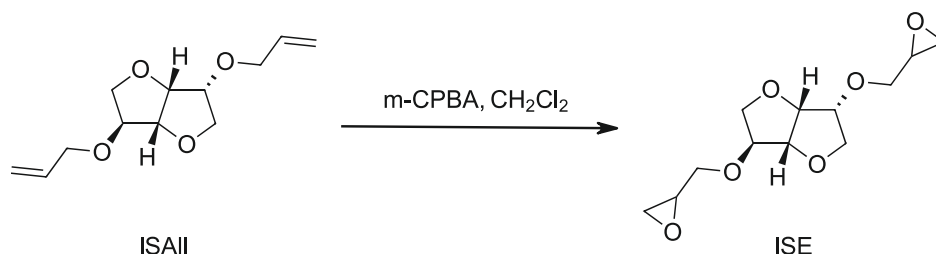
**R<sub>f</sub>:** 0.61 (PE:EE = 1:1)

**<sup>1</sup>H NMR** (400 MHz, CDCl<sub>3</sub>) δ 6.00 – 5.83 (m, 2H), 5.29 (ddq, J = 17.2, 7.1, 1.6 Hz, 2H), 5.20 (ddq, J = 10.4, 5.4, 1.3 Hz, 2H), 4.63 (t, J = 4.4 Hz, 1H), 4.51 (dd, J = 4.3, 1.1 Hz, 1H), 4.20 (ddt, J = 12.6, 5.6, 1.4 Hz, 1H), 4.04 (dddd, J = 12.3, 6.8, 6.1, 2.1 Hz, 5H), 3.99 – 3.90 (m, 3H), 3.63 – 3.57 (m, 1H).

$^{13}\text{C}$  NMR (101 MHz,  $\text{CDCl}_3$ )  $\delta$  134.66/134.32, 117.96/117.64, 86.49, 83.94, 80.37, 79.61, 73.61, 71.81, 70.69, 69.97.

$^1\text{H}$ -NMR and  $^{13}\text{C}$ -NMR are in accordance with literature.<sup>66 170</sup>

### 2.1.2.3. Synthesis of Epoxidized Isosorbide (ISE)



	M [g/mol]	Eq.	n [mmol]	m [g]	V [mL]
ISAI	226.3	1.0	52.00	11.73	-
m-CPBA (70%)	172.6	2.2	114.1	28.12	-
DCM	-	-	-	-	225.0

The synthesis was carried out similar to *Cheng et al.*<sup>171</sup> m-CPBA (70% in  $\text{H}_2\text{O}$ , 28.12 g, 114 mmol) was dissolved in 160 mL anh. DCM and cooled to 0 °C. Afterwards, ISAI (11.73 g, 52 mmol, 1 eq) was dissolved in 65 mL DCM and added to the cooled solution over the course of 2 h. After 1 h of stirring, a white precipitate was formed and the suspension was stirred for another 18 h. The reaction mixture was cooled and filtrated. The precipitate was washed 2x with cold DCM and the filtrate was washed with sat. aq.  $\text{Na}_2\text{S}_2\text{O}_3$  (2x100 mL), sat. aq.  $\text{NaHCO}_3$  (3x 200 mL) and water (200 mL). Combined aq. layers were washed with DCM (2x 150 mL). Combined organic layers were dried over  $\text{Na}_2\text{SO}_4$  and the solvent was stripped and the light-yellow crude oil was further purified *via* column chromatography (pure EE), yielding 8.31 g of the desired product.

**Yield:** 8.31 g (65 % of theory), turbid oil

**R<sub>f</sub>:** 0.34 (100 % EE)

**<sup>1</sup>H NMR** (400 MHz, CDCl<sub>3</sub>): δ 4.67 (dq, J = 10.09, 4.21 Hz, 1H), 4.52 (ddt, J = 11.19, 4.40, 1.04 Hz, 1H), 4.16 – 3.36 (m, 10H), 3.24 – 3.09 (m, 2H), 2.84 – 2.76 (m, 2H), 2.67 – 2.55 (m, 2H).

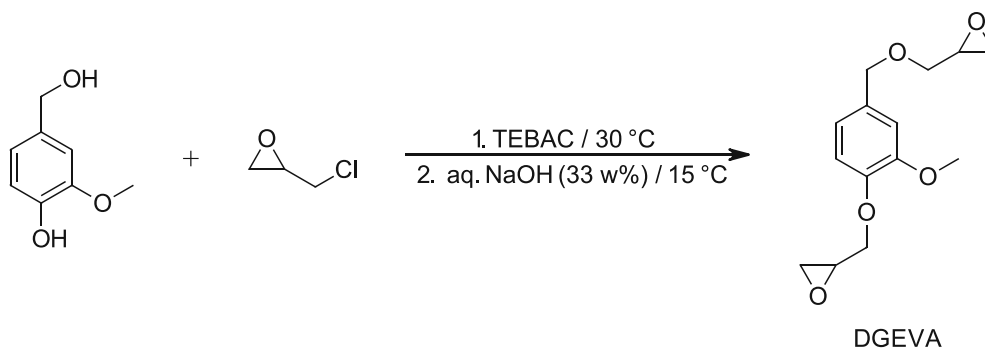
**<sup>13</sup>C NMR** (101 MHz, CDCl<sub>3</sub>) δ 86.32, 85.09, 80.57, 80.37, 73.62, 71.97, 70.48-70.01, 50.74, 44.48.

<sup>1</sup>H-NMR and <sup>13</sup>C-NMR are in accordance with literature.<sup>171 170</sup>

## 2.2. Monomers from lignin

### 2.2.1. Overview

### 2.2.2. Synthesis of Diglycidyl Ether of Vanillyl Alcohol



	M [g/mol]	Eq.	n [mmol]	m [g]	V [mL]
Vanillyl Alcohol	154.2	1.0	65.02	9.980	-
Epichlorohydrin	92.53	10	650.1	-	51.00
Tetrabutylammonium chloride (TEBAC)	227.8	0.1	6.120	1.520	-
NaOH	40.00	15	973.0	38.96	-

The synthesis was conducted according to Fache *et al.*<sup>172</sup> The reaction was conducted in inert atmosphere. Vanillyl alcohol (9.98 g, 65 mmol, 1 eq) was stirred with Epichlorohydrin (51 mL, 650 mmol, 10 eq) and TEBAC (1.52 g, 6 mmol, 0.1 eq) at room temperature for 4 hours using a mechanical stirrer. The clear pink solution was cooled to 0 °C with an ice/NaCl bath and an aqueous solution of NaOH (33 wt%, 38.96 g, 973 mmol, 15 eq) was added dropwise over 30 min. The ice bath was left to melt over time and the white suspension stirred for 18h. Thereafter, 250 mL of deionized water were added and washed with 200 mL of ethyl acetate. The aqueous layer was washed two more times with ethyl acetate (200 mL). Pooled organic layers were washed with water (100 mL) and brine (100 mL) and consequently dried over Na<sub>2</sub>SO<sub>4</sub>. The solvent was stripped *in vacuo*, giving a white crude product. Further purification was done by column chromatography (435 g silica, PE:EE = 1:3), obtaining the desired compound as a white solid in 82 % yield.

**Yield:** 14.23 g (82 % of theory), white solid

**Melting point:** 52.7 – 53.1 °C (lit.: 53 °C<sup>172</sup>)

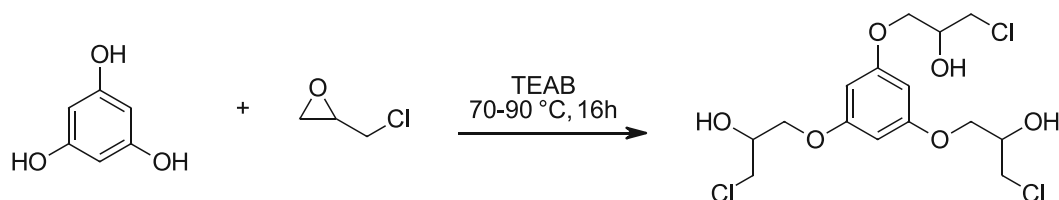
**<sup>1</sup>H NMR** (400 MHz, CDCl<sub>3</sub>) δ 6.95 – 6.82 (m, 3H), 4.52 (q, J = 11.6 Hz, 2H), 4.24 (dd, J = 11.4, 3.6 Hz, 1H), 4.04 (dd, J = 11.4, 5.5 Hz, 1H), 3.88 (s, 3H), 3.76 (dd, J = 11.5, 3.0 Hz, 1H), 3.42 – 3.34 (m, 2H), 3.19 (ddt, J = 5.8, 4.2, 2.9 Hz, 1H), 2.89 (dd, J = 5.0, 4.1 Hz, 1H), 2.81 (dd, J = 5.0, 4.1 Hz, 1H), 2.74 (dd, J = 4.9, 2.7 Hz, 1H), 2.67 – 2.58 (m, 1H).

**<sup>13</sup>C NMR** (101 MHz, CDCl<sub>3</sub>) δ 149.85, 147.79, 131.75, 120.48, 114.07, 111.79, 73.31, 70.84, 70.47, 56.08, 51.02, 50.34, 45.11, 44.44.

Melting point and NMR spectra are in accordance with literature.<sup>172</sup>

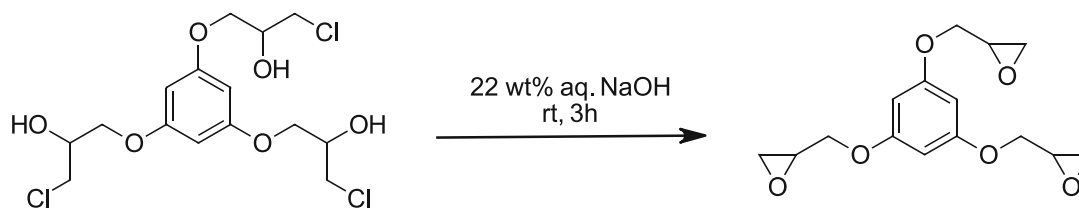
## 2.2.3. Synthesis of Triglycidyl Ether of Phloroglucinol (PHTE)

### 2.2.3.1. Synthesis of PHTE via tetraethylammonium bromide



	M [g/mol]	Eq.	n [mmol]	m [g]
Phloroglucinol	126.1	1.0	79.01	9.920
Epichlorohydrin	92.53	15	1189	110.2
Tetraethylammonium bromide (TEAB)	210.2	0.75	59.10	11.91

The reaction was conducted according to Sangermano *et al.*<sup>53</sup> Phloroglucinol (9.92 g, 79 mmol, 1 eq), Epichlorohydrin (110.2 g, 1189 mmol, 15 eq) and Tetraethylammonium bromide (11.91 g, 59 mmol, 0.75 eq) were stirred using a mechanical stirrer at 70 °C. During the reaction, the mechanical stirrer got stuck several times due to the formation of a highly viscous and sticky mass, that could only be dissolved at elevated temperatures. After 16h, a red viscous liquid was obtained and cooled to room temperature. The mixture was poured into 250 mL of DCM, washed with water (3x 100 mL) and dried over Na<sub>2</sub>SO<sub>4</sub>. The excess of solvent and epichlorohydrin was removed on the rotary evaporator, giving 32.02 g of viscous crude product, that was directly used for the second step of the reaction.



	M [g/mol]	Eq.	n [mmol]	m [g]	V [mL]
Intermediate from step 1	403.7	1.0	79.02	32.02	-
NaOH	40.00	1.4	111.0	13.32	-
Tetraethylammonium bromide (TEAB)	210.2	0.07	6.156	1.170	-
dry DCM				-	330.0

For the second step, the intermediate (32.02 g, 79 mmol, 1 eq) was solubilized in 330 mL dry DCM and TEAB (1.17 g, 6 mmol, 0.07 eq) was added at room temperature. NaOH (13.32 g, 111 mmol, 1.4 eq) was dissolved in 53.7 g water and added dropwise to the solution over 30 min. The biphasic mixture was stirred for 3h. After the addition of 100 mL water, the phases were separated and the organic layer washed two more times with 100 mL water. The organic phase was dried over Na<sub>2</sub>SO<sub>4</sub> and evaporated to dryness, giving 20.01 g of a yellow crude oil. Further purification was done by column chromatography (435 g silica, PE:EE=1:3), yielding the desired compound as a white solid.

**Yield:** 8.37 g (36% of theory), white solid

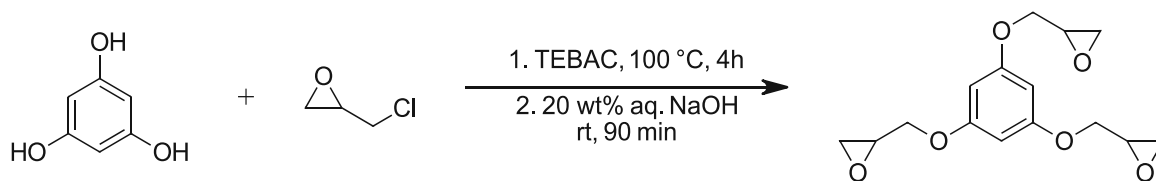
**Melting point:** 52.8 – 54.0 °C (lit.: 53 °C<sup>153</sup>)

**<sup>1</sup>H NMR** (400 MHz, CDCl<sub>3</sub>) δ 6.14 (s, 3H), 4.18 (dd, J = 11.0, 3.0 Hz, 3H), 3.89 (dd, J = 11.0, 5.7 Hz, 3H), 2.90 (dd, J = 5.0, 4.1 Hz, 3H), 2.74 (dd, J = 4.9, 2.6 Hz, 3H).

**<sup>13</sup>C NMR** (101 MHz, CDCl<sub>3</sub>) δ 160.46, 94.84, 68.96, 50.15, 44.83.

Melting point and NMR spectra are in accordance with literature.<sup>153</sup>

### 2.2.3.2. Synthesis of PHTE via tetrabutylammonium chloride



	M [g/mol]	Eq.	n [mmol]	m [g]
Phloroglucinol	126.1	1.0	83.12	10.26
Epichlorohydrin	92.53	19	1580	146.7
Tetrabutylammonium chloride (TEBAC)	227.8	0.14	12.26	2.650
NaOH	40.00	6.0	500.1	20.00

The synthesis was conducted according to Guzman *et al.*<sup>153</sup> Phloroglucinol (10.26 g, 83 mmol, 1 eq) was dissolved in Epichlorohydrin (146.71 g, 1580 mmol, 19 eq) and Tetrabutylammonium chloride (2.65 g, 12 mmol, 0.14 eq) was added and the reaction mixture was heated to 100 °C and stirred mechanically for 4h. After cooling down to room temperature, NaOH (20.00 g, 500 mmol, 6 eq) was added as a 20 wt% aqueous solution over 30 min. The suspension was stirred for 90 min at room temperature. After the addition of 60 mL ethyl acetate, the phases were separated and the organic layer was washed with water (50 mL) and brine (2 x 50 mL) and dried over Na<sub>2</sub>SO<sub>4</sub>. The solvent was removed in vacuo, giving a yellow crude oil. Further purification was done *via* column chromatography (435 g silica, PE:EE=1:3), giving the desired compound as a white solid.

**Yield:** 12.6 g (52% of theory), white solid

**Melting point:** 53.1-53.8 °C (lit.: 53 °C<sup>153</sup>)

**<sup>1</sup>H NMR** (400 MHz, CDCl<sub>3</sub>) δ 6.14 (s, 3H), 4.18 (dd, J = 11.0, 3.0 Hz, 3H), 3.89 (dd, J = 11.0, 5.7 Hz, 3H), 2.90 (dd, J = 5.0, 4.1 Hz, 3H), 2.74 (dd, J = 4.9, 2.6 Hz, 3H).

**<sup>13</sup>C NMR** (101 MHz, CDCl<sub>3</sub>) δ 160.46, 94.84, 68.96, 50.15, 44.83.

Melting point and NMR spectra are in accordance with literature.<sup>153</sup>

## 2.3. Photopolymerization of bio-based epoxy monomers

### 2.3.1. Photoreactivity *via* Photo-DSC analysis

Photoreactivity experiments were conducted as previously stated in the Experimental part chapter 1.3.1. By contrast, the cationic photoinitiator UVI 6976 (Figure 71) was used, which is composed of a mixture of triarylsulfonium hexafluoroantimonate salts in propylene carbonate.

### 2.3.2. Epoxy group conversion *via* ATR-IR

In order to obtain a more detailed information about the conversion of the epoxy monomers, ATR-IR measurements were performed. FT-IR spectra were recorded from each formulation of 2.3.1 before and after the photo-DSC measurement. Both uncured formulations and cured specimens were measured in ATR mode on a Spectrum 65 FTIR spectroscope from Perkin Elmer, which is equipped with a Specac MKII Golden Gate Single Reflection ATR System. Analysis of the spectrum was done with the software PerkinElmer Spectrum in version 10.03.07.0112. IR spectra were recorded in a wavenumber range from 4000 to 500  $\text{cm}^{-1}$  with 4 scans

In the spectra, the signal at 915  $\text{cm}^{-1}$  was assigned to the epoxy group. Additionally, aromatic ring and phenyl ether signals were observed at around 750  $\text{cm}^{-1}$  and 1180  $\text{cm}^{-1}$  and used as references.<sup>159</sup> For the cycloaliphatic monomer **ISE**, the -CH signal at 1460  $\text{cm}^{-1}$  was used as reference IR signal<sup>101</sup>, whereby for **TMPTG** the reference IR-band was the -CH signal at 2900  $\text{cm}^{-1}$ .<sup>160</sup> The epoxy group conversion was calculated by reducing the area of the signal at 915  $\text{cm}^{-1}$  compared to the reference signal according to equation ( 7 ).

$$\text{Epoxy group conversion (\%)} = \left( 1 - \frac{\frac{A_{\text{Epoxy,Polymer}}}{A_{\text{Ref,Polymer}}}}{\frac{A_{\text{Epoxy,Monomer}}}{A_{\text{Ref,Monomer}}}} \right) \cdot 100\% \quad (7)$$

$A_{\text{Epoxy,Polymer/Monomer}}$ ... area of epoxy signal at 915  $\text{cm}^{-1}$  in the polymer/monomer

$A_{\text{Ref,Polymer/Monomer}}$ ... area of the reference band in the polymer/monomer

### 2.3.3. Thermomechanical properties of photopolymers

Determination of the viscoelastic properties of photopolymerized epoxy monomers was done by DMTA measurements as stated in Experimental part chapter 1.4.1. Therefore, monomer formulations containing 1 wt% of the cationic photoinitiator UVI 6976 were prepared. The exact compositions for the formulations are depicted in Table 41.



Table 41: Formulations used for DMTA measurements and tensile tests.

monomer	$m_{\text{Epoxy-Monomer}}$ [mg]	$m_{\text{PI}}$ [mg]
TMPTG	3024	30.19
ISE	3099	31.12
DGEVA	3499	35.01
RDGE	2222	32.12
PHTE	3502	34.99

Photoresins were cured using a Uvitron International INTELLI-RAY 600 UV-oven equipped with a 320-500 nm Hg broadband UV lamp (600 W; UV-A: 125 mW cm<sup>-2</sup>; Vis: 125 mW cm<sup>-2</sup>) for 300 s at 100% power. After the first curing, the sample was taken out of the mold and the reversed side of the specimen was exposed to the same curing procedure with the same parameters once again. It has to be mentioned, that liquid monomers **TMPTG**, **ISE** and **RDGE** were photopolymerized at ambient temperatures, whereas the solid monomers **DGEVA** and **PHTE** were cured in its molten state at 60 °C. After the irradiation period, polymerized specimens were thermally post-cured at 90 °C for 16-18h, to increase the total epoxy conversion. Epoxy group conversion of cured polymer specimens was determined as stated in chapter 2.3.2.

#### 2.3.4. Tensile tests of photopolymers

To complete the study on the thermomechanical properties of cationically photopolymerized monomers, tensile tests were conducted as stated in Experimental part chapter 1.4.2. Photopolymerization of tensile test specimens was performed in accordance with the procedure for DMTA specimens in chapter 2.3.3.

## 2.4. Thermal polymerization of bio-based epoxy monomers

### 2.4.1. Investigation of suitable co-monomers

Formulations containing epoxy monomers from chapter 2.3 were mixed with various polyfunctional alcohols (Figure 80) in order to test solubility and miscibility of the components. Epoxy monomers **TMPTG**, **ISE**, **RDGE**, **DGEVA** and **PHTE** were mixed in a 1:1 ratio (in respect to reactive groups) with the alcohols depicted in Figure 70.

All of the alcohols from Figure 70 are white solids with melting points of 58 °C (trimethylolpropane), 60 °C (isosorbide) or even higher for vanillyl alcohol (114-115 °C), resorcinol (110 °C) and phloroglucinol (218-222 °C). Miscibility was determined as follows: epoxy and alcohol monomers were mixed at 25 °C, 60 °C or 5 °C above the melting points of the solid components using a vortex and ultrasonic bath. Thereafter the formulations were cooled to 60 °C or room temperature.

### 2.4.2. Investigation of suitable catalysts

For the investigation of suitable catalyst systems, **TMPTG** was used as the epoxy monomer and **TMP** was used as alcohol component. Formulations were prepared as follows: **TMPTG** and **TMP** (in a 1:1 ratio in respect to reactive groups) were weighed into glass vials and placed in a water bath (60 °C) to melt the solid alcohol component. Afterwards, the catalyst (in 1-10 wt%) was added, the liquid mixture was mixed and furthermore degassed for 5 minutes in an ultrasonic bath. Thereafter, the liquid resins were poured into silicon molds for DMTA specimens (2x5x40 mm<sup>3</sup>) and cured in a drying oven. The exact compositions of the formulations and curing conditions are depicted in Table 42 and Table 43. Epoxy conversion was monitored and calculated *via* IR spectroscopy as stated in chapter 2.3.2.

Table 42: Formulations containing TMPTG:TMP and 1-10 wt% of catalysts.

formulation	m <sub>TMPTG</sub> [mg]	m <sub>TMP</sub> [mg]	m <sub>cat</sub> [mg]
TMPTG:TMP_5wt%TEA	1055	471.0	75.80
TMPTG:TMP_10wt%TEA	1057	468.8	154.2
TMPTG:TMP_5wt%DMA	1060	469.3	77.21
TMPTG:TMP_10wt%DMA	1059	470.2	148.7
TMPTG:TMP_5wt%TMG	1054	471.8	77.30
TMPTG:TMP_10wt%TMG	1053	468.9	147.7
TMPTG:TMP_5wt%DBN	1060	467.2	75.74
TMPTG:TMP_10wt%DBN	1059	469.2	150.1
TMPTG:TMP_5wt%IM	1055	470.3	75.20
TMPTG:TMP_10wt%IM	1058	469.3	152.2
TMPTG:TMP_5wt%1MIM	1056	471.2	74.83
TMPTG:TMP_10wt%1MIM	1059	470.8	152.0
TMPTG:TMP_1wt%IM	1061	470.5	15.29
TMPTG:TMP_0.1wt%IM	1060	469.9	1.510

Table 43: Curing conditions for formulations containing TMPTG:TMP and 1-10 wt% of catalysts.

formulation	curing condition
TMPTG:TMP_5wt%TEA	120 °C, 20 h
TMPTG:TMP_10wt%TEA	
TMPTG:TMP_5wt%DMA	120 °C, 48 h
TMPTG:TMP_10wt%DMA	
TMPTG:TMP_5wt%TMG	120 °C, 18 h
TMPTG:TMP_10wt%TMG	
TMPTG:TMP_5wt%DBN	120 °C, 18 h
TMPTG:TMP_10wt%DBN	
TMPTG:TMP_5wt%IM	90 °C, 18 h
TMPTG:TMP_10wt%IM	90 °C, 1 h
TMPTG:TMP_5wt%1MIM	90 °C, 18 h
TMPTG:TMP_10wt%1MIM	90 °C, 1 h
TMPTG:TMP_1wt%IM	90 °C, 18 h
TMPTG:TMP_0.1wt%IM	

### 2.4.3. Proton NMR study

To get a detailed insight of the polyaddition mechanism, an NMR study was conducted. Formulations of around 1 g were composed as follows: one epoxy monomer (either **ISE**, **RDGE** or **DGEVA**) was mixed in a 50 mol% ratio (in respect to reactive groups) with **hexanediol** and stirred in a heated aluminum block at 60 °C. 1 sample per formulation was prepared for proton NMR analysis by diluting the resins with ~0.5 mL  $d_6$ -DMSO. Afterwards, 1 wt% of the catalyst **imidazole** was added and stirring continued at 60 °C. Every 30 min, a sample was prepared for proton NMR analysis as stated above and analyzed *via* 400 MHz NMR spectroscopy. The peaks marked in Figure 86, Figure 89 and Figure 91 were used as internal standards. The conversion of epoxy and alcohol peaks was determined by following the decrease in epoxy and OH signal integrals over time, using formula ( 8 ).

$$\text{Conversion (\%)} = \left( 1 - \frac{\text{integral}(t_x)}{\text{integral}(t_0)} \right) \cdot 100\% \quad (8)$$

*integral* ( $t_x$ )... area of corresponding peaks at determined time points ( $t=t_x$ )

*integral* ( $t_0$ )... area of corresponding peaks at the beginning ( $t=t_0$ )

The rate of polymerization  $R_p$  was determined according to formula ( 9 ). Therefore, monomer conversion (%) was plotted against the reaction time (s) and the slope of the graph gave the rate of polymerization ( $R_{p,s}$ ) in 1/s, which describes the conversion of the monomer per time (s). In order to obtain the rate of polymerization as concentration (mol/L) per time (s), the density ( $\rho$  in g/L) and molecular mass (g/mol) of the monomer are used.<sup>173</sup>

$$R_p \left[ \frac{\text{mol}}{\text{L} \cdot \text{s}} \right] = \frac{R_{p,s} \left[ \frac{1}{\text{s}} \right] \cdot \rho \left[ \frac{\text{g}}{\text{L}} \right]}{M \left[ \frac{\text{g}}{\text{mol}} \right]} \quad (9)$$

$R_p$  ... rate of polymerization [mol/L\*s]

$R_{p,s}$ ... rate of polymerization derived from the slope of conversion per time graphs [1/s]

$\rho$ ... density of the monomer at 60 °C [g/L]

$M$ ... molecular weight of the monomer [g/mol]

Density of the monomers was determined by using a pycnometer with an exact volume of 1 mL. Table depicts the densities of the monomers ISE, RDGE and DGEVA as well as  $R_{p,s}$  and the calculated  $R_p$ .

Table 44: Density and rate of polymerization of ISE, RDGE and DGEVA as determined by equation (9).

	$\rho$ [g/mL]	$R_{p,s}$ [1/s]	$R_p$ [mmol/L*s]
<b>ISE</b>	1.13	$5.49 \cdot 10^{-3}$	24.0
<b>RDGE</b>	1.33	$1.26 \cdot 10^{-2}$	74.0
<b>DGEVA</b>	1.27	$5.02 \cdot 10^{-3}$	24.1

#### 2.4.4. Thermal reactivity via differential scanning calorimetry (DSC)

In order to evaluate the thermal properties, particularly the exothermic curing behavior, of the bio-based polyaddition polymers, dynamic scanning calorimetry (DSC) was performed.

Therefore, formulations (see Table 45) with an exact stoichiometric ratio (1:1 in respect to reactive groups) of the epoxy and OH-compounds were prepared: both monomers were weighed into an amber glass vial, gently heated to 60 °C and homogenized with a vortex. Afterwards, 1 wt% of the catalyst imidazole was added and the formulations homogenized again.

Table 45: Composition of formulations used for DSC measurements and (thermo)mechanical tests.

	$m_{\text{Epoxy-Monomer}}$ [mg]	$m_{\text{TMP}}$ [mg]	$m_{\text{IM}}$ [mg]
<b>TMPTG:TMP</b>	2122	941.1	30.22
<b>ISE:TMP</b>	2582	893.4	35.01
<b>DGEVA:TMP</b>	2397	805.0	32.02
<b>RDGE:TMP</b>	2222	894.5	31.17
<b>PHTE:TMP</b>	2354	1073	34.28

~10 mg ( $\pm 0.1$  mg) of each formulation were weighed into 25  $\mu\text{L}$  aluminum crucibles and closed with an aluminum lid. An empty crucible was used as reference. Measurements were conducted on a STA 449 F1 Jupiter instrument from Netzsch, rising the temperature from 25-200 °C with a heating rate of 5 K/min. For analysis of the DSC plots, the onset of the exothermal peak was evaluated by laying tangents and intersecting them. Heat of reaction was determined through the integration of heat flow over the exothermal peak. All measurements were conducted in duplicates and the results were averaged.

The released heat during the polymerization can be used to determine the epoxy group conversion, with the theoretical polymerization enthalpy of epoxy monomers, using equation (6) from 1.3.1. After the DSC measurements, the obtained polymers were taken out of the crucible and prepared for ATR-IR measurements as stated in 2.3.2.

## 2.4.5. Rheology and Storage stability

### 2.4.5.1. Rheology measurements

Formulations for rheology measurements were prepared as stated in 2.4.4 containing the epoxy monomers **TMPTG**, **ISE**, **DGEVA**, **RDGE** and **PHTE** as well as 50 mol% (in respect to reactive groups) of **TMP** (Table 46).

Table 46: Composition of formulations for rheology measurements.

	<b>m<sub>Epoxy-Monomer</sub> [mg]</b>	<b>m<sub>TMP</sub> [mg]</b>
<b>TMPTG:TMP</b>	302.1	133.7
<b>ISE:TMP</b>	387.2	134.0
<b>DGEVA:TMP</b>	212.9	72.31
<b>RDGE:TMP</b>	224.2	88.10
<b>PHTE:TMP</b>	235.2	108.1

Rheology measurements were conducted on a modular compact rheometer MCR 300 by Physica Anton Paar. Viscosity of the formulations was measured from 60–100 °C with a CP-25 measuring system (diameter 25 mm), a gap of 48 µm and a constant shear rate of 100 s<sup>-1</sup>.

### 2.4.5.2. Storage stability of polyaddition formulations

Formulations for the stability were prepared as stated in 2.4.4 containing the epoxy monomers **TMPTG**, **ISE**, **DGEVA**, **RDGE** and **PHTE** as well as 50 mol% (in respect to reactive groups) of **TMP** (Table 47) and 1 wt% of imidazole.

Table 47: Composition of formulations for the storage stability study.

	<b>m<sub>Epoxy-Monomer</sub> [mg]</b>	<b>m<sub>TMP</sub> [mg]</b>	<b>m<sub>IM</sub> [mg]</b>
<b>TMPTG:TMP</b>	1209	534.4	17.49
<b>ISE:TMP</b>	776.2	270.2	10.61
<b>DGEVA:TMP</b>	1065	357.9	14.27
<b>RDGE:TMP</b>	888.9	357.7	12.51
<b>PHTE:TMP</b>	883.2	402.9	12.84

The formulations were stored at room temperature for 1 month and their viscosity was measured at predetermined time points (0, 1, 3, 5, 7, 10, 14, 21, 28 days). Rheology measurements were conducted on a modular compact rheometer MCR 300 by Physica Anton Paar. After 5 min of acclimatization time, the viscosity of the formulations was measured at 60 °C with a CP-25 measuring system (diameter 25 mm), a gap of 48 µm and a constant shear rate of 100 s<sup>-1</sup>.

#### **2.4.6. Thermomechanical properties of polyaddition polymers**

Formulations from chapter 2.4.4 were used for the preparation of DMTA specimens. Homogenized formulations were poured into silicon molds (2x5x40 mm<sup>3</sup>) and cured in a drying oven at 90 °C for 16-18 h. After cooling down to room temperature, the specimens were sanded to remove surface imperfections and thereafter stored under inert atmosphere. Epoxy group conversion was determined as described in chapter 2.3.2 and DMTA measurements were conducted as in chapter 2.3.3.

#### **2.4.7. Tensile tests of polyaddition polymers**

Tensile tests specimens of shape 5B were prepared from the DMTA-formulations in chapter 2.4.6 and the measurements were conducted as previously described in chapter 1.4.2.

### 3 Interpenetrating Polymer Networks (IPNs)

#### 3.1. Initiation and co-reactivity study

##### 3.1.1. Proton NMR study

In order to exclude initiation of the UV-curable methacrylates by the thermal initiator imidazole, a model substance (benzyl methacrylate, **BMA**) was reacted with 1 wt% of imidazole. Formulations of 1g (100 wt% BMA, 1 wt% imidazole) were stirred at 60 °C in a heated aluminum block. 1 sample per formulation was prepared for proton NMR analysis by diluting the resins with ~0.5 mL  $d_6$ -DMSO. Every 10 min, a sample was prepared for proton NMR analysis as stated above and analyzed *via* 400 MHz NMR spectroscopy.

Determination of the methacrylate peak conversion was calculated using equation ( 8 ).

##### 3.1.2. Photo-DSC study

Photo-DSC measurements using **RDGE**, **TMP** and **IBMA** were performed similar to 1.3.1 with 1 wt% TPO-L and 1 wt% of imidazole at 60 °C.

#### 3.2. Form-stability of IPNs

Formulations containing the epoxy matrix RDGE:TMP were mixed with the soft matrix (20IBMA80PEG) to form IPNs. The composition of the soft matrix was varied, adding 0, 20 and 50 wt% of the reactive diluent IBMA to the neat PEG20kMA (Table 48, Table 49, Table 50).

*Table 48: IPNs containing RDGE:TMP as hard matrix monomers and a soft matrix consisting of 100% PEG20kMA*

	soft matrix (100 w% PEG20kMA)			hard matrix (RDGE:TMP)		
	$m_{IBMA}$ [mg]	$m_{PEG20kMA}$ [mg]	$m_{TPO-L}$ [mg]	$m_{RDGE}$ [mg]	$m_{TMP}$ [mg]	$m_{IM}$ [mg]
IPN15PEG	0	164.97	2.11	667.20	268.10	9.37
IPN30PEG	0	270.17	3.12	445.10	180.21	6.21
IPN45PEG	0	320.17	3.12	334.20	134.01	4-72



Table 49: IPNs containing RDGE:TMP as hard matrix monomers and a soft matrix consisting of 80% PEG20kMA and 20 w% IBMA

	soft matrix (80 w% PEG20kMA, 20 w% IBMA)			hard matrix (RDGE:TMP)		
	m <sub>IBMA</sub> [mg]	m <sub>PEG20kMA</sub> [mg]	m <sub>TPO-L</sub> [mg]	m <sub>RDGE</sub> [mg]	m <sub>TMP</sub> [mg]	m <sub>IM</sub> [mg]
IPN15PEG	32.20	132.10	2.81	667.20	271.12	9.40
IPN30PEG	54.0	212.8	3.21	445.21	178.24	6.01
IPN45PEG	64.72	257.93	3.12	332.20	134.17	4.74

Table 50: IPNs containing RDGE:TMP as hard matrix monomers and a soft matrix consisting of 50% PEG20kMA and 50 w% IBMA

	soft matrix (50 w% PEG20kMA, 50 w% IBMA)			hard matrix (RDGE:TMP)		
	m <sub>IBMA</sub> [mg]	m <sub>PEG20kMA</sub> [mg]	m <sub>TPO-L</sub> [mg]	m <sub>RDGE</sub> [mg]	m <sub>TMP</sub> [mg]	m <sub>IM</sub> [mg]
IPN15PEG	82.51	82.49	2.21	668.21	268.02	9.40
IPN30PEG	134.60	131.74	3.12	444.19	178.71	6.19
IPN45PEG	162.11	161.79	3.21	333.19	135.42	4.62

Preparation was done as follows: all monomers were weighed into amber glass vials, heated to 60 °C in a water bath to melt solid components and vortexed. Afterwards, 1 wt% of the catalyst imidazole and the PI TPO-L were added, the liquid mixture was mixed and furthermore degassed for 5 minutes in an ultrasonic bath.

Thereafter, the liquid resins were poured into silicon molds for DMTA specimens (2x5x40 mm<sup>3</sup>) and cured in via a two-step procedure: the UV-curable methacrylate matrix was irradiated in a Lumamat 100 light oven, provided by Ivoclar Vivadent AG, with 6 Osram Dulux L Blue 18 W lamps. The emitted wavelength spectrum of this oven ranges from 400-580 nm at a measured total intensity of ~20 mW/cm<sup>2</sup>. Samples were cured on both sides in a transparent silicon mold for 10 min.

The form-stability of the soft matrix was examined by taking the green bodies out of the mold with a spatula. Afterwards, the IPNs were thermally cured in a 90 °C curing oven for 16-18 h.

### 3.3. Investigation of Investigation of (thermo)mechanical properties of IPNs

DMTA and tensile test specimens were prepared as described in 3.2. from the formulations depicted in Table 51, Table 52, Table 53 and Table 54.

Table 51: IPNs containing ISE:TMP as hard matrix monomers and a soft matrix consisting of 80% PEG20kMA and 20 w% IBMA.

	soft matrix (80 w% PEG20kMA, 20 w% IBMA)			hard matrix (ISE:TMP)		
	m <sub>IBMA</sub> [mg]	m <sub>PEG20kMA</sub> [mg]	m <sub>TPO-L</sub> [mg]	m <sub>ISE</sub> [mg]	m <sub>TMP</sub> [mg]	m <sub>IM</sub> [mg]
IPN10ISE	77.28	309.12	4.01	2582.99	894.22	32.99
IPN15ISE	122.72	490.91	6.13	2583.02	893.78	34.81
IPN30ISE	298.05	1192.21	14.90	2584.01	893.89	35.00
IPN45ISE	398.29	1593.18	19.91	1808.01	626.13	24.12

Table 52: IPNs containing RDGE:TMP as hard matrix monomers and a soft matrix consisting of 80% PEG20kMA and 20 w% IBMA.

	soft matrix (80 w% PEG20kMA, 20 w% IBMA)			hard matrix (RDGE:TMP)		
	m <sub>IBMA</sub> [mg]	m <sub>PEG20kMA</sub> [mg]	m <sub>TPO-L</sub> [mg]	m <sub>RDGE</sub> [mg]	m <sub>TMP</sub> [mg]	m <sub>IM</sub> [mg]
IPN10RDGE	69.26	277.11	3.01	2222.52	894.91	32.00
IPN15RDGE	122.72	490.91	6.13	2222.41	893.59	33.71
IPN30RDGE	267.12	1086.59	14.01	2222.12	894.19	31.19
IPN45RDGE	510.03	2040.12	26.02	2221.89	894.13	34.12

Table 53: IPNs containing DGEVA:TMP as hard matrix monomers and a soft matrix consisting of 80% PEG20kMA and 20 w% IBMA.

	soft matrix (80 w% PEG20kMA, 20 w% IBMA)			hard matrix (DGEVA:TMP)		
	m <sub>IBMA</sub> [mg]	m <sub>PEG20kMA</sub> [mg]	m <sub>TPO-L</sub> [mg]	m <sub>DGEVA</sub> [mg]	m <sub>TMP</sub> [mg]	m <sub>IM</sub> [mg]
IPN10DGEVA	63.24	316.22	3.19	2129.88	717.01	27.99
IPN15DGEVA	100.44	400.98	5.02	2130.00	716.32	28.49
IPN30DGEVA	243.93	975.71	12.12	2130.17	715.99	28.00
IPN45DGEVA	407.48	1629.92	20.37	1846.02	625.97	24.30

Table 54: IPNs containing PHTE:TMP as hard matrix monomers and a soft matrix consisting of 80% PEG20kMA and 20 w% IBMA.

	soft matrix (80 w% PEG20kMA, 20 w% IBMA)			hard matrix (PHTE:TMP)		
	$m_{IBMA}$ [mg]	$m_{PEG20kMA}$ [mg]	$m_{TPO-L}$ [mg]	$m_{PHTE}$ [mg]	$m_{TMP}$ [mg]	$m_{IM}$ [mg]
IPN10PHTE	61.89	247.67	3.09	1913.13	872.68	28.03
IPN15PHTE	98.29	393.17	4.94	1912.56	873.14	27.99
IPN30PHTE	238.72	954.90	12.07	1913.08	872.22	27.94
IPN45PHTE	420.66	1682.80	21.03	1766.04	805.26	25.73

### 3.3.1. DMTA-Analysis

DMTA measurements were performed according to chapter 2.3.3.

### 3.3.2. Tensile tests

Tensile test specimens were prepared from the same formulations as DMTA specimens in chapter 3.3.1 and performed similar to chapter 1.4.2.

## Abbreviations

AMT	Additive Manufacturing Technology
1MIM	1-methylimidazole
3D	3 dimensional
AC	activated chain end mechanism
AFCT	addition fragmentation chain transfer
AM	activated monomer mechanism
BADGE	bisphenol-A diglycidyl ether
BHT	butylhydroxytoluol
BMA	benzyl methacrylate
CAD	computer-aided-design
CTA	chain transfer agent
Da	Dalton
DB	double bond
DBC	double bond conversion
DBN	1,5-diazabicyclo[4.3.0]non-5-en
DCM	dichloromethane
DETA	diethylenetriamine
DGEVA	diglycidyl ether of vanillyl alcohol
DLP	digitallight processing
DMA	dimethyl aniline
DMAMP	o-[(Dimethylamino)methyl]phenol
DMAP	dimethyl aminopyridine
DMTA	dynamic mechanical analysis
DSC	differential scanning calorimetry
ECC	3,4-epoxycyclohexylmethyl-3,4-epoxycyclohexylcarboxylate
EGC	epoxy group conversion
eq	equivalent
Et <sub>3</sub> N	triethyl amine
FDM	fused deposition modelling
FT-IR	fourier transformed infrared
G'	storage modulus
G''	loss modulus
GPC	gel permeation chromatogaphy
HDDA	hexanediol diacrylate
HFIP	1,1,1,3,3,3-hexafluoroisopropanol
HPHA	hexahydrophthalic anhydride
IBA	isobornyl acrylate
IBMA	isobornyl methacrylate
IM	imidazole

IPN	interpenetrating polymer network
IR	infrared
IS	isosorbide
ISAI	diallyl isosorbide
ISE	isosorbide diepoxide
kDa	kilo Dalton
L-AMT	lithography-based AMT
LED	light emission diode
m-CPBA	m-chloroperbenzoic acid
$M_n$	number average molecular weight
MPD	m-phenylenediamine
$M_w$	molecular weight
NMR	nuclear magnetic resonance
PA	phthalic acid anhydride
PACM	4,4-diaminodicyclohexylmethane
PAG	photoacid generator
PE	polyethylene
PEG	poly(ethylene glycol)
PEG20kMA	poly(ethylene glycol) dimethacrylate, 20 kDa
PEGDMA	poly(ethylene glycol) dimethacrylate
PHTE	phloroglucinol triepoxide
PI	photoinitiator
RDGE	resorcinol diglycidyl ether
$R_p$	rate of polymerization
RT-NIR	real time near infrared
SEC	size exclusion chromatography
SLA	stereolithography
SLS	selective laser sintering
$\tan\delta$	loss factor
TBAB	tetrabutylammonium bromide
TDMAMP	2,4,6-Tris[(dimethylamino)methyl]phenol
TEA	triethyl amine
TEAB	tetraethylammonium bromide
TEBAC	benzyl triethylammonium chloride
TEGDMA	triethylenglykol dimethacrylat
$T_G$	glass transition temperature
$t_g$	time until gelation
THF	tetrahydrofuran
TMDP	2-chloro-4,4,5,5-tetramethyl-1,3,2-dioxaphospholane
TMG	1,1,3,3-tetramethylguanidine
TMP	trimethylolpropane

TMPTA	trimethylolpropane triacrylate
TMPTG	trimethylolpropane triglycidyl ether
TPO-L	ethyl (2,4,6-trimethylbenzoyl) phenylphosphinate
UDMA	urethane methacrylate
$U_T$	tensile toughness
UV	ultraviolet
UVI6976	triarylsulfonium hexafluoroantimonate salts in propylene carbonate
VIS	visible
$\Delta H_p$	heat of polymerization
$\epsilon_B$	elongation at break
$\sigma_M$	maximum tensile strength

## Materials and Methods

All chemicals, that were necessary for the synthesis of the final products and were commercially available are listed below, together with their commercial supplier. Unless otherwise noted, all chemicals were used without further treatment. Solvents and reagents were, unless otherwise noted, applied in a quality that is common for organic synthesis. Commercially grade methylene chloride ( $\text{CH}_2\text{Cl}_2$ , Donauchemie) and tetrahydrofuran (THF, Donau Chemie) were dried using a PureSolv system (Inter, Amesbury, MA).

Polyethylene glycol	Sigma Aldrich
1,1,3,3-Tetramethylguanidin	Fluka
1,6-Hexanediol	Fluka
1-Methyl imidazole	Sigma Aldrich
2-chloro-4,4,5,5-tetramethyl-1,3,2-dioxaphospholane	Sigma Aldrich
Allyl bromide	TCI Chemicals
Chloroform-d	Euriotop
Cyclohexanol	Sigma Aldrich
Diazabicyclo[4.3.0]non-5-en	Fluka
Diethylether	Donauchemie
Dimethyl Aminopyridine	Sigma Aldrich
DMSO-d <sub>6</sub>	Eurisotop
Epichlorohydrin	Sigma Aldrich
Ethyl acetate	Donauchemie
Imidazole	Fluka
Isobornyl Methacrylate	Sartomer
Isosorbide	TCI Chemicals
m-Chloroperbenzoic acid	Sigma-Aldrich
Methacrylic Anhydride	Sigma Aldrich
Methylene chloride	Donauchemie
Petroleum ether	Donauchemie
Phloroglucinol	Sigma Aldrich
Polyethylene glycol dimethacrylate	Sigma Aldrich
Potassium tert-butoxide	TCI Chemicals
Pyridine	Sigma Aldrich
Resorcinol	Sigma Aldrich
Resorcinol Diglycidyl Ether	NAGASE
Sodium bicarbonate	Donauchemie
Sodium hydroxide	Merck
Sodium sulfate	VWR
Sodium thiosulfate	Merck
Speedcure TPO-L	Lambson

Tetrabutyl ammonium bromide	TCI Chemicals
Tetrabutylammonium chloride	TCI Chemicals
Tetraethylammonium bromide	TCI Chemicals
Tetrahydrofuran	Donauchemie
Triethylamine	Sigma Aldrich
Trimethylolpropane	ACROS
Trimethylolpropane Triglycidyl Ether	Sigma Aldrich
UVI6976	DOW
Vanillyl Alcohol	TCI Chemicals

**ATR-IR** experiments of the cured sample were performed on a PerkinElmer Spectrum 65 FT-IR Spectrometer, using a Specac MKII Golden Gate Single Reflection ATR System.

**Column chromatography** was performed on a Büchi Sepacore Flash System (Büchi pump module C-605, Büchi control unit C-620, Büchi UV-Photometer C-635, Büchi fraction collector C-660), using glass columns, packed with silica gel 60 (Merck, 0.040-0.063 mm) or aluminum oxide 90 neutral (Carl Roth).

**DMTA** measurements were performed with an Anton Paar MCR 301 with a CTD 450 oven if not stated differently. DMTA measurement in 3-point bending mode were conducted on a DMTA 2980 from TA instruments.

**Gel permeation analysis (GPC)** was performed with a Waters GPC, with three columns connected in series (Styragel HR 0.5, Styragel HR 3 and Styragel HR4) and three attached detectors (Waters 2410 RI, UV Detector Module 2550 for TDA 305, VISCOTEK SEC-MALS 9 for light scattering). Molecular weight of the polymers was examined using conventional calibration with polystyrene standards of 375 – 177 000 Da. OmniSEC 5.12 from Malvern was used for data analysis.

**Melting points** were determined with an Optimelt devise from SRS Stanford Research Systems.

**NMR** spectra were recorded on a Bruker DPX-200 FT-NMR spectrometer at 200 MHz for  $^1\text{H}$  and 50 MHz for  $^{13}\text{C}$ , as well as on a Bruker Avance DRX-400 FT-NMR spectrometer at 400 MHz for  $^1\text{H}$  and 100 MHz for  $^{13}\text{C}$ . The signals are recorded according to their chemical shifts, which were reported in ppm (s = singlet, d = doublet, t = triplet, q = quartet, qn = quintet, sep = septet, m = multiplet, bs = broad singlet) in comparison to tetramethylsilane (d = 0 ppm). Deuterated chloroform  $\text{CDCl}_3$  or deuterated  $\text{d}_6$ -DMSO were used as NMR- solvents. All spectra were analyzed using the software MestreNova 12.0.4 by Mestrelab research.



**Photo-DSC measurements** were conducted on a Photo-DSC 204 F1 from Netzsch, using 15  $\mu\text{L}$  aluminum pans. An Omnicure 2000 from Lumen Dynamics with glass fiber light wave guides was used as light source, which was calibrated *via* an Omnicure R2000 radiometer. All measurements were conducted under  $\text{N}_2$ -atmosphere (flow rate: 20  $\text{mL min}^{-1}$ ). The data analysis was performed with the program Netzsch Proteus Thermal Analysis in version 8.0.1.

**Preparation of the test specimens** All formulations for test specimens were prepared in the orange light laboratory. Wavelengths below 480 nm were filtered with adhesive window foils. Curing of the specimens was performed in an Uvitron INTELLI- RAY 600 UV-oven with a 320-500 nm Hg broadband lamp (600 W; UV-A: 125  $\text{mW cm}^{-2}$ ; vis: 125  $\text{mW cm}^{-2}$ ) or in a Lumamat 100 light oven (provided by Ivoclar Vivadent), using 6 Osram Dulux L Blue 18 W lamps (400-580 nm).

**Rheology** was measured on a Anton Paar MCR 300 rheometer with a Peltier PTD 150 system and a CP-25 measuring system. The software used for evaluation was RheoPlus v3.40.

**STA** was conducted on a Netzsch Jupiter STA 449 F1 thermal analysis instrument with auto sampler.

**Tensile tests** were conducted employing a Zwick Z050 with a maximum test force of 50 kN. The recorded data was processed and evaluated via the software TestXpert II.

**Thin layer chromatography** (TLC) was performed on aluminum TLC-plates coated with silica gel 60 F245 (supplier: Merck).

## References

1. Ligon, S. C.; Liska, R.; Stampfl, J.; Gurr, M.; Mülhaupt, R., Polymers for 3D Printing and Customized Additive Manufacturing. *Chemical Reviews* **2017**, *117* (15), 10212-10290.
2. Gebhardt, A.; Hötter, J. S., *Additive Manufacturing: 3D Printing for Prototyping and Manufacturing*. Carl Hanser Verlag GmbH & Company KG: 2016.
3. Raos, P.; Klapan, I.; Galeta, T., Additive Manufacturing of Medical Models--Applications in Rhinology. *Collegium antropologicum* **2015**, *39*, 667-673.
4. Wohlers, T. T. C. T., *Wohlers report 2015 : 3D printing and additive manufacturing state of the industry annual worldwide progress report*. Wohlers Associates: Fort Collins, Colo., 2015.
5. Medelli'n-Castillo, H. I.; Pedraza Torres, J. E., Rapid Prototyping and Manufacturing: A Review of Current Technologies. In *ASME 2009 International Mechanical Engineering Congress and Exposition*, 2009; pp 609-621.
6. Kruth, J. P.; Wang, X.; Laoui, T.; Froyen, L., Lasers and materials in selective laser sintering. *Assembly Automation* **2003**, *23* (4), 357-371.
7. Voet, V. S. D.; Guit, J.; Loos, K., Sustainable Photopolymers in 3D Printing: A Review on Biobased, Biodegradable, and Recyclable Alternatives. *Macromolecular Rapid Communications* **2020**, *n/a* (n/a), 2000475.
8. Appuhamillage, G. A.; Chartrain, N.; Meenakshisundaram, V.; Feller, K. D.; Williams, C. B.; Long, T. E., 110th Anniversary: Vat Photopolymerization-Based Additive Manufacturing: Current Trends and Future Directions in Materials Design. *Industrial & Engineering Chemistry Research* **2019**, *58* (33), 15109-15118.
9. Ligon-Auer, S. C.; Schwentenwein, M.; Gorsche, C.; Stampfl, J.; Liska, R., Toughening of photo-curable polymer networks: a review. *Polymer Chemistry* **2016**, *7* (2), 257-286.
10. Costumpart.net <https://www.custompartnet.com/wu/stereolithography> (accessed 24.11.2021).
11. Gmeiner, R.; Mitteramskogler, G.; Stampfl, J.; Boccaccini, A. R., Stereolithographic Ceramic Manufacturing of High Strength Bioactive Glass. *International Journal of Applied Ceramic Technology* **2015**, *12* (1), 38-45.
12. Lalevée, J.; Fouassier, J. P., *Photopolymerisation Initiating Systems*. Royal Society of Chemistry: 2018.
13. Fouassier, J. P.; Allonas, X.; Burget, D., Photopolymerization reactions under visible lights: principle, mechanisms and examples of applications. *Progress in Organic Coatings* **2003**, *47* (1), 16-36.
14. Yagci, Y.; Jockusch, S.; Turro, N. J., Photoinitiated Polymerization: Advances, Challenges, and Opportunities. *Macromolecules* **2010**, *43* (15), 6245-6260.
15. Jenkins, A. D.; Kratochvíl, P.; Stepto, R. F. T.; Suter, U. W., Glossary of basic terms in polymer science (IUPAC Recommendations 1996). *Pure and Applied Chemistry* **1996**, *68* (12), 2287-2311.
16. Wu, J.; Eduard, P.; Thiyagarajan, S.; van Haveren, J.; van Es, D. S.; Koning, C. E.; Lutz, M.; Fonseca Guerra, C., Isohexide Derivatives from Renewable Resources as Chiral Building Blocks. *ChemSusChem* **2011**, *4* (5), 599-603.
17. Matyjaszewski, K.; Gaynor, S. G., FREE RADICAL POLYMERIZATION. In *Applied Polymer Science: 21st Century*, Craver, C. D.; Carraher, C. E., Eds. Pergamon: Oxford, 2000; pp 929-977.
18. Green, W. A., *Industrial Photoinitiators: A Technical Guide*. CRC Press: 2010.
19. Dietliker, K.; Jung, T.; Benkhoff, J.; Kura, H.; Matsumoto, A.; Oka, H.; Hristova, D.; Gescheidt, G.; Rist, G., New Developments in Photoinitiators. *Macromolecular Symposia* **2004**, *217* (1), 77-98.
20. Moszner, N.; Fischer, U. K.; Ganster, B.; Liska, R.; Rheinberger, V., Benzoyl germanium derivatives as novel visible light photoinitiators for dental materials. *Dent Mater* **2008**, *24* (7), 901-7.

21. Qin, X.-H.; Ovsianikov, A.; Stampfl, J.; Liska, R., Additive manufacturing of photosensitive hydrogels for tissue engineering applications. *BioNanoMaterials* **2014**, *15* (3-4), 49-70.
22. Moad, G.; Solomon, D. H., *The Chemistry of Radical Polymerization*. Elsevier Science: 2006.
23. Gorsche, C.; Seidler, K.; Knaack, P.; Dorfinger, P.; Koch, T.; Stampfl, J.; Moszner, N.; Liska, R., Rapid formation of regulated methacrylate networks yielding tough materials for lithography-based 3D printing. *Polymer Chemistry* **2016**, *7* (11), 2009-2014.
24. Studer, K.; Decker, C.; Beck, E.; Schwalm, R., Overcoming oxygen inhibition in UV-curing of acrylate coatings by carbon dioxide inerting, Part I. *Progress in Organic Coatings* **2003**, *48* (1), 92-100.
25. Crivello, J. V.; Dietliker, K., *Photoinitiators for free radical cationic and anionic photopolymerisation*. John Wiley & Sons, Ltd: 2000; Vol. 49, p 1729-1729.
26. Crivello, J. V.; Lam, J. H. W., Diaryliodonium Salts. A New Class of Photoinitiators for Cationic Polymerization. *Macromolecules* **1977**, *10* (6), 1307-1315.
27. Crivello, J. V.; Lam, J. H. W., Photoinitiated cationic polymerization with triarylsulfonium salts. *Journal of Polymer Science: Polymer Chemistry Edition* **1979**, *17* (4), 977-999.
28. Crivello, J. V., The discovery and development of onium salt cationic photoinitiators. *Journal of Polymer Science Part A: Polymer Chemistry* **1999**, *37* (23), 4241-4254.
29. Dadashi-Silab, S.; Doran, S.; Yagci, Y., Photoinduced Electron Transfer Reactions for Macromolecular Syntheses. *Chemical Reviews* **2016**, *116* (17), 10212-10275.
30. Bulut, U.; Crivello, J. V., Investigation of the Reactivity of Epoxide Monomers in Photoinitiated Cationic Polymerization. *Macromolecules* **2005**, *38* (9), 3584-3595.
31. Sipani, V.; Scranton, A. B., Dark-cure studies of cationic photopolymerizations of epoxides: Characterization of the active center lifetime and kinetic rate constants. *Journal of Polymer Science Part A: Polymer Chemistry* **2003**, *41* (13), 2064-2072.
32. Decker, C.; Moussa, K., Kinetic study of the cationic photopolymerization of epoxy monomers. *Journal of Polymer Science Part A: Polymer Chemistry* **1990**, *28* (12), 3429-3443.
33. Dillman, B.; Jessop, J. L. P., Chain transfer agents in cationic photopolymerization of a bis-cycloaliphatic epoxide monomer: Kinetic and physical property effects. *Journal of Polymer Science Part A: Polymer Chemistry* **2013**, *51* (9), 2058-2067.
34. Dall'Argine, C.; Hochwallner, A.; Klikovits, N.; Liska, R.; Stampf, J.; Sangermano, M., Hot-Lithography SLA-3D Printing of Epoxy Resin. *Macromolecular Materials and Engineering* **2020**, *305* (10), 2000325.
35. Crivello, J. V.; Falk, B.; Zonca Jr, M. R., Photoinduced cationic ring-opening frontal polymerizations of oxetanes and oxiranes. *Journal of Polymer Science Part A: Polymer Chemistry* **2004**, *42* (7), 1630-1646.
36. Sangermano, M., Advances in cationic photopolymerization. *Pure and Applied Chemistry* **2012**, *84* (10), 2089-2101.
37. O'Connor, J. C.; Chapin, R. E., Critical evaluation of observed adverse effects of endocrine active substances on reproduction and development, the immune system, and the nervous system. *Pure and Applied Chemistry* **2003**, *75* (11-12), 2099-2123.
38. Lawrence, W. H.; Malik, M.; Turner, J. E.; Autian, J., Toxicity Profile of Epichlorohydrin. *Journal of Pharmaceutical Sciences* **1972**, *61* (11), 1712-1717.
39. Spurr, A. R., A low-viscosity epoxy resin embedding medium for electron microscopy. *Journal of Ultrastructure Research* **1969**, *26* (1), 31-43.
40. Liu, W.; Wang, Z.; Xiong, L.; Zhao, L., Phosphorus-containing liquid cycloaliphatic epoxy resins for reworkable environment-friendly electronic packaging materials. *Polymer* **2010**, *51* (21), 4776-4783.
41. Dušek, K.; Ilavský, M.; Luňák, S., Curing of epoxy resins. I. Statistics of curing of diepoxides with diamines. *Journal of Polymer Science: Polymer Symposia* **1975**, *53* (1), 29-44.
42. Woo, E. M.; Seferis, J. C., Cure kinetics of epoxy/anhydride thermosetting matrix systems. *Journal of Applied Polymer Science* **1990**, *40* (7-8), 1237-1256.
43. <https://polymerdatabase.com/polymer%20chemistry/Chain%20versus%20Step%20Growth.html> (accessed 26.11.2021).

44. Vidil, T.; Tournilhac, F.; Musso, S.; Robisson, A.; Leibler, L., Control of reactions and network structures of epoxy thermosets. *Progress in Polymer Science* **2016**, *62*, 126-179.
45. Rozenberg, B. A. In *Kinetics, thermodynamics and mechanism of reactions of epoxy oligomers with amines*, Epoxy Resins and Composites II, Berlin, Heidelberg, 1986//; Dušek, K., Ed. Springer Berlin Heidelberg: Berlin, Heidelberg, 1986; pp 113-165.
46. Jin, F.-L.; Li, X.; Park, S.-J., Synthesis and application of epoxy resins: A review. *Journal of Industrial and Engineering Chemistry* **2015**, *29*, 1-11.
47. Hakala, K.; Vatanparast, R.; Li, S.; Peinado, C.; Bosch, P.; Catalina, F.; Lemmetyinen, H., Monitoring of Curing Process and Shelf Life of the Epoxy-Anhydride System with TICT Compounds by the Fluorescence Technique. *Macromolecules* **2000**, *33* (16), 5954-5959.
48. Antoon, M. K.; Koenig, J. L., Crosslinking mechanism of an anhydride-cured epoxy resin as studied by fourier transform infrared spectroscopy. *Journal of Polymer Science: Polymer Chemistry Edition* **1981**, *19* (2), 549-570.
49. Gritter, R. J., Reactions of cyclic ethers. In *The Ether Linkage (1967)*, 1967; pp 373-443.
50. Yang, E.; Miao, S.; Zhong, J.; Zhang, Z.; Mills, D. K.; Zhang, L. G., Bio-Based Polymers for 3D Printing of Bioscaffolds. *Polym Rev (Phila Pa)* **2018**, *58* (4), 668-687.
51. Li, W.; Mille, L. S.; Robledo, J. A.; Uribe, T.; Huerta, V.; Zhang, Y. S., Recent Advances in Formulating and Processing Biomaterial Inks for Vat Polymerization-Based 3D Printing. *Advanced Healthcare Materials* **2020**, *9* (15), 2000156.
52. Meier, M. A. R.; Metzger, J. O.; Schubert, U. S., Plant oil renewable resources as green alternatives in polymer science. *Chemical Society Reviews* **2007**, *36* (11), 1788-1802.
53. Noè, C.; Malburet, S.; Bouvet-Marchand, A.; Graillet, A.; Loubat, C.; Sangermano, M., Cationic photopolymerization of bio-renewable epoxidized monomers. *Progress in Organic Coatings* **2019**, *133*, 131-138.
54. Guit, J.; Tavares, M. B. L.; Hul, J.; Ye, C.; Loos, K.; Jager, J.; Folkersma, R.; Voet, V. S. D., Photopolymer Resins with Biobased Methacrylates Based on Soybean Oil for Stereolithography. *ACS Applied Polymer Materials* **2020**, *2* (2), 949-957.
55. Branciforti, D. S.; Lazzaroni, S.; Milanese, C.; Castiglioni, M.; Auricchio, F.; Pasini, D.; Dondi, D., Visible light 3D printing with epoxidized vegetable oils. *Additive Manufacturing* **2019**, *25*, 317-324.
56. Liang, B.; Li, R.; Zhang, C.; Yang, Z.; Yuan, T., Synthesis and characterization of a novel tri-functional bio-based methacrylate prepolymer from castor oil and its application in UV-curable coatings. *Industrial Crops and Products* **2019**, *135*, 170-178.
57. Hu, Y.; Shang, Q.; Bo, C.; Jia, P.; Feng, G.; Zhang, F.; Liu, C.; Zhou, Y., Synthesis and Properties of UV-Curable Polyfunctional Polyurethane Acrylate Resins from Cardanol. *ACS Omega* **2019**, *4* (7), 12505-12511.
58. Breitmaier, E., Terpenes: Importance, General Structure, and Biosynthesis. In *Terpenes*, 2006; pp 1-9.
59. Kukhta, N. A.; Vasilenko, I. V.; Kostjuk, S. V., Room temperature cationic polymerization of  $\beta$ -pinene using modified  $AlCl_3$  catalyst: toward sustainable plastics from renewable biomass resources. *Green Chemistry* **2011**, *13* (9), 2362-2364.
60. Park, H. J.; Ryu, C. Y.; Crivello, J. V., Photoinitiated cationic polymerization of limonene 1,2-oxide and  $\alpha$ -pinene oxide. *Journal of Polymer Science Part A: Polymer Chemistry* **2013**, *51* (1), 109-117.
61. Li, J.-M.; Zhang, L.-M., Characteristics of Novel Starch-based Hydrogels Prepared by UV Photopolymerization of Acryloylated Starch and A Zwitterionic Monomer. *Starch - Stärke* **2007**, *59* (9), 418-422.
62. Woelk, H. U., Stärke als Chemierohstoff — Möglichkeiten und Grenzen. *Starch - Stärke* **1981**, *33* (12), 397-408.
63. Miao, J.-T.; Peng, S.; Ge, M.; Li, Y.; Zhong, J.; Weng, Z.; Wu, L.; Zheng, L., Three-Dimensional Printing Fully Biobased Heat-Resistant Photoactive Acrylates from Aliphatic Biomass. *ACS Sustainable Chemistry & Engineering* **2020**, *8* (25), 9415-9424.



64. Cok, B.; Tsiropoulos, I.; Roes, A. L.; Patel, M. K., Succinic acid production derived from carbohydrates: An energy and greenhouse gas assessment of a platform chemical toward a bio-based economy. *Biofuels, Bioproducts and Biorefining* **2014**, *8* (1), 16-29.
65. Robert, T.; Friebel, S., Itaconic acid – a versatile building block for renewable polyesters with enhanced functionality. *Green Chemistry* **2016**, *18* (10), 2922-2934.
66. Modjinou, T.; Versace, D.-L.; Abbad-Andallousi, S.; Bousserhine, N.; Babinot, J.; Langlois, V.; Renard, E., Antibacterial Networks Based on Isosorbide and Linalool by Photoinitiated Process. *ACS Sustainable Chemistry & Engineering* **2015**, *3* (6), 1094-1100.
67. Fertier, L.; Ibert, M.; Buffe, C.; Saint-Loup, R.; Joly-Duhamel, C.; Robin, J. J.; Giani, O., New biosourced UV curable coatings based on isosorbide. *Progress in Organic Coatings* **2016**, *99*, 393-399.
68. Mohan, D.; Teong, Z. K.; Bakir, A. N.; Sajab, M. S.; Kaco, H., Extending Cellulose-Based Polymers Application in Additive Manufacturing Technology: A Review of Recent Approaches. *Polymers* **2020**, *12* (9), 1876.
69. Ebers, L.-S.; Arya, A.; Bowland, C. C.; Glasser, W. G.; Chmely, S. C.; Naskar, A. K.; Laborie, M.-P., 3D printing of lignin: Challenges, opportunities and roads onward. *Biopolymers* **2021**, *112* (6), e23431.
70. Sutton, J. T.; Rajan, K.; Harper, D. P.; Chmely, S. C., Lignin-Containing Photoactive Resins for 3D Printing by Stereolithography. *ACS Applied Materials & Interfaces* **2018**, *10* (42), 36456-36463.
71. Fache, M.; Boutevin, B.; Caillol, S., Vanillin Production from Lignin and Its Use as a Renewable Chemical. *ACS Sustainable Chemistry & Engineering* **2016**, *4* (1), 35-46.
72. Stanzione Iii, J. F.; Sadler, J. M.; La Scala, J. J.; Wool, R. P., Lignin Model Compounds as Bio-Based Reactive Diluents for Liquid Molding Resins. *ChemSusChem* **2012**, *5* (7), 1291-1297.
73. Mohanty, A. K.; Misra, M.; Drzal, L. T., Sustainable Bio-Composites from Renewable Resources: Opportunities and Challenges in the Green Materials World. *Journal of Polymers and the Environment* **2002**, *10* (1), 19-26.
74. Kojima, Y.; Usuki, A.; Kawasumi, M.; Okada, A.; Fukushima, Y.; Kurauchi, T.; Kamigaito, O., Mechanical properties of nylon 6-clay hybrid. *Journal of Materials Research* **1993**, *8* (5), 1185-1189.
75. Pearson, R. A.; Yee, A. F., Influence of particle size and particle size distribution on toughening mechanisms in rubber-modified epoxies. *Journal of Materials Science* **1991**, *26* (14), 3828-3844.
76. Sultan, J. N.; McGarry, F. J., Effect of rubber particle size on deformation mechanisms in glassy epoxy. *Polymer Engineering & Science* **1973**, *13* (1), 29-34.
77. Hillmyer, M. A.; Lipic, P. M.; Hajduk, D. A.; Almdal, K.; Bates, F. S., Self-Assembly and Polymerization of Epoxy Resin-Amphiphilic Block Copolymer Nanocomposites. *Journal of the American Chemical Society* **1997**, *119* (11), 2749-2750.
78. Hoyle, C. E.; Lee, T. Y.; Roper, T., Thiol-enes: Chemistry of the past with promise for the future. *Journal of Polymer Science Part A: Polymer Chemistry* **2004**, *42* (21), 5301-5338.
79. Moad, G.; Rizzardo, E.; Thang, S. H., Radical addition-fragmentation chemistry in polymer synthesis. *Polymer* **2008**, *49* (5), 1079-1131.
80. Campos, L. M.; Meinel, I.; Guino, R. G.; Schierhorn, M.; Gupta, N.; Stucky, G. D.; Hawker, C. J., Highly Versatile and Robust Materials for Soft Imprint Lithography Based on Thiol-ene Click Chemistry. *Advanced Materials* **2008**, *20* (19), 3728-3733.
81. Erhard, G., *Designing with plastics*. Carl Hanser Verlag: Munich, 2006; p 34-38.
82. Sperling, L. H., Interpenetrating Polymer Networks: An Overview. In *Interpenetrating Polymer Networks*, American Chemical Society: 1994; Vol. 239, pp 3-38.
83. Sperling, L. H., *Interpenetrating Polymer Networks and Related Materials*. Springer US: 2012.
84. Fouassier, J. P.; Lalevée, J., Photochemical Production of Interpenetrating Polymer Networks; Simultaneous Initiation of Radical and Cationic Polymerization Reactions. *Polymers* **2014**, *6* (10), 2588-2610.
85. Rocco, C.; Karasu, F.; Croutxé-Barghorn, C.; Allonas, X.; Lecomère, M.; Riess, G.; Zhang, Y.; Esteves, A. C. C.; van der Ven, L. G. J.; van Benthem, R. A. T. M.; de With, G.,

Highly-interpenetrated and phase-separated UV-cured interpenetrating methacrylate–epoxide polymer networks: Influence of the composition on properties and microstructure. *Materials Today Communications* **2016**, *6*, 17-27.

86. Decker, C.; Nguyen Thi Viet, T.; Decker, D.; Weber-Koehl, E., UV-radiation curing of acrylate/epoxide systems. *Polymer* **2001**, *42* (13), 5531-5541.

87. Decker, C.; Decker, D., Photoinitiated Polymerization of Vinyl Ether and Acrylate Monomer Mixtures. *Journal of Macromolecular Science, Part A* **1997**, *34* (4), 605-625.

88. Huang, Y.-M.; Lan, H.-Y., Compensation of distortion in the bottom exposure of stereolithography process. *The International Journal of Advanced Manufacturing Technology* **2006**, *27* (11), 1101-1112.

89. Ratna, D.; Dalvi, V. G.; Billa, S.; Sharma, S. K.; Rath, S. K.; Sudarshan, K.; Pujari, P. K., Interpenetrating Polymer Network of Rubbery Epoxy and Glassy PMMA: Network Inhomogeneities and Dynamic Heterogeneities. *ACS Applied Polymer Materials* **2021**, *3* (10), 5073-5086.

90. Bassett, A. W.; Honnig, A. E.; La Scala, J. J.; Stanzione Iii, J. F., Network toughening of additively manufactured, high glass transition temperature materials via sequentially cured, interpenetrating polymers. *Polymer International* **2021**, *70* (6), 749-758.

91. Jansen, B. J. P.; Rastogi, S.; Meijer, H. E. H.; Lemstra, P. J., Rubber-Modified Glassy Amorphous Polymers Prepared via Chemically Induced Phase Separation. 4. Comparison of Properties of Semi- and Full-IPNs, and Copolymers of Acrylate–Aliphatic Epoxy Systems. *Macromolecules* **1999**, *32* (19), 6290-6297.

92. Miao, S.; Zhu, W.; Castro, N. J.; Nowicki, M.; Zhou, X.; Cui, H.; Fisher, J. P.; Zhang, L. G., 4D printing smart biomedical scaffolds with novel soybean oil epoxidized acrylate. *Scientific Reports* **2016**, *6* (1), 27226.

93. Lebedevaite, M.; Ostrauskaite, J.; Skliutas, E.; Malinauskas, M., Photoinitiator Free Resins Composed of Plant-Derived Monomers for the Optical  $\mu$ -3D Printing of Thermosets. *Polymers (Basel)* **2019**, *11* (1), 116.

94. Cui, Y.; Yang, J.; Lei, D.; Su, J., 3D Printing of a Dual-Curing Resin with Cationic Curable Vegetable Oil. *Industrial & Engineering Chemistry Research* **2020**, *59* (25), 11381-11388.

95. Wu, B.; Sufi, A.; Ghosh Biswas, R.; Hisatsune, A.; Moxley-Paquette, V.; Ning, P.; Soong, R.; Dicks, A. P.; Simpson, A. J., Direct Conversion of McDonald's Waste Cooking Oil into a Biodegradable High-Resolution 3D-Printing Resin. *ACS Sustainable Chemistry & Engineering* **2020**, *8* (2), 1171-1177.

96. Noè, C.; Cosola, A.; Chiappone, A.; Hakkarainen, M.; Grützmacher, H.; Sangermano, M., From polysaccharides to UV-curable biorenewable organo/hydrogels for methylene blue removal. *Polymer* **2021**, *235*, 124257.

97. Cosola, A.; Conti, R.; Grützmacher, H.; Sangermano, M.; Roppolo, I.; Pirri, C. F.; Chiappone, A., Multiacrylated Cyclodextrin: A Bio-Derived Photocurable Macromer for VAT 3D Printing. *Macromolecular Materials and Engineering* **2020**, *305* (9), 2000350.

98. Dussenne, C.; Delaunay, T.; Wiatz, V.; Wyart, H.; Suisse, I.; Sauthier, M., Synthesis of isosorbide: an overview of challenging reactions. *Green Chemistry* **2017**, *19* (22), 5332-5344.

99. Park, H.-S.; Gong, M.-S.; Knowles, J. C., Synthesis and biocompatibility properties of polyester containing various diacid based on isosorbide. *Journal of Biomaterials Applications* **2012**, *27* (1), 99-109.

100. Kim, H.-J.; Kang, M.-S.; Knowles, J. C.; Gong, M.-S., Synthesis of highly elastic biocompatible polyurethanes based on bio-based isosorbide and poly(tetramethylene glycol) and their properties. *Journal of Biomaterials Applications* **2014**, *29* (3), 454-464.

101. Chrysanthos, M.; Galy, J.; Pascault, J.-P., Preparation and properties of bio-based epoxy networks derived from isosorbide diglycidyl ether. *Polymer* **2011**, *52* (16), 3611-3620.

102. Herrera-González, A. M.; Pérez-Mondragón, A. A.; Cuevas-Suárez, C. E., Evaluation of bio-based monomers from isosorbide used in the formulation of dental composite resins. *Journal of the Mechanical Behavior of Biomedical Materials* **2019**, *100*, 103371.

103. Owji, N.; Aldaadaa, A.; Cha, J.-R.; Shakouri, T.; García-Gareta, E.; Kim, H.-W.; Knowles, J. C., Synthesis, Characterization, and 3D Printing of an Isosorbide-Based, Light-

Curable, Degradable Polymer for Potential Application in Maxillofacial Reconstruction. *ACS Biomaterials Science & Engineering* **2020**, 6 (5), 2578-2587.

104. Guo, Z.-X.; Gandini, A., Polyesters from lignin—2. The copolyesterification of kraft lignin and polyethylene glycols with dicarboxylic acid chlorides. *European Polymer Journal* **1991**, 27 (11), 1177-1180.

105. Gandini, A.; Belgacem, M. N.; Guo, Z.-X.; Montanari, S., Lignins as Macromonomers for Polyesters and Polyurethanes. In *Chemical Modification, Properties, and Usage of Lignin*, Hu, T. Q., Ed. Springer US: Boston, MA, 2002; pp 57-80.

106. Nonaka, Y.; Tomita, B.; Hatano, Y., Synthesis of Lignin /Epoxy Resins in Aqueous Systems and Their Properties. *Holzforschung* **1997**, 51 (2), 183-187.

107. Zhang, X.; Keck, S.; Qi, Y.; Baudis, S.; Zhao, Y., Study on Modified Dealkaline Lignin as Visible Light Macromolecular Photoinitiator for 3D Printing. *ACS Sustainable Chemistry & Engineering* **2020**, 8 (29), 10959-10970.

108. Bassett, A. W.; Honnig, A. E.; Breyta, C. M.; Dunn, I. C.; La Scala, J. J.; Stanzione, J. F., Vanillin-Based Resin for Additive Manufacturing. *ACS Sustainable Chemistry & Engineering* **2020**, 8 (14), 5626-5635.

109. Ding, R.; Du, Y.; Goncalves, R. B.; Francis, L. F.; Reineke, T. M., Sustainable near UV-curable acrylates based on natural phenolics for stereolithography 3D printing. *Polymer Chemistry* **2019**, 10 (9), 1067-1077.

110. Navaruckiene, A.; Kasetaitė, S.; Ostrauskaite, J., Vanillin-based thiol-ene systems as photoresins for optical 3D printing. *Rapid Prototyping Journal* **2019**, 26 (2), 402-408.

111. Aylsworth, J. W. Electrical-insulation composition and method of preparing the same. 1914.

112. Millar, J. R., 263. Interpenetrating polymer networks. Styrene–divinylbenzene copolymers with two and three interpenetrating networks, and their sulphonates. *Journal of the Chemical Society (Resumed)* **1960**, (0), 1311-1317.

113. Frisch, H. L.; Klempner, D.; Frisch, K. C., A topologically interpenetrating elastomeric network. *Journal of Polymer Science Part B: Polymer Letters* **1969**, 7 (11), 775-779.

114. Shibayama, K.; Suzuki, Y., Viscoelastic Properties of Multiple Network Polymers. IV. Copolymers of Styrene and Divinylbenzene. *Rubber Chemistry and Technology* **1967**, 40 (2), 476-483.

115. Silverstein, M. S., Interpenetrating polymer networks: So happy together? *Polymer* **2020**, 207, 122929.

116. Widmaier, J. M.; Sperling, L. H., Phase continuity in sequential poly(n-butyl acrylate)/polystyrene interpenetrating polymer networks. *Macromolecules* **1982**, 15 (2), 625-631.

117. Widmaier, J.-M.; Sperling, L. H., The use of labile crosslinker for morphological studies in interpenetrating polymer networks. *British Polymer Journal* **1984**, 16 (1), 46-48.

118. Macro-, Meso-, and Nanoporous Systems Designed from IPNs. In *Micro- and Nano-structured Interpenetrating Polymer Networks*, 2016; pp 127-143.

119. Sperling, L. H.; Chiu, T.-W.; Hartman, C. P.; Thomas, D. A., Latex Interpenetrating Polymer Networks. *International Journal of Polymeric Materials and Polymeric Biomaterials* **1972**, 1 (4), 331-341.

120. Sperling, L. H.; Thomas, D. A.; Lorenz, J. E.; Nagel, E. J., Synthesis and behavior of poly(vinyl chloride)-based latex interpenetrating polymer networks. *Journal of Applied Polymer Science* **1975**, 19 (8), 2225-2233.

121. Ilmain, F.; Tanaka, T.; Kokufuta, E., Volume transition in a gel driven by hydrogen bonding. *Nature* **1991**, 349 (6308), 400-401.

122. Gudeman, L. F.; Peppas, N. A., Preparation and characterization of pH-sensitive, interpenetrating networks of poly(vinyl alcohol) and poly(acrylic acid). *Journal of Applied Polymer Science* **1995**, 55 (6), 919-928.

123. Schoener, C. A.; Hutson, H. N.; Peppas, N. A., Amphiphilic Interpenetrating Polymer Networks for the Oral Delivery of Chemotherapeutics. *AIChE Journal* **2013**, 59 (5), 1472-1478.

124. Sangermano, M.; Malucelli, G.; Bongiovanni, R.; Priola, A., Photopolymerization of oxetane based systems. *European Polymer Journal* **2004**, 40 (2), 353-358.



125. Sangermano, M.; Carbonaro, W.; Malucelli, G.; Priola, A., UV-Cured Interpenetrating Acrylic-Epoxy Polymer Networks: Preparation and Characterization. *Macromolecular Materials and Engineering* **2008**, 293 (6), 515-520.
126. Lecamp, L.; Pavillon, C.; Lebaudy, P.; Bunel, C., Influence of temperature and nature of photoinitiator on the formation kinetics of an interpenetrating network photocured from an epoxide/methacrylate system. *European Polymer Journal* **2005**, 41 (1), 169-176.
127. Salmoria, G. V.; Ahrens, C. H.; Beal, V. E.; Pires, A. T. N.; Soldi, V., Evaluation of post-curing and laser manufacturing parameters on the properties of SOMOS 7110 photosensitive resin used in stereolithography. *Materials & Design* **2009**, 30 (3), 758-763.
128. Huang, B.; Du, Z.; Yong, T.; Han, W., Preparation of a novel hybrid type photosensitive resin for stereolithography in 3D printing and testing on the accuracy of the fabricated parts. *Journal of Wuhan University of Technology-Mater. Sci. Ed.* **2017**, 32 (3), 726-732.
129. Zhao, T.; Li, X.; Yu, R.; Zhang, Y.; Yang, X.; Zhao, X.; Wang, L.; Huang, W., Silicone-Epoxy-Based Hybrid Photopolymers for 3D Printing. *Macromolecular Chemistry and Physics* **2018**, 219 (10), 1700530.
130. Yu, R.; Yang, X.; Zhang, Y.; Zhao, X.; Wu, X.; Zhao, T.; Zhao, Y.; Huang, W., Three-Dimensional Printing of Shape Memory Composites with Epoxy-Acrylate Hybrid Photopolymer. *ACS Applied Materials & Interfaces* **2017**, 9 (2), 1820-1829.
131. Tataru, G.; Coqueret, X., Hybrid free-radical and cationic photo-polymerization of bio-based monomers derived from seed oils – control of competitive processes by experimental design. *Polymer Chemistry* **2020**, 11 (31), 5067-5077.
132. Sands, J. M.; Jensen, R. E.; Fink, B. K.; McKnight, S. H., Synthesis and properties of elastomer-modified epoxy-methacrylate sequential interpenetrating networks. *Journal of Applied Polymer Science* **2001**, 81 (3), 530-545.
133. Nowers, J. R.; Costanzo, J. A.; Narasimhan, B., Structure-property relationships in acrylate/epoxy interpenetrating polymer networks: Effects of the reaction sequence and composition. *Journal of Applied Polymer Science* **2007**, 104 (2), 891-901.
134. Kuang, X.; Zhao, Z.; Chen, K.; Fang, D.; Kang, G.; Qi, H. J., High-Speed 3D Printing of High-Performance Thermosetting Polymers via Two-Stage Curing. *Macromolecular Rapid Communications* **2018**, 39 (7), 1700809.
135. New route planned to biobased ethylene glycol. *C&EN Global Enterprise* **2017**, 95 (46), 10-10.
136. Buntara, T.; Noel, S.; Phua, P. H.; Melián-Cabrera, I.; de Vries, J. G.; Heeres, H. J., Caprolactam from Renewable Resources: Catalytic Conversion of 5-Hydroxymethylfurfural into Caprolactone. *Angewandte Chemie International Edition* **2011**, 50 (31), 7083-7087.
137. Jung, J. H.; Ree, M.; Kim, H., Acid- and base-catalyzed hydrolyses of aliphatic polycarbonates and polyesters. *Catalysis Today* **2006**, 115 (1), 283-287.
138. Fiore, G. L.; Klinkenberg, J. L.; Pfister, A.; Fraser, C. L., Iron Tris(bipyridine) PEG Hydrogels with Covalent and Metal Coordinate Cross-Links. *Biomacromolecules* **2009**, 10 (1), 128-133.
139. Pu, Y.; Cao, S.; Ragauskas, A. J., Application of quantitative <sup>31</sup>P NMR in biomass lignin and biofuel precursors characterization. *Energy & Environmental Science* **2011**, 4 (9), 3154-3166.
140. Fang, C.; Zhu, X.; Cao, Y.; Xu, X.; Wang, S.; Dong, X., Toward replacement of methyl methacrylate by sustainable bio-based isobornyl methacrylate in latex pressure sensitive adhesive. *International Journal of Adhesion and Adhesives* **2020**, 100, 102623.
141. Hexig, B.; Alata, H.; Asakawa, N.; Inoue, Y., Generation of Compositional-Gradient Structures in Biodegradable, Immiscible, Polymer Blends by Intermolecular Hydrogen-Bonding Interactions. *Advanced Functional Materials* **2005**, 15 (10), 1630-1634.
142. Peer, G.; Dorfinger, P.; Koch, T.; Stampfl, J.; Gorsche, C.; Liska, R., Photopolymerization of Cyclopolymerizable Monomers and Their Application in Hot Lithography. *Macromolecules* **2018**, 51 (22), 9344-9353.
143. Grady, M. C.; Simonsick, W. J.; Hutchinson, R. A., Studies of higher temperature polymerization of n-butyl methacrylate and n-butyl acrylate. *Macromolecular Symposia* **2002**, 182 (1), 149-168.



144. Gorsche, C.; Harikrishna, R.; Baudis, S.; Knaack, P.; Husar, B.; Laeuger, J.; Hoffmann, H.; Liska, R., Real Time-NIR/MIR-Photorheology: A Versatile Tool for the in Situ Characterization of Photopolymerization Reactions. *Analytical Chemistry* **2017**, *89* (9), 4958-4968.
145. Gotro, J. Thermoset Characterization Part 14: Introduction to Dynamic Mechanical Analysis (DMA). <https://polymerinnovationblog.com/thermoset-characterization-part-14-introduction-dynamic-mechanical-analysis-dma/> (accessed 10.12.2021).
146. Polymerdatabase <https://polymerdatabase.com/polymer%20physics/Stress-Strain%20Behavior.html> (accessed 10.12.2021).
147. Kury, M. Tough photopolymers for 3D printing. PhD thesis, TU Wien, Vienna, 2019.
148. Fenouillot, F.; Rousseau, A.; Colomines, G.; Saint-Loup, R.; Pascault, J. P., Polymers from renewable 1,4:3,6-dianhydrohexitols (isosorbide, isomannide and isoidide): A review. *Progress in Polymer Science* **2010**, *35* (5), 578-622.
149. Feng, X.; East, A. J.; Hammond, W. B.; Zhang, Y.; Jaffe, M., Overview of advances in sugar-based polymers. *Polymers for Advanced Technologies* **2011**, *22* (1), 139-150.
150. Stensrud, K. Monoallyl, monoglycidyl ethers and bisglycidyl ethers of isohexides. US 9.290.509 B2, 2016.
151. Deepa, A. K.; Dhepe, P. L., Lignin Depolymerization into Aromatic Monomers over Solid Acid Catalysts. *ACS Catalysis* **2015**, *5* (1), 365-379.
152. Gandini, A., The irruption of polymers from renewable resources on the scene of macromolecular science and technology. *Green Chemistry* **2011**, *13* (5), 1061-1083.
153. Guzmán, D.; Santiago, D.; Serra, À.; Ferrando, F., Novel Bio-Based Epoxy Thermosets Based on Triglycidyl Phloroglucinol Prepared by Thiol-Epoxy Reaction. *Polymers* **2020**, *12* (2).
154. Nouailhas, H.; Aouf, C.; Le Guerneve, C.; Caillol, S.; Boutevin, B.; Fulcrand, H., Synthesis and properties of biobased epoxy resins. part 1. Glycidylation of flavonoids by epichlorohydrin. *Journal of Polymer Science Part A: Polymer Chemistry* **2011**, *49* (10), 2261-2270.
155. Gulino, D.; Galy, J.; Pascault, J.-P.; Tighzert, L.; Pham, Q. T., Etude des prépolymères époxydes par chromatographie et 1H NMR à 350 MHz. *Die Makromolekulare Chemie* **1983**, *184* (2), 411-429.
156. Brandrup, J., *Polymer Handbook*. 4 ed.; Wiley & Sons: New York, 1999.
157. Crivello, J. V., Effect of Temperature on the Cationic Photopolymerization of Epoxides. *Journal of Macromolecular Science, Part A* **2008**, *45* (8), 591-598.
158. Mete, Y. Novel initiators and green monomers for ionic photopolymerization. PhD Thesis, TU Wien, 2021.
159. Theophile, T., *Infrared Spectroscopy: Materials Science, Engineering and Technology*. IntechOpen: 2012.
160. Purut Koc, O.; Bekin Acar, S.; Uyar, T.; Tasdelen, M. A., In situ preparation of thermoset/clay nanocomposites via thiol-epoxy click chemistry. *Polymer Bulletin* **2018**, *75* (11), 4901-4911.
161. Fedtke, M.; Domaratus, F., Curing of epoxide resins by anhydrides of dicarboxylic acids: model reactions. *Polymer Bulletin* **1986**, *15* (1), 13-19.
162. Nicolau, A.; Mariath, R. M.; Martini, E. A.; dos Santos Martini, D.; Samios, D., The polymerization products of epoxidized oleic acid and epoxidized methyl oleate with cis-1,2-cyclohexanedicarboxylic anhydride and triethylamine as the initiator: Chemical structures, thermal and electrical properties. *Materials Science and Engineering: C* **2010**, *30* (7), 951-962.
163. Salmi, H.; Allonas, X.; Ley, C.; Defoin, A.; Ak, A., Quaternary ammonium salts of phenylglyoxylic acid as photobase generators for thiol-promoted epoxide photopolymerization. *Polymer Chemistry* **2014**, *5* (22), 6577-6583.
164. Hoyle, C. E.; Lowe, A. B.; Bowman, C. N., Thiol-click chemistry: a multifaceted toolbox for small molecule and polymer synthesis. *Chemical Society Reviews* **2010**, *39* (4), 1355-1387.
165. Foix, D.; Ramis, X.; Ferrando, F.; Serra, A., Improvement of epoxy thermosets using a thiol-ene based polyester hyperbranched polymer as modifier. *Polymer International* **2012**, *61* (5), 727-734.

166. Farooq, U.; Teuwen, J.; Dransfeld, C., Toughening of Epoxy Systems with Interpenetrating Polymer Network (IPN): A Review. *Polymers* **2020**, *12* (9), 1908.
167. Millipore, M. [https://www.merckmillipore.com/AT/de/product/msds/MDA\\_CHEM-818897?Origin=PDP](https://www.merckmillipore.com/AT/de/product/msds/MDA_CHEM-818897?Origin=PDP) (accessed 09.03.2022).
168. Taniguchi, I.; Duan, S.; Kai, T.; Kazama, S.; Jinnai, H., Effect of the phase-separated structure on CO<sub>2</sub> separation performance of the poly(amidoamine) dendrimer immobilized in a poly(ethylene glycol) network. *Journal of Materials Chemistry A* **2013**, *1* (46), 14514-14523.
169. ÇAkmakÇI, E.; ŞEn, F.; Kahraman, M. V., Isosorbide Diallyl Based Antibacterial Thiol–Ene Photocured Coatings Containing Polymerizable Fluorous Quaternary Phosphonium Salt. *ACS Sustainable Chemistry & Engineering* **2019**, *7* (12), 10605-10615.
170. Li, Q.; Ma, S.; Wei, J.; Wang, S.; Xu, X.; Huang, K.; Wang, B.; Yuan, W.; Zhu, J., Preparation of Non-Planar-Ring Epoxy Thermosets Combining Ultra-Strong Shape Memory Effects and High Performance. *Macromolecular Research* **2020**, *28* (5), 480-493.
171. Cheng, J.; Zhang, P.; Liu, T.; Zhang, J., Preparation and properties of hydrogels based on PEG and isosorbide building blocks with phosphate linkages. *Polymer* **2015**, *78*, 212-218.
172. Fache, M.; Auvergne, R.; Boutevin, B.; Caillol, S., New vanillin-derived diepoxy monomers for the synthesis of biobased thermosets. *European Polymer Journal* **2015**, *67*, 527-538.
173. Dworak, C.; Kopeinig, S.; Hoffmann, H.; Liska, R., Photoinitiating monomers based on di- and triacryloylated hydroxylamine derivatives. *Journal of Polymer Science Part A: Polymer Chemistry* **2009**, *47* (2), 392-403.

## Appendix

A preliminary study on the base-catalyzed degradation of poly( $\epsilon$ -caprolactone) was conducted to test the applicability of PCL as a precursor for the photopolymerizable soft matrix in IPNs, as the hard matrix is formed *via* base-catalyzed polyaddition of epoxy and alcohol monomers.

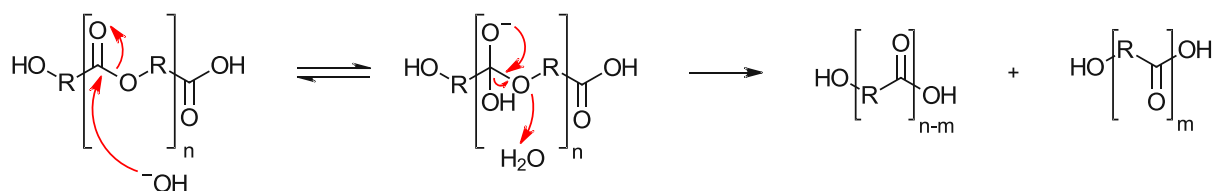


Figure 124: Schematic overview of base-catalyzed degradation of a polyester.

So, a degradation study was conducted that should imitate the thermal curing step of the IPN. Therefore, unmodified PCL ( $M_n \sim 16$  kDa) was reacted with sodium methanolate (NaOMe) at 90 °C. IPNs in this thesis contained a minimum soft matrix content of 10 wt% and a maximum hard matrix content of 90 wt%. In this composition, a maximum amount of base (1 wt% in respect to the hard network) is achieved and the calculated amount of NaOMe was added to unmodified PCL. After 24 h and 36 h of stirring at 90 °C, samples were drawn and analyzed *via* GPC. Table 55 shows the results of the GPC analysis.

Table 55: Results of the GPC analysis of alkaline-catalyzed PCL degradation

time [h]	$M_n$ [kDa]	$M_w$ [kDa]
<b>0</b>	15.8	29.3
<b>24</b>	4.11	5.12
	0.680	0.710
<b>36</b>	3.50	4.13
	0.650	0.730
	0.360	0.370

When comparing the results of the GPC analysis, it can be seen that the molecular weight of PCL is significantly decreased after 24 h and even more after 36 h. Therefore, it can be assumed, that alkaline-catalyzed degradation may occur during thermal curing of the IPN, making PCL an unsuitable toughness modifier.